Master's thesis

NTNU
Norwegian University of Science and Technology
Faculty of Natural Sciences
Department of Materials Science and Engineering

Eirik Bugten Hamnes

Softening Behaviour of a Commercial Al-Mn-Mg Alloy

Mikrostruktur og egenskaper under tilbakegløding av en kaldvalset Al-Mn-Mg legering

Master's thesis in Materials Science and Engineering (MIMT)
Supervisor: Knut Marthinsen
June 2019

NTNU
Norwegian University of
Science and Technology

Eirik Bugten Hamnes

Softening Behaviour of a Commercial Al-Mn-Mg Alloy

Mikrostruktur og egenskaper under tilbakegløding av en kaldvalset Al-Mn-Mg legering

Master's thesis in Materials Science and Engineering (MIMT)
Supervisor: Knut Marthinsen
June 2019

Norwegian University of Science and Technology
Faculty of Natural Sciences
Department of Materials Science and Engineering

NTNU
Norwegian University of
Science and Technology

PREFACE

This report is the result of the master project work (TMT4920) done at the Department of Materials Science and Engineering at the Norwegian University of Science and Technology (NTNU), during the spring semester of 2019. I would like to express my gratitude to my supervisor, Professor Knut Marthinsen, for his enthusiasm, encouragement and for providing me with valuable feedback throughout the project.

I would also like to acknowledge PhD-student Håkon Wiik Ånes for his extensive guidance throughout the entire project period. He has provided me Matlab and Python scripts, guided me with sample preparations and testing, and have always been prepared to help me when I needed it. Yingda Yu has guided me in the Electron Microscopy lab, and I would like to thank him for his technical support, helpful comments and for making me smile every day on the lab. Finally, I would like to thank my co-supervisors (and sponsors) Marte Brynjulfsen and Vibeke Hybertsen, Hydro Aluminium Rolled Products (HARP), Holmestrand for their guidance and support, and for supplying the material used.

Trondheim, June 2019
Eirik Bugten Hamnes

ABSTRACT

The work carried out in this master thesis project was conducted to investigate the softening behaviour of a non-heat treatable Al-Mn-Mg model alloy. The primary objective of the present work was set out to investigate the influence of processing conditions and associated changes in microchemistry, i.e. amount elements in solid solution and the precipitation state (dispersoids) on the softening behaviour of the alloy, after different degrees of deformation (cold rolling) and annealing temperatures, with a particular focus on concurrent precipitation.

The alloy investigated in the present work is a 3005-type aluminium alloy with the nominal chemical composition of 1.2 wt% Mn, 0.53 wt% Fe, 0.52 wt% Si, 0.43 wt% Mg, 0.24 wt% Zn, 0.20 wt% Cu, 0.03 wt% Mg and 0.02 wt% Ni. The investigated samples from the alloy came from the same coil, and the samples were thus processed similarly prior to cold rolling: The ingot was cast and subsequently preheated to 565°C. The preheated ingot was then hot rolled to a coil with a thickness of 3.5 mm. Finally, the coil was cold rolled to different degrees of deformations in the range between 46% and 87%. Subsequent to cold rolling, samples from the first, second and fourth deformation pass, i.e. corresponding to cold reductions of 46%, 67% and 87%, respectively, were annealed to different temperatures between 180°C and 330°C.

Measurements of electrical conductivity (EC), as well as the size and volume fraction of dispersoids, were carried out on the material to study the influence of microchemistry on the softening behaviour. The softening behaviour was quantified through measurements of mechanical properties, hardness, recrystallization texture and grain size.

From the obtained results, it has been shown that the softening behaviour upon annealing after cold rolling was found to be significantly influenced by the degree of deformation. Subgrain size measurements showed (as expected) that the driving force for recrystallization (P_D) was highest in the most deformed samples and lowest in the least deformed samples. The EC measurements also indicated that the former was most affected by precipitation and thus Zener pinning (P_Z), and the latter was presumably least affected, resulting in comparable softening kinetics. Another balance between driving force and Zener drag (large effective driving force; $P_D - P_Z$) resulted in recrystallization to initiate slightly earlier with somewhat faster softening kinetics in the intermediate deformations (%CR = 67).

The analysis of the softening behaviour was consistent with differences in recrystallized grain structure and texture between the different cold rolled samples, which clearly indicated that concurrent precipitation was most pronounced in the most heavily cold rolled samples. The

strength of P-texture, well known to correlate with the degree of concurrent precipitation, was found to be strongest in the most deformed condition (%CR = 87) and to increase most significantly from %CR = 67 to %CR = 87, and where also larger and more elongated recrystallized grains were observed in the latter. It was hoped that the quantitative dispersoid analysis could confirm the assumptions and interpretations made above, but the dispersoid analysis turned out to be uncertain and inconclusive in this respect, most probably due to limited statistics.

SAMMENDRAG

Arbeidet utført i denne masteroppgaven ble gjort for å undersøke tilbakeglødingsresponsen til en ikke utherdbar Al-Mn-Mg type legering. Hovedmålet med oppgaven var å undersøke hvordan forskjellige prosessbetingelser og endringer i mikrokjemi, dvs. mengde av elementer i fast løsning og dispersoider, påvirker gløderesponsen av legeringen etter forskjellige deformasjonsgrader (kaldvalsing) og glødetemperaturer, med spesielt fokus på dispersoider som utfelles under gløding ved temperaturer hvor recovery- og rekrystallisasjon skjer.

Legeringen som undersøkes i oppgaven er en 3005-type aluminiumslegering med følgende kjemiske sammensetning i vektprosent: 1.2% Mn, 0.53% Fe, 0.52% Si, 0.43% Mg, 0.24% Zn, 0.20% Cu, 0.03% Mg and 0.02% Ni. De undersøkte prøvene fra legeringen kom fra samme kveil, og prøvene var derfor prosessert på samme måte før kaldvalsing: Støpeblokker ble først støpt, og deretter forvarmet til 565°C. Etterpå ble de forvarmede støpeblokkene varmvalset til en kveil med tykkelse på 3.5 mm. Tilslutt ble kveilene kaldvalset til forskjellige deformasjonsgrader mellom 46% (1.90 mm) og 87% (0.47 mm). Etter kaldvalsing ble prøvene fra første, andre og fjerde valsestikk, dvs. deformasjonsgrader på henholdsvis 46%, 67% og 87%, glødet til forskjellige temperaturer mellom 180°C og 330°C.

Målinger av elektrisk ledningsevne, og størrelse og volumfraksjon av dispersoider ble utført på materialet for å studere påvirkningen av mikrokjemi på gløderesponsen. Gløderesponsen ble kvantifisert gjennom målinger av mekaniske egenskaper, hardhet, rekrystallisasjonstekstur og kornstørrelse. Gløderesponsen ved gløding etter kaldvalsing var sterkt påvirket av deformasjonsgraden. Subkornstørrelsemålinger viste (som ventet) at drivkraften for rekrystallisasjon (P_D) var høyest i de mest deformerte prøvene, og lavest i de minst deformerte prøvene. Endringene i elektrisk ledningsevne indikerte at de mest deformerte prøvene var mest påvirket av presipitering og dermed «Zener pinning» (P_Z), og de minst deformerte antagelig minst påvirket, som resulterte i at gløderesponsen ble sammenlignbar for disse to deformasjonsgradene. Et noe annet forhold mellom drivkraft og «Zener drag» (større effektiv drivkraft, ($P_D - P_Z$) resulterte i at rekrystallisasjonen startet litt tidligere med noe raskere oppmykningskinetikk i de mellomliggende deformasjonsgradene.

Denne analysen av gløderesponsen var konsistent med de rekrystalliserte kornstrukturene og teksturene mellom de forskjellige kaldvalsede prøvene, som indikerte at «concurrent precipitation» var mest utpreget i de mest deformerte prøvene, i tråd med styrken av P-tekstur

i de fullstendige rekrystalliserte tilstandene. P-teksturen økte mest signifikant fra %CR = 67 til %CR = 87, og større og mer langstrakte rekrystalliserte korn ble observert i %CR = 87.

Det var en forhåpning om at kvantitative analyser av dispersoider kunne bekrefte antagelsene og tolkningene gjort ovenfor, men analysene av dispersoider viste seg å være usikre og mangelfulle (begrenset statistikk), slik at det var vanskelig å trekke noen klare konklusjoner på basis av disse.

TABLE OF CONTENTS

LIST OF FIGURES

LIST OF TABLES

1. INTRODUCTION

In recent years, possible applications for aluminium alloys have steadily increased because they possess low weight, low melting point, easy recycling and high corrosion resistance. Due to such attractive features, aluminium alloys have shown a remarkable increase in the application in the automotive and food packaging industry. Aluminium is perfect for food packaging, it is completely impermeable, even when it is rolled at very low thicknesses. It lets neither taste, light nor aroma in or out. Also, because of the easy recycling of aluminium, only 5% of the energy initially required to produce primary aluminium is needed in the recycling process [1]. Hydro Aluminium in Holmestrand has a foundry, a rolling mill and a lacquering line. In the foundry, recycled beverage cans are melted and cast into ingots. Furthermore, the ingots are rolled to different thicknesses with different properties. The ingots are transformed into coils with thicknesses as low as 50 µm. The products made from rolled aluminium are utilized in several applications, e.g. car parts, food packaging and welded tubes. To keep up with the market, Hydro Aluminium in Holmestrand needs both a status on their products as well as assistance on optimization of their semi-finished products.

Hot and cold rolling are important processes of aluminium sheets. The deformation pass during rolling and the following annealing temperature are two important parameters during the rolling process, which determine the final properties of the rolled products. For example, annealing can improve ductility. Therefore, it is necessary to study the effects of rolling reductions and annealing on microstructural and mechanical characteristics of sheet Al alloys.

The present work was focused on a 3005-type model aluminium alloy with 1.2 wt% Mn, 0.53 wt% Fe, 0.52 wt% Si, 0.43 wt% Mg, 0.24 wt% Zn, 0.20 wt% Cu, 0.03 wt% Mg and 0.02 wt% Ni. The main objective was to study the influence of processing conditions and associated changes in microchemistry, i.e. amount elements in solid solution and precipitation state (dispersoids) on the softening behaviour of the alloy. More specifically, the alloy was pre-heated and hot rolled, and subsequently cold rolled to different degrees of deformation. Three variants of the alloy were achieved by taking samples from the first, second and fourth deformation pass after cold rolling, i.e. different degrees of deformation were obtained. A sample from the hot rolled condition was also studied. The three cold rolled variants were subsequently annealed at different temperatures ranging from 180°C to 330°C. Quantitative results for the microchemistry evolution in view of electrical conductivity as well as the size

and volume fraction of dispersoids and its influence on the softening behaviour, in terms of mechanical properties, hardness, recrystallization texture and microstructure were established.

2. THEORY

The first part of this section is intended to give a general description of aluminium and process route during rolling. Then the microstructure evolution during cold rolling and annealing (recovery and recrystallization) will be discussed. The presentation in these subsections are to a large extent based on the textbook description of the deformed state and softening kinetics as found in the textbook "Recrystallization and related annealing phenomena" by Humphreys et al. The next part describes the precipitation reactions that occur during homogenization and recrystallization (concurrent precipitation). In the last part, the deformation and recrystallization textures are considered, together with the most important recrystallization texture components.

2.1 Introduction

2.1.1 Aluminium

Second to steels, aluminium alloys are the most used as structural materials. Aluminium alloys display good ductility, low density, high strength and superior formability. In addition, the natural oxide layer created on the surface of the metal provides good corrosion resistance [2]. Because of the unique combination of properties, aluminium is one of the most versatile and popular materials for several applications. Aluminium has a density of 2,7 g/cm^3, which is one-third of the weight of steel. The low weight of aluminium and its alloys causes a reduced consumption of energy during transportation and is an advantage during the assembly of structures [1, 3]. Aluminium the third most abundant element after silicon and oxygen. Besides, it can be recycled without losing the quality of the metal. Compared to the energy needed for the production of primary aluminium, only about 5 percent of this energy consumption is required when aluminium is re-melted for new uses [1, 4].

2.1.2 3xxx Alloys

Wrought aluminium alloys are principally subdivided into two groups: Non-heat treatable alloys and heat-treatable alloys. The latter can be strengthened by heat treatment. Non-heat treatable alloys, on the other hand, cannot be strengthened by heat treatment. These alloys obtain their strength by initially alloying the aluminium by adding other elements. Various degrees of cold working (also known as strain hardening) is a method to further increase the strength of these alloys. The Al-Mn alloys are the wrought alloys that can be produced in the largest tonnage, and due to their good formability by pressing, rolling and drawing, they are used for beverage can bodies. The beverage can bodies that are produced annually matches

approximately 15% of the world's primary aluminium production. 3xxx alloys are popular because of their relatively high thermal conductivity, medium strength and good corrosion resistance, and are therefore often used in heat-exchangers [5-7]. Mn is the main alloying element in the 3xxx alloys and increases strength somewhat through solid solution strengthening. Al-Mn-Mg alloys belong to this group of alloys. In addition, fine $Al_6(Mn,Fe)$ dispersoids pin the grain and subgrain boundaries and increase the strength. Al-Mn alloys often contain 0.4-1.0% Mg, which provides a greater increase to strength than Mn in solid solution (ss). Fe and Si are also added to the 3xxx alloys to create large Mn-bearing constituent particles. These particles will act as nucleation sites for recrystallization after deformation. Dispersoids may precipitate during thermomechanical processing and influence the recovery and recrystallization behaviour of the 3xxx alloys [6, 7].

2.1.3 Processing Route

A typical processing route for non-heat treatable Al alloy sheets is given in Figure 2.1. After DC casting, sawing and milling, the alloy is heat treated (homogenization or pre-heating) to reduce micro-segregation, i.e to get an even particle structure and a uniform microstructure, and to relieve internal stresses [8].

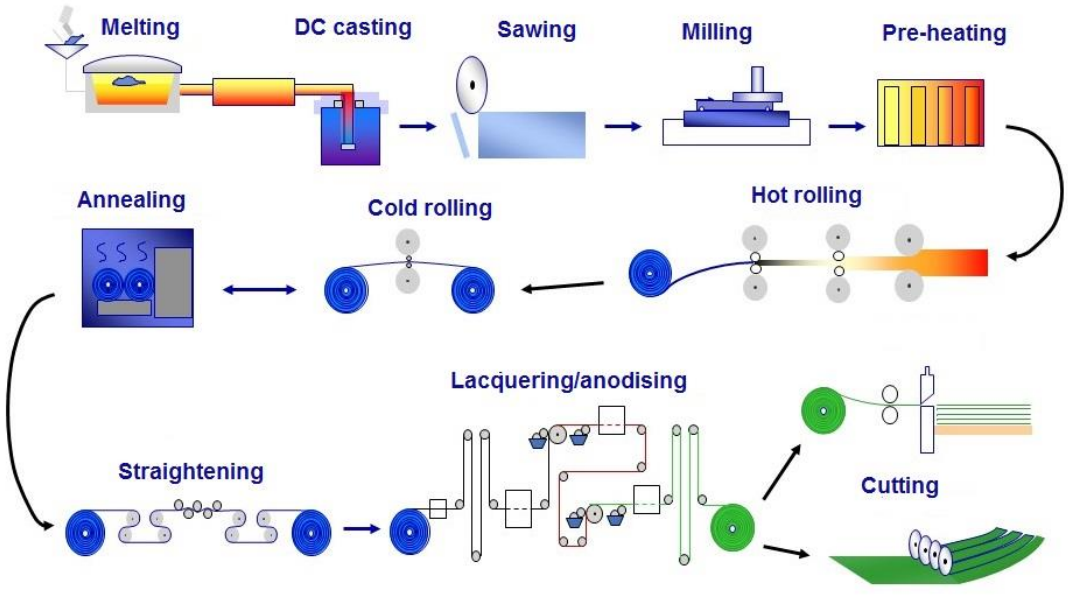

Figure 2.1: Schematic drawing showing a typical rolling process for aluminium alloys. The image was provided by Hydro Holmestrand.

The alloy is subsequently rolled. Rolling is the process of plastically deforming metal by passing it between rotating rolls. During rolling, the rollers pull the material forward only due to the existing friction between the metal and the roll surface, and the cross-section of the

material is subsequently reduced as the length increases. The initial material for rolled products is usually a rectangular cast ingot, with a weight of up to 30 tonnes each [9]. These ingots are typically homogenized at temperatures above around 550°C, but in some instances the ingots are pre-heated. After this heat treatment, the ingots are cooled to around 500°C and held for a sufficient time to ensure a uniform temperature for the subsequent hot rolling. Hot rolling is carried out at about 300°C, and coiled metal of about 2.5 mm that recrystallizes without furnace annealing is produced. The final sheet is achieved by cold rolling, a procedure which is further explained in the section below. Aluminium alloys are cold rolled at temperatures below 150°C to avoid recovery and recrystallization [5].

2.2 Microstructure evolution during cold deformation

Cold rolling is a typical cold work process in which metal stock is passed through a pair of rolls until the desired material thickness is achieved. During cold rolling, the microstructure in the material is considerably changed. These changes include elongated grains along the rolling direction (RD), and the total grain boundary area increases substantially [7], as can be seen from Figure 2.2.

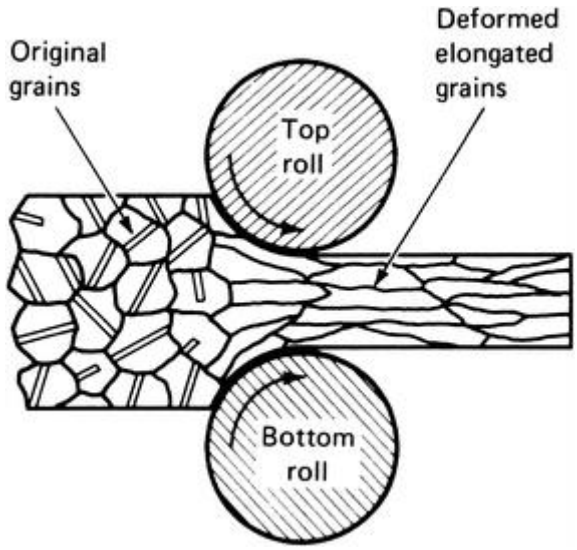

Figure 2.2: Illustration of a material work hardened during cold rolling [10].

The mechanics of metal deformation relay upon motion of dislocations and the slip system. During deformation, there is a preferred crystallographic plane with specific crystallographic directions where dislocation motion will occur. Dislocations move in response to resolved shear stresses applied in a slip system, and the magnitude of these depends on the applied stress and the orientation of the slip plane and the corresponding slip direction. The resolved shear stress τ_R can be expressed as [11]:

$$\tau_R = \sigma \cdot \cos\varphi \cdot \cos\lambda \quad (2.1)$$

σ is the applied tensile stress, φ is the angle between the direction of σ and the normal of the slip plane and λ is the angle between the direction of σ and the slip direction. Slip occurs in the most favourably oriented slip system, in other words, the slip system with the highest resolved shear stress, corresponding to angles of $\varphi = \lambda = 45°$. This critical value is termed the critical resolved shear stress τ_R *(max)* and determines when yielding of the material occurs. Plastic deformation initiates when the yield stress σ_y is reached, from the equation [11]:

$$\sigma_y = \frac{\tau_R(\max)}{(cos\varphi \cdot cos\lambda)_{\max}} \quad (2.2)$$

The denominator of this equation is called the Schmid factor, and the slip system with the highest Schmid factor will initiate plastic deformation. A Taylor orientation factor, *M*, is used to relate the yield strength of polycrystal metals to the critical resolved shear stress, τ_R*(max)* [12]:

$$\sigma_y = M \cdot \tau_R(max) \quad (2.3)$$

The Taylor factor depends on the crystallographic nature of the slip systems and the texture [13]. Texture is further explained in Section 2.5. Taylor has calculated $M = 3.06$ for face-centered cubic (FCC) metals for a random distribution of the grain orientations [14].

The internal structure within the grains is changed largely because of the accumulation of dislocations, and a typical subgrain structure is formed. The grain size of polycrystalline materials influences the mechanical properties. By reducing the grain size, the number of grains increase, and the amount of grain boundary area is increased. Furthermore, the grain boundaries act as a barrier against dislocation movement during plastic deformation. As a result, a fine-grained material will exhibit higher strength than a coarse-grained material. The grain size can be related to the yield strength through the Hall-Petch equation [11, 15]:

$$\sigma_y = \sigma_0 + kd^{-1/2} \quad (2.4)$$

where σ_0 and k are material constants, and d is the average diameter of the grains in mm. In contrast to strain hardening, this strengthening mechanism will generally not reduce ductility [11, 15].

The deformed state after cold deformation is closely linked with the microstructural evolution during and after annealing, in terms of grain size, shape and texture. During deformation, several microstructural phenomena occur and the most common will be described briefly in the following section. The deformation structure, as well as deformation heterogeneities introduced during cold work, will determine the softening behaviour during subsequent annealing. If the possibility exists for concurrent precipitation, the temperature and heating rate will play a significant role as well in the softening behaviour [16].

When the stress and strain measured from a tensile test are plotted against each other a typical stress-strain is obtained, as displayed in Figure 2.3. Stage II is the elastic range, where Hooke's law is valid, stage III is the curved part and stage IV is the part where stress is linearly increased with strain [7, 17].

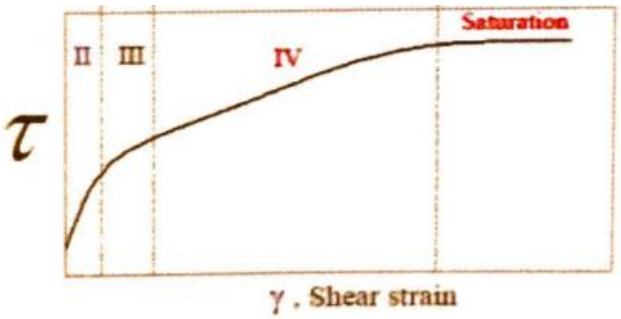

Figure 2.3: Schematic illustration of a stress strain curve deformed with a large strain at low-medium temperature, with the different stages indicated [18].

2.2.1 Substructure Development

Deformation occurs by slip in alloys with a high or medium value of stacking fault energy (γ_{SFE}). Aluminium alloys are high stacking fault energy alloys. The dislocations are typically arranged in a cell structure after deformation, as shown in Figure 2.4, and the cell boundaries are complex dislocations tangles. Large strain promotes the accumulation of dislocations in cell boundaries, and these boundaries become more defined with defined misorientations. Thus, subgrains can be obtained in a well-developed microstructure [16].

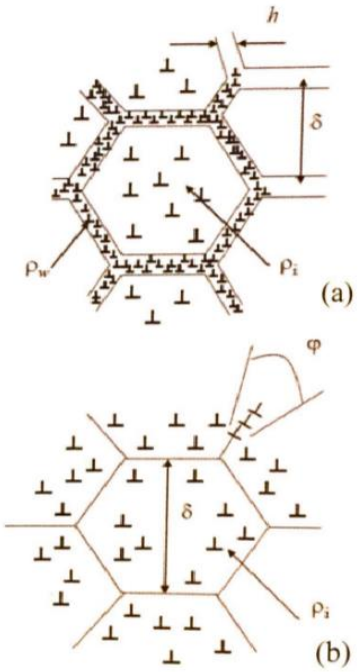

Figure 2.4: Microstructural description with the corresponding cell/subgrain size, boundary misorientation, and dislocation density in the interior of cells during (a) small deformations and (b) large strains [18].

The cell/subgrain size (δ), boundary misorientation (φ) and dislocation density in the interior of cells (ρ_i) are the most common parameters related to the microstructure changes. If metals are formed at room temperature, e.g. cold rolled, the cell/subgrain size will decrease with increasing strain, as shown in Figure 2.5 [16].

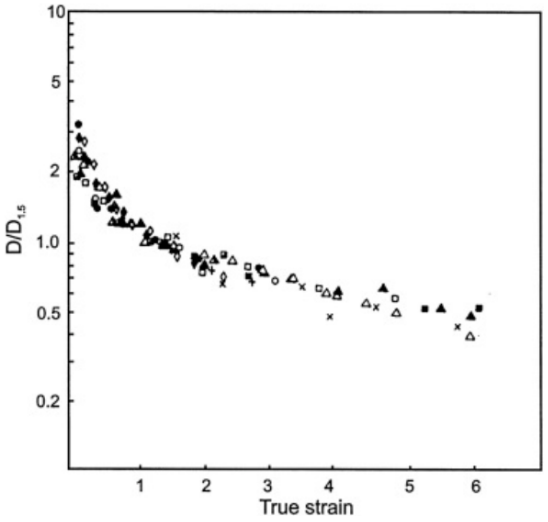

Figure 2.5: The average grain size as a function of true strain. The different metals studied are Al, Cu, Fe, Ni, Cr and Nb [16].

Misorientation is the difference in crystallographic orientation between two grains in a polycrystalline material. These parameters are shown for a typical stress-strain curve of plastic

deformation at relatively low temperatures divided into the four stages: II, III, IV and saturation. During stage II, the dislocation density in the interior of the cells increases with shear strain, as can be seen from Figure 2.6. After the increase during stage II, ρ_i saturates [16]. Nord-Varhaug et al. [19] investigated the evolution of microstructure in AA1050 and AA3207. They measured the dislocation density and subgrain size for these alloys for different deformation modes and found that the dislocation density reached a saturation density after cold rolling to strains larger than 0.2. Figure 2.6 shows that the boundary misorientation increases with shear strain during stage II and III. After the increase during stage II and III, the misorientation saturates. Furu et al. [20] studied the Al alloys 99.5%Al and 99.98%Al deformed to different strains and found that the misorientation rapidly increased with strain and then saturated at approximately 3° after a strain of about 1. The size of the cell/subgrain is decreased at a slower rate at later stages, as observed in Figure 2.6. At strains typically below 0.2, a uniform structure of equiaxed cells is formed. At higher strains (stage III) the originally equiaxed grains start to elongate in the direction of deformation. Gil Sevillano et al. [21] investigated the variation of average cell/subgrain size with increasing strains and found that during the initial deformation period of small strains, cell multiplication dominates the evolution of the microstructure, and the cell size decreased rapidly. At large strains, the slope of the reduction of cell size decreased [16]. The grain boundaries separating the different grains can either be low angle grain boundaries (LAGBs, also known as subgrain boundaries) or high angle grain boundaries (HAGBs), where LAGBs are those with a misorientation less than 15° and the latter are those with a misorientation more than 15°. The fraction of HAGBs is increased with deformation [22].

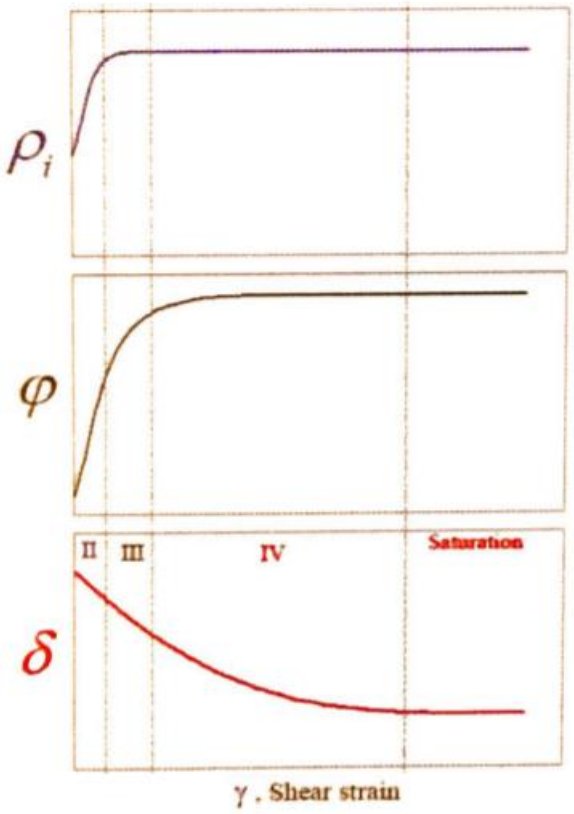

Figure 2.6: The corresponding cell/subgrain size, boundary misorientation and dislocation density in the interior of cells during the different deformation stages of a stress-strain curve deformed with a large strain at low-medium temperature are shown together [18].

Most of the work done during deformation of metal is released as heat and only about 1% remains as energy stored in the material. The stored energy during deformation is the driving pressure for recrystallization, where higher strains lead to increased stored energy and thereby accelerated recrystallization kinetics. Furthermore, the stored energy (P_D) can be described as a function of the average cell/subgrain size (δ) and the dislocation density in the interior of the subgrains (ρ_i) as follows [16, 23]:

$$P_D = \rho_i \frac{Gb^2}{2} + \alpha \frac{\gamma_{SB}}{\delta} \tag{2.5}$$

Here γ_{SB} is the subgrain boundary energy, G is the shear modulus, b is the Burgers vector and α is a geometric constant ($\alpha = 3$) [16]. The dislocation density within the subgrains is relatively low and amounts of typically only 1-2% of the total stored energy. As a result, the first term in Eq. 2.5 is often ignored [23]. The subgrain boundary energy can be calculated using the Read-Shockley relationship [16]:

$$\gamma_{SB} = \frac{Gb}{4\pi(1-\nu)}\varphi ln\left(\frac{e\varphi_c}{\varphi}\right) \quad (2.6)$$

φ is the angle of misorientation, φ_c is the critical misorientation for a boundary defined as a HAGB (usually ≈ 15°), and ν is the Poisson's ratio [16]. The cell/subgrain size will be referred to as only "subgrain size" in the rest of the thesis.

2.2.2 Deformation Heterogeneities

During cold deformation, certain microstructural characteristics for the deformed state develop. Equiaxed dislocation cells form at the initial stage of small strains and are considered the smallest volume element in a grain. Blocks of dislocations cells are surrounded by dislocation boundaries, and the boundaries include dense dislocation walls and microbands. Microbands are substructural features illustrated in Figure 2.7 (a) and dominate the substructure evolution at low to intermediate strains, and are present at most strains [24]. Microbanding becomes the typical slip mode if an aluminium alloy contains a substantial number of elements in solid solution [25]. As can be seen from the figure, microbands consist of double dislocation walls, approximately 0.2 µm and enclosing a volume possessing 1-3° misorientation with respect to the surrounding matrix. The low misorientation means that they are of no significance as nucleation sites for recrystallization. Dislocations generated by further deformation to large strains ($\varepsilon > 1.0$) are absorbed, and the microstructure consists of a banded subgrain structure parallel to the rolling direction separated by lamellar dislocation boundaries, as illustrated in Figure 2.7 (b) [26, 27].

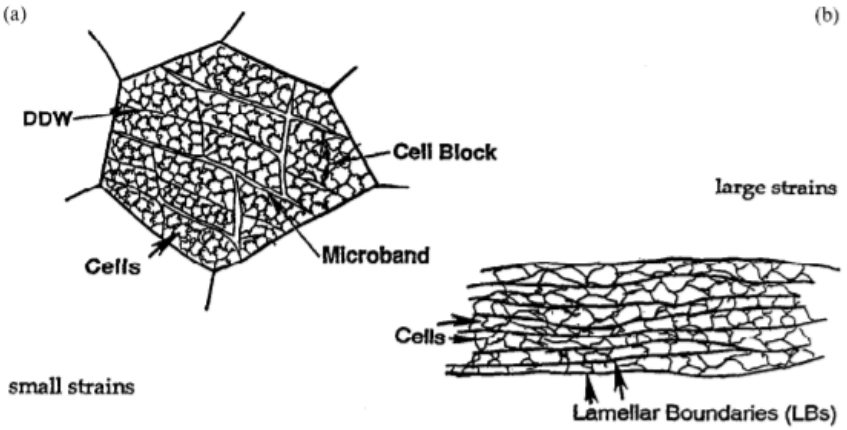

Figure 2.7: Schematic drawing of grain subdivision at (a) small strains (b) large strains [28].

When the dislocation density saturates at intense shearing strain, a phenomenon called shear banding occurs, and becomes the alternative slip mode. Shear bands are not crystallographic in

nature and may pass through several grains [16]. Fine subgrains are formed in the band with large misorientations to their surroundings, as shown in Figure 2.8. Shear banding is less frequent in aluminium as the formation of them are largely influenced by the stacking fault energy, and the critical rolling reduction for the onset of shear banding becomes higher [29].

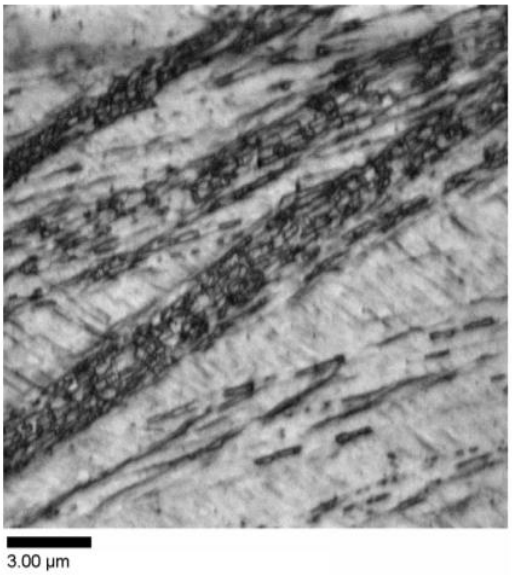

Figure 2.8: EBSD pattern quality map of a shear band in a material cold rolled to a deformation of 77%, where the subgrains can clearly be seen [29].

Individual grains might divide into regions of different orientation. They provide a source of high angle boundaries within grains, which is required for nucleation of recrystallization (see Section 2.3.3). These regions of different orientations in individual grains are called deformation bands. The narrow region separating the deformation bands are termed transition bands, and they are regions of sharp orientation gradients indicating an ideal site for nucleation of recrystallization [16]. Humphreys et al. [16] define the orientation gradient, $\Omega = d\theta/dx$, as "the rate of accumulation of misorientation across some region of the microstructure".

In aluminium alloys, the development of deformation zones occurs around the hard non-deformable constituent particles larger than approximately 1-2 µm during deformation, as illustrated in Figure 2.9. The size of the deformation zones and the microstructure are determined mainly by the particle size, temperature and applied strain. These zones are associated with high dislocation density and small subgrain size, i.e. locally a high stored energy, as well as high angle boundaries to the surrounding. As a result, they can act as nucleation zones for recrystallization [16]. This nucleation mechanism termed particle stimulated nucleation (PSN) is further discussed in Section 2.3.3.

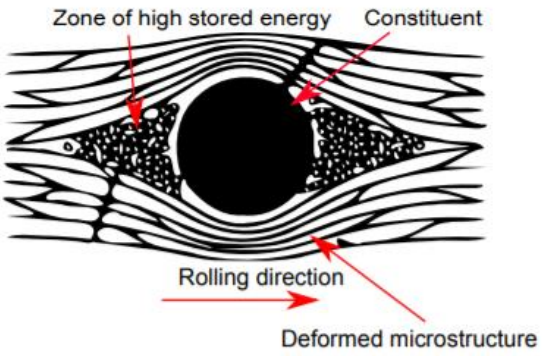

Figure 2.9: Schematic illustration of a deformation zone around a constituent particle [30].

2.3 Softening behaviour of deformed material

Cold working will increase properties such as yield strength and ultimate tensile strength as a result of increased dislocation density. However, some effects from cold working are undesirable, such as the loss of ductility and the presence of residual stresses. Annealing can be carried out to reverse the effects of cold working by eliminating the achieved strain hardening and eliminate residual stresses, and thereby achieve proper formability properties for the subsequent forming processes. Also, a specific microstructure can be produced [31].

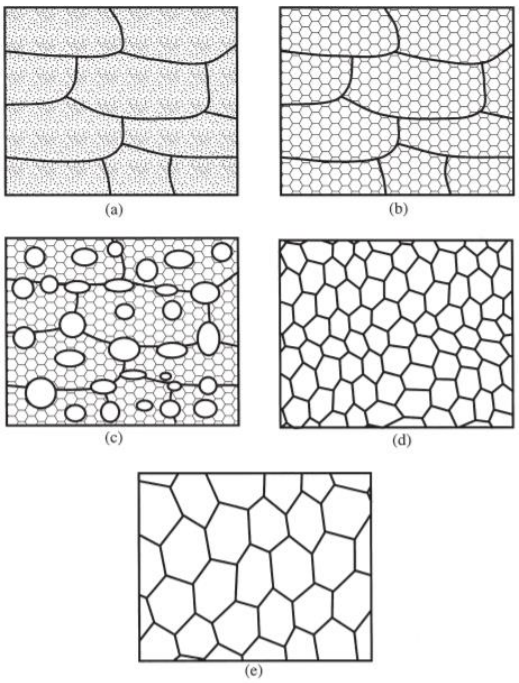

Figure 2.10: Schematic diagram displaying the effect of annealing temperature on the microstructure of deformed metals. The different pictures illustrate the main reactions occurring during the annealing process: (a) Deformed state (b) Recovered (c) Partially recrystallized (d) Fully recrystallized (e) Grain growth [32].

When a metal is annealed, it is first heated to a specific temperature and then kept at that temperature for an adequate amount of time. The metal is finally cooled, usually at room temperature. Three main reactions occur during the annealing process of a deformed metal: *Recovery* at a low-temperature stage, *recrystallization* where new grains nucleate and finally *grain growth* if the annealing is allowed to continue after completed recrystallization [31, 33]. Recovery involves the loss and rearrangement of dislocations, whereas recrystallization is dominated by the migration of grain boundaries [34]. The effect of annealing temperature on the microstructure of cold worked metals can be seen in Figure 2.10.

2.3.1 Recovery

The definition of the word recovery is "the process of returning to a normal condition" [26]. Recovery is a softening process by which the microstructure evolves from a chaotic and high energy state into a well-defined, low energy structure consisting of dislocation free subgrains. Deformed grains can reduce their stored energy by the removal or rearrangement of defects, primarily dislocations, in the grain structure. This process occurs prior to recrystallization when heat treatment is carried out on a deformed material, which partially restores the properties to their values before deformation, and is termed *static recovery* [26, 34]. Figure 2.11 shows the change in mechanical properties as a function of static recovery, recrystallization and grain growth.

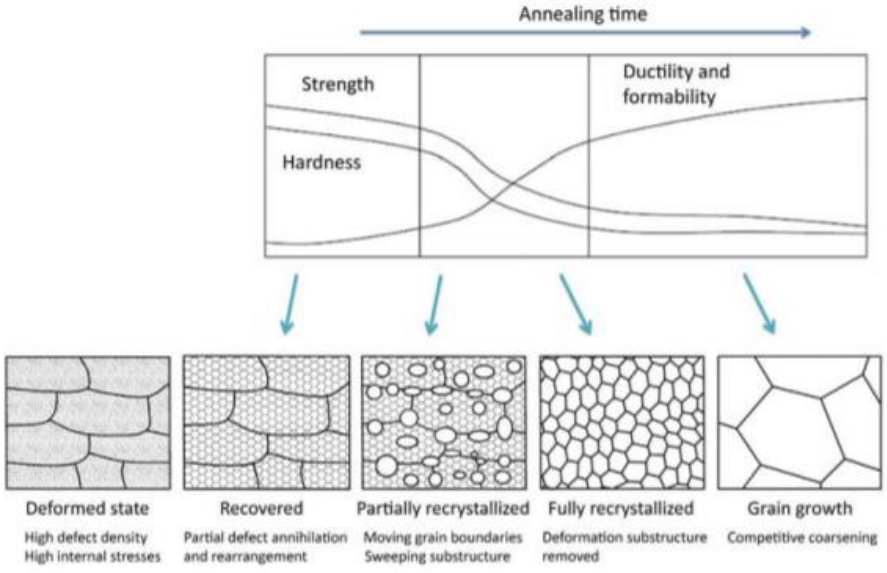

Figure 2.11: Typical change in mechanical properties during recovery, static recrystallization, and grain growth [35].

Raabe [35] states that "static recovery can be well observed at rather modest temperatures already far below the recrystallization temperature of about 1/3-1/2 of the absolute melting

point". Humphreys et al. defined the recrystallization temperature as "the temperature at which the material is 50% recrystallized" for experiments where annealing is carried out at various temperatures for a constant time. If recovery occurs during deformation at high temperatures it is termed *dynamic recovery*, where stored energy continues to be introduced even as it is decreased by the recovery process. However, the latter phenomenon will not be discussed further in this thesis. Both recovery and recrystallization are driven by the stored energy produced in the material after deformation, and they will therefore be competing processes. A significant amount of prior recovery can influence the recrystallization kinetics, due to the lowering of stored energy from deformation work. It is sometimes difficult to distinguish between recovery and the early stages of recrystallization as subgrain growth plays an important role in the nucleation of recrystallization [34]. However, Doherty et al. [36] differentiated recovery from recrystallization with the recommendation that recovery can be defined as "all annealing process occurring in deformed materials that occur without the migration of a high angle grain boundary". The substructure will be consumed as a result of recrystallization, and recovery can no longer occur [34].

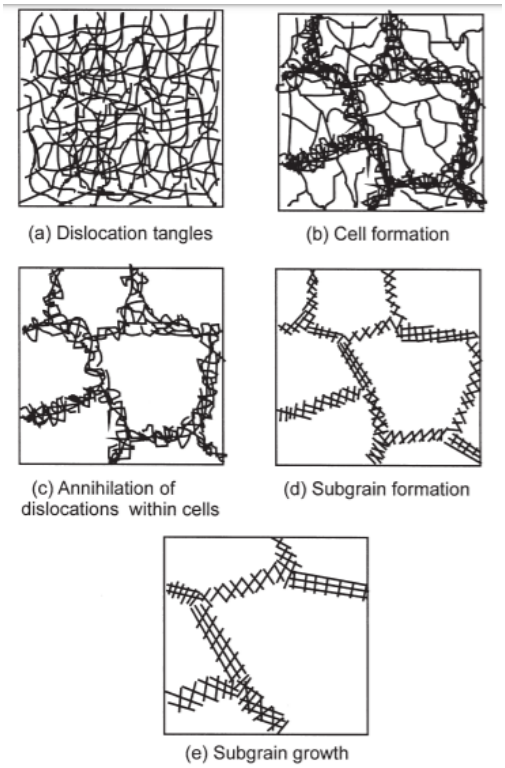

Figure 2.12: Various stages in the recovery of a plastically deformed material [34].

Recovery results in a series of microstructural changes, schematically shown in Figure 2.12. Dislocations are first annealed out following a subsequent subgrain formation and growth stage. The decrease of stored energy of deformation is caused by two mechanisms: The annihilation of dislocations and the rearrangement of dislocations [34]. In metals with high stacking fault energy such as aluminium, the dislocations arrange themselves from the deformed condition into cell networks within the existing grains, where the cell walls consist of tangles of dislocations, as illustrated in Figure 2.12 (b) [36]. Dislocations with Burgers vectors of opposite directions may annihilate by glide, climb and cross-slip, and their contribution to the stored energy is removed. During the recovery process, the dislocation density within the subgrains decreases. An unequal number of dislocations with opposite signs are produced during deformation, and the excess dislocations will rearrange into LAGBs as annealing continues, and the cell structure becomes a subgrain structure [7, 34]. The simplest case of rearrangements of dislocations in aluminium is often known as polygonization, where a particularly simple type of LAGBs is formed called tilt boundaries. The tilt boundaries consist only of edge dislocations, and Humphreys et al. [37] state that "if the spacing of the dislocations of Burgers vector b in the boundary is h, the crystals on either side of the boundary are misoriented by a small angle θ", where [37]:

$$\theta = \frac{b}{h} \tag{2.7}$$

The energy of such a boundary is given by the Read-Shockley equation (cf. Eq. 2.6). As recovery proceeds fewer boundaries with a higher misorientation are formed. The driving force is the increase in subgrain boundary energy and decrease in energy per dislocation with increasing misorientation [37].

A subgrain structure differentiates from normal grain structures as it consists mainly of LAGBs. Following the subgrain formation, recovery will continue with coarsening of the subgrains, and the stored energy in the material is further lowered. The most accepted mechanism to explain subgrain growth is subgrain boundary migration, where large subgrains grow on the expense of the smaller ones similarly to ordinary grain growth; the average size increases, while the number of subgrains decreases [34].

If the boundary energy, γ_s, is constant the driving pressure for subgrain growth can be expressed as [34]:

$$P = \frac{\alpha \gamma_s}{R} \tag{2.8}$$

2.3.2 The Zener Drag

The Zener drag is a retarding force on the nucleation of recrystallization as well as the recrystallization kinetics because of the dispersion of small precipitates/dispersoids. The effect of these small, closely spaced particles is primarily in pinning LAGBs and HAGBs [38-40], as illustrated in Figure 2.13. The growing grain boundary moves unhindered at $t = t_1$. When a boundary intersects a particle at $t = t_2$, a region of the boundary is effectively removed by the particle and the energy is consequently lowered. In other words, boundaries are attracted to particles. To move the boundary past the particle at $t = t_3$, a force must be applied to separate them [26, 40]. If the particles are randomly distributed and incoherent, and spherical particles with radius *R* are assumed, the following equation can be given for the Zener drag [40]:

$$P_Z = \frac{3 f \gamma}{2 R} \tag{2.9}$$

where *f* is the volume fraction of particles and γ is the grain boundary energy.

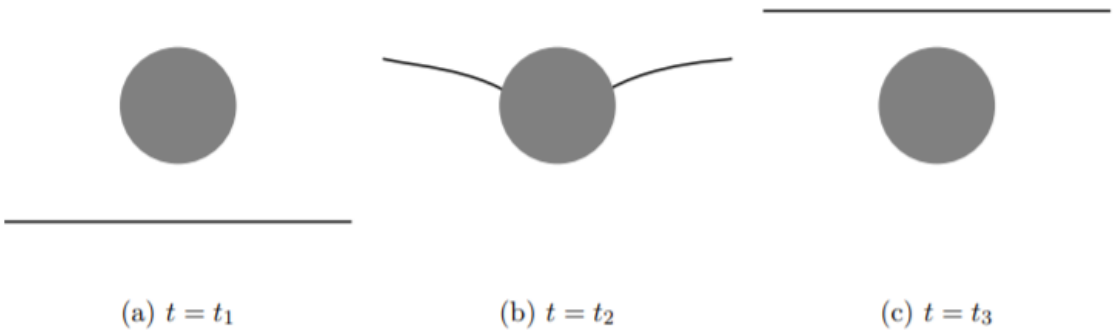

Figure 2.13: The effect of the Zener-drag on a growing grain boundary. The black line represents a grain boundary growing upwards. The gray circle is a dispersoid. Time is increasing from left to right, so $t_3 > t_2 > t_1$ [30].

The precipitation of small particles influences subgrain growth during recovery, recrystallization and grain growth during recrystallization. During recovery precipitated dispersoids prevent the subgrains to grow large enough to nucleate new viable grains, which

means that finely dispersed, small particles will retard both the nucleation and the growth of recrystallized grains [34]. Hansen and Bay [41] found that the oxide particles in an aluminium-alumina alloy retarded subgrain growth and delayed the formation and growth of recrystallization nuclei, but nucleation sites remained unchanged. These effects result in larger recrystallized grain size and slower recrystallization kinetics. As Wang [7] mentions in his work, a study conducted on dilute Al-Fe alloys has shown that precipitation and pinning of sub-boundaries are very effective in retarding the subgrain coalescence, thus the nucleation of recrystallization. Subgrain coalescence is also a mechanism to explain subgrain growth but is not considered in this thesis.

2.3.3 Recrystallization

Recrystallization is a softening process and involves the nucleation of dislocation free grains that grow until the recovered or deformed microstructure is consumed. Recrystallization further reduces the amount of stored energy, which provides the driving force for recrystallization. As long as there are un-recrystallized regions left behind in the microstructure, nucleation of dislocation free grains can occur at any point in time during the recrystallization process [26, 42]. Doherty et al. [36] defined recrystallization as: "The formation of a new grain structure in a deformed material by the formation and migration of high angle grain boundaries driven by the stored energy of deformation." In this thesis, HAGBs are defined as boundaries with a misorientation angle greater than 15°. As previously mentioned, HAGBs do not migrate during recovery, which differentiates recovery from recrystallization [34]. When the accumulated strain energy is the driving force for recrystallization, the process is termed *static recrystallization* and occurs when deformed materials are held at high temperatures. Recrystallization can occur during deformation (e.g. hot rolling) if sufficient energy is stored, which is termed *dynamic recrystallization* [43]. However, the latter recrystallization process is not discussed further in this thesis.

There are some rules of recrystallization that are in most cases obeyed and rationalizes the recrystallization behaviour of materials [7, 42]:

1. In order to provide a nucleus and enough stored energy to provide its growth, a minimum deformation is needed.
2. Recrystallization requires a minimum temperature for the necessary microscopic mechanisms to occur and this temperature decreases as the time of annealing increases.
3. The stored energy, which provides the driving force for recrystallization, and the number of potential nuclei increase with deformation. As a result, the temperature at which recrystallization occurs decreases with the degree of deformation.
4. A higher degree of deformation results in a smaller recrystallized grain size, as higher deformation provides more nuclei per unit volume.
5. A larger starting grains size and higher deformation temperature results in an increased recrystallization temperature.

The texture, initial grain size and the presence of second phase particles will influence recrystallization. The rate of recrystallization can depend on the starting texture and the final deformation texture. Furthermore, the deformation texture and the texture resulting from recrystallization may be affected by the initial grain size. In other words, the recrystallization temperature and kinetics are dependent on the grain orientations. Depending on the size, density and distribution of second phase particles, they may either act to retard or encourage recrystallization [42]. Coarse particles above approximately a micron often accelerate recrystallization through PSN, resulting in weaker recrystallization textures, and will be further explained in Section 2.5.2. On the other hand, small dispersoids below approximately a micron can retard the nucleation step of recrystallization through Zenner pinning, resulting in slow kinetics and large recrystallized grain size [40, 44]. The Zener drag was discussed in Section 2.3.2.

Nucleation is the process by which recrystallization initiates. In this initial nucleation period, the nuclei form and occurs predominantly at deformation heterogeneities. In other words, all the nuclei are pre-existing in the deformed state of aluminium alloys. During the nucleation period the subgrains are growing at a constant rate consuming the deformed material, and must reach a certain diameter to form a viable recrystallization grain, calculated from the Gibbs-Thomson relationship [23, 42]:

$$\delta > \delta_{\mathrm{C}} = \frac{4\gamma_{\mathrm{GB}}}{P_{\mathrm{D}} - P_{\mathrm{Z}}} \tag{2.10}$$

where γ_{GB} is the specific grain boundary energy, P_{D} is the stored energy (cf. Eq. 2.5) and P_{Z} is the Zener drag, a retarding force due to finely dispersed dispersoids (cf. Eq. 2.9). The growth rate of a recrystallized grain is given by [23]:

$$v = \frac{dR}{dt} = M(P_{\mathrm{D}} - P_{\mathrm{Z}}) \tag{2.11}$$

where the mobility of the grain boundary, M, is defined by [23]:

$$M = \frac{M_0}{RT} exp(-\frac{U_{\mathrm{GB}}}{RT}) \tag{2.12}$$

M_0 is a material constant and U_{GB} is the activation energy for grain boundary migration. Mobility is assumed to be independent of orientation.

The JMAK equation predicts the fraction recrystallized based on a few known constants [45]:

$$X_{\mathrm{V}} = 1 - exp(-kt^n) \tag{2.13}$$

where k is a constant and n is the growth exponent. The growth exponent is, according to theory, equal to 4 if a constant nucleation rate is applied, and equal to 3 in case of site saturation nucleation kinetics. According to Humphreys et al. [42] site saturation occurs "when nucleation rate decreases so rapidly that all nucleation events effectively occur at the start of recrystallization", and is an assumption often made for nucleation of recrystallization in aluminium alloys. For aluminium alloys, the n-values are often measured to be around 2 or

even smaller [7, 42]. If site saturation nucleation kinetics applies, the final recrystallized grain size, D_{RX}, can be calculated from the following equation [46]:

$$D_{RX} = 1/\sqrt[3]{N_{tot}} \quad (2.14)$$

where N_{tot} is the total number of nucleation sites.

As previously mentioned, nucleation occurs at inhomogeneities in the deformed microstructure and includes nucleation at pre-existing HAGBs, transition bands and shear bands and PSN. The mentioned nucleation sites and mechanisms are briefly presented below.

Nucleation at pre-existing HAGBs is a nucleation mechanism which can be operated by two phenomena, *strain induced grain boundary migration (SIBM)* and *ordinary grain boundary nucleation* [42]. The former mechanism was first reported by Beck and Sperry [47] in high purity aluminium and occurs when a pre-existing HAGB bulges out as a result of differences in stored energy between two sides of the grain boundary and is illustrated in Figure 2.14. The difference in stored energy is due to differences in subgrain size. Furthermore, the side with a larger subgrain size (and thus lower stored energy) will grow at the expense of the side with smaller subgrain size [42]. According to Bellier and Doherty [48], SIBM is the dominant recrystallization mechanism for reductions of less than 20%. In the present study, only reductions above 46% have been investigated, which indicates that this mechanism will not be of great importance in this work. However, Somerday and Humphreys [49] found that SIBM was also an important nucleation mechanism in Al-1.3wt%Mn cold rolled to a reduction of 90%, similar to one of the cold reductions investigated in the present study.

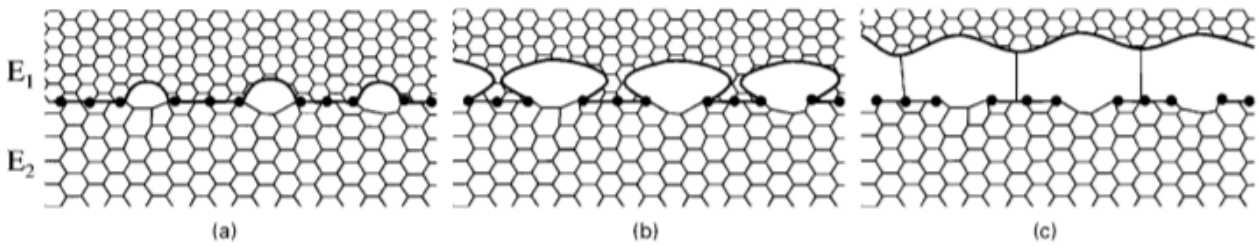

Figure 2.14: Schematic diagrams illustrating the mechanism of SIBM [49].

Ordinary grain boundary nucleation also occurs at pre-existing grain boundaries, and this nucleation mechanism originates in regions of large orientation gradients. The new grains are

separated from their parent grains by sharp boundaries. The orientation of the new grains and the parent grains, respectively, differ a lot [42]. An example of this nucleation mechanism was observed by Hutchinson [50] in iron bicrystal specimens in which the new grains were misoriented by 30° from the parent grains.

Transition bands, as described in Section 2.2.2, separates parts of a grain into regions of different orientations, as a result of inhomogeneous deformation. A transition band has been shown to act as a favoured site for recrystallization by Dillamore et al. [51]. Adjacent volumes of a grain can deform on different slip systems and rotate towards different stable end orientations. Sharp orientation gradients will occur in the region between the different parts of the grain, indicating an ideal site for recrystallization [42, 51].

Shear bands. Nucleation may easily take place in shear bands due to the high stored energy and the large orientation gradients to the surrounding areas [42]. In aluminium, the grains were oriented close to the S-texture component, as reported by Hjelen et al. [52]. On the other hand, a study conducted by Duggan et al. [53] showed that the orientations of the grains in α-brass were widely scattered.

PSN. Large non-deformable second phase particles (constituent particles) form during casting and solidification if the alloy contains a certain amount of alloying elements. The subsequent homogenization will not remove these particles, but they can break up during deformation (e.g. cold rolling). PSN can occur in the material if the size after deformation is still larger than a critical diameter [40]. Humphreys [54] investigated the nucleation of recrystallization at large second phase particles in deformed aluminium alloys single crystals and found that PSN occurs above a critical particle diameter of 1 μm, which typically increases with decreasing strain. However, a study conducted by Ye et al. [55] showed that the critical particle diameter could be even smaller. Deformation zones are formed around the large second phase particle during deformation, characterized by high dislocation densities, high stored energy and large orientation gradients, and are ideal sites for the development of recrystallization nuclei. The number of nucleation sites is controlled by alloy composition and processing. Thus, PSN provides a way to control the recrystallization by controlling the number and size of particles. In Al alloys that contain these large second phase particles, the recrystallization is strongly accelerated compared to single-phase materials because of PSN [26, 40, 56]. Figure 2.15 shows the occurrence of PSN in an Al-Si alloy.

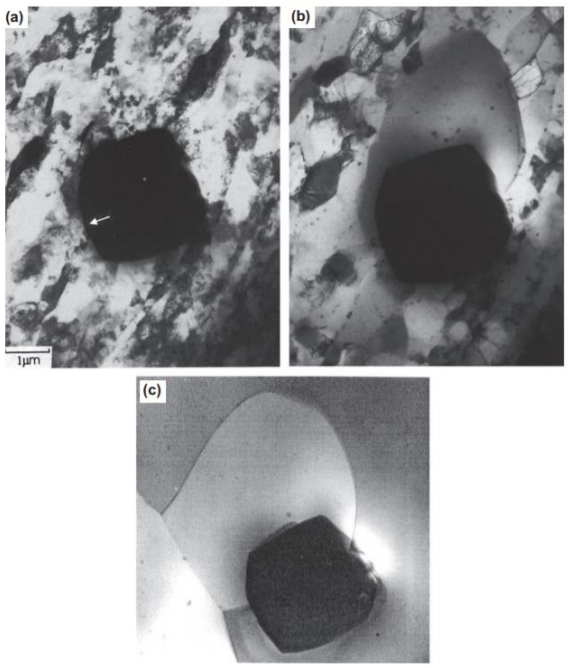

Figure 2.15: The occurrence of PSN in an Al-Si alloy. (a) Recrystallization originates in the arrowed region of the deformation zone close to the particle, (b) recrystallization has consumed the deformation zone, (c) further growth of the PSN grain is prevented by recrystallization, which has originated elsewhere [40].

The growth velocity of a subgrain is proportional to the magnitude of the orientation gradient (not shown in the present work), and the misorientation increases as a subgrain grow in an orientation gradient [34, 40]. Potential recrystallization nucleation is formed when the misorientation has reached 10°-15°, which is that of a HAGB. A subgrain must grow in the magnitude inversely proportional to the orientation gradient to achieve a HAGB. If this equation is derived, the time for the formation of a nucleus will be inversely proportional to the square of the orientation gradient. The orientation gradient is greatest close to a particle surface. Nucleation will therefore be favoured there.

The nucleus formed within the deformation zone is subject to two pressures: A driving pressure due to dislocation density which is proportional to the strain, and a retarding pressure due to its radius of curvature. If the driving pressure is higher than the latter, the nucleus will grow [7, 40]. According to work by Humphreys [54] and Vatne et al. [23], the critical particle diameter for a successful nucleation event is given by the Gibbs-Thompson equation (cf. Eq. 2.10).

Many commercial alloys will naturally contain both large and small particles. The former will act as sites for PSN, whereas the latter will act as a retarding force on the nucleation of recrystallization. From the Gibbs-Thompson relationship (cf. Eq. 2.10) it can be observed that

as the Zener drag force increases, the critical diameter for PSN increases. As a result, fewer particles can act as nucleation sites and the recrystallized grain size will increase [40].

2.4 Precipitation

Particles are precipitated from supersaturated solid solutions. A supersaturated solid solution is a solid solution that contains more of the dissolved material than could be dissolved by the solvent under normal conditions [57]. During heating of a sample, decomposition of a supersaturated solid solution occurs by nucleation and growth of a precipitate. During nucleation and growth, there is an interface between the precipitate and the matrix, and matrix solute atoms reach the interface through diffusion. Nucleation is controlled by the Gibbs free energy and is mainly occurring at heterogeneities, i.e. at clusters of vacancies, dislocations and subgrain and grain boundaries, because they are associated with a higher average free energy compared to the metal matrix. These heterogeneities act as nucleation sites for precipitation and speed up diffusion significantly [17, 26].

Constituent particles and dispersoids are the two categories of particles influencing the recrystallization kinetics in 3xxx Al alloys. The difference between them is defined by the size of the particles and when they are formed. Constituent particles are relatively large (radius ≈ 1-50 μm) primary particles precipitated mainly on grain boundaries during casting and solidification. As mentioned in the previous section, large particles can act as nucleation sites during recrystallization through PSN. Dispersoids, however, are considerably smaller (radius ≈ 0.1 μm) particles precipitated mainly during homogenization and the subsequent annealing processes. Because dispersoids are smaller than the critical diameter (cf. Eq. 2.10), they will not act as nucleation sites [7, 58]. However, they will still have an impact on recrystallization kinetics through the Zener drag (cf. Eq. 2.9) because of the small particle size, as described in Section 2.3.2

2.4.1 Precipitation During Homogenization or Pre-heating

As previously stated, the main alloying element in the 3xxx Al alloys is Mn, together with Si and Fe. Most of the Mn exists in the solid solution during the ingot solidification of 3xxx Al alloys, which results in the supersaturation of the solid solution in the as-cast state. Less Mn in solid solution leads to a decreased supersaturation and thus less potential for precipitation. The first processing step after casting is the homogenization, or in some instances pre-heating. Homogenization or pre-heating is essential to reduce the concentration of Mn in solid solution and to obtain the right size, density and distribution of small dispersoids, which will influence

the further processing of the material. During subsequent heat treatment after casting, different types of second-phase particles will precipitate from the aluminium matrix due to the decomposition of the supersaturated solid solution [7, 59-61]. The cubic $Al_6(Mn,Fe)$ and orthorhombic α-Al(Mn,Fe)Si will form in the 3xxx Al alloys, possibly as both constituent particles and dispersoids. The emphasis in this thesis will be on the latter. Dispersoids have a small direct effect on the mechanical properties, but due to their rather high density and high thermal stability they can have a strong effect to prevent recovery, recrystallization and grain growth [7, 61].

The precipitation behaviour of dispersoids depends on chemical composition. Studies [62, 63] show that the addition of Fe and Si in Al-Mn alloys has a strong influence on precipitation behaviour. It has been found that Fe and Si accelerate the precipitation rate of Mn-containing dispersoids and decrease the solubility of Mn in solid solution. Increasing the Fe content favours the precipitation of $Al_6(Mn,Fe)$, while increasing the Si content favours the precipitation of α-Al(Mn,Fe)Si when Fe is also present in the alloy [61, 64]. The latter phase is the commonly observed dispersoid phase in commercial alloys [61], and the dispersoids are formed if the Si-content is larger than 0.07 wt% [65]. α-Al(Mn,Fe)Si is an important phase in 3xxx Al alloys, the amount of Si necessary to enhance the precipitation of the phase is very low and these dispersoids are considered to be incoherent with the Al matrix. Some Al-Mn alloys contain Mg, and the precipitation behaviour in these alloys are different due to the presence of Mg. β'-Mg_2Si is the first phase to precipitate during heating at industrial heat-up rates. Between the β' phase and the α phase, there is a u-phase. The α-Al(Mn,Fe)Si dispersoids nucleate on the β'-Mg_2Si needles at higher temperatures and the latter will dissolve [66]. This is schematically shown in Figure 2.16.

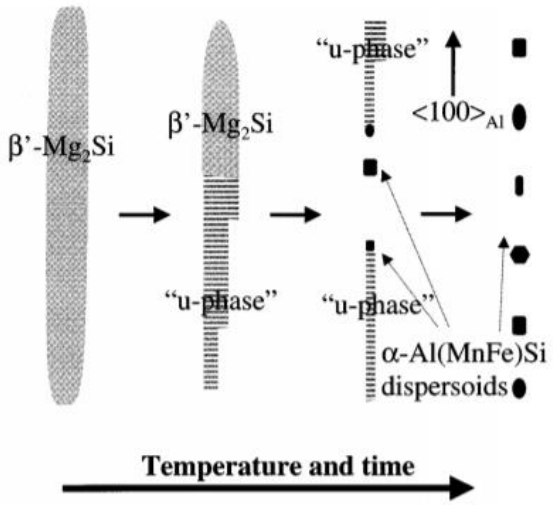

Figure 2.16: A model of the precipitation of the dispersoids in 3xxx Al alloys containing Mg [66].

The temperature and time of the heat treatment will influence the precipitation behaviour as well as the composition. If the heating is slow, a large number of precipitates are formed. On the other hand, if the heating is more rapid, the density of the dispersoids decreases and they become less uniform [66]. Li and Arnberg [60] studied the precipitation behaviour of dispersoids in DC-cast AA3003 alloy during heating and homogenization. They found that at about 300℃ the supersaturated solid solution of 3003 alloy starts to decompose by precipitation of dispersoids during heating at a rate of 50 ℃/h. The number density increases with temperature during heating and reaches a maximum at approximately 400 ℃, then it decreases quickly with temperature, while the size of the dispersoids grows continuously with heating temperature. When the alloy is heated to 530℃, some of the dispersoids dissolve into the matrix due to the increase of the solubility of Mn, while coarsening is the dominant mechanism to make the size of dispersoids grow. During homogenization at 600℃, the evolution of dispersoids is controlled predominantly by dissolution and coarsening. The size of dispersoids increases with holding time at the beginning of homogenization, but after a while, the number density and size of dispersoids decrease. This indicates a quick dissolution of dispersoids. Due to the dissolution behaviour, no dispersoids can be found in the matrix after a long time of homogenization.

During hot rolling of 3xxx Al alloys a little further precipitation occurs. Large constituent particles, which can be present at volume fractions of 2% or more, are broken down [5].

2.4.2 Concurrent Precipitation

Recovery and recrystallization may be influenced by the precipitation reaction during annealing of a deformed and supersaturated commercial aluminium alloy. As previously mentioned, the supersaturated solid solution may decompose and small dispersoids will precipitate. The pinning effect from these precipitates will retard the softening reactions and this phenomenon is commonly referred to as *concurrent precipitation* [26, 44]. Concurrent precipitation has been observed experimentally in many alloy systems [67-69].

The recrystallization and precipitation behaviour can be explained by the time-temperature-transformation (TTT) diagram in Figure 2.17 for a material that has been rapidly heated to the annealing temperature. "The precipitation line represents the occurrence of sufficient precipitation to affect recrystallization behaviour" [40]. The regime I, II and III as well as the points A and B are important regarding the interaction between recrystallization and precipitation. As discussed in Section 2.3.2, the precipitation of small particles (dispersoids) on the substructure before any recrystallization has occurred can prevent recrystallization through the Zener drag, and this is illustrated in regime I in the TTT-diagram at low temperatures. However, as also can be observed from the TTT-diagram, the heating rate is important. If the heating rate is low (10°C/h), the number of precipitates may be so high that the recrystallization is inhibited even at high temperatures [26, 40].

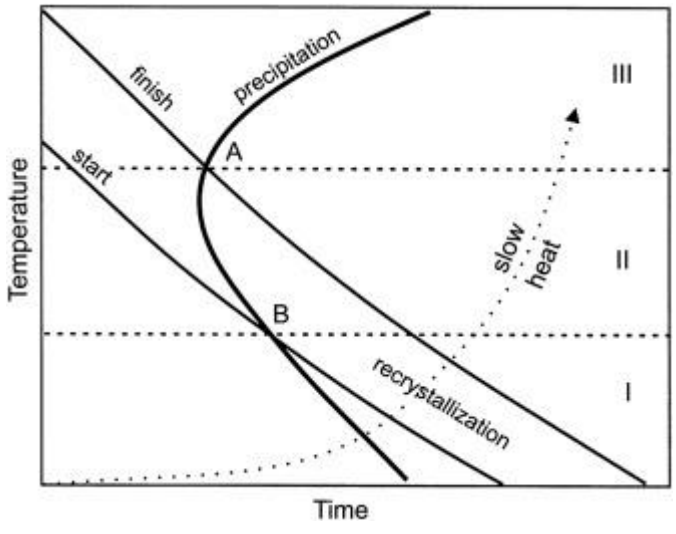

Figure 2.17: Schematic TTT diagram for recrystallization and precipitation in cold rolled supersaturated aluminum alloys, rapidly heated to temperature [40].

At annealing temperatures between points A and B, in regime II, precipitation occurs during recrystallization (concurrent precipitation) and slows down the recrystallization kinetics. Recrystallization has already started, and precipitation then begins. Anyhow, the precipitation

will affect the recrystallization before it is completed. At temperatures just above point B, only a small amount of recrystallization occurs. However, at higher temperatures, there is more recrystallization and at temperatures just below point A full recrystallization is possible. The grain boundaries are pinned by precipitates, and thus the recrystallization is slowed down. As a result, the number of recrystallized grains is quite low, each grain has a lot of space to grow and the resulting grain structure will be coarse and elongated along the rolling direction [26, 40], as shown in Figure 2.18 (b). Pancake-shaped grains are typical for cases affected by precipitation [70]. Above point A in regime III recrystallization occurs and completes without the occurrence of precipitation, and an equiaxed grain structure is formed [40], as shown in Figure 2.18 (a). This can be supported by the findings of Sjølstad [17], who identified a temperature T_A that defined the annealing temperature below which precipitation interacted strongly with the recovery and recrystallization. Below this temperature recovery and recrystallization reactions were retarded due to precipitation of high densities of very small dispersoids, while above this temperature the softening reaction was not affected by precipitation. An equiaxed and fine grain structure was found above T_A. The same tendency was found in Al-Mn-Mg alloys in a study conducted by Daaland and Nes [71].

During long time annealing at high temperatures where recrystallization usually is completed, it is often observed that particles coarsen or dissolve [38]. The average diameter of particles will increase with a corresponding decrease in particle number. Not every single particle grows, and small particles continuously reduce in size until they dissolve, while larger second phase particles grow, resulting in increased average particle diameter. This type of coarsening is also called Ostwald ripening [72].

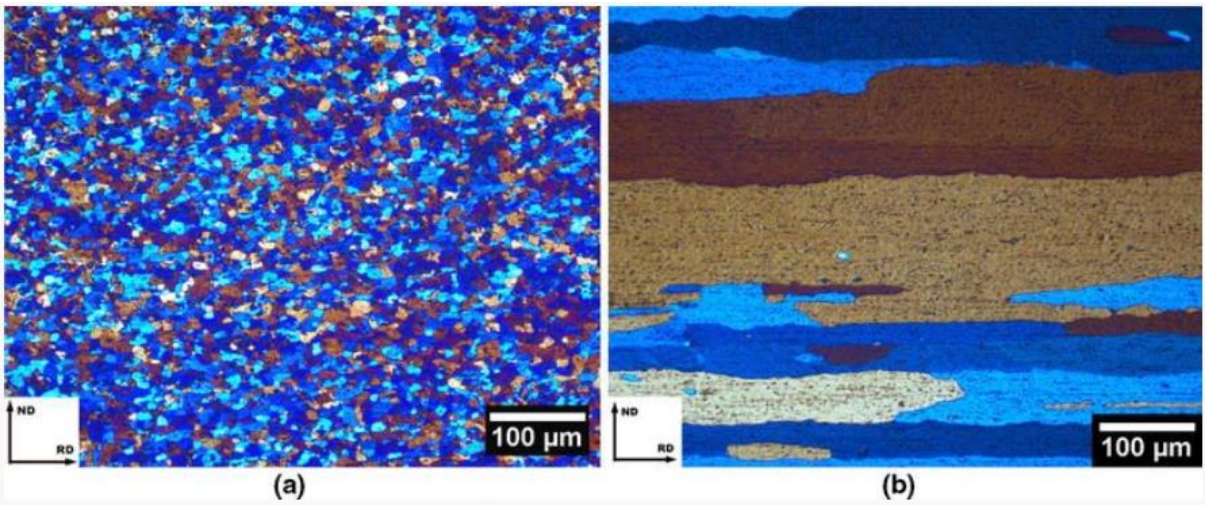

Figure 2.18: Recrystallized grain structures for an as-cast Al-Mn alloy (0.72 wt% Mn) cold rolled to a true strain of 3.0 (95%) and isothermally annealed at a temperature of (a) above T_c and (b) below T_c [44].

2.5 Texture

Texture is defined as the crystallographic preferred orientation in a crystalline material. This is an important component of the microstructure of these materials and may give rise to anisotropic properties. The crystallographic orientation refers to how the atomic planes of a crystal are positioned relative to a fixed reference and three parameters are needed to quantify it. For a rolled sheet this reference system usually consists of RD, the transverse direction (TD) and the normal direction (ND). The grains in Al will develop a preferred orientation during heat treatment or when it undergoes deformation (e.g. rolling), and the degree of texture is dependent on the percentage of crystals having this preferred orientation. Furthermore, texture is usually represented by pole figures, orientation distribution functions (ODF) or inverse pole figures (IPF) [73, 74]. The most common methods of measuring texture are electron back-scattered diffraction (EBSD) and X-ray diffraction (XRD), and the two methods will be further explained in Section 3.4.2 and 3.5, respectively.

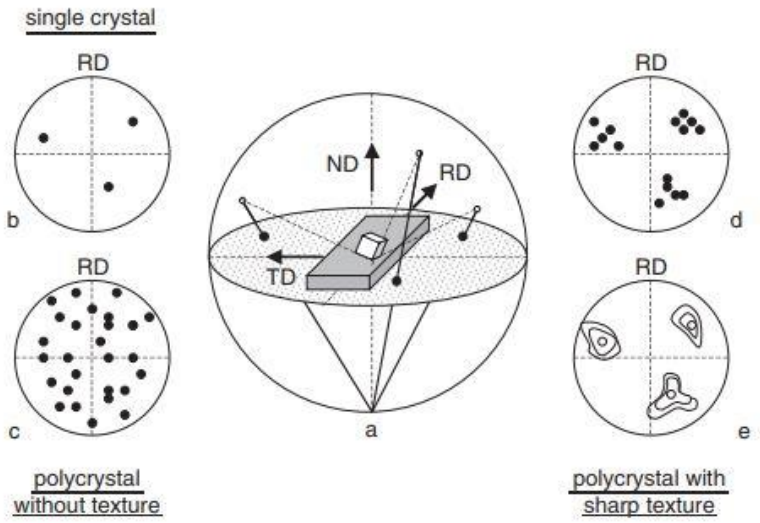

Figure 2.19: Construction of a (100) pole figure. (a) Stereographic projection of the (100) poles; (b) projection of the (100) poles of one grain on the equatorial plane; (c) projection of the (100) poles of a polycrystal; (d) projection of the (100) poles of a textured polycrystal; (e) contour map of the (100) pole density distribution [75].

A *pole figure* represents how the grains are oriented in the sample, and is a stereographic projection of the variation in density of a chosen crystallographic plane normal, along with the reference system of the sample [73]. As can be seen from Figure 2.19 (a), a unit cube is located in the centre of the reference system, surrounded by a unit sphere to represent the cube faces in the stereographic projection. In order to draw the pole figure, a particular crystal direction must be chosen (e.g. the normal to the <100> planes as in Figure 2.19 (a)), and the point of intersection with the unit sphere from the normal vector of each cube face is determined. Furthermore, a line from these points intersects the equatorial plane and ends at the south pole of the unit sphere. This is done for each crystal relative to the reference system [76]. A polycrystal with strong texture can be seen in Figure 2.19 (d), where the projections will cluster together. However, it is often more convenient to use contour lines, as shown in Figure 2.19 (e) [75].

However, it is not possible to obtain a complete orientation of the individual grains from the pole figures, and the ODF provides a better description of the distribution of orientations of all the material in the sample. The orientation of individual grains is described in terms of Euler angles $\mathbf{g} = \{\varphi_1, \Phi, \varphi_2\}$, which transform the specimen reference coordinate system (RD, TD, ND) onto the crystal coordinate system [73]. The most commonly used notation is the one suggested by Bunge, which is illustrated in Figure 2.20. The rotations are as follows [76]:

1. φ_1 is about the normal direction and transforms the transverse direction into TD' and the rolling direction into RD'
2. Φ is about the new rolling direction RD' and
3. φ_2 is about the new normal direction ND''

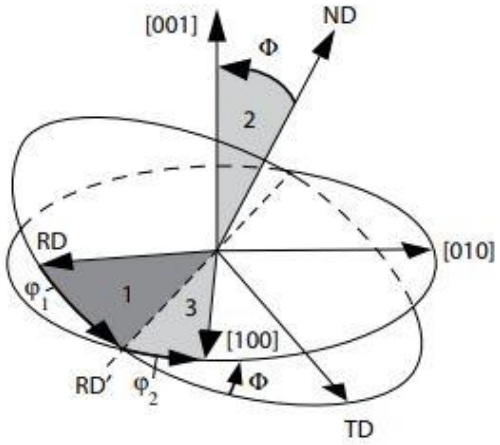

Figure 2.20: Diagram showing how rotation through the Euler angles φ_1, Φ, φ_2, in order 1, 2, 3 as shown describes the rotation between the specimen and crystal axes [76].

Orientations expressed in terms of its Euler angles can be represented in a 3-dimensional space with φ_1, Φ, and φ_2 defining the axes called the Euler space. Each grain represents an orientation g in the Euler space, and the angles are defined in the range of $0° \leq (\varphi_1, \varphi_2) \leq 360°$ and $0° \leq \Phi \leq 180°$ for the most general case of no sample symmetry and triclinic crystal symmetry. Because of the orthorhombic sample symmetry in a rolled product, however, the range of the angles will be reduced to $0° \leq \varphi_1, \Phi, \varphi_2 \leq 90°$. Furthermore, when the definition of the texture is given by an ODF, the angles are represented in two dimensions where φ_2 is divided into intervals [76]. In literature, φ_2 is most commonly divided into 5° intervals. This is illustrated in Figure 2.21, where the 3-dimensional Euler space for a rolled FCC material is shown in Figure 2.21 (a) and the series of 5° intervals through the Euler space is illustrated in Figure 2.21 (b). $\varphi_2 = 0°$ and $\varphi_2 = 90°$ show the same information [73].

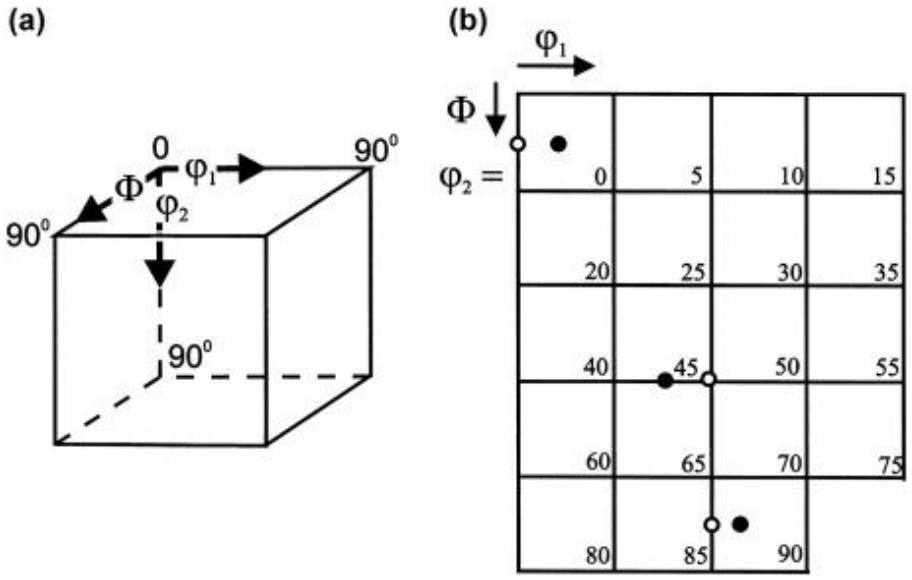

Figure 2.21: (a) The 3-dimensional Euler space for a rolled FCC material where the angles have been reduced to 0° ≤ φ_1, Φ φ_2 ≤ 90°. (b) Series of 5° through the Euler space, where φ_2 = 0° and φ_2 = 90° show the same texture information [73].

An ODF is calculated through evaluation of a set of pole figures (usually 4), and is defined as the volume fraction of grains with the orientation g, where *dV(g)* is the totality of all volume elements of the sample which possess the orientation g within the element of orientation dg, and V is the total sample volume [77]:

$$ODF = f(g)dg = f(\varphi_1, \Phi, \varphi_2)dg = \frac{dV(g)}{V} \tag{2.15}$$

The maximum value of the *ODF* is often a useful representation of the texture strength in a material. Another method of defining the anisotropy, and thus the texture of a material, is the *texture index*. A totally random texture will give isotropic properties to a crystal of cubic symmetry, and a textured material will have more anisotropic properties. The texture index is based on the volume fraction of crystals in a material having a certain orientation, and a higher texture index is equivalent to a higher amount of crystals having this particular orientation. In other words, the higher the texture index, the more textured the material [78]. The texture index was first introduced by Bunge, and is equal to the volume-averaged integral of squared orientation densities over the *ODF* [78]:

$$t = \int f(g)^2 dg \tag{2.16}$$

In the case of cold worked metals, the yield and tensile strength will increase in the direction of preferred orientation as the texture index increases. However, these properties are reduced in the transverse direction of the preferred direction. Samples without texture show texture index equal to 1 [78].

2.5.1 Deformation Textures

The distribution of orientations acquired during cold rolling is not random, and the deformation texture of an FCC material can be represented in a somewhat idealized form, as shown in Figure 2.22 (a). This texture consists of an α-fibre and a β-fibre, respectively, and they form a tube through the Euler space. As can be seen from the figure, the α-fibres have a <011> axis parallel with the rolling plane normal and consist of Brass- and Goss-orientations. The β-fibres, however, starts at Brass and moves through the S-orientation before it ends at the Copper-orientation. A description of the ODF of a 90% cold rolled Al specimen can be seen from Figure 2.22 (b), with the position of some important orientations. Moreover, the rolling texture of FCC metals will evolve during rolling and the texture intensity increases with increasing deformation. It is also important to mention that the initial texture of the material before cold rolling will influence the final texture after cold rolling [75].

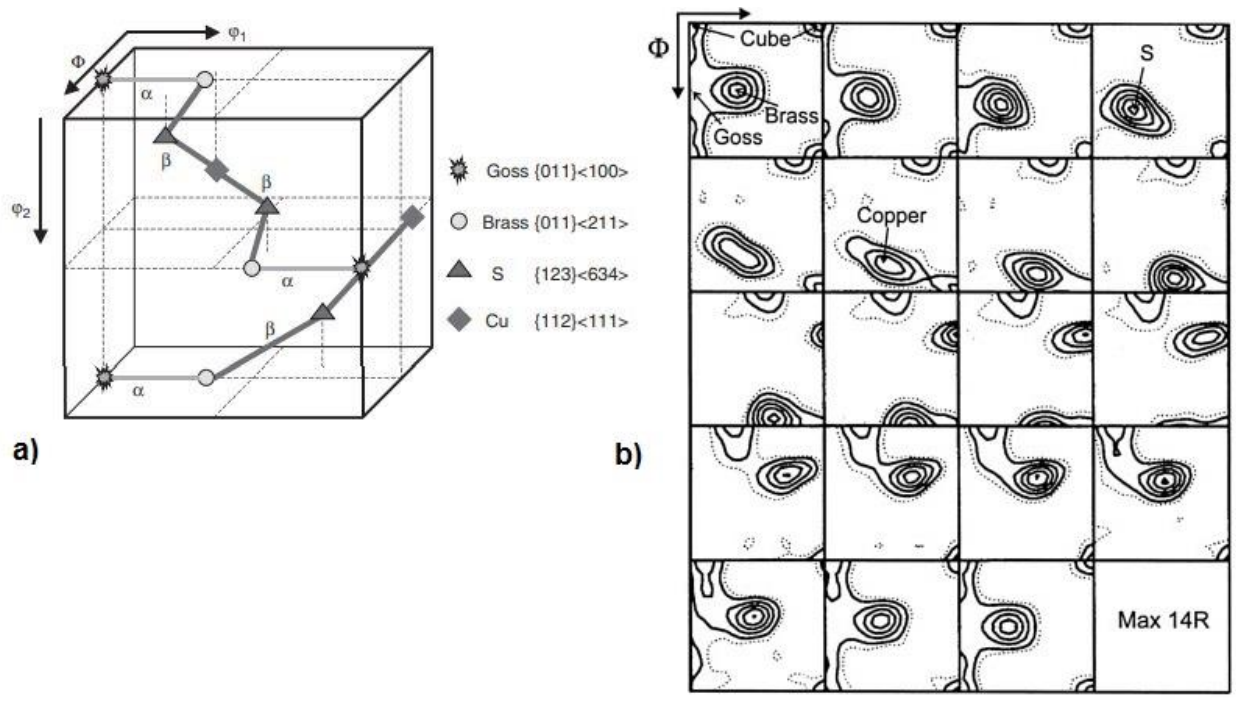

Figure 2.22: a) Schematic representation of the cold rolling texture of FCC materials [75]. b) ODF of 90% cold rolled aluminium with the positions of some important orientations indicated [79].

The β-fibre texture is generally observed in industrial hot rolled Al alloys. Figure 2.23 shows the texture of a non-recrystallized AA6016 hot strip, where recrystallization has been suppressed because of precipitation of Mg_2Si particles during hot rolling and subsequent coil cooling [80]. Strain channel die compression tests (hot deformation) at temperatures between 200 °C and 400 °C have shown an increase of both the Brass and the Cube-component with increasing temperature and decreasing strain rate, where the latter component originates during recrystallization. These components increase at the expense of the S- and Cu-components [79].

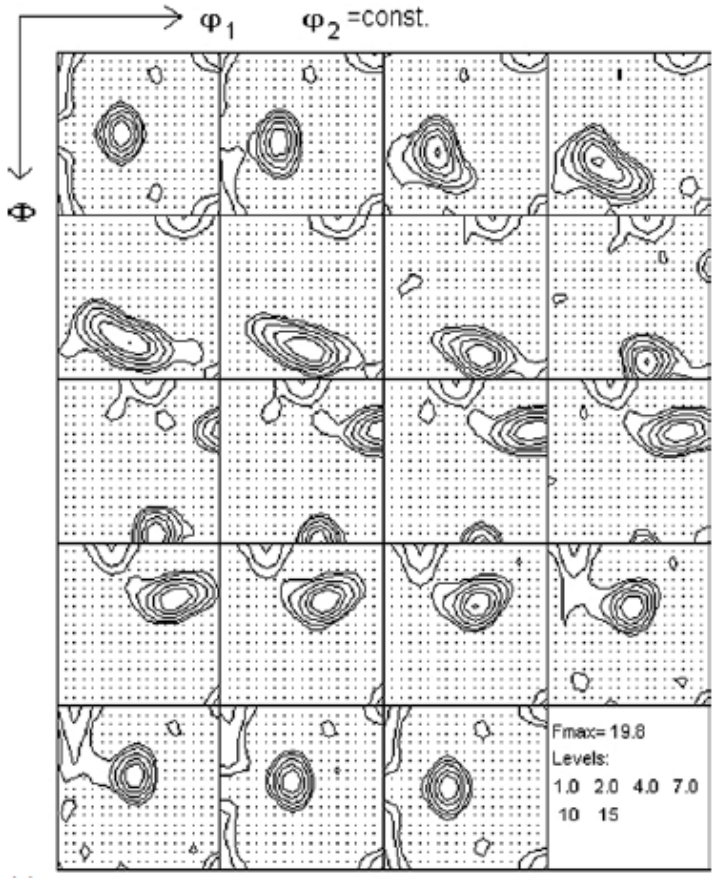

Figure 2.23: Typical texture obtained in non-recrystallized aluminium hot strips (AA6016) [80].

Some common texture components in rolled FCC metals are displayed in Table 2.1 with the corresponding Euler angles. ODF sections for $\varphi_2 = 0$, 45 and 65 are often chosen to show the most important components [81].

Table 2.1: Texture components in rolled FCC metals [81]

Component, Symbol	{hkl}	<uvw>	φ_1	Φ	φ_2
Copper, Cu	112	111	90	35	45
S	123	634	59	37	63
Goss, G	011	100	0	45	90
Brass, Br	011	211	35	45	90

2.5.2 Recrystallization Textures

The change in microstructure during recrystallization has the potential to considerably change the texture. According to Engler [82], "the recrystallization textures of aluminium alloys can be explained by a growth selection of grains with an approximate 40° orientation relationship out of a limited spectrum of preferentially formed nucleus orientations". Common texture components found in recrystallized FCC metals differ from the components found in rolled FCC metals and are displayed in Table 2.2 and the ODF in Figure 2.24. From the figure, it is difficult to differentiate between the S- and the R-texture components. There are numerous definitions of the Euler angles of these components. In this work, the Euler angles are based on the work of Humphreys et al. [83].

Table 2.2: Components of recrystallization textures in FCC metals [81].

Component, Symbol	{hkl}	<uvw>	φ_1	Φ	φ_2
Cube	001	100	0	0	0
Rotated Cube	001	110	22	0	0
	001	110	45	0	0
Goss, G	011	100	0	45	90
R	124	211	57	29	63
P	011	122	70	45	0
Q	013	231	58	18	0

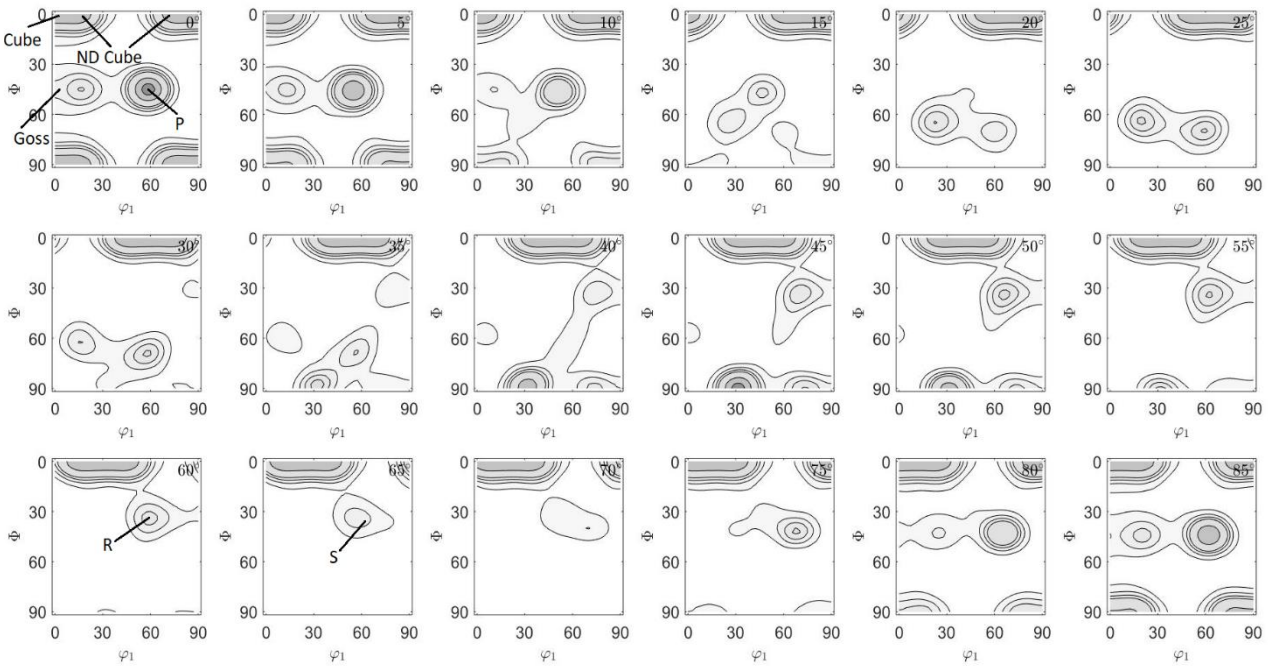

Figure 2.24: Recrystallization texture components for a recrystallized AA3005 alloy.

All the dominating recrystallization textures except the R-component are found in the $\varphi_2 = 0°$ section of the ODF, and the position of these components are shown in Figure 2.25. In the following, the most important recrystallization texture components found in Al alloys are described (the components displayed in Table 2.2). The R-component has not been calculated in this thesis and is therefore not further described.

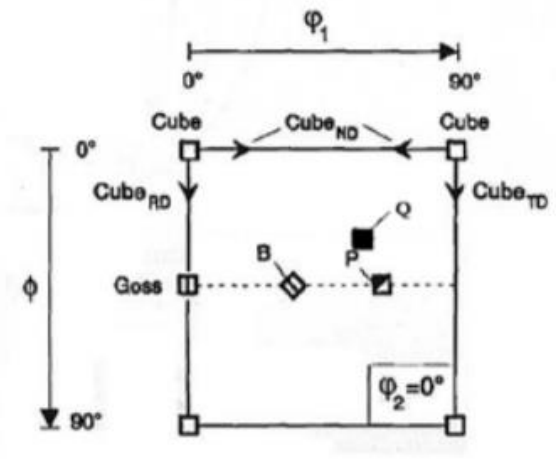

Figure 2.25: Position of different texture components of the $\varphi_2 = 0°$ section of an ODF [17].

Cube-texture. The main texture component in a typical recrystallization texture for cold rolled aluminium is very often Cube. Dillamore and Katoh [84] suggested that grains of Cube-orientation existed in the deformed state as transition bands separating volumes of major rolling texture components in cold rolled FCC metals. As previously mentioned, a large orientation

gradient is present in these bands, and therefore the Cube oriented grains have a growth advantage as potential recrystallization nuclei. The Cube-component is strengthened by increasing temperature and deformation up to a certain point. The Taylor factor of Cube oriented grains is low, which tends to lower the stored dislocation density in the grains. In severely cold rolled aluminium, the Cube-component may be suppressed since it is assumed to rotate around RD towards the Goss-orientation, as fewer Cube grains from the initial state has retained deformation. The increase in stored energy and driving force for recrystallization can also be an explanation for the decrease with severe deformation. As a result, a larger number of nucleating sites compete, especially PSN sites. The PSN effect leads to a random texture (i.e. pure metal texture) or selected nucleation of P- and ND-rotated Cube texture components, as mentioned in Section 2.3.3. The Cube-texture has a 40°<111>-orientation relationship to the S-component and from each S-variant (four different types) there is one 40°<111>-rotation that yields the Cube-texture. Only orientations which have the <111>-rotation relationship with most of the deformed matrix are favourable for growth, and 40°<111> boundaries have higher mobility than random boundaries. The volume fraction of S-oriented grains is usually high after deformation, and this high-volume fraction is a part of the reason why the Cube-texture usually is very strong in rolled and recrystallized aluminium alloys [7, 17, 85].

ND-Rotated Cube. The ND-rotated Cube has an approximate 40°<111> rotation relationship to the Cu-orientation and nuclei form early and is not as influenced by precipitation as for example nuclei formed at large constituent particles [26]. In the case of concurrent precipitation, Daaland et al. [85] found that the ND-rotated Cube has a growth rate advantage compared to other orientations, due to the grains having a shorter incubation time than other orientation. This resulted in less precipitation upon these nuclei, which made them grow larger than other orientations. Tangen et al. [44] observed strong ND-rotated Cube when concurrent precipitation occurred during annealing, and the texture component was gradually reduced with less precipitation.

P-texture. Similar to the ND-rotated Cube, the P-texture component has an approximate 40°<111>-rotation to the Cu-orientation. It has been found in cold rolled and annealed Al-Cu, Al-Mn-Mg and AA3103 with a high saturation of alloying elements [17]. It was reported by Engler et al. [86] and Sjølstad [17] that the P and ND rotated Cube-components preferred to nucleate in the deformation zones around large constituent particles (i.e. PSN). Furthermore, Tangen et al. [44] observed strong P-components in the case of concurrent precipitation of Mn-rich dispersoids in 3xxx Al alloys, and the texture component was gradually reduced with less

precipitation, similar to the ND-rotated Cube. PSN in polycrystalline materials, such as aluminium, is generally known to give random recrystallization texture. However, Tangen et al. also found PSN to play a significant role in the nucleation of P and ND-rotated Cub -texture components. The intensity of the P- and ND-rotated Cube textures strengthened with increasing initial cold rolling strain, supersaturation of Mn, and dispersoid density, but decreased with increasing annealing temperature. Considering Figure 2.17 in Section 2.4.2, Daaland and Nes [71] found a strong P-texture in combination with weak ND-rotated Cube when annealing was carried out below T_A and were found to have a growth advantage in the early stages of annealing, while in the later stages all grains seemed to grow with a constant rate. Besides, PSN was found to have a significant role in the nucleation of the P and ND-rotated Cube texture components below T_A. Daaland and Nes concluded that the P and ND-rotated Cube texture components grew significantly faster than the randomly oriented grains during low-temperature annealing subsequent to cold rolling

Goss-texture. The Goss-texture component is usually present as a minor component in the deformation texture, but a pronounced Goss-orientation can be present as a result of poor formability. Transition bands have been found to favour the formation of the Goss-texture by Hutchinson et al. [50].

3. METHOD

All the material is from the same Al-Mn-Mg alloy. The experiments conducted in this work and how they were done are described in this section, together with relevant theory. First, the delivered material is characterized, and the experiments carried out by Hydro Aluminium Rolled Products in Holmestrand before the material was handed out are presented. The rest of the experiments in the present study were carried out at NTNU Gløshaugen. The second part of this section describes the hardness measurements, and these measurements were carried out to study the softening behaviour. The third part describes the electrical conductivity measurements. Electrical conductivity can give an indication of the precipitation behaviour. Furthermore, the fourth part describes the measurements carried out in SEM, i.e. the analysis of dispersoids and EBSD. Dispersoids were characterized to study the precipitation behaviour, especially in terms of concurrent precipitation. EBSD was performed to investigate the softening behaviour, in terms of grain size and fraction recrystallized. The fifth and last part describes the texture measurements performed by XRD. Texture measurements were carried out on the recrystallized samples, as texture has an influence on the recrystallization behaviour of the material.

3.1 Delivered Material

In the present work, the investigated material was a commercial Al-Mn-Mg alloy (AA3005), deformed by rolling. The rolling of the aluminium alloy was carried out by Hydro Aluminium Rolled Products AS at the rolling mill in Holmestrand and delivered to NTNU Gløshaugen. All material was collected from the same coil with the same composition, and all the samples were machined from the central region of the coil. The as-received materials were in hot rolled, cold rolled, and cold rolled and annealed conditions with the nominal chemical composition given in Table 3.1.

Table 3.1: Exact composition of AA3005 in wt%.

Composition [*wt%*]								
Si	**Fe**	**Cu**	**Mn**	**Mg**	**Cr**	**Ni**	**Zn**	**Al**
0.52440	0.53345	0.20084	1.17360	0.42597	0.03243	0.01691	0.24555	96.84398

The process route of the delivered material can be seen in Figure 3.1.

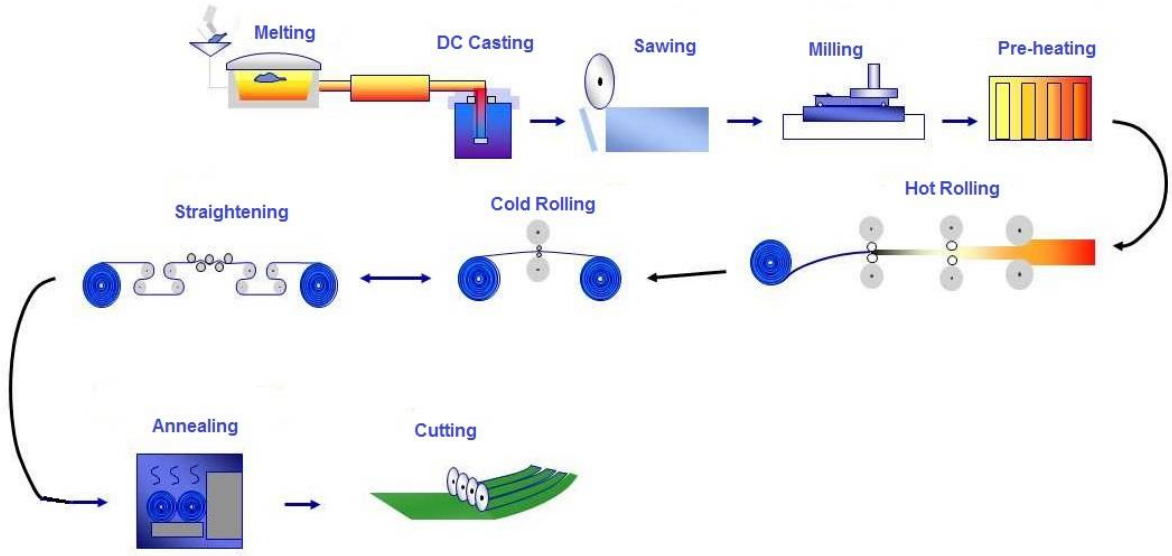

Figure 3.1: Schematic drawing of the process route for the delivered material.

There was no homogenization between DC-casting and hot rolling. However, the billet was preheated to 565°C and subsequently hot rolled to 3.5 mm. Samples were collected from the hot rolled coil. Furthermore, the hot rolled coil was cold rolled in four cold rolling steps to a final thickness of 0.47 mm and samples were collected from three of the deformation passes (1.9 mm, 1.15 mm and 0.47 mm). The different rolling thicknesses with corresponding percentage cold reduction (%CR) and logarithmic strains (ε) are displayed in Table 3.2. Finally, the cold rolled samples were annealed at different temperatures. The samples cold rolled to %CR = 80% were not investigated in the present study.

Table 3.2: Rolling thickness, percentage cold reduction and strain. The samples cold rolled to %CR = 80% were not investigated in the present study.

Thickness [*mm*]	Cold Reduction [*%*]	Strain [ε]
3.5	0	0
1.9	46	0.61
1.15	67	1.11
0.7	80	1.61
0.47	87	2.01

3.1.1 Non-Isothermal Annealing Experiment

Non-isothermal back-annealing was carried out by Hydro Aluminium Rolled Products AS at Holmestrand to investigate the softening behaviour of the alloy after different cold rolling

deformations and annealing temperatures. The samples with corresponding cold rolling reductions of 46%, 67% and 87% were annealed at 15 different temperatures in the range 180 – 500 °C. The samples were heated at 100 °C/h until the furnace reached the specific temperature and held for 3 hours. Finally, the samples were air cooled. The heating programs for the 15 annealing experiments are presented in Figure 3.2, including indications of when samples were taken out of the furnace and air cooled.

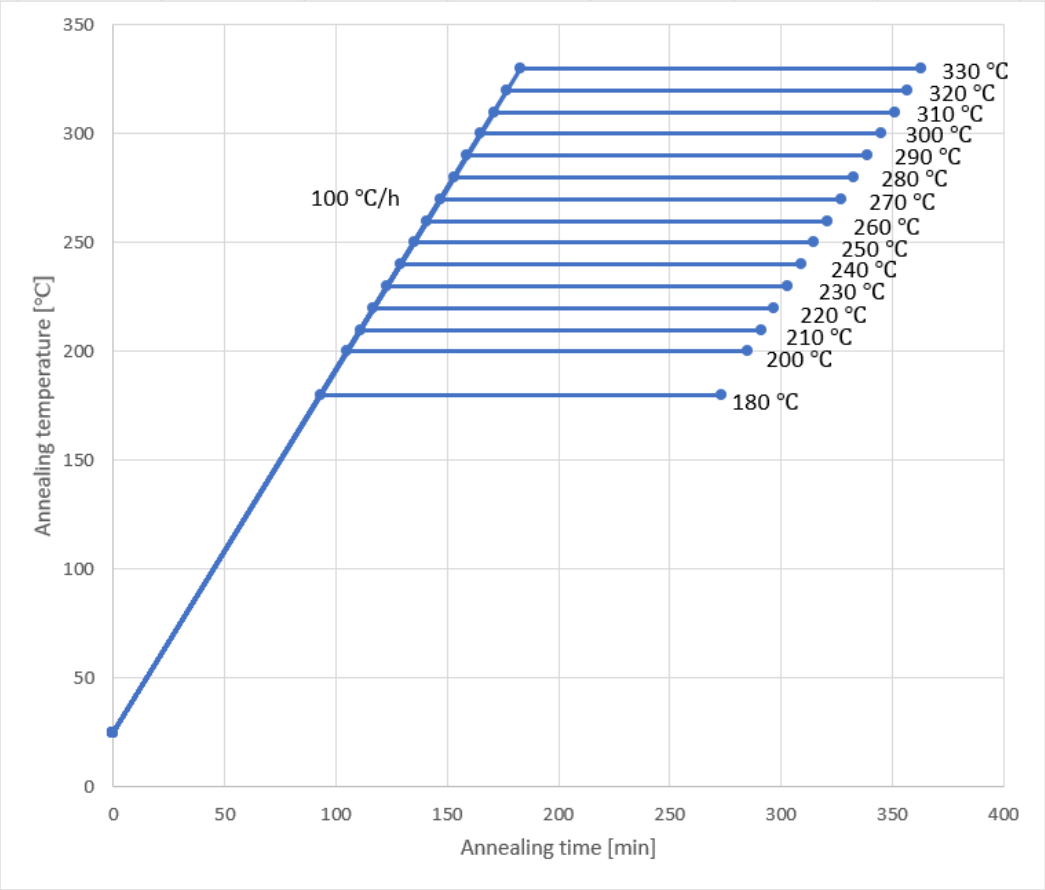

Figure 3.2: Holding temperatures for the different annealed samples. Constant increase in heating at 100°C/h until the specific heating temperature is reached. The samples with corresponding cold reduction of %CR = 46 were also annealed at 283 and 285°C, the samples with %CR = 67 were also annealed at 273 and 275°C, while the samples with corresponding strain of %CR = 87 were also annealed at 275 and 285°C.

3.1.2 Tensile Test

Uniaxial tensile tests were carried out to study the mechanical response of the annealed samples, as the mechanical strength will give an indication of the softening behaviour. During recovery, there is a partial restoration of certain physical properties such as a decrease in the yield strength and ultimate tensile strength, and a limited amount of softening occurs. During recrystallization, the amount of softening is much more significant. Hence, tensile strength is

a strong indication of the degree of recrystallization and suggests the recrystallization temperature. Strength will decrease with the degree of recrystallization as displayed schematically in Figure 2.11 in Section 2.3.1. The tensile testing was carried out at the Metallurgical Laboratory by Hydro Aluminium Rolled Products AS in Holmestrand. The tensile tests of the dog bone samples are performed in the Zwick/Roell 8497 20 kN test machine, displayed in Figure 3.3.

Figure 3.3: Picture of the tensile test machine in the Metallurgical Laboratory in Holmestrand.

The samples were loaded in the tensile test machine and tested for the cold reductions displayed in Table 3.2 at room temperature, as well as the annealed samples displayed in Figure 3.2. Three specimens were machined out parallel to rolling direction for each annealing temperature. The rolling direction, transverse direction and normal direction are illustrated in Figure 3.4, and the geometry of the dog bone samples is shown in Figure 3.5.

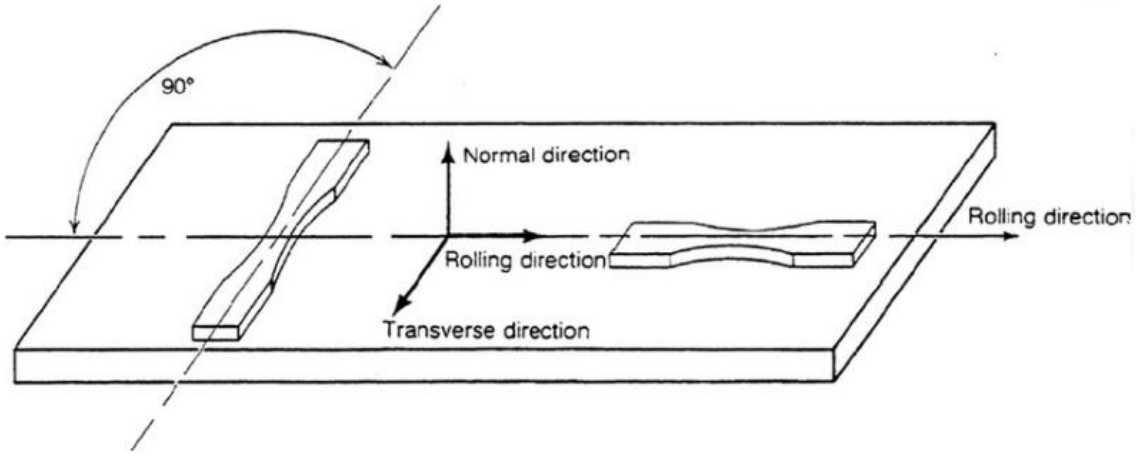

Figure 3.4: An illustration describing the rolling, transverse and normal direction [87].

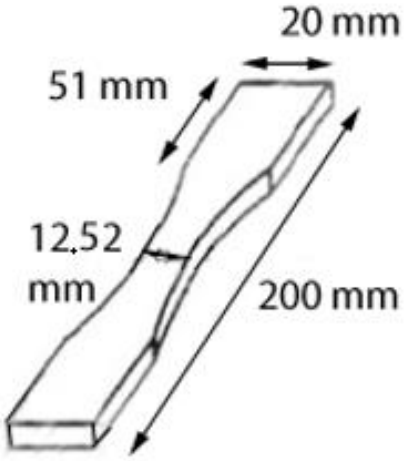

Figure 3.5: Tensile test dog bone sample geometry [87].

Before the samples were mounted in the tensile test machine, the actual thickness was measured with a micrometer. The sample was subsequently mounted by the top and bottom grips of the machine. During the tensile test, the grips are moved apart to stretch the specimen. Furthermore, the force applied (20 kN) on the sample and its displacement is continuously monitored and plotted on a stress-strain curve until failure. The data generated during tensile testing provides the following quantitative measurements: yield strength, ultimate tensile strength and elongation, as schematically illustrated in Figure 3.6.

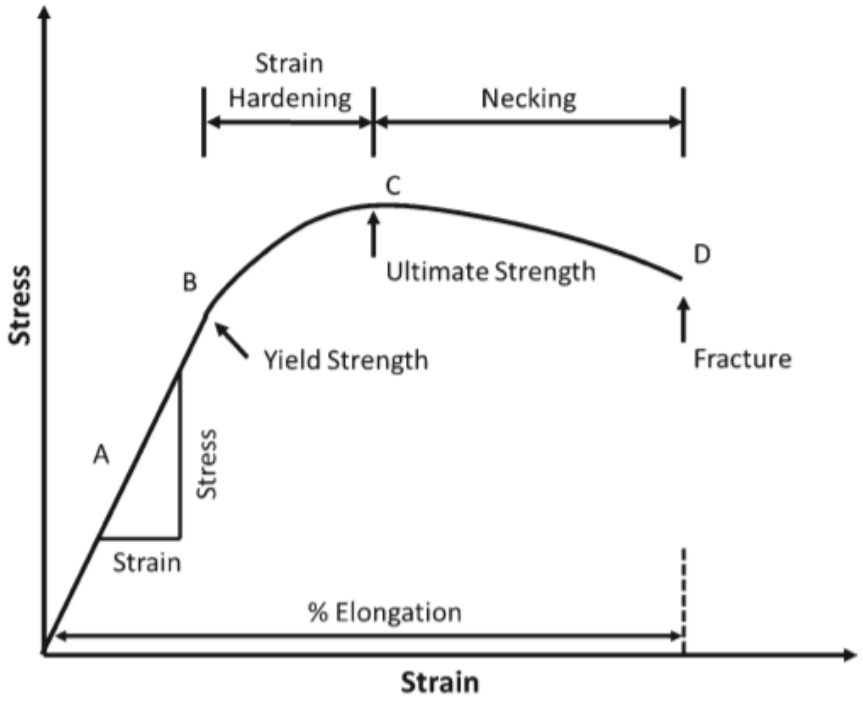

Figure 3.6: A typical stress strain curve [88].

3.2 Hardness Measurement

Hardness measurement is a fast and efficient way to monitor the softening behaviour after annealing compared to tensile testing. These measurements were carried out to compare the hardness against the measured tensile strength. Like tensile testing, hardness is strongly correlated with the degree of recrystallization and indicates the recrystallization temperature. Hardness will decrease with the degree of recrystallization as displayed in Figure 2.11 in Section 2.3.1. The basic principle of the hardness test is to observe a material's ability to withstand plastic deformation from a standard source. A constant load is applied on the sample surface through an indenter, and by studying the dimension of the indentation the ability to resist plastic deformation can be characterized [7].

Vickers hardness (VHN) was measured by a Matsuzawa DVK-1S instrument, with a load of 1 kg, loading speed of 100 µm/s and holding time of 15 s. The dimensions of the indentation caused by the compression load on the surface of samples were measured to calculate the values of VHN. The measurements were performed on a clean and planar surface, and the cold rolled sheets were mounted on a sample holder to make sure the samples were lying flat in the apparatus. Furthermore, the resulting hardness was the average of at least four measurements, and the indentations were measured on the RD-TD-plane, illustrated in Figure 3.4. This is a

section parallel to the rolling direction. Like tensile testing, hardness was measured for the cold reductions displayed in Table 3.2 at room temperature, as well as the annealed samples displayed in Figure 3.2.

The fraction recrystallized was derived from the hardness values by using the following formula [89]:

$$X_{\text{recrystallized}} = \frac{VHN_{\max} - VHN_i}{VHN_{\max} - VHN_{\min}} \tag{3.1}$$

VHN_{max} is the maximum hardness corresponding to the as cold rolled sample, VHN_{min} is the minimum hardness corresponding to the fully recrystallized sample and VHN_i is the hardness at the annealing temperature i.

3.3 Electrical Conductivity Measurements

Electrical conductivity is used to specify the electrical character of a material and indicates how easy a material can conduct an electrical current. Materials are either conductors, semiconductors or insulators, depending on how easily they conduct electrical current. Metals are generally good conductors, and aluminium is one of the best conductors with an electrical conductivity of typically 3.8 x 10^7 $(\Omega m)^{-1}$ at room temperature. The conductivity (σ) of metals is a product of the number of electrons (n), the charge of each electron (q) and the mobility (μ) of the electrons. Furthermore, electrical conductivity is the reciprocal of the resistivity (ρ) [90, 91].

Electrical conductivity measurements were performed to measure the number of solute elements in the alloy and to follow the degree of precipitation during annealing. In alloys, the electrical conductivity is generally influenced by two factors: The temperature dependent contribution independent of the defect density and the temperature independent contribution of solute elements or other defects. Alloying elements in the solid solution will through a distortion of the atomic lattice reduce the conductivity of the metal. Besides, the electrical conductivity generally decreases with an increasing percentage of cold deformation, because of the introduction of defects, vacancies, etc. Larger incoherent particles have a limited effect on electrical conductivity and can generally be neglected [7, 17, 47].

According to Altenpohl [92], by neglecting the temperature term in the Matthiessen's rule, the relationship between the concentration (in wt%) of Fe, Mn and Si in solid solution and the electrical conductivity can be expressed as:

$$\frac{1}{\sigma} = 0.0267 + 0.032Fe_{ss}\% + 0.033Mn_{ss}\% + 0.0068Si_{ss}\% \quad (3.2)$$

$Fe_{ss}\%$, $Mn_{ss}\%$ and $Si_{ss}\%$ are the amount of Fe, Mn and Si, respectively, in solid solution. The electrical conductivity measurements can only give an indication of the amount in solid solution, and it is impossible to separate the contribution from the three elements from each other. However, the solubility of Fe in aluminium is very low and nearly all the Fe content forms intermetallic primary particles. The contribution from Si is much lower than for the two other elements (cf. Eq. 3.2). The contribution from Fe and Si to the change in electrical conductivity during annealing is often neglected compared to the influence of the Mn concentration, and electrical conductivity can thus be used as a measure to indicate the amount of Mn-containing dispersoids precipitated [7, 17].

In the present work, a conductivity meter (Foerster Sigmatest 2.069) was used, which is a portable eddy current test instrument that measures the electrical conductivity in the unit MS/m (megasiemens per meter). MS/m converts to 10^6 $(\Omega m)^{-1}$. It was calibrated by measuring the electrical conductivity of air and two reference samples with a conductivity of 58.50 MS/m and 4.415 MS/m, respectively. The electrical conductivity was measured for all the samples, including the hot rolled one. The probe was mounted on the sample surface (i.e. the RD-TD plane), and the average of ten measuring points distributed on both sides of the samples are used in the results.

If the actual material thickness is less than three times the effective penetration depth, this will mean that measurement accuracy can no longer be guaranteed. The highest measuring frequency possible for the instrument was chosen, 960 kHz, as lower frequency will result in lower penetration depth. The same frequency was applied to all the samples. The effective penetration depth, δ_{eff}, can be determined from the frequency and the conductivity [93]:

$$\delta_{\text{eff}} = \frac{503}{\sqrt{\sigma * f}} \, [mm] \quad (3.3)$$

σ is the measured electrical conductivity in MS/m, and f is the measuring frequency in Hz. Equation 3.3 is fulfilled for all the measured samples, meaning that none of the samples was too thin. The instrument is also dependent upon temperature, as the conductivity drops with increasing temperature according to the following relationship [93]:

$$\sigma_T = \sigma_{20}(1 - \alpha \cdot dT) \tag{3.4}$$

where σ_T is the conductivity at temperature T, σ_{20} is the conductivity at 20°C, α is the material-specific temperature coefficient and dT is the temperature difference between the actual temperature and 20°C.

3.4 Scanning Electron Microscope

In a scanning electron microscope, primary electrons are generated and formed into a finely focused beam by electromagnetic lenses, and systematically scanned across a surface of interest. The electrons interact with the atoms in the sample, causing various charged particles and photons to be generated. Those that are emitted can be collected and used to form an image, diffraction pattern or chemical spectrum. These include the signals displayed in Figure 3.7, whereas secondary electrons, backscatter electrons (BSEs) and X-rays photons are the most commonly used signals. However, secondary electrons are mainly used for topography observations of the surface, which is not used in the present work. BSEs collide with atoms to such an extent that their path takes them back up through the sample surface. Diffraction of BSEs is used for EBSD. BSEs are also used for atomic number contrast and phase contrast. SEM can in principle detect small particles and give information about the orientation of grains in the specimen [7, 94].

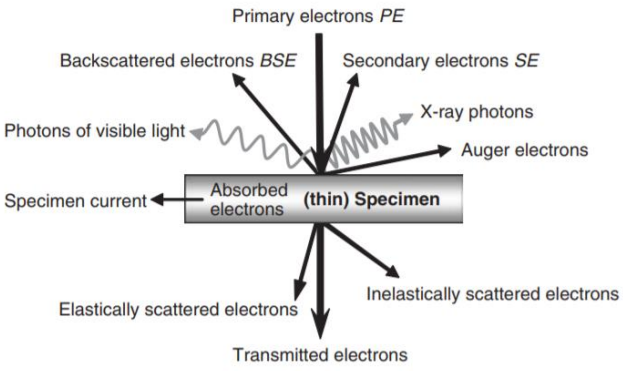

Figure 3.7: Some of the useful signals that are generated when a focused electron beam strikes a specimen. Note that, for a 'thick' specimen, i.e. more than a few hundred nanometres, electrons become absorbed within the sample and hence are not transmitted [94].

The microstructure characterization of the samples in the present work was done with a Zeiss Ultra 55 – Limited Edition field-emission scanning electron microscope (FESEM) equipped with an EBSD detector for crystal orientation mapping and a BSE for the particle characterization. The microscope is located at the Electron Microscopy Lab. Some of the annealed samples, together with the hot rolled and cold rolled samples, were chosen for further microstructural characterization in SEM, with both EBSD and BSE. The temperatures were chosen based on having samples before (180℃), during (280℃) and after (330℃) recrystallization. Based on the strain and the annealing temperature, the samples were labelled with different names displayed in Table 3.3.

Table 3. 3: Different samples studied with EBSD and BSE.

Name	%CR	Annealing Temperature [℃]	Final Polishing Method
HR	0	25 (As hot rolled)	Vibration polishing
%CR46	46	25 (As cold rolled)	Electropolishing and ion beam polished
%CR67	67	25 (As cold rolled)	Electropolishing and ion beam polished
%CR87	87	25 (As cold rolled)	Electropolishing and ion beam polished
%CR46-180	46	180	Electropolishing
%CR67-180	67	180	Electropolishing
%CR87-180	87	180	Electropolishing
%CR46-280	46	280	Electropolishing
%CR67-280	67	280	Electropolishing
%CR87-280	87	280	Electropolishing
%CR46-330	46	330	Vibration polishing
%CR67-330	67	330	Vibration polishing
%CR87-330	87	330	Electropolishing

The same samples were used for both particle analysis with BSE and microstructure characterization with EBSD. Sample preparation is especially important for the EBSD technique. The deformed layer after mechanical grinding and polishing should be removed, and the sample preparation of the samples is described below.

(i) The samples for SEM analysis were first cut to required dimensions (approximately 20 x 14 mm), and subsequently cold mounted in Epofix Cold-setting Resin. ND-RD (black rectangle in Figure 3.8) section of the samples was mechanically ground at 800 and 1200 grid size on SiC-paper.

(ii) The grinding was followed by polishing on Al-discs by program 9 µm – 6 µm – 3 µm – 1 µm, describing the average diameters of diamond particles in the solution that are used to moisten the Al-discs during polishing. An ultrasonic cleaner was used to remove residual polishing particles etc in the polished surface of samples between the polishing programs.

(iii) The final polishing step was carried out by electropolishing with Struers Lectropol-5, in an 80% ethanol (CH_3CH_2OH) and 20% perchloric acid ($HClO_4$) cooled down to -35 °C, with a voltage of 20 V for 10 seconds or by vibration polishing in a Buehler VibroMet 2 vibratory polishing machine. Vibration polishing was carried out on the samples HR, %CR67-330 and %CR87-330, while electropolishing was carried out on the rest of the samples. In addition to electropolishing, ion beam polishing was performed on the surface of the as cold rolled samples (%CR46, %CR67 and %CR87). Plasma cleaning was carried out on the samples before characterization in SEM.

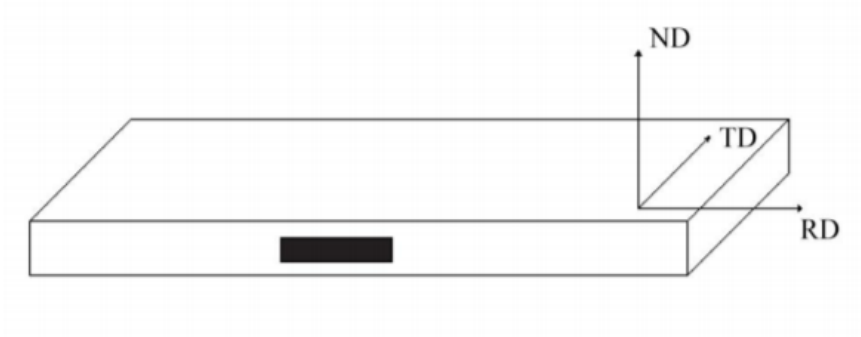

Figure 3.8: Schematic illustration of a rolled sheet with given directions [65].

3.4.1 The BSE-technique

The FESEM provides excellent channelling and atomic number contrast with the use of a solid-state BSE detector. BSEs are reflected out of the sample interaction volume by elastic scattering interactions with sample atoms. *Channelling contrast* is the result of changes in the lattice structure of a crystalline sample. Depending on the direction of the primary electron beam to the lattice, the atomic density near the surface will change. At one particular direction the atomic density near the surface can be very high. However, when the incident beam has a slightly different direction, electrons can pass through the channels of atoms and penetrate deeper into the sample. These electrons are more likely to not contribute to the BSE signal. At

a fixed incident beam angle, even small changes of the crystal lattice can give rise to the channelling contrast. In the present work, this technique is applied to image microstructures in terms of subgrain and grain structure [7, 95].

Atomic number contrast (Z-contrast) is a technique used to detect contrast between areas with different chemical composition. Elements with high atomic number backscatter electrons more strongly than elements with low atomic number, and will therefore appear brighter in the image. In the alloy studied in this work (AA3005), small particles (dispersoids) are present in the samples. Dispersoids are often in the size range from 10 nm to 500 nm. Due to the content of iron, silicon and manganese in these particles as well as the high resolution of the FESEM, they can be characterized using BSE [7].

In the present work, three BSE images per sample were taken at a magnification of 5000x to obtain statistics for the particle analyses. Areas without constituent particles were selected to perform the measurements of dispersoids, and a minimum of 400 particles was taken into account for each measured image. A Python script attached in Appendix D.2 was used to derive the average size and size distribution of dispersoids. Mean particle size, particle density, particle size distribution and particle area were measured in order to fully characterize the dispersoids. The measurement procedure carried out in Python is schematically shown in Figure 3.9. The following steps were performed in Python [96]:

a) The image is converted to grayscale.

b) An elevation map is created with particle edges highlighted.

c) Markers are found for each particle and the background, with different thresholds depending on the image contrast.

d) A watershed transformation is performed by flooding the elevation map starting from the markers.

e) Particles are segmented from the binary image and particles are removed after filtering on pixels, eccentricity and circularity. Particles less than 5 pixels are removed, equivalent to 55 nm.

f) The different parameters are calculated from the successful segmentation.

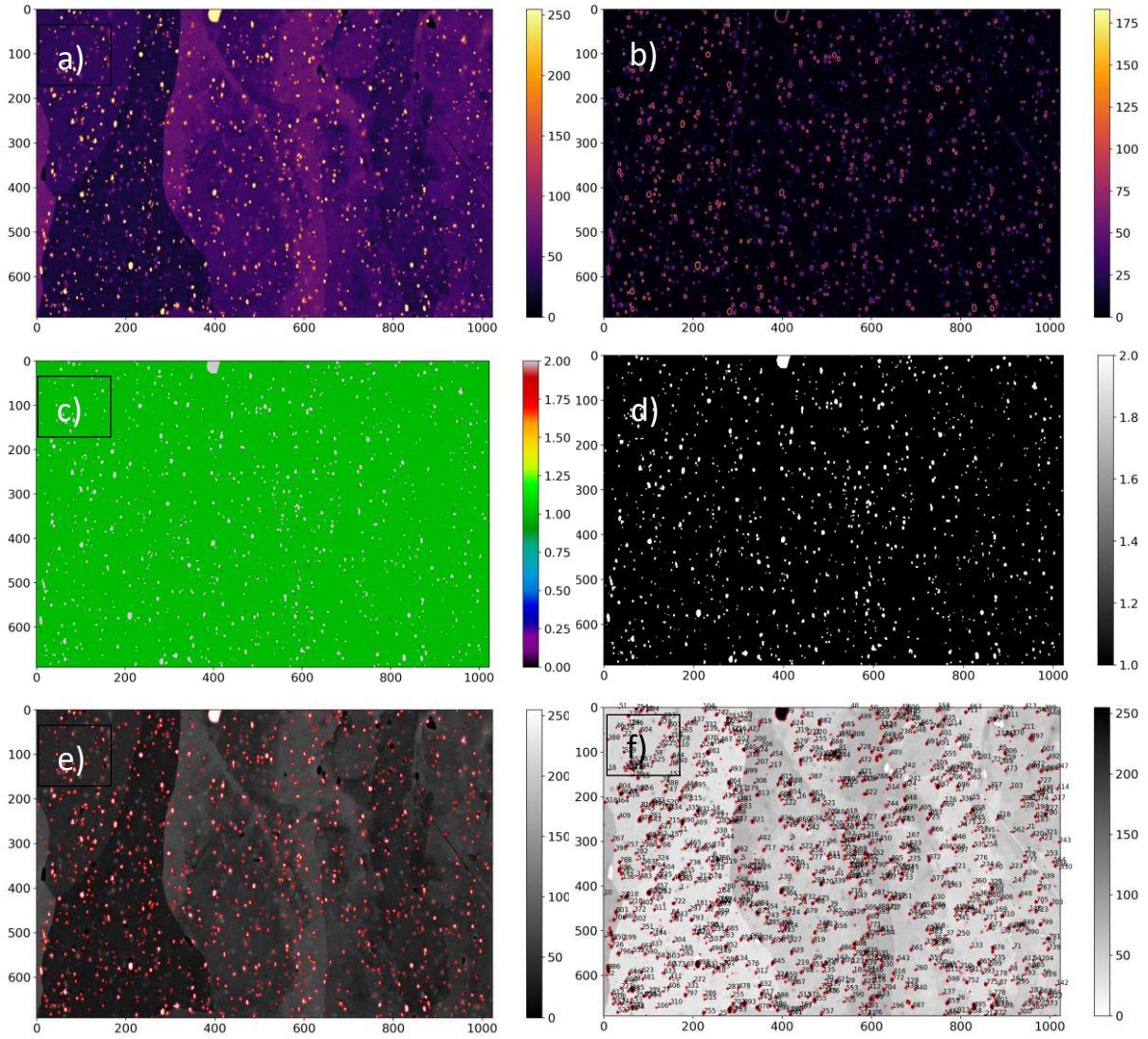

Figure 3.9: Schematic illustration of the particle distribution analysis.

The BSE scans were performed with 10 kV acceleration voltage and approximately 10 mm working distance. Holes from removed particles in the sample surface as a result of electropolishing are present in some of the samples. The minimum and maximum threshold for the markers found for each particle and the background, as well as an indication of samples containing holes, are displayed in Table 3.4.

Table 3.4: Minimum and maximum threshold and if holes are present in the samples

Sample	Min. threshold, I_{min}	Max. threshold, I_{max}	Holes: Yes/No
HR	110	120	No
%CR46	110	160	No
%CR67	130	140	No
%CR87	120	130	No
%CR46-180	110	120	Yes
%CR67-180	130	140	Yes
%CR87-180	130	140	No
%CR46-280	110	120	Yes
%CR67-280	90	110	Yes
%CR87-280	110	120	Yes
%CR46-330	100	120	No
%CR67-330	90	110	No
%CR87-330	90	110	Yes

3.4.2 The EBSD-technique

EBSD [97] was used to investigate hot rolled, cold rolled and annealed microstructures with respect to subgrain and recrystallized grain size measurement and fraction recrystallized. EBSD can determine the local crystal structure and crystal orientation at the surface of a specimen and is conducted using a SEM equipped with an EBSD detector containing a phosphor screen, compact lens and low light CCD camera, as schematically illustrated in Figure 3.10. When the electron beam hits the tilted sample (70°) in a single point, BSEs are elastically scattered, and a certain fraction of these electrons are diffracted according to Bragg's law. The phosphor screen in the detector collects the scattered BSEs, which results in a diffraction pattern made up by Kikuchi bands. This pattern provides a representation of the lattice structure and its orientation for that specific point. A CCD camera behind the phosphor screen images the pattern and sends it to a computer.

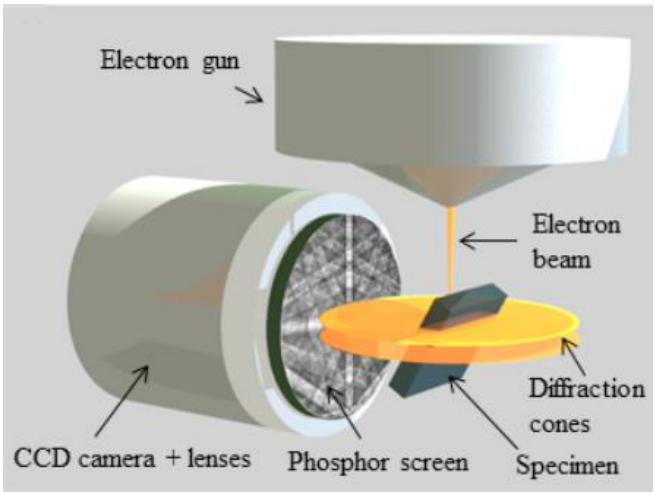

Figure 3.10: The EBSD detection geometry and a conventional EBSD detector [98].

The raw pattern is noisy, has low contrast and is more intense in the middle, and therefore the background intensity is subtracted from the pattern before further analysis. The Kikuchi patterns are analysed by an appropriate software, and the orientation of a specific grain or subgrain can be obtained by indexing them. A Hough transformation is performed on the patterns, where each band in Cartesian space is represented by a point in Hough space. Thousands of orientations can be recorded in this manner and an orientation map of the sample is created [99]. Combined with statistical tools, the orientation maps can provide information about grain- and subgrain size, misorientation, texture etc. The obtained orientation map is constructed by pixels, and an assembly of equally oriented pixels (>10 pixels) is considered a grain. The quantity of the pixels is determined by the step size, and step size is therefore very important for the resulting EBSD map [7, 99]. Typical Kikuchi patterns of different materials are shown in Figure 3.11.

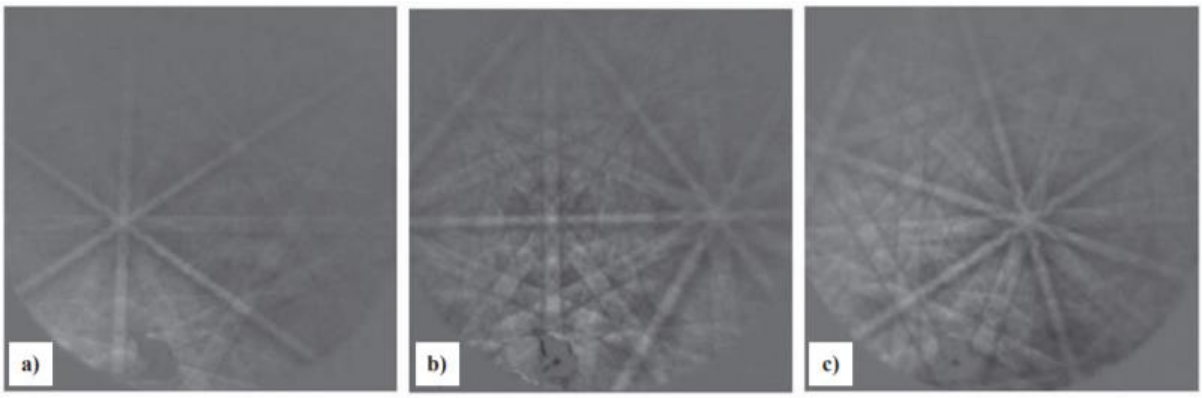

Figure 3.11: EBSD patterns from: a) Commercially pure aluminium with FCC structure, b) electrical steel (Fe-Si alloy) with body-center-cubic (BCC) structure, c) alpha phase titanium with hexagonal-close-packed (HCP) structure [100].

A Zeiss Ultra 55 – Limited Edition FESEM equipped with an EBSD detector was utilized for microstructure characterization, and a detector (NORDIF UF1100) controlled by the NORDIF 3.1 software was used to gather the EBSD patterns. The operating parameters for FESEM-EBSD and NORDIF UF-390 are displayed in Table 3.5.

Table 3.5: Operating parameters for FESEM and NORDIF UF1100.

FESEM-Parameter	Value
Acceleration Voltage	20 kV
Working Distance	25 mm
Tilt angle	70°
Magnification	200X – 1000X
Scan Area	
Step Size	150 – 300 nm
Calibration Settings	
Frame Rate	120 fps
Resolution	160 x 160 px
Exposure Time	8283 µs
Gain	4
Acquisition Settings	
Frame Rate	300 fps
Resolution	120 x 120 px/ 160 x 160
Exposure Time	3283 µs
Gain	4

The chosen magnification and step size depended on the grain size of the samples, and if the samples were recrystallized or not. Smaller grain sizes require higher magnification and smaller step size to obtain sufficient grain statistics. The scan order for the different samples is displayed in Table 3.6.

Table 3.6: Scan order for the different samples investigated in SEM.

Sample	No. of Scans	Step Size [*nm*]	Magnification [*X*]
HR	1	200	500
%CR46	1	150	1000
%CR67	1	150	1000
%CR87	1	150	1000
%CR46-180	3	200	500
%CR67-180	1	200	500
%CR87-180	1	200/150	500/1000
%CR46-280	3	200	200
%CR67-280	3	200	200
%CR87-280	3	200	200
%CR46-330	6	300	200/500
%CR67-330	5	300	200/500
%CR87-330	4	300	200/500

The EBSD patterns for the hot rolled sample and the samples annealed to 280°C and 330°C collected by NORDIF UF-1100 were indexed in the TSL OIM Data Collection 7 software. The software is an offline system for data postprocessing, which means that data indexing is performed after the acquisition of the EBSD pattern on an external computer. In order to detect bands in the diffraction patterns, a classic Hough transformation with 7x7 convolution mask, 0.5° theta step size and 96 binned pattern size was carried out. TSL OIM Analysis 6.1 was used for rotating the indexed data, as the default setting of the scanned plane in the software is the RD-TD section. In the present work, the ND-RD section (see Figure 3.8) is the investigated plane, and the data was therefore rotated 90° around RD to obtain the correct orientation. The data was further analysed in MTEX. MTEX [101] is a MATLAB toolbox for analysing and modelling crystallographic textures by means of EBSD data (or XRD).

The cold rolled and low temperature annealed samples (180°C) were harder to index, as the large amount of stored energy in the samples made it difficult to gather adequate EBSD patterns. As a result, several grains and orientations were not indexed, and a new method had to be utilized to better index these patterns. The EBSD pattern collected by NORDIF UF-1100 were analysed by Håkon Wiik Ånes using the dictionary indexing (DI) approach available in the open-source software EMsoft [102-104]. Typical simulations of EBSD patterns for all possible crystal orientations are generated in a dictionary. The experimental EBSD patterns are indexed by comparing them to the dictionary using a dot-product algorithm, and the orientation

of the simulated pattern with the highest dot product is assigned to the experimental pattern. The DI method is highly precise and surpasses the performance of previously available methods [105]. However, it is time and memory consuming. The estimate of the detector geometry (pattern centre and distance from the sample to the scintillator) from TSL was converted into internal units utilized in the DI approach. Knowledge of the detector pixel size was also required. An ang-file containing orientation data is obtained from the approach, and this data was further analysed in MTEX. These samples have not been rotated 90° around RD, and the orientations are therefore not valid and will not be discussed.

The post-processing procedure performed by MATLAB in the scripts attached in Appendix B.1.1 (TSL approach) and B.1.2 (DI approach) is briefly described in the following. More information can be found on the MTEX homepage [106]. The crystal symmetry and axis directions are first specified. The orientations are then colourized according to their position in a fixed IPF. The next step is to remove low-quality measurements/pixels by filtering on pattern fit for the samples indexed with TSL OIM Data Collection 7 and filtering on confidence index for the samples indexed with EMsoft. The fit parameter defines the average angular deviation between the recalculated bands and the detected bands, whereas the confidence index describes how confident the software is that it has correctly indexed the EBSD patterns. The EBSD data is then denoised following these steps:

1. Grains are reconstructed including the smallest grains in the bigger grains based upon a minimum pixel threshold of 10 pixels with a misorientation angle threshold of 10°.
2. The not indexed pixels are filled in with an orientation averaging using a half-quadratic filter [107].
3. Grains are reconstructed again still including the smallest grains in the bigger grains, with a misorientation angle threshold of 0.5° or 0.6° for the samples indexed with the TSL OIM Data Collection 7 software and a threshold of 0.4° or 0.3° for the samples indexed with the EMsoft software. Grains are smoothed as well.
4. The not indexed pixels are filled in with a given filter again. LAGBs and HAGBs are separated, where HAGBs are defined as boundaries with a misorientation angle of > 15°.
5. Finally, the boundaries are plotted on the orientation map.

MTEX was used to produce orientation maps, and the script in Appendix B.2 was used to measure grain- and subgrain size, grain orientation spread (GOS) and amount of HAGBs. According to Allain-Bonasso et al. [108] for grain i, the *GOS* is

$$GOS(i) = \left[\frac{1}{J(i)}\right] \sum_{\mathrm{j}} \theta_{\mathrm{ij}} \tag{3.5}$$

where *J(i)* is the number of pixels in the grain i and θ_{ij} is the misorientation angle between the orientation of pixel j and the mean orientation of grain i. For a set of *I* grains, the average *GOS* becomes

$$GOS = \left(\frac{1}{I}\right) \sum_{\mathrm{i}} GOS(i) \tag{3.6}$$

Grains with a minimum equivalent circular diameter of 3 µm, a minimum fraction of HAGBs of 0.5 and a maximum GOS of 2° were specified as recrystallized grains or nuclei. Grains that did not fulfil these criterions were specified as subgrains. The amount of recrystallized grains was used to determine the fraction recrystallized in each sample.

The grain size of the recrystallized samples, %CR46-330, %CR67-330 and %CR87-330, were measured in both RD- and ND-direction using the linear intercept method to study to what extent the grains were elongated in RD. Five measurements were performed in both directions from three different images for each sample to achieve proper statistics (all in all 30 measurements for each sample). ImageJ was used to measure the grain size from the relationship:

$$Average\ Grain\ Size\ (\mu m) = \frac{Line\ Length\ (\mu m)}{Number\ of\ Grains} \tag{3.7}$$

3.5 Macrotexture Measurements – XRD

XRD is a conventional method to determine an unknown crystal orientation in practical applications and is used in this work. The instrument utilized in this work for XRD measurements is called a *goniometer*, which is one of several instruments available for XRD. The samples are mounted in the instrument and step motors allow positioning of the goniometer to any arbitrary angular position of the four axes: 2θ, ω, r, and φ within a certain range. The polar angle, r, and the azimuthal angle, φ, are the axes in the pole figure, and the angles range between 0° and 90°, and 0° and 360°, respectively. A detection system is embedded in the

instrument, and the goniometer positions the detector with respect to the incident beam ray at the appropriate Bragg angles 2θ for diffraction from the required plane. The (111), (200), (220) and (311) pole figures were measured by selecting a constant angle which gives diffraction according to Bragg's law. The distribution of the plane normal to the desired plane was recorded by tilting and rotating the samples.

The recrystallized samples (%CR46-330, %CR67-330 and %CR87-330) were studied in the Siemens D5000 diffractometer and recorded with the Bruker DIFFRAC Plus software. The samples annealed at the highest temperature were chosen to ensure complete recrystallization. The latter was used to gather the various pole figures. TexEval was then utilized to adjust the pole figures for defocusing error, which arises from decreasing intensities as a result of increasing polar angles, r. A RES-file containing pole figure intensities is obtained from the analysis, and these intensities were further analysed in MTEX (see Section 3.4.2). ODFs were estimated from the corrected pole figure intensities with the polar angles up to 80° using the MTEX algorithm [109]. Default settings were used, i.e. the de la Vallee Pousson kernel with a halfwidth of 5°. The Matlab script was used to create an MTEX pole figure object from the four adjusted pole figures, and then calculate the ODF, plot intensities along fibres (beta and Cube-Goss) and calculate volume fractions of specific texture components. Volume fractions of the different texture components were computed with ±10° tolerance for each of the ODFs (spread = 10° in the MATLAB script). The MATLAB script is shown in Appendix C.1. A set of raw pole figures corrected for defocusing error can be observed in Figure 3.12.

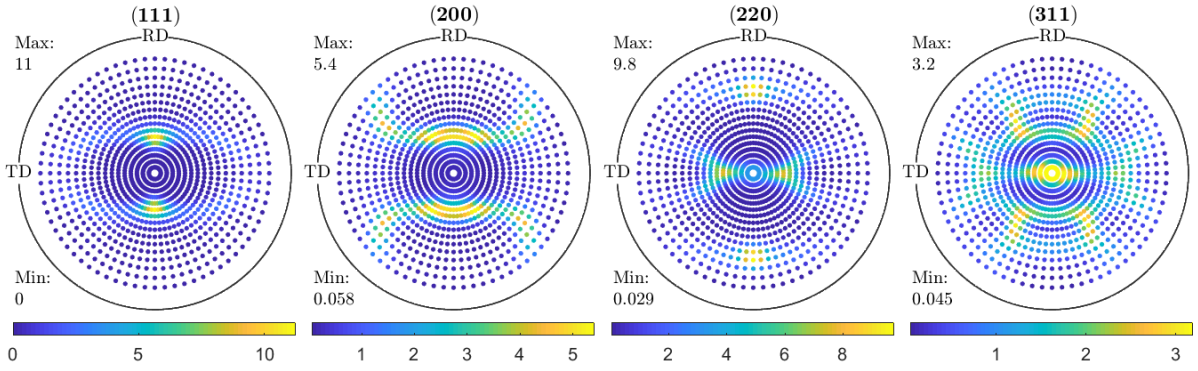

Figure 3.12: Raw (111), (200), (220) and (311) pole figures obtained from MTEX adjusted for defocusing error in TexEval. The range of the polar angles is between 0° and 80°.

The samples were prepared as follows:

(i) Cut to dimensions 22 x 14 mm with Struers Accutom-5, with the shortest direction in the rolling direction, as shown in Figure 3.13.

(ii) Ground on SiC paper with the finest mesh size (4000).

(iii) Etching for 10 minutes in Alubeis (10-20% NaOH + 1 teaspoon sugar per litre liquid) and at last

(iv) Etching for 30 seconds in 20-30% HNO_3. The three last steps were performed to remove the deformed surface layer.

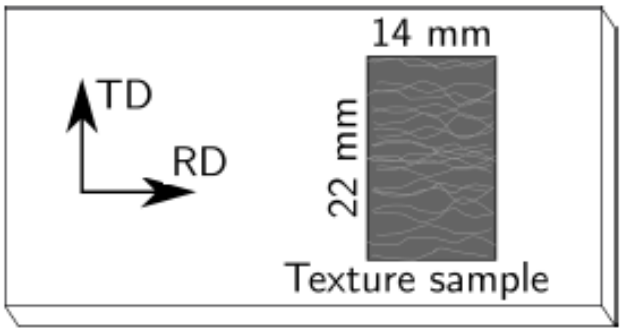

Figure 3.13: Texture sample geometry [110].

4. RESULTS

The experimental results are presented in the following section. It is divided into six parts. The first part contains the results of the tensile test. Second, the hardness curve is presented and described, followed by a presentation of the electrical conductivity. Results from EBSD, including OIM-maps, fractions recrystallized and grain size measurements, are presented in the fourth part. The texture results are presented in the fifth part of this section, including ODFs and fraction of texture components. The results from the particle analysis are given in the sixth and final part.

4.1 Annealing Curves

This subsection considers the evolution of mechanical properties during annealing. The samples were heated at 100°C/h to target temperature and subsequently held at the target temperature for three hours. The annealing curves in Figures 4.1, 4.2 and 4.3 show the temperature dependence of yield strength, ultimate tensile strength and elongation, respectively, for the hot rolled, cold rolled and annealed AA3005 samples. These curves help describe the softening behaviour of the different samples cold rolled to different deformation degrees. The error bars, which are so insignificant that they are not possible to observe for most of the measurements, signify the standard deviation calculated from the three samples for each temperature. The mechanical properties at 25°C correspond to the properties for the as cold rolled samples. The initial yield strength of the most deformed sample is much higher than the strengths of the two other samples; samples cold rolled to %CR = 46, 67 and 87 show yield strengths of 212.7 MPa, 228.7 MPa and 283.3 MPa, respectively. Yield strength remains relatively constant between room temperature and 180°C. At higher annealing temperatures, from 180°C to 260°C, the reduction in yield strength is somewhat steeper. In this temperature region, the yield strength of the samples with a corresponding %CR = 87 decreases most rapidly, from 243.7 MPa to 167.0 MPa, and the reduction in yield strength decreases with decreasing cold rolling. At 280°C, the strength of %CR = 87 and %CR = 46 samples are approximately the same (≈150 MPa, see Table 4.1).

Recrystallization initiates when a significant decrease in strength (or hardness) occurs. As indicated by both Figures 4.1 and 4.2, a significant decrease in strength is observed at 270°C for the samples with a cold reduction of 67%, while a rapid decrease in strength is first observed

at approximately 280°C for the two remaining cold reductions. This indicates that the softening reaction occurs earliest in %CR = 67.

A corresponding trend can be observed for the measured elongation, where a rapid increase in elongation occurs at 273°C for %CR = 67, and approximately 285°C for %CR = 46 and 87. The general trend is that the elongation is inversely proportional with the strength. When the ultimate tensile strength and yield strength decrease, the elongation increases, with some exceptions. A significant drop in elongation can be observed for %CR = 46 at 283°C. After annealing at 290°C, the yield strength and ultimate tensile strength for %CR = 67 reach a stable value, which indicates that recrystallization is complete. A stabilization in strength can be observed after annealing at 300°C for %CR = 87 and after annealing at 310°C for %CR = 46. The annealing curves indicate that the recrystallization kinetics are faster for %CR = 67 compared to %CR = 87, and that the kinetics are faster for %CR = 87 compared to %CR = 46. It must be emphasised that it is difficult to tell exactly when the recrystallization initiates for the different samples, and if recovery or recrystallization is the main reason for the softening behaviour at intermediate temperatures. Considering the tensile strength and ultimate yield strength of the hot rolled sample, it can be observed that the strengths are similar to the strengths of the %CR = 67 sample annealed at 275°C, and the %CR = 46 and %CR = 87 samples annealed at 285°C.

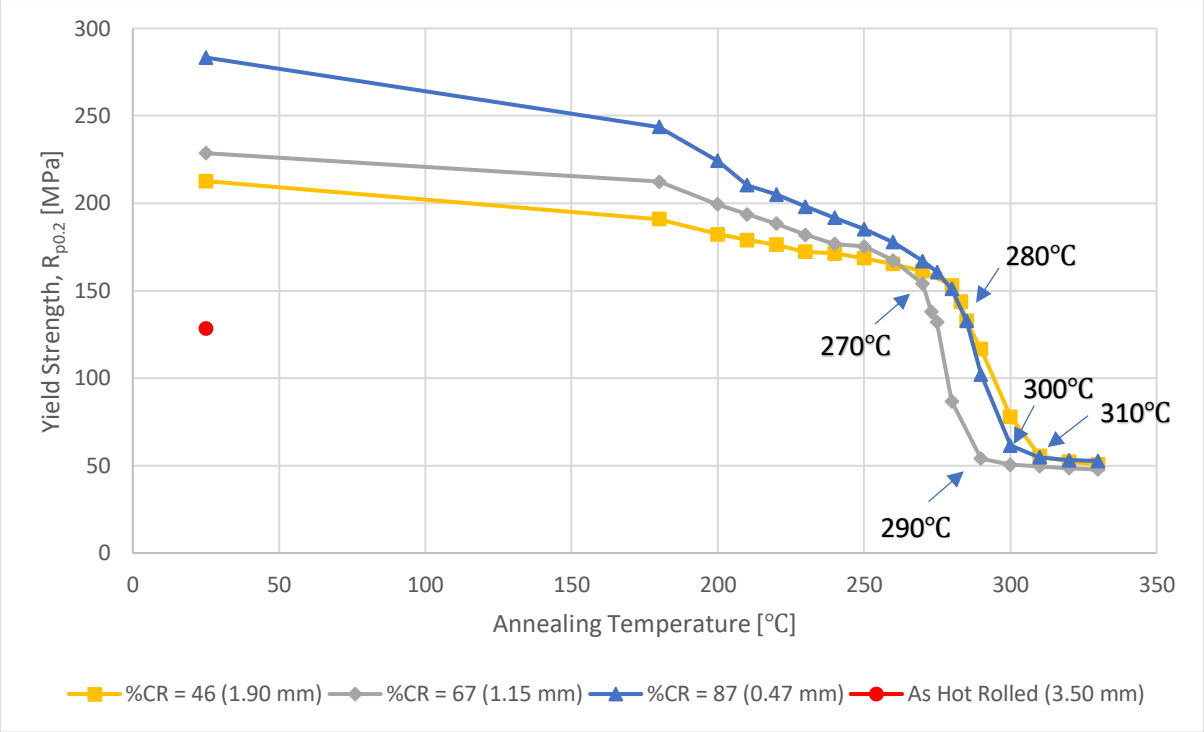

Figure 4.1: Yield strength, $R_{p0.2}$, in RD for the samples cold rolled to %CR = 46, 67 and 87, as well as the yield strength in RD for the as hot rolled sample when the samples were heated at 100 °C/h to the target temperature and kept at this temperature for three hours. The annealing temperatures of 25°C correspond to the as cold rolled samples.

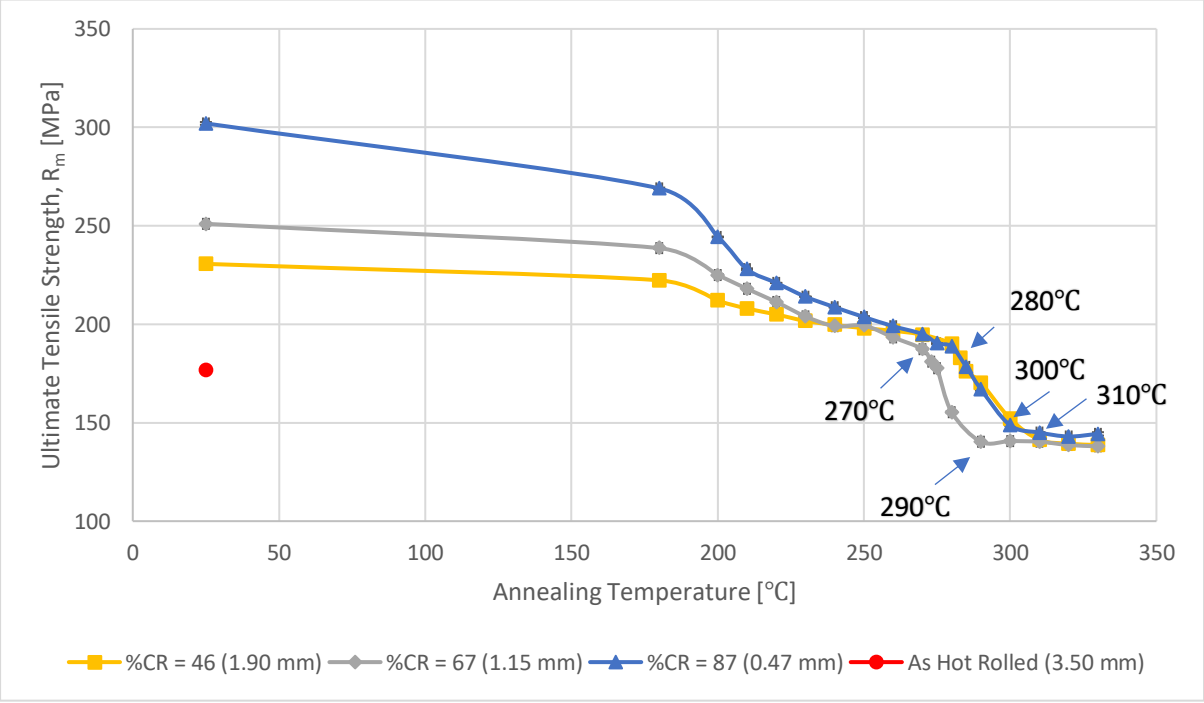

Figure 4.2: Ultimate tensile strength, R_m, in RD for the samples cold rolled to %CR = 46, 67 and 87, as well as the ultimate tensile strength in RD for the as hot rolled sample when the samples were heated at 100 °C/h to the target temperature and kept at this temperature for three hours. The annealing temperatures of 25°C correspond to the as cold rolled samples.

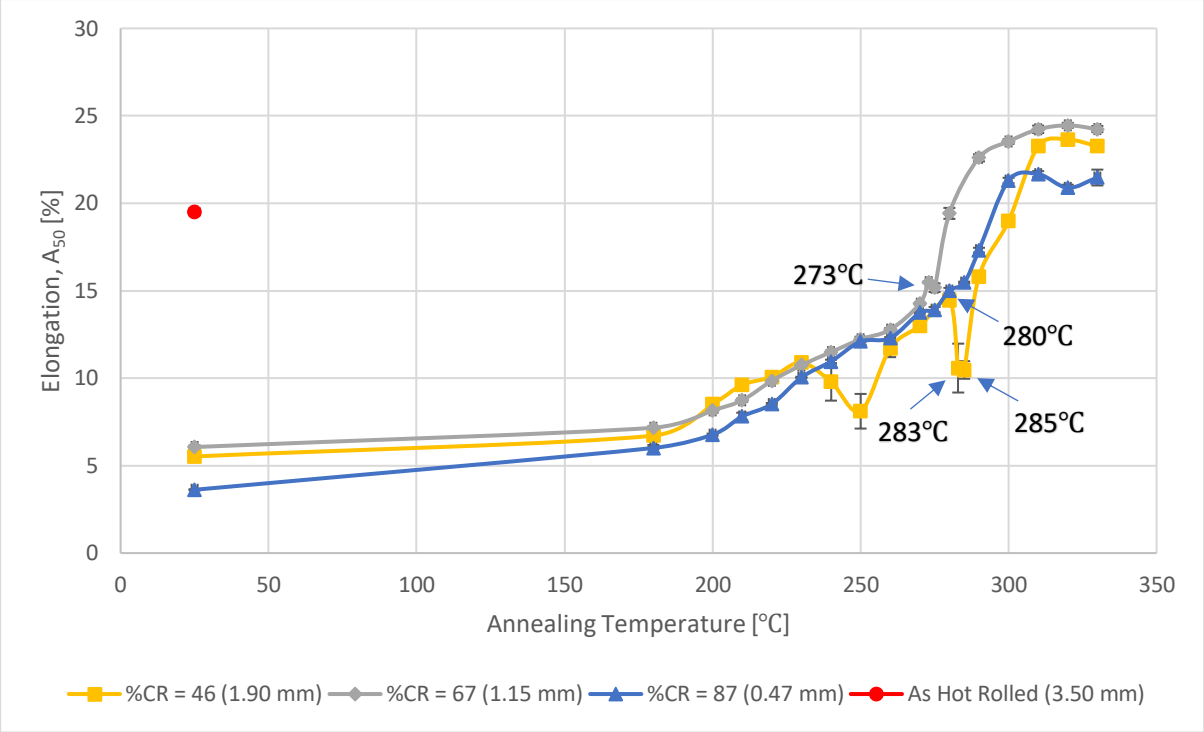

Figure 4.3: Elongation, A_{50}, in RD for the samples cold rolled to %CR = 46, 67 and 87, as well as the elongation in RD for the as hot rolled sample when the samples were heated at 100 °C/h to the target temperature and kept at this temperature for three hours. The annealing temperatures of 25°C correspond to the as cold rolled samples.

The mechanical properties of the samples investigated in SEM are displayed in Table 4.1. Some of these properties will be compared with the measurements carried out in SEM (particle analysis and EBSD), and it is therefore reasonable to list the exact values.

Table 4.1: Mechanical properties of the samples investigated in SEM.

Sample	$R_{p0.2}$ [*MPa*]	R_m [*MPa*]	A_{50} [*%*]
HR	128.3	176.7	19.52
%CR46	212.7	230.7	5.53
%CR67	228.7	251.0	6.06
%CR87	283.3	302.0	3.62
%CR46-180	191.0	222.3	6.72
%CR67-180	212.3	238.7	7.17
%CR87-180	243.7	269.0	6.01
%CR46-280	153.0	190.0	14.45
%CR67-280	86.7	155.3	19.42
%CR87-280	151.0	188.7	15.01
%CR46-330	50.6	138.7	23.27
%CR67-330	47.8	138.0	24.25
%CR87-330	53.2	144.3	21.47

4.2 Hardness

This subsection considers the evolution of hardness during annealing. The samples were heated at 100°C/h to target temperature and subsequently held at the target temperature for three hours. Like the annealing curves, the evolution of hardness for the three different cold reductions can help understand the softening reactions occurring during annealing up to 330°C. However, the annealing curves provide a more complete understanding of the softening behaviour. The yield strength and hardness show the same tendencies. Recrystallization initiates rather simultaneously in %CR = 67 and 87, at temperatures somewhere between 260°C and 270°C. However, recrystallization initiates slightly earlier in %CR = 67. Recrystallization occurs at a temperature around 270°C in %CR = 46. At these temperatures, a significant decrease in hardness can be observed. The slope of the curves between 180°C and the start of recrystallization indicate that recovery is the main softening reaction. Furthermore, the hardness levels out with a further increase in annealing temperature for %CR = 67 at approximately 300°C. The hardness curve levels out at approximately 310°C for %CR = 46

and 87%. This indicates that recrystallization is complete earlier for %CR = 67 and that the recrystallization kinetics are slower in %CR = 87.

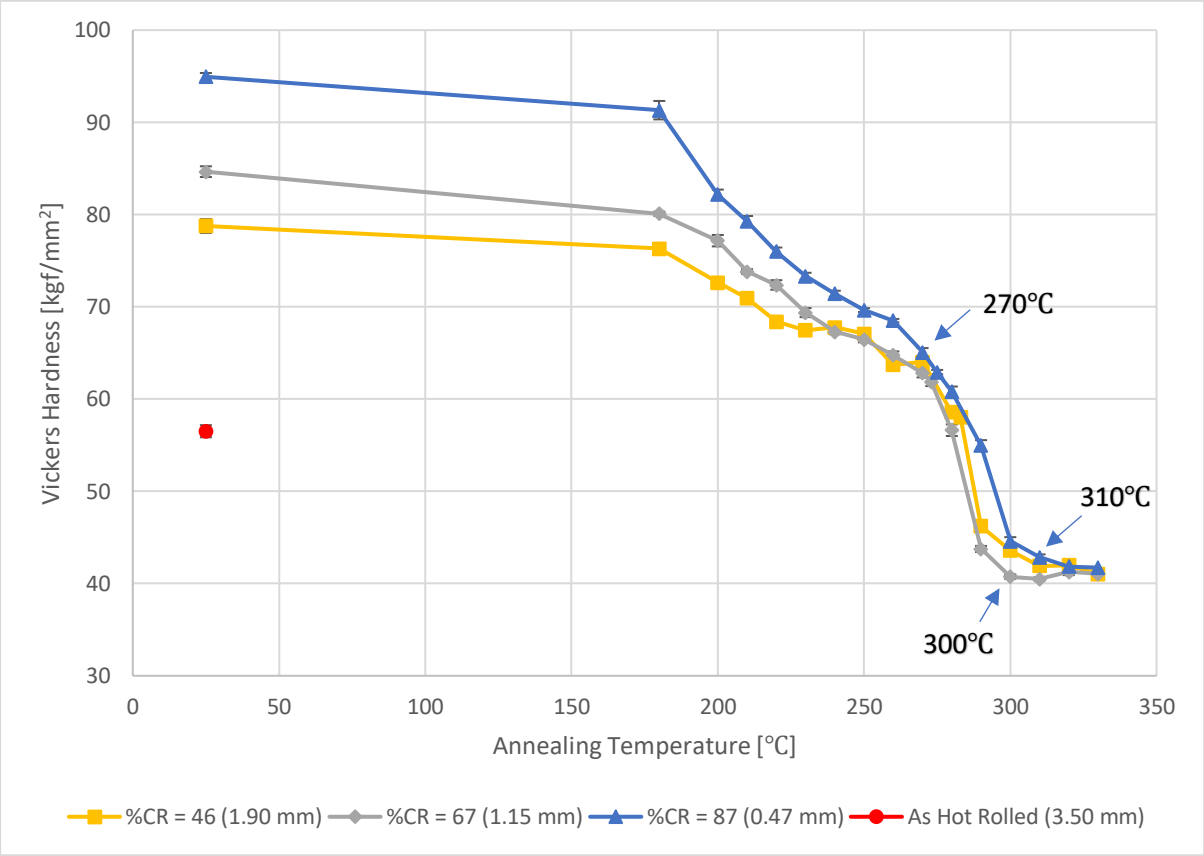

Figure 4.4: Hardness evolution for %CR = 46, 67 and 87, as well as the hardness value for the as hot rolled sample, when the samples were heated at 100 °C/h to the target temperature and kept at this temperature for three hours. The annealing temperatures of 25°C correspond to the as cold rolled samples.

4.3 Electrical Conductivity

The change in electrical conductivity during heat treatment at different temperatures between 180°C to 330°C (100°C/h) with holding time of three hours is shown for the three cold rolled variants in Figure 4.5. The values for the as hot rolled and cold rolled samples are also shown in the figure. The standard deviation did not exceed 0.4%. In the as cold rolled conditions, the electrical conductivity is highest in %CR = 46 and lowest in %CR = 67. The electrical conductivity for the as hot rolled sample is higher than in the as cold rolled samples.

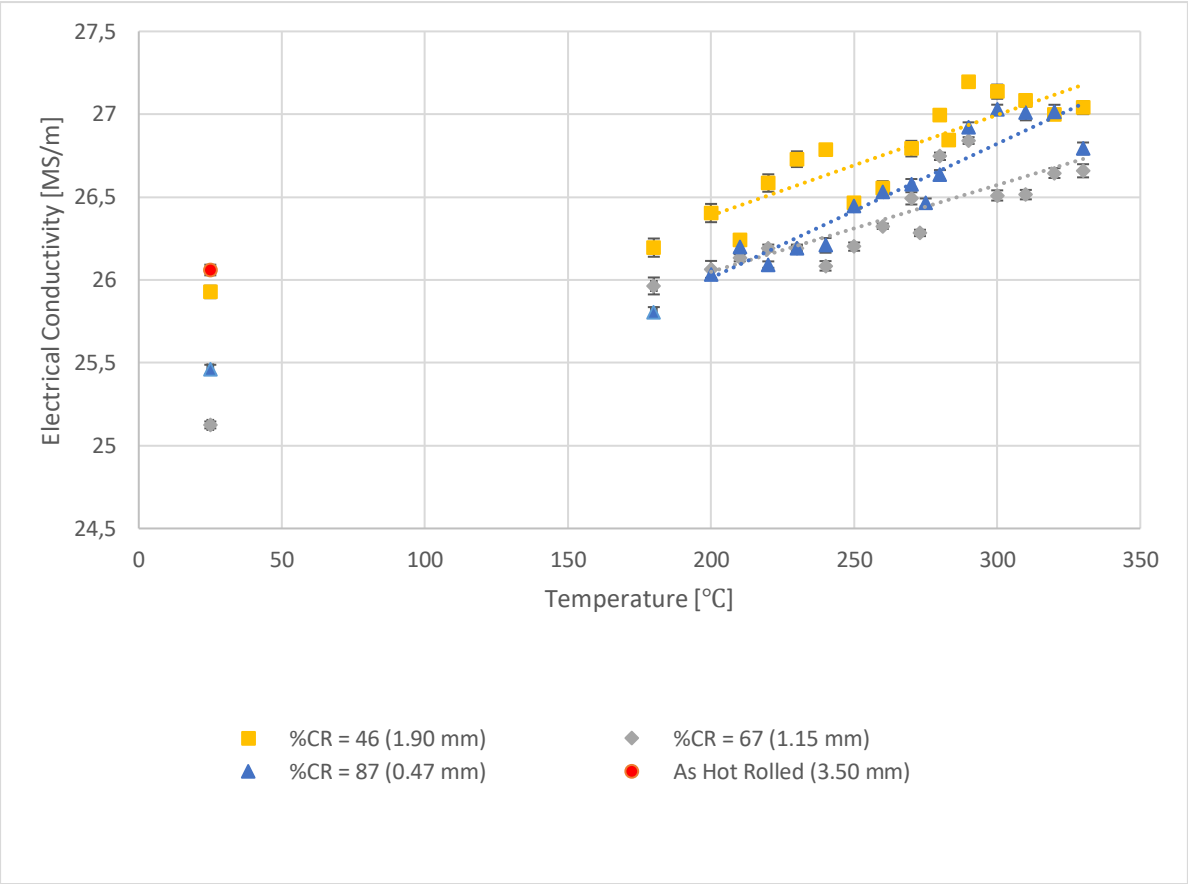

Figure 4.5: Electrical conductivity evolution for %CR = 46, 67 and 87, as well as the electrical conductivity value for the as hot rolled sample, when the samples were heated at 100 °C/h to the target temperature and kept at this temperature for three hours. The annealing temperatures of 25°C correspond to the as cold rolled samples. Trendlines have been added to the chart (the dotted linear lines).

The electrical conductivity results displayed in Figure 4.5 can be used together with Matthiessen's rule (cf. Eq. 3.2 in Section 3.3) by neglecting the contribution from iron and silicon to roughly estimate the amount of manganese in solid solution for the samples investigated in SEM. The estimations of Mn in solid solution are presented in Table 4.2. A calculation example is shown in Appendix A.1. These are not exact values and are only rough estimates. However, the estimations still give an indication of the difference in Mn in solid solution content between the different cold rolled variants. The different deformation degrees will also influence the electrical conductivity, and thus the amount of Mn in solid solution, whereas electrical conductivity generally decreases with an increasing percentage of cold deformation (see Section 3.3). The reduction of dislocation density during recovery (and recrystallization to a certain extent) will increase the electrical conductivity but has been disregarded in the estimation of Mn in solid solution. As can be seen from the table, the

variations of Mn in solid solution is relatively significant. The largest amount is 0.397 wt% (%CR67), and the smallest amount is 0.312 wt% (%CR46-330).

Table 4.2: Estimations of the amount of Mn in solid solution.

Sample	EC [*MS/m*]	Mn in ss [*wt%*]
HR	26.06	0.354
%CR46	25.93	0.360
%CR67	25.13	0.397
%CR87	25.46	0.381
%CR46-180	26.20	0.348
%CR67-180	25.96	0.358
%CR87-180	25.80	0.365
%CR46-280	27.00	0.313
%CR67-280	26.75	0.324
%CR87-280	26.64	0.328
%CR46-330	27.04	0.312
%CR67-330	26.66	0.328
%CR87-330	26.79	0.322

A notable increase in electrical conductivity is observed already when the temperature has reached 180°C for all cold rolled variants. However, the electrical conductivity increases considerably more in %CR = 67 than for %CR = 46 and 87. At 290°C, a maximum is reached in both %CR = 46 and 67, while the electrical conductivity continues to increase for %CR = 87, suggesting that concurrent precipitation is still predominant in the most deformed sample. A maximum is reached at 300°C in %CR = 87. Trendlines have been added between 200°C and 330°C, where the precipitation reaction most likely is the main contributor to an increase in electrical conductivity. It is seen that the increase in electrical conductivity is most significant for %CR = 87 and least significant for CR% = 67, which indicates that concurrent precipitation during annealing is most pronounced for the former and least pronounced for the latter. In must be emphasised that the observed differences are small, and the change in electrical conductivity is a result of the combination of the annihilation of dislocations and precipitation.

4.4 EBSD Measurements

In the following subsection, the results from the EBSD measurements are presented. First, the initial condition, the hot rolled sample, is presented with an OIM-map and a corresponding

image separating subgrains and recrystallized grains. In the cold rolled samples and the samples annealed to 180℃, OIM-maps with and without highlighted HAGBs and LAGBs are presented, together with the subgrain size, fraction HAGBs and GOS. OIM-maps and corresponding images separating the subgrains and the recrystallized grains are presented for the samples annealed to 280℃ and 330℃, together with grain size, fraction HAGBs, GOS and fraction recrystallized.

Subgrains and recrystallized grains are defined according to the description in Section 3.4.2. Furthermore, LAGBs are defined as boundaries with a misorientation between 0.3°-0.6° and 15° to the neighbouring grains, and HAGBs are defined as boundaries with a misorientation above 15° to the neighbouring grains. At last, the linear intercept measurement for the recrystallized samples (%CR46-330, %CR67-330 and %CR87-330) are presented. The rest of the OIM-maps from EBSD can be found in Appendix B.3.

4.4.1 Initial Condition – as Hot Rolled

Figures 4.6 (a) and (b) show the OIM-maps and amount of HAGBs and LAGBs, respectively, for the as hot rolled sample. The microstructure is partially recrystallized, and the sample shows small misorientations less than 15° inside some of the grains, and thus not large enough to form HAGBs. Most of the grains are elongated along RD. In parts of the sample, original elongated grains are broken and refined to finer un-recrystallized and equiaxed grains with non-uniform orientations. The recrystallized grains are either elongated along RD or more equiaxed. From the pattern acquired with EBSD, it has been calculated that the grain size of the as hot rolled sample is 3.17 µm, the GOS is 0.41° and the fraction of HAGBs is 52.3%, resulting in a fraction recrystallized of 19.7%.

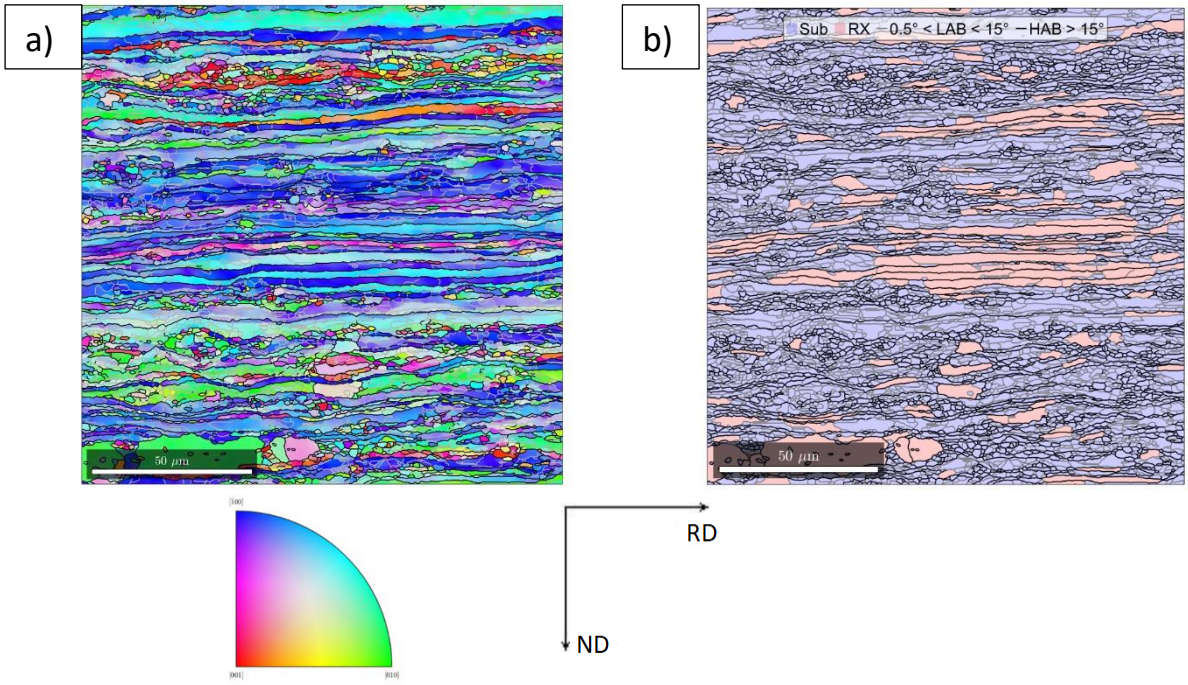

Figure 4.6: EBSD images (500x) showing the microstructure of the hot rolled sample (HR) (a) – (b), showing the OIM-map (a) and the amount of HABGs and LAGBs (b).

4.4.2 As Cold Rolled

Figures 4.7 (a), (c) and (e), and (b), (d) and (f) show the OIM-maps with and without highlighted grain boundaries, respectively, for the cold rolled samples. As seen from Figure 4.6, the hot rolled material was in a partly recrystallized condition prior to cold rolling and the total stored energy for recovery and recrystallization may be somewhat higher. From Figures 4.7 (a) – (f) it can be seen that the least deformed sample, %CR46, is most comparable to the as hot rolled microstructure in Figure 4.6 (a). As deformation increases the grains become more elongated in the rolling direction with increasing amounts of HAGBs. Most of the observed HAGBs are so-called lamellar grain boundaries.

Particles are indicated with the arrows in Figures 4.7 (a), (c) and (e). The particles were quantified by filtering on the confidence index (see Section 3.4.2). As can be observed, the large constituent particles are identified as relatively large subgrains with high misorientations to the surrounding grains. However, this is not actually the case as these are particles and not grains. As a result, the calculated grain size is increased compared to the actual size and a higher amount of HABGs are detected. Deformation zones can be seen around the large particles and seem to be more apparent around the more deformed samples (%CR = 67 and 87). These zones can act as nucleation sites for recrystallization through the nucleation mechanism PSN (see Section 2.3.3). Shear bands can also clearly be observed in the samples, indicated by arrows in Figures 4.17 (b), (d) and (f). Similar to deformation zones, shear bands can act as nucleation sites due to the high stored energy in the bands.

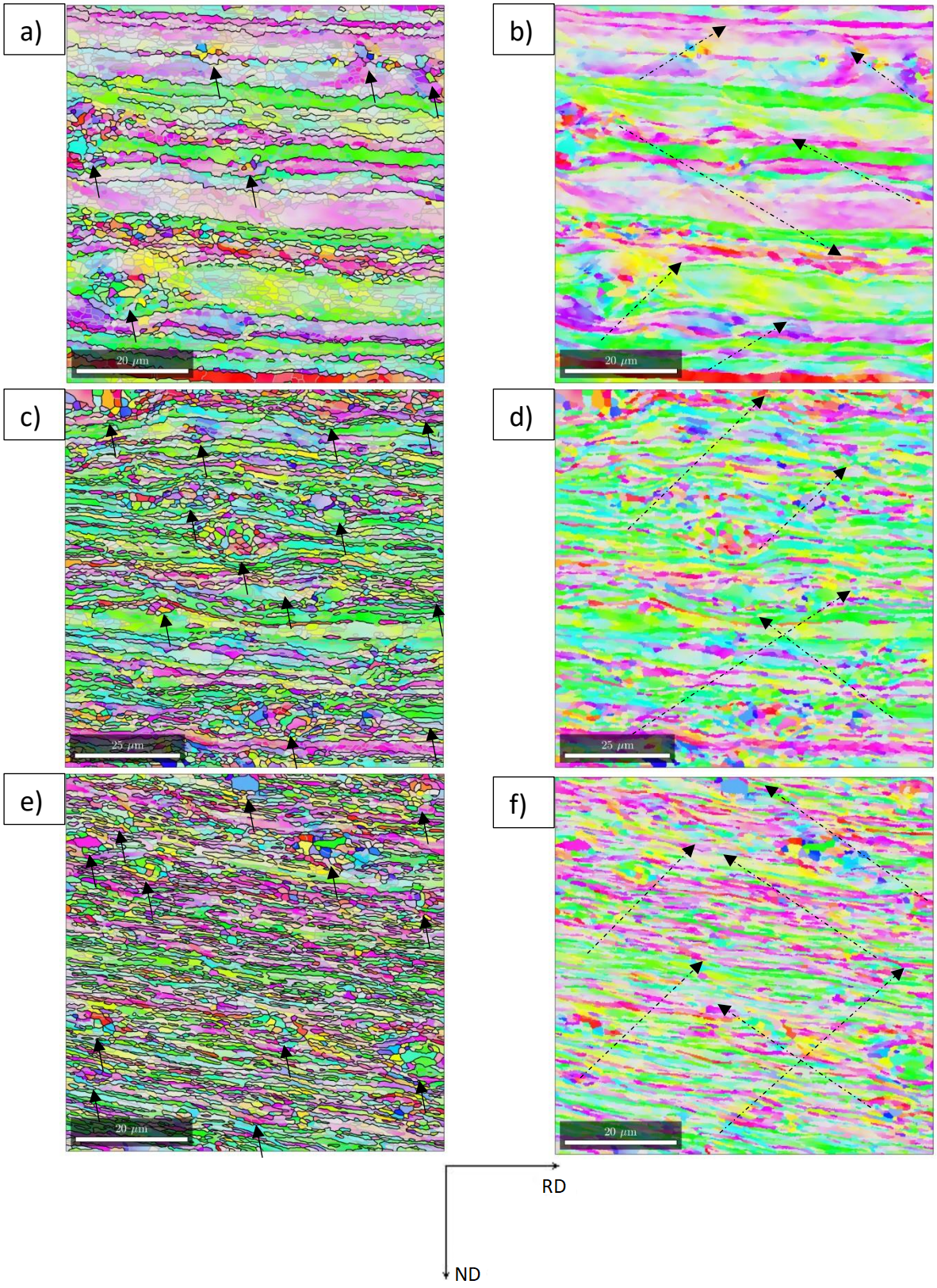

Figure 4.7: EBSD images (1000x) showing the microstructure of the %CR46 sample (a) – (b), %CR67 sample (c) – (d) and %CR87 sample (e) – (f), showing the OIM-map indicating particles with highlighted grain boundaries (a), (c) and (e), and OIM-map indicating shear bands (b), (d) and (f).

Table 4.3 displays the subgrain size, fraction HAGBs and GOS for the cold rolled samples. As the degree of deformation increases from 46% to 87% the subgrain size decreases and the fraction of HABGs increases. No correlation between the deformation degree and GOS can be observed. The values presented in the table are important during the subsequent annealing since they determine the stored energy of the samples and thus the driving force for recrystallization, and the possibility of nucleation. It must be emphasised that only one image was investigated for each cold rolled sample.

Table 4.3: Different properties calculated with MTEX from the EBSD patterns collected from SEM.

Sample	Subrain size [μm]	Fraction HAGBs [%]	GOS [°]
%CR46	1.81	35.1	26.8
%CR67	1.46	59.6	25.6
%CR87	1.04	70.1	28.1

4.4.3 Annealed - 180°C

Figures 4.8 (a), (c) and (e), and (b), (d) and (f) show the OIM-maps with and without highlighted grain boundaries, respectively, for the samples annealed to 180°C. None of the grains recrystallized at this temperature and the microstructures are rather similar to the as cold rolled samples (see Figure 4.7). As deformation increases from %CR = 46 to %CR = 67 the grains become more elongated in the rolling direction with increasing amounts of HAGBs. However, it is difficult to observe a significant difference between the microstructures of %CR67-180 and %CR87-180 as the magnification is different in the two images.

Particles are indicated with the arrows in Figures 4.8 (a), (c) and (e). Like the as cold rolled samples, the large constituent particles are identified as relatively large subgrains with high misorientations to the surrounding grains. The calculated grain size will be increased compared to the actual size and a higher amount of HABGs are detected. When comparing the particles in the as cold rolled samples and the annealed samples, the reconstructed grains in the particles in %CR87 are observed to be significantly larger than in %CR87-180. It is difficult to compare the particles in the two other cold reductions as the magnifications are different. Furthermore, deformation zones can be observed around the largest particles. Shear bands can also be observed, as indicated by the arrows in Figures 4.8 (b), (d) and (f).

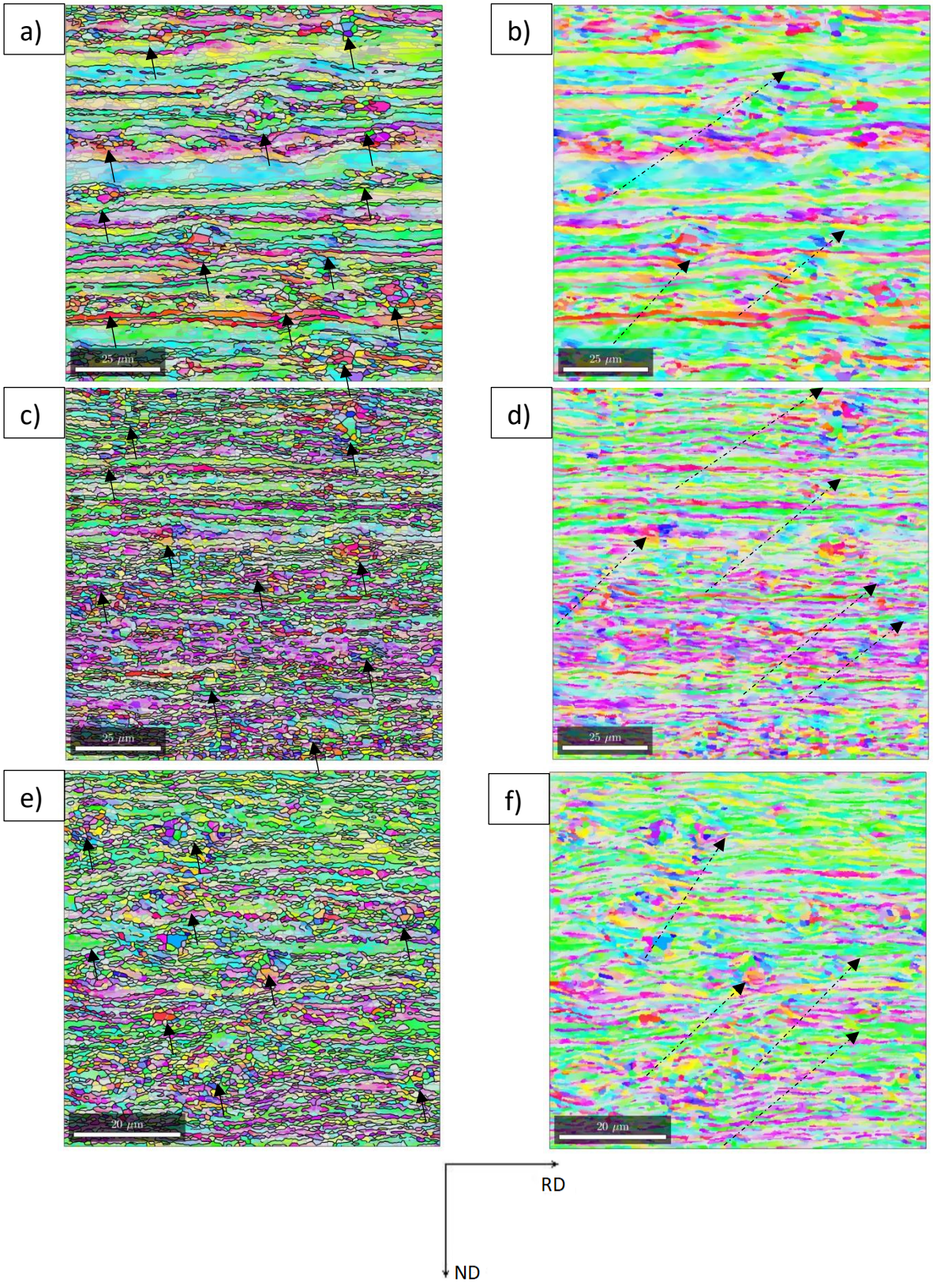

Figure 4.8: EBSD images showing the microstructure of the %CR46-180 (500x) sample (a) – (b), %CR67-180 (500x) sample (c) – (d) and %CR87-180 (1000x) sample (e) – (f), showing the OIM-map indicating particles with highlighted grain boundaries (a), (c) and (e), and OIM-map indicating shear bands (b), (d) and (f).

Table 4.4 displays the subgrain size, fraction HAGBs and GOS for the cold rolled samples. It can be seen that as the degree of deformation increases from 46% to 87% the subgrain size decreases and the fraction of HABGs increases. No correlation between the deformation degree and GOS can be observed. However, the subgrain size is smaller in all the samples compared to as cold rolled condition. This decrease in subgrain size can most likely be attributed to the smaller grain size detected inside the particles. Only one image was investigated for samples %CR87-180 and %CR67-180.

Table 4.4: Different properties calculated with MTEX from the EBSD patterns collected from SEM.

Sample	Subrain size [μm]	Fraction HAGBs [%]	GOS [°]
%CR46-180	1.51	53.5	21.7
%CR67-180	1.19	65.0	15.8
%CR87-180	0.90	67.0	15.8

4.4.4 Annealed - 280°C

Figures 4.9 (a) – (f) show the OIM-maps and amount of HAGBs and LAGBs, respectively, for the samples annealed to 280℃. The images clearly indicate that the samples are partially recrystallized, with some recrystallized grains and several subgrains/deformed grains. When Figures 4.9 (a) – (f) are studied together with the images in Appendix B.3.2, it can be observed that most recrystallized grains are found in %CR67-280 and %CR87-280, and least recrystallised grains are found in %CR46-280, suggesting that the fraction recrystallized is highest in the two most deformed samples. It is difficult to observe any clear difference between %CR67-280 and %CR87-280. The grain structure in %CR46-280 seems to be more recovered than recrystallized, where grains with LAGBs are surrounded by HAGBs, typical for a recovered grain structure. These results are in accordance with the annealing curve in Section 4.1, which suggests recrystallization to initiate earlier for %CR = 67 and 87. The grains in CR% = 67 and 87 show similar orientations.

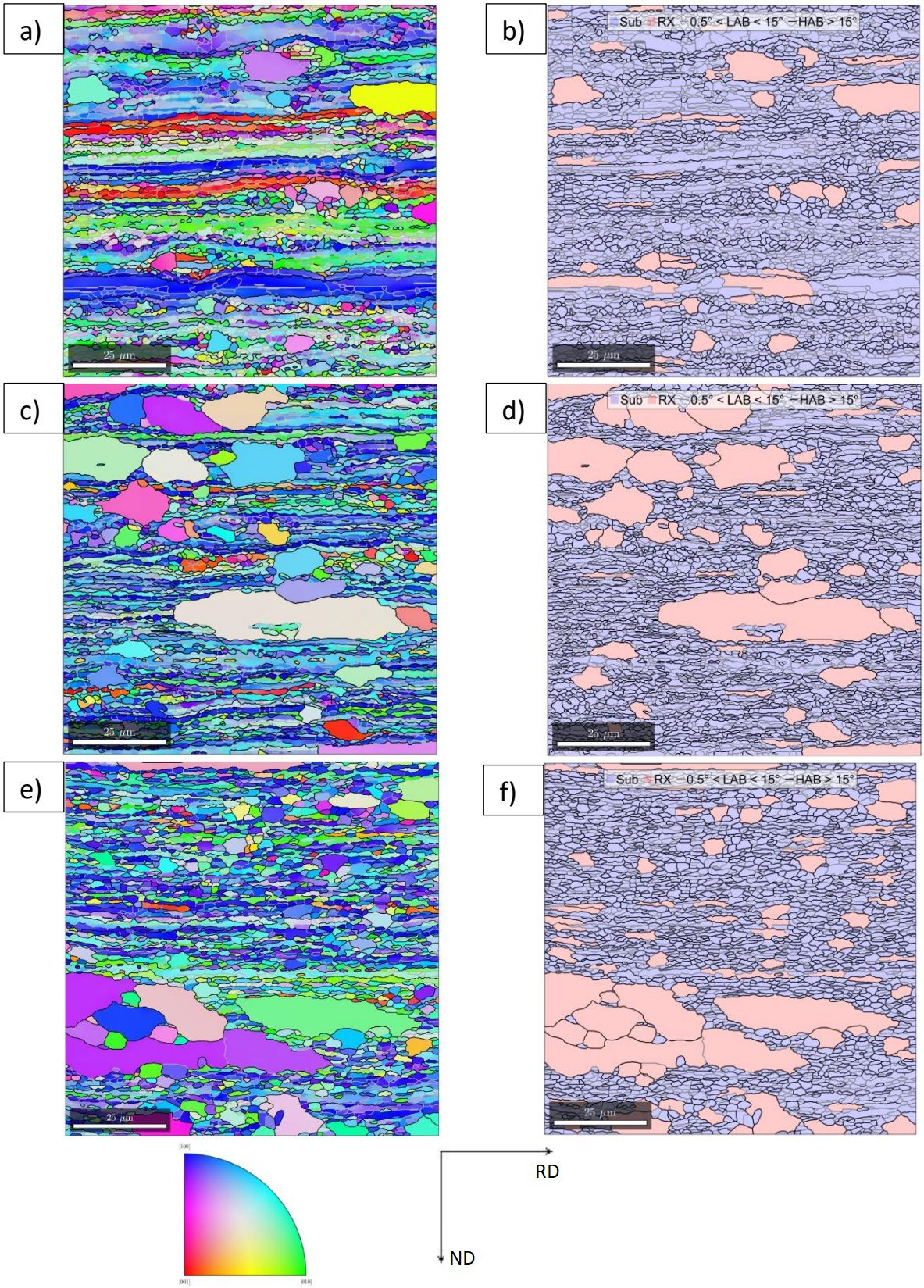

Figure 4.9: EBSD images (500x) showing the microstructure of the %CR46-280 sample (a) – (b), %CR67-280 sample (c) – (d) and %CR87-280 sample (e) – (f), showing the OIM-map (a), (c) and (e), and the amount of HABGs and LAGBs (b), (d) and (f). The figure on the bottom left is the IPF indicating the orientation for each grain.

Table 4.5 displays the fraction recrystallized, the subgrain size, recrystallized grain size and the properties used to determine the fraction recrystallized: Fraction of HAGBs, GOS and the mean grain size for the samples annealed to 280°C. The average grain size is largest in %CR67-280 and smallest in %CR46-280. However, the recrystallized grain size is slightly larger in %CR87-280 than %CR67-280, and the recrystallized grain size is evidently smallest in %CR46-280. The subgrains developed during cold rolling are still smallest in the most deformed sample. As a result, the average grain size is higher in %CR67-280 than in %CR87-280. Furthermore, the subgrain size decreases gradually with increasing deformation. The fraction of HAGBs increases with deformation, while the GOS decreases with deformation. The different properties calculated from the EBSD patterns are used to calculate fraction recrystallized, and it was found that the fraction recrystallized is significantly higher in %CR67-280 and %CR87-280 than for the least deformed sample, %CR46-280. The similar values of fraction recrystallized for %CR67-280 and %CR87-280 are in accordance with Figure 4.5, where the fraction recrystallized is found to be virtually the same for the two samples. This suggests that recrystallization occurs rather simultaneously in %CR67-280 and %CR87-280 and that recrystallization started earlier in the samples cold rolled to %CR = 87 and 67 than for %CR = 46. The fraction recrystallized shows the same tendency as observed in the images in Figures 4.9 (a) – (f). As previously mentioned, these results are in accordance with the hardness measurements.

Table 4.5: Different properties calculated with MTEX from the EBSD patterns collected from SEM.

Sample	Average grain size [μm]			Fraction HAGBs [%]	GOS [°]	Fraction recrystallized [%]
	All grains	Subgrains	Recrystallized grains			
%CR46-280	2.69	1.87	7.02	51.5	0.31	15.5
%CR67-280	3.24	1.58	8.94	62.3	0.29	21.2
%CR87-280	3.06	1.48	9.02	69.0	0.22	20.6

4.4.5 Annealed - 330°C

Figures 4.10 (a) – (f) show the OIM-maps and amount of HAGBs and LAGBs, respectively, for the samples annealed to 330℃. The images clearly indicate that the samples are fully recrystallized, with mostly recrystallized grains and only very few subgrains/deformed grains. This is in accordance with the hardness results in Figure 4.4, where a levelling of the softening curve can be observed at 330℃, consistent with a recrystallized microstructure. Notice the different scale bar in Figures 4.10 (e) and (f). When Figures 4.10 (a) – (d) are studied together with the images in Appendix B.3.3 the grain size is clearly coarser in %CR46-330, and the grain structure seems more elongated along RD. Because of the different magnification in %CR87-330 it is difficult to compare the grain structure in terms of shape and size with the two other samples.

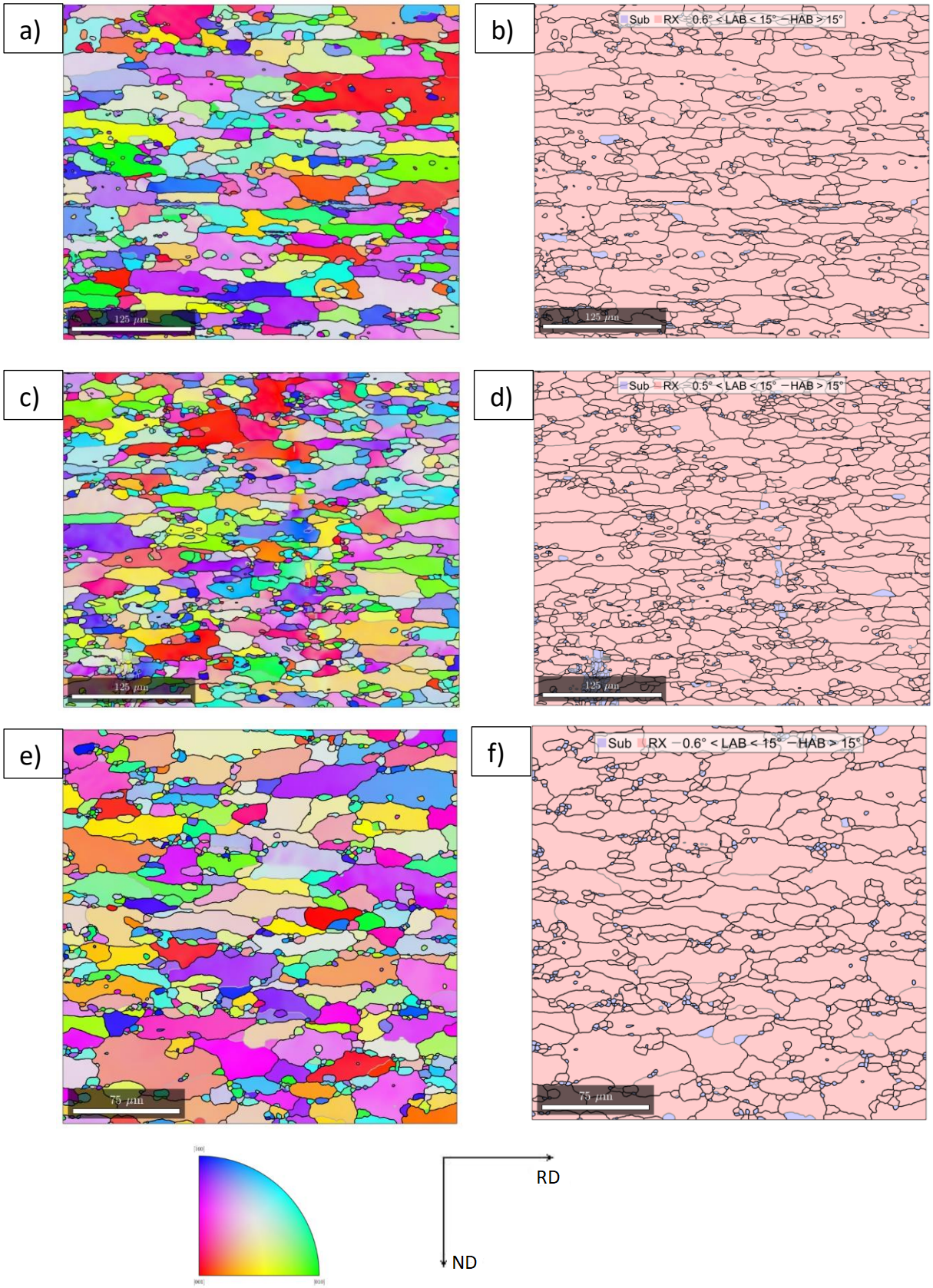

Figure 4.10: EBSD images showing the microstructure of the %CR46-330 (200x) sample (a) – (b), %CR67-280 (200x) sample (c) – (d) and %CR87-280 (300x) sample (e) – (f), showing the OIM-map (a), (c) and (e), and the amount of HABGs and LAGBs (b), (d) and (f). The figure on the bottom left is the IPF indicating the orientation for each grain.

Table 4.6 displays the fraction recrystallized, the subgrain size, recrystallized grain size and the properties used to determine the fraction recrystallized: Fraction of HAGBs, GOS and the mean grain size for the samples annealed to 280°C. The average and recrystallized grain size are evidently largest in %CR46-330, and slightly larger in %CR87-330 than %CR67-330. Furthermore, the subgrains are still finer in %CR87-330 and similar in %CR46-330 and %CR67-330, probably due to the higher deformation in %CR87-330. The fraction of HAGBs increases with deformation and the resulting fraction recrystallized is ≈ 97% for the three samples annealed at 330°C, confirming that the samples are fully recrystallized.

Table 4.6: Different properties calculated with MTEX from the EBSD patterns collected from SEM

Sample	Average grain size [μm]			Fraction HAGBs [%]	GOS [°]	Fraction recrystallized [%]
	All grains	Subgrains	Recrystallized grains			
%CR46-330	26.7	3.77	27.2	87.8	0.18	97.3
%CR67-330	18.3	3.76	18.8	89.5	0.32	96.9
%CR87-330	19.1	3.36	19.7	93.8	0.13	96.7

4.4.6 Grain Size Measurement – Linear Intercept Method

The grain sizes measured in the RD- and ND-direction with the linear intercept method (described in Section 3.4.2) are presented in Table 4.7. The measured samples, %CR46-330, %CR67-330 and %CR87-330, are confirmed in the previous subchapters to be fully recrystallized. If the results from Table 4.7 are compared with the measured grain size from MTEX in Table 4.7, it can be observed that the measured grain sizes are in good accordance with each other, where the grain size is largest in %CR46-330 and smallest in %CR67-330 for both measurements. When studying the ratio between the grain size in the two directions, the ratio is highest in %CR46-330 and lowest in %CR67-330. These observations indicate that the grains in %CR67-330 are finer and more equiaxed, while the grains in %CR46-330 are coarser and more elongated along RD.

Table 4.7: Grain size of the recrystallized samples %CR46-330, %CR67-330 and %CR87-330 measured in RD and ND with the linear intercept method. 5 measurements were carried out on three different images in each direction.

Sample	Recrystallized grain size [μm]		RD/ND
	RD direction	ND direction	
%CR46-330	26.4	10.9	2.42
%CR67-330	15.9	8.8	1.80
%CR87-330	17.1	8.2	2.09

4.5 Recrystallization Texture

The preferred orientation of crystallites, or texture, has an influence on physical properties such as strength, ductility and electrical conductivity, as well as the recrystallization behaviour of the material. The texture measurements described in Section 3.5 for the three samples heated at 100°C/h to 330°C and held at that temperature for 3 hours, %CR46-330, %CR67-330 and %CR87-330, are presented in the following. The pole figures from the texture measurements for these samples are presented in Appendix C.2. Figure 4.11 displays the ODFs of %CR46-330, %CR67-330 and %CR87-330, and the same maximum intensity (ODF_{max}) has been utilized for the three images to illustrate the difference in intensity between the three samples. It can be observed that the recrystallization texture is similar for the three deformation degrees. In general, it is seen that all the recrystallization textures are relatively strong, whereas %CR67-330 has the strongest texture, and %CR87-330 has the weakest texture. The dominating recrystallization textures are found by studying the $\varphi_2 = 0°$ section of the ODFs, as explained in Section 2.5.2. The textures are mainly dominated by the Cube- and ND-rotated Cube ($\Phi = 0$) components. A relatively strong P- and Goss-texture can also be observed, and the deformation textures Copper and Brass are to some extent retained in the recrystallization texture. By studying the $\varphi_2 = 65°$ section of the ODFs, it can be observed that the S-component is strongest in %CR87-330. The texture index, ODF_{max} and the deformation texture components are displayed in Table 4.8 for %CR46-330, %CR67-330 and %CR87-330. The strength of the Brass- and Copper-textures are more or less identical, and the strength of the S-component increases gradually with cold reduction. Moreover, the values in the table confirm that the texture is strongest in %CR67-330 and weakest in %CR87-330.

Table 4.8: Texture index, ODF_{max} and the volume fractions of the deformation texture components for %CR46-330, %CR67-330 and %CR87-330

Sample	Texture Index	ODF_{max}	Brass-texture [%]	Copper-Texture [%]	S-texture [%]
%CR46-330	3.85	18.73	3.30	3.18	4.11
%CR67-330	4.60	20.17	2.81	2.98	5.34
%CR87-330	3.41	13.53	3.00	3.12	7.33

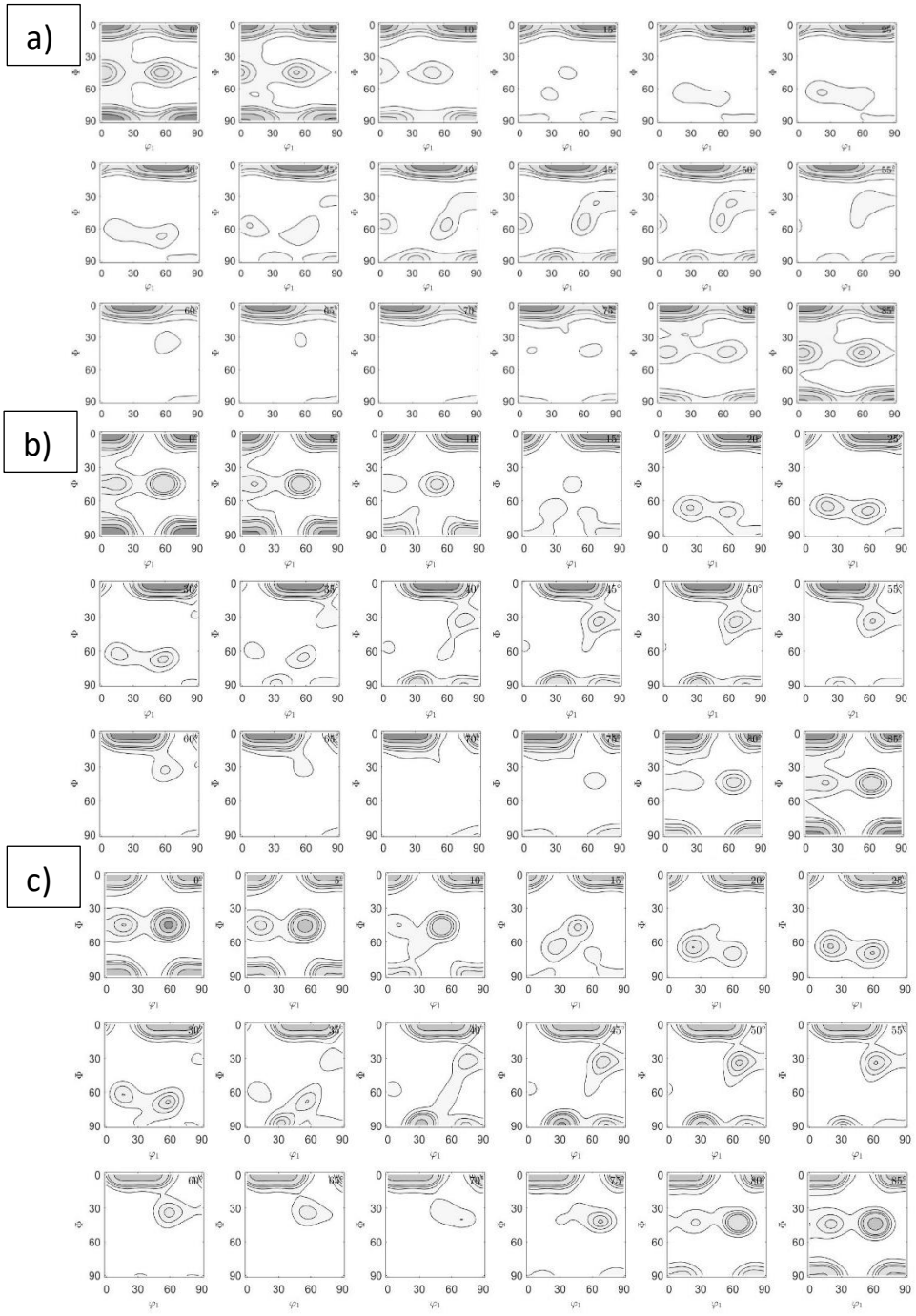

Figure 4. 11: Recrystallization textures (ODFs) of (a) %CR46-330, (b) %CR67-330 and (c) %CR87-330.

Figure 4.12 illustrates how the different recrystallization texture components change with increasing cold reduction. For %CR46-330, the recrystallization texture is dominated by Cube and ND-rotated Cube 22°, with relatively small amounts of ND-rotated Cube 45°, Goss and P present in the sample. As the cold reduction increases to %CR = 67, the volume fraction of the Cube-, P-texture and ND-rotated Cube 22° components increase slightly. The ND-rotated Cube 45° decreases from 6.40% to 1.96% and Goss decreases from 8.56% to 4.81%. At the final cold reduction (%CR = 87), the Cube-component decreases significantly from 32.64% to 19.76%, and the ND-Rotated Cube 22° decreases from 19.76% to 13.80%. The P-component increases to 10.13%, and with a factor of approximately 2 from %CR = 46 to %CR = 87. The Goss- and ND-rotated Cube 45° components decrease slightly. At %CR = 46 and 67, Cube- and ND-rotated cube 22° dominate the recrystallization texture, while at the highest cold reduction, %CR = 87, the recrystallization texture is dominated by the P-texture as well.

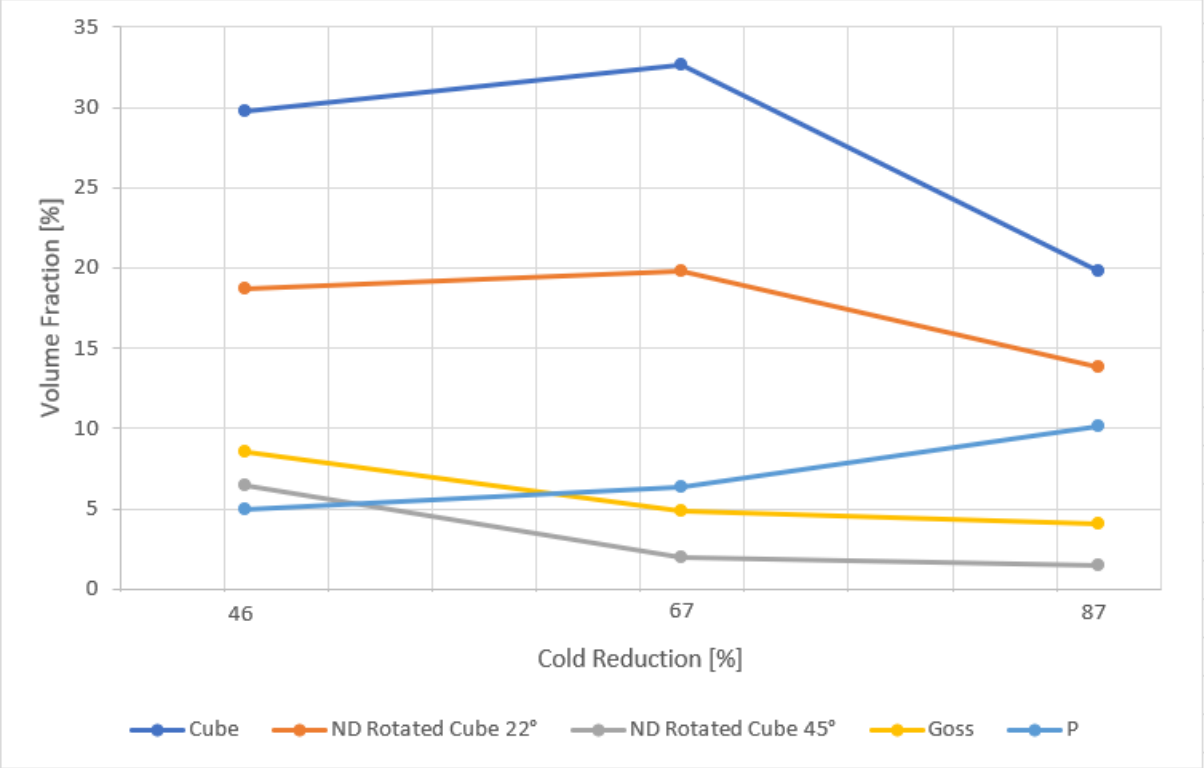

Figure 4.12: Volume fraction of the recrystallization texture components for %CR46-330, %CR67-330 and %CR87-330.

4.6 Analysis of Dispersoids in SEM

In the following subsection, the results from the particle analysis will be presented. BSE imaging was used to study the number of dispersoids present in the samples displayed in Table 3.3. In this thesis, dispersoids are defined as small particles below approximately 1 µm. The rest of the images taken at 5000x magnification as well as the images taken at 1000x magnification are displayed in Appendix D.1. As observed from Figures D.1 (c) – D.13 (c) in Appendix D.1, primary particles larger than 1 µm are present in the samples. However, these particles have not been investigated in the present study. The SEM images shown in Figures 4.13 and 4.14 display the distribution of dispersoids in the as hot rolled and as cold rolled conditions, respectively. Furthermore, the SEM images shown in Figures 4.15, 4.16 and 4.17 display the distribution of dispersoids in the samples after annealing to 180℃, 280℃ and 330℃, respectively.

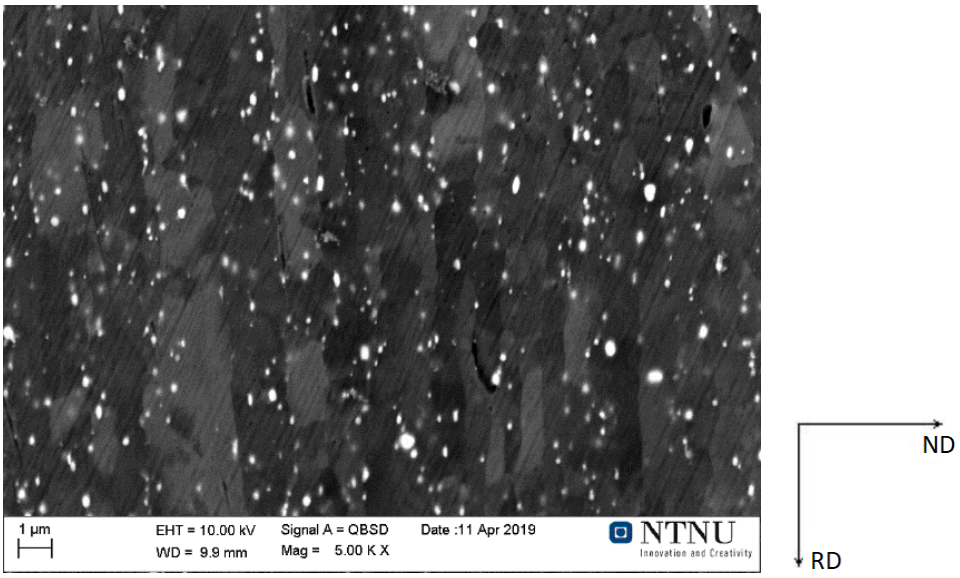

Figure 4.13: SEM-BSE image of dispersoids present in HR.

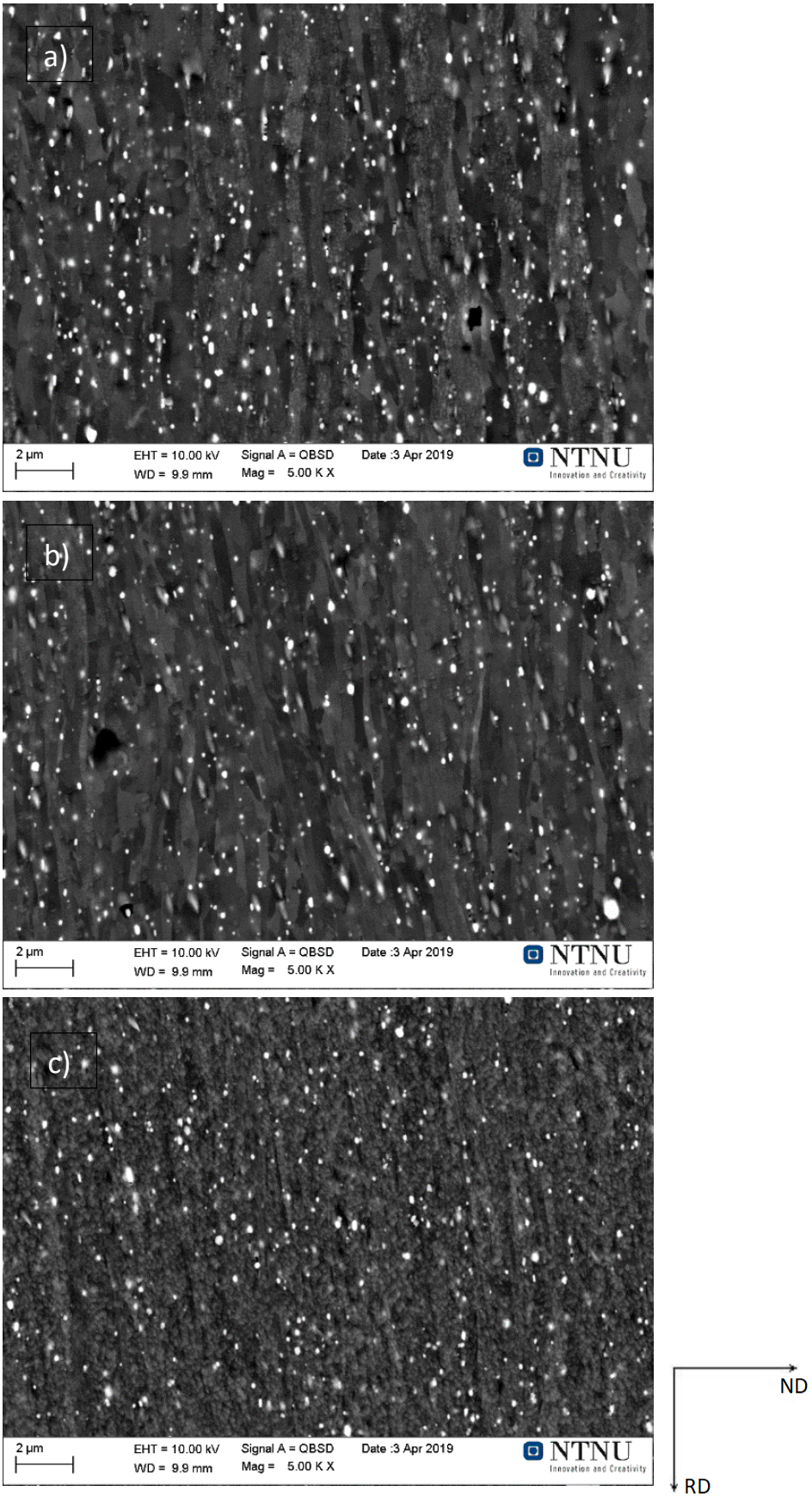

Figure 4.14: SEM-BSE images of dispersoids present in (a) %CR46, (b) %CR67 and (c) %CR87.

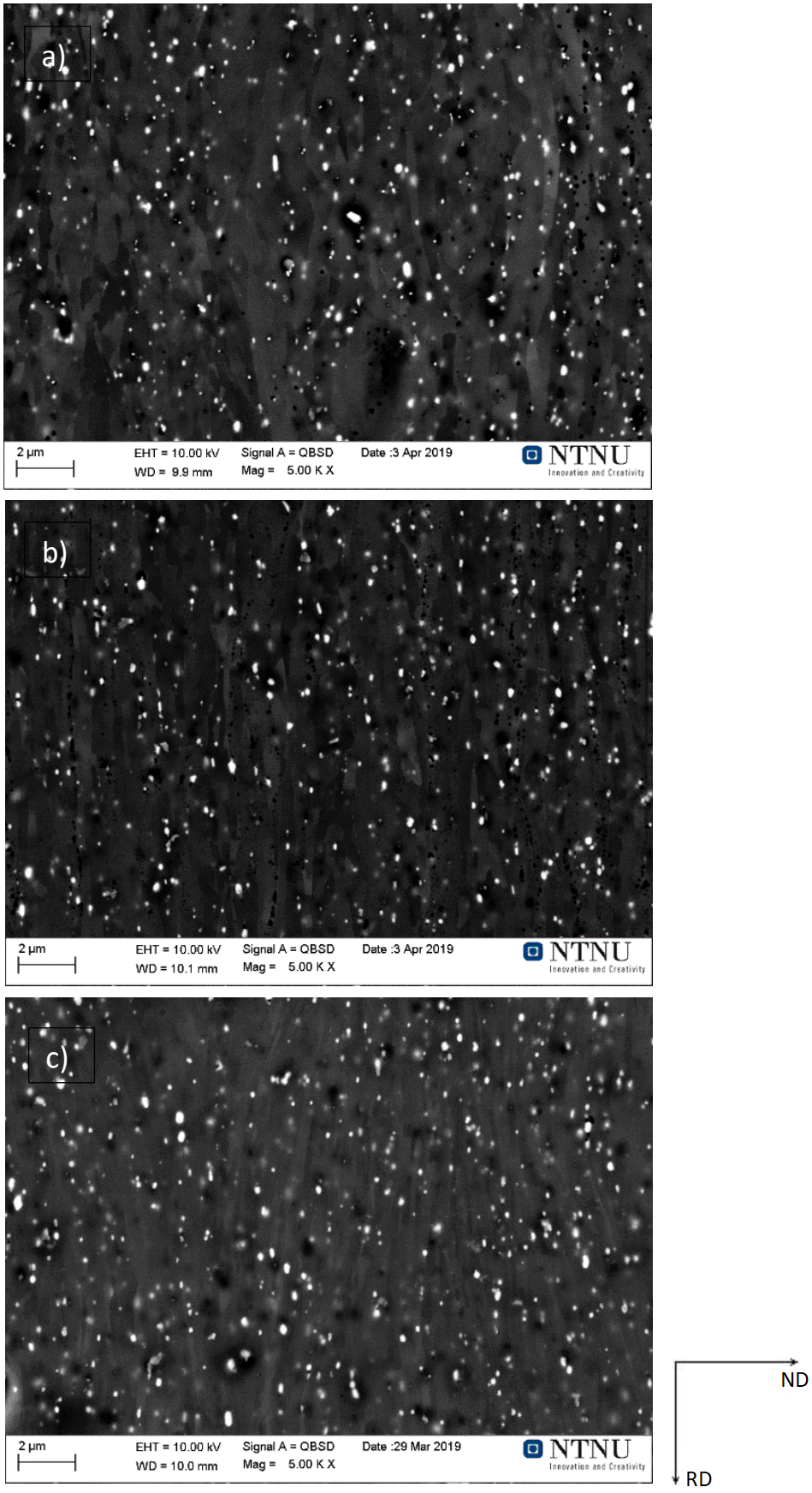

Figure 4.15: SEM-BSE images of dispersoids present in (a) %CR46-180, (b) %CR67-180 and (c) %CR87-180.

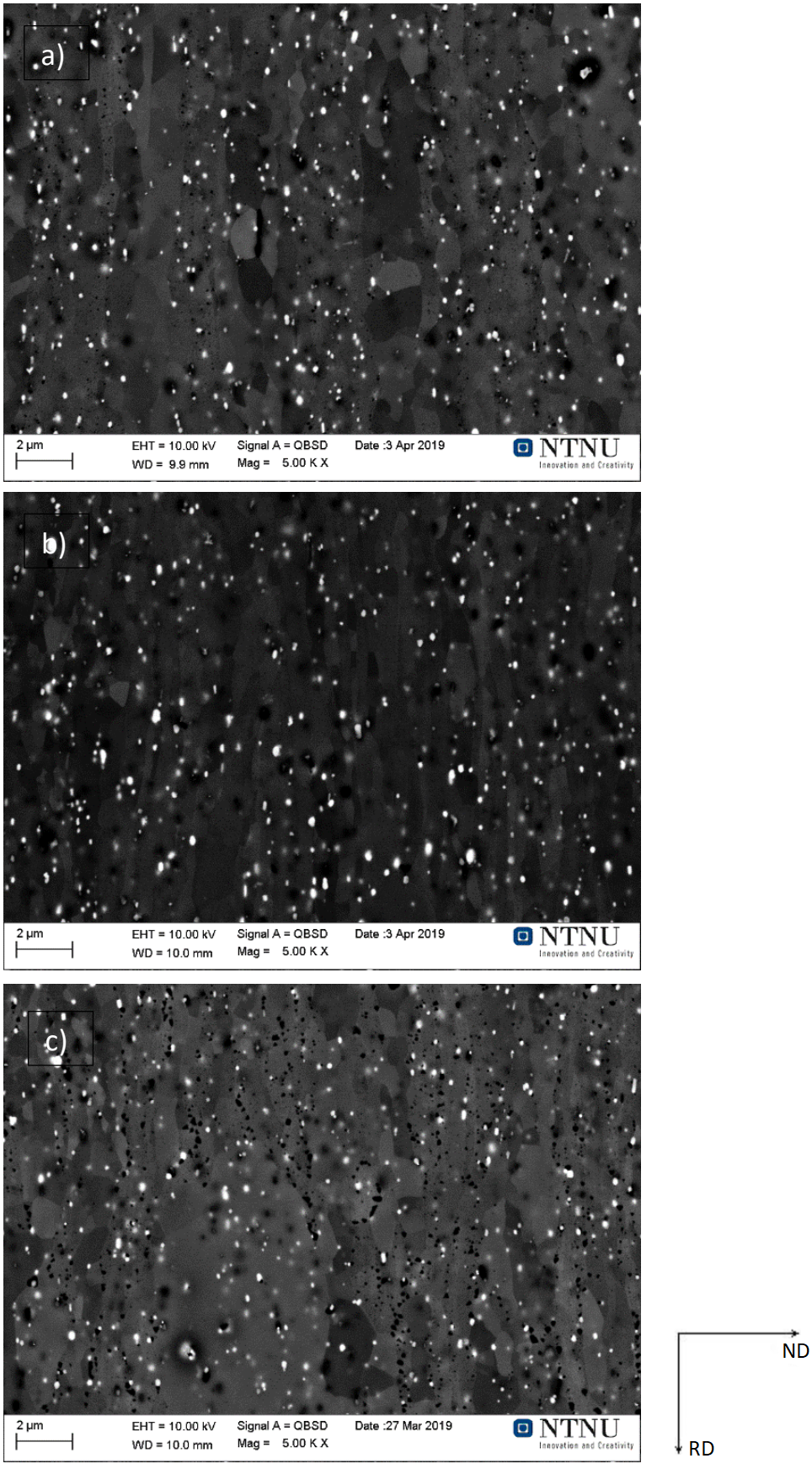

Figure 4.16: SEM- BSE images of dispersoids present in (a) %CR46-280, (b) %CR67-280 and (c) %CR87-280.

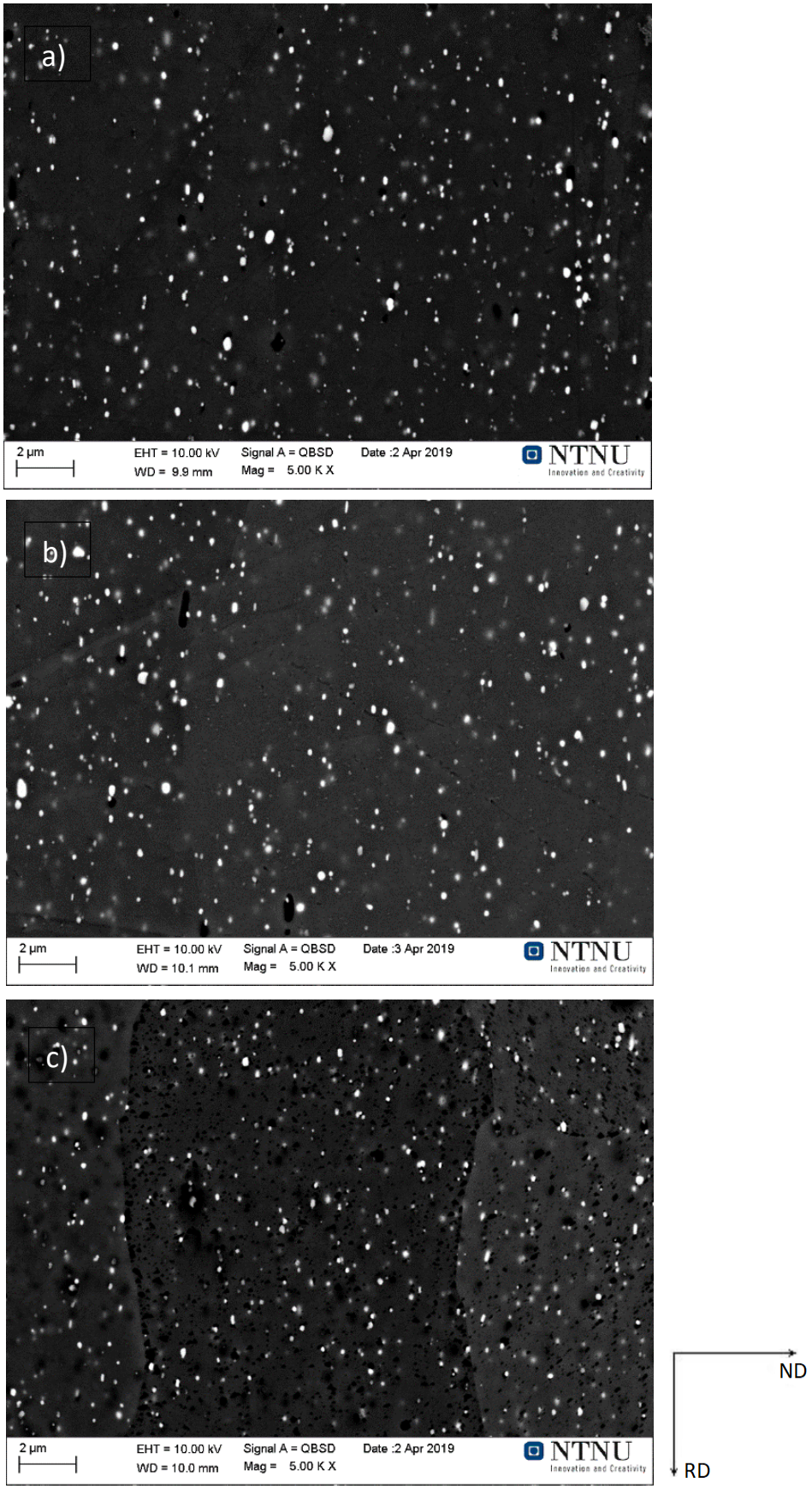

Figure 4.17: SEM- BSE images of dispersoids present in the recrystallized samples (a) %CR46-330, (b) %CR67-330 and (c) %CR87-330.

It is seen from Figures 4.13 and 4.14 that there are only minor differences in the particle density between the as hot rolled samples and the as cold rolled samples. The figures show that the number of dispersoids is somewhat lower in HR compared to %CR46, %CR67 and %CR87 and that dispersoids are larger in HR. It is not possible to visually observe a significant difference in particle density between the as cold rolled samples and the samples annealed to 180°C, 280°C and 330°C, respectively. Appendix D.3 displays the particle distribution of the three images taken from each sample investigated in SEM, while Figure 4.18 shows one example of the particle distribution from each of the as cold rolled samples, %CR46, %CR67 and %CR87. From the particle distributions, no dispersoids larger than approximately 550 nm, 550 nm, 680 nm and 410 nm could be detected for HR, %CR46, %CR67 and %CR87, respectively. HR, %CR46, %CR67 and %CR87 contain a large percentage of small dispersoids with a maximum in the size distribution in the range 100 – 175 nm, 100 – 150 nm, 125 – 150 nm and 75 -125 nm, respectively. HR has a lower peak value than the cold rolled samples, whereas %CR87 has the highest peak value.

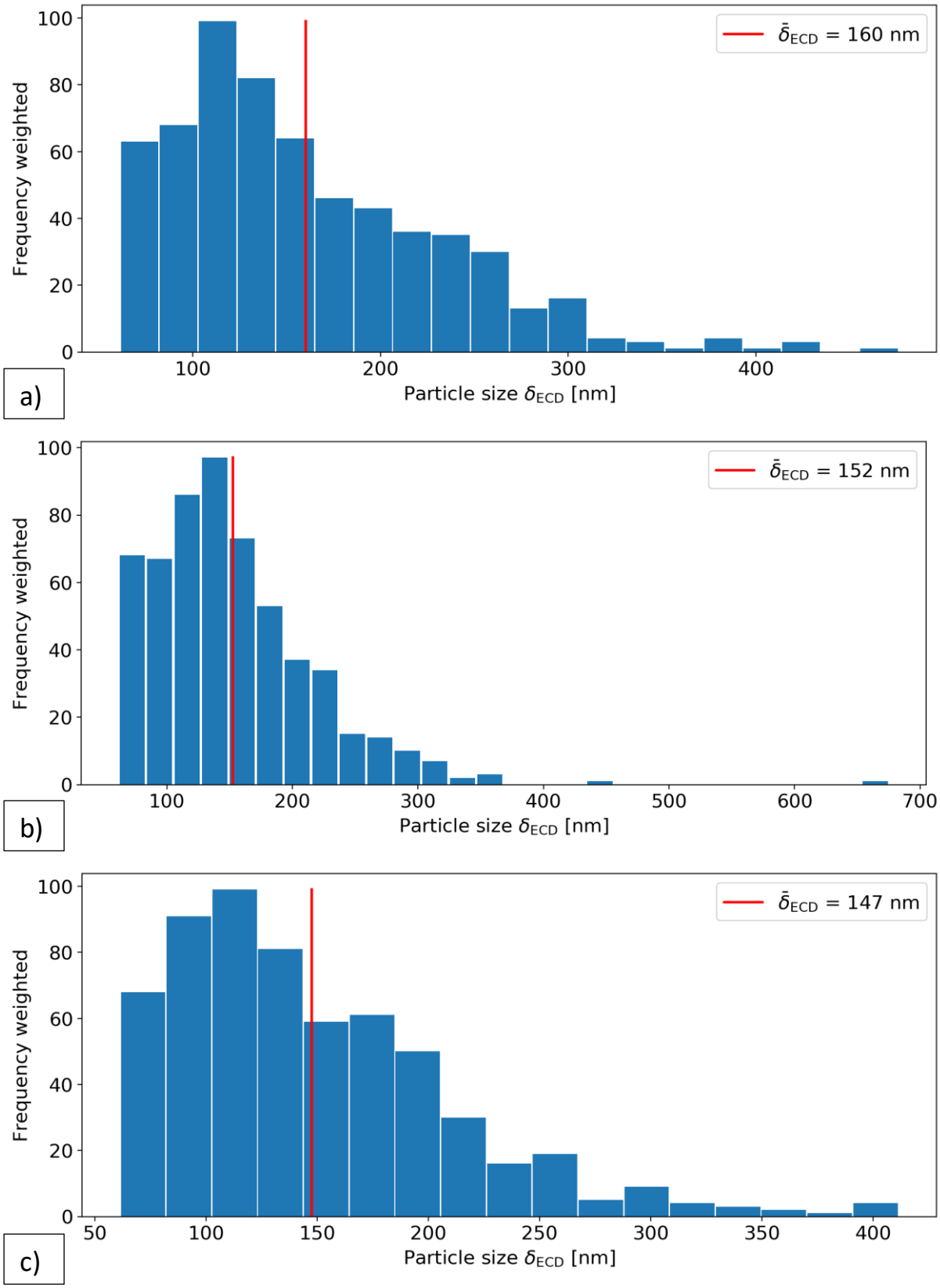

Figure 4.18: Particle distributions of (a) %CR46, (b) %CR67 and (c) %CR87.

No dispersoids larger than approximately 475 nm, 425 nm and 525 nm could be detected for %CR46-180, %CR67-180 and %CR87-180, respectively. %CR46-180, %CR67-180 and %CR87-180 contain a large percentage of small dispersoids with a maximum in the size distribution at 100 nm, in the range 75 – 175 nm and 100 – 150 nm, respectively. %CR46-180 and %CR87-180 have a broader distribution than %CR67-180. The peak value is highest in %CR46-180 and lowest in %CR67-180.

Furthermore, no dispersoids larger than approximately 500 nm, 500 nm and 800 nm could be detected for %CR46-280, %CR67-280 and %CR87-280, respectively. %CR46-280, %CR67-280 and %CR87-280 contain a large percentage of small dispersoids with a maximum in the size distribution in the range 100 – 150 nm, 125 – 150 nm and 125 – 175 nm, respectively. No difference in broadness in the distribution can be observed, but the diameters of %CR46-280 and %CR87-280 are shifted against higher values compared to %CR67-280. The peak values are highest in %CR46-280 and %CR87-280.

From the microstructures in Figure 4.17, a recrystallized microstructure can clearly be seen. Considering the particle distribution of the recrystallized samples, no dispersoids larger than approximately 450 nm, 650 nm and 360 nm could be detected for %CR46-330, %CR67-330 and %CR87-330, respectively. %CR46-330, %CR67-330 and %CR87-330 contain a large percentage of small dispersoids with a maximum in the size distribution in the range 75 – 150 nm, 100 – 175 nm and 100 – 150 nm, respectively. No significant difference in broadness can be observed between the three samples. The distributions of %CR67-330 and %CR87-330 are very similar, and %CR46-330 has a sharper distribution than %CR67-330 and %CR87-330, with a higher peak value. Even though there are some differences in the particle distributions, they seem to be rather similar for all the samples studied in SEM.

Black pits/holes can be detected in the electropolished samples (Figures 4.15 (a) – (c), 4.16 (a) – (b) and 4.17 (c) and Figures D.5 – D.10 and D.13 in Appendix D.1), in the same order of magnitude as the dispersoids. By comparing the figures, it can be observed that a high number of small holes are observed in %CR67-180, mainly located on the grain boundaries. Less and coarser holes can be seen in %CR46-180, and they seem to be more randomly distributed in the matrix. However, some holes are still observed at the grain boundaries. Considering %CR87-180, very few holes in the same order of magnitude as the largest dispersoids are observed, randomly distributed in the matrix. When the annealing temperature is increased to 280°C, more and finer holes are present in the microstructure of %CR46-280. They do not tend

to be located at grain boundaries, but several recrystallized grains are completely free of both holes and dispersoids. In %CR67-280 the number of holes is significantly decreased, and they are much coarser than the holes observed in %CR67-180. A significant number of holes is observed in %CR87-280, and they seem to be in the same order of magnitude as the holes observed in %CR46-280. A clear tendency of holes located on grain boundaries is seen. When this sample is further annealed to 330°C the holes are uniformly distributed in the matrix, and most of them are in the same order of magnitude as the smallest dispersoids observed in the sample. A significantly higher number of holes than dispersoids can be seen.

The evolution of mean particle diameter, particle density and particle area with temperature is illustrated in Figures 4.19, 4.20 and 4.21, respectively. These measurements were carried out to study the difference in concurrent precipitation at different temperatures and deformation degrees.

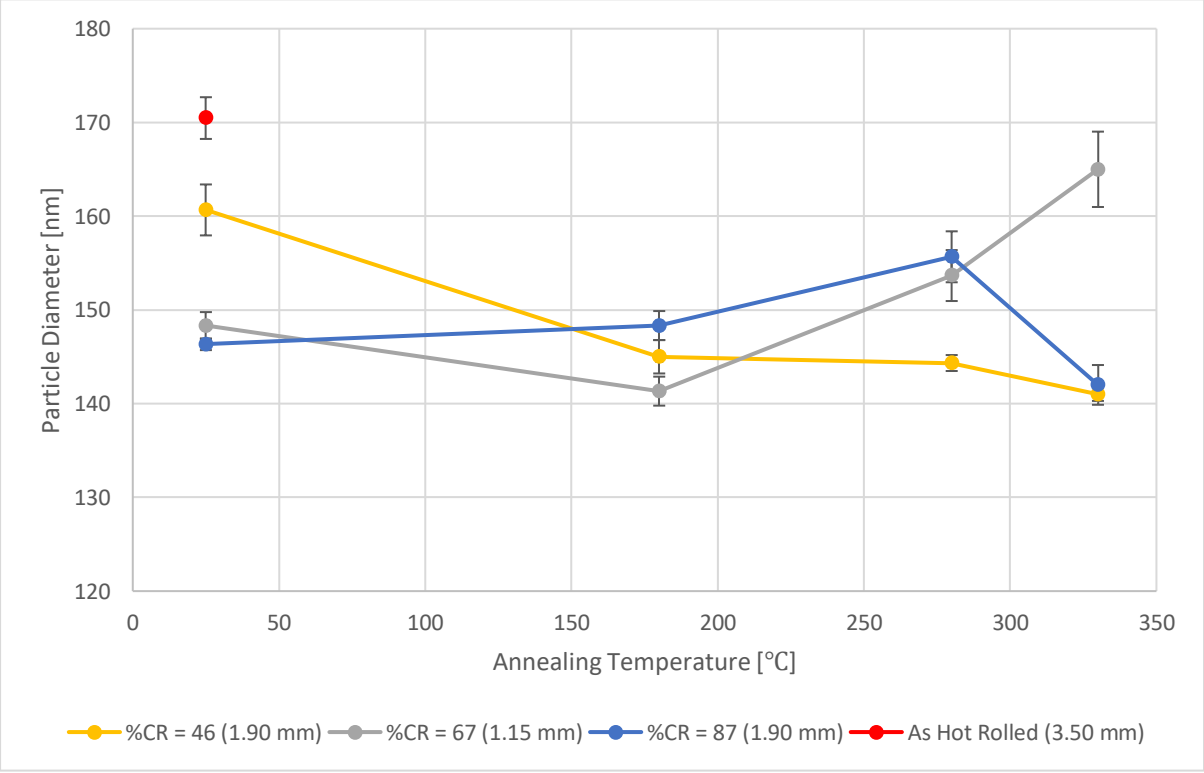

Figure 4.19: Mean particle diameter of dispersoids in the samples investigated in SEM. The annealing temperatures of 25°C correspond to the as cold rolled samples.

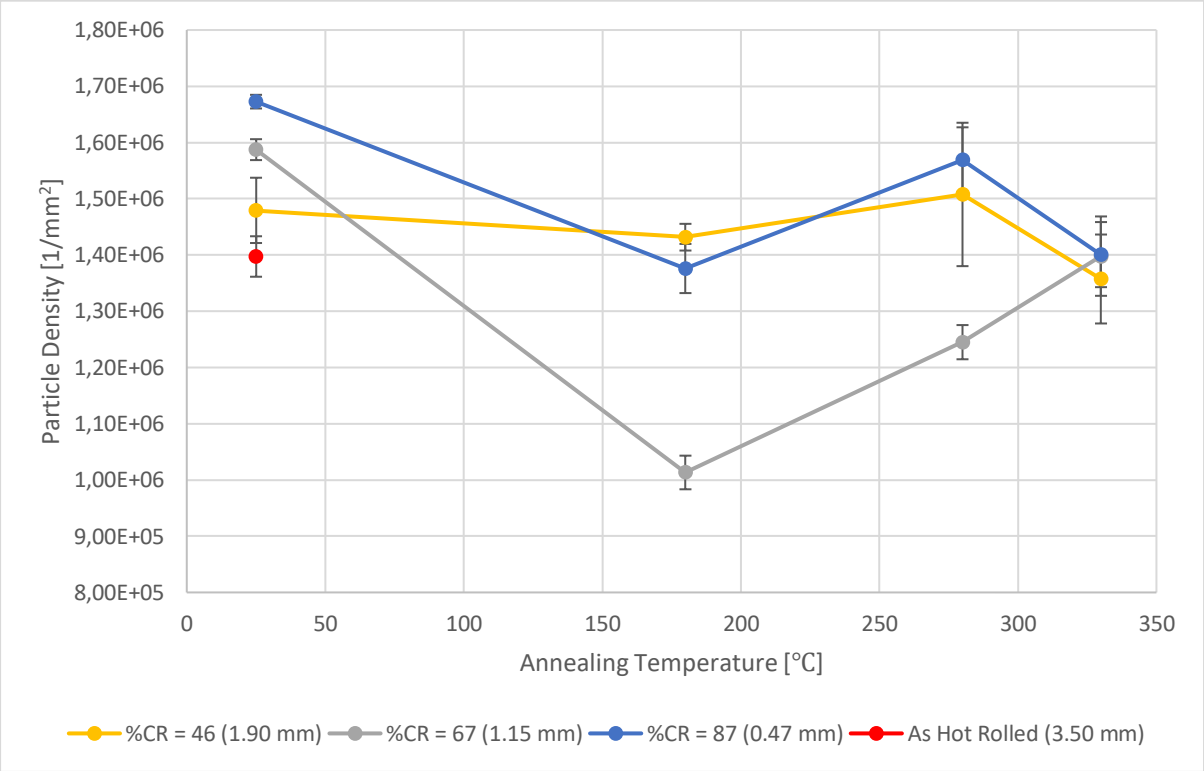

Figure 4.20: Particle density of dispersoids in the samples investigated in SEM. The annealing temperatures of 25°C correspond to the as cold rolled samples.

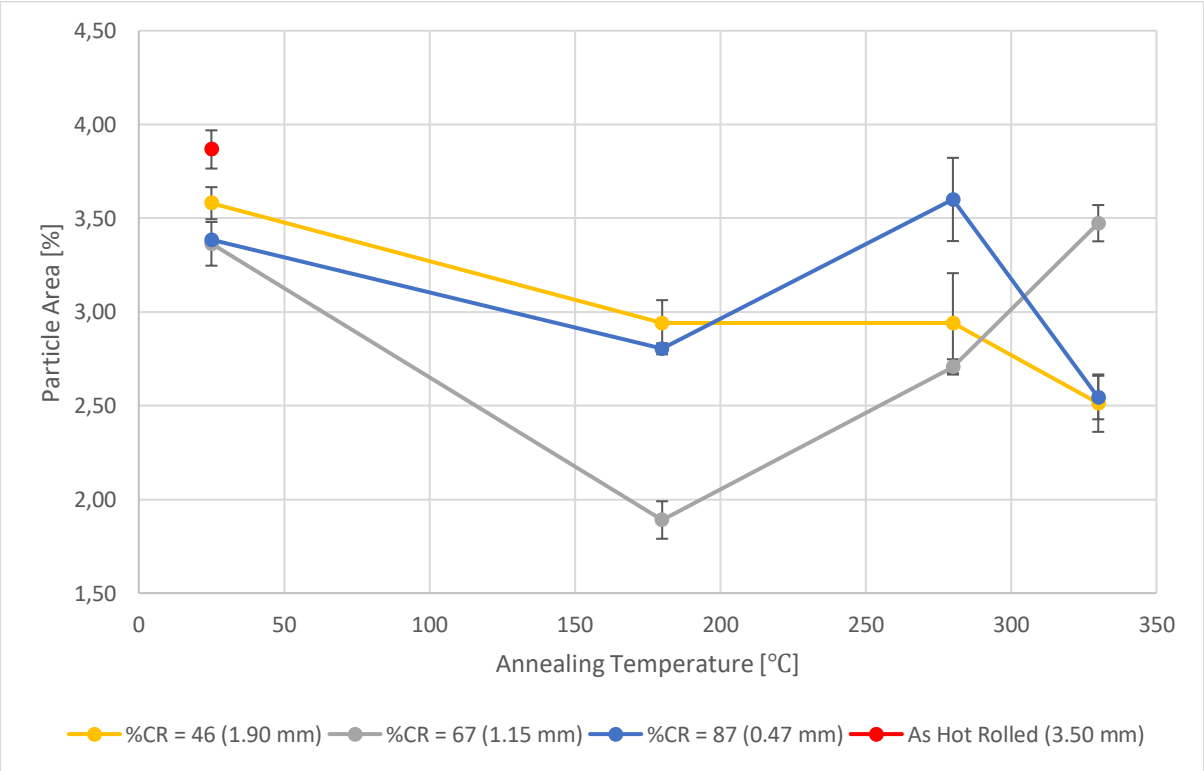

Figure 4.21: Area fraction of dispersoids in the samples investigated in SEM. The annealing temperatures of 25°C correspond to the as cold rolled samples.

For the as hot rolled sample, less and coarser dispersoids are observed compared to the as cold rolled samples. The mean diameter and area fraction are higher in the as hot rolled sample than for the recrystallized cold rolled samples (%CR46-330, %CR67-330 and %CR87-330), while the particle density is slightly lower.

Less and coarser dispersoids are observed for %CR46 compared to %CR67 and %CR87, as seen from the values of mean particle diameter and particle density in Figures 4.19 and 4.20. More and smaller particles are observed as the deformation increases. However, only very small differences are detected for %CR67 and %CR87. %CR67 shows the lowest electrical conductivity and the highest amount of Mn in solid solution (Table 4.2), and thus a higher potential for concurrent precipitation of Mn-containing dispersoids during subsequent annealing. Furthermore, the electrical conductivity increases most significantly in %CR = 87 when the samples are annealed up to 330°C. A larger increase in electrical conductivity promotes concurrent precipitation. However, as can be seen from Figures 4.20 and 4.21, the particle density and area fraction decrease during annealing.

More and coarser dispersoids are observed in %CR46-180 and %CR87-180 compared to %CR67-180, leading to a significantly higher particle area, as seen from Figures 4.19, 4.20 and 4.21. The dispersoid density is lowest in %CR67-180, and the mean particle diameter is nearly the same for all samples at this temperature. The level of Mn in solid solution is somewhat higher in %CR87-180 compared to %CR46-180 and %CR67-180, giving a higher potential for concurrent precipitation during further annealing.

When the samples are heated from 180°C to 280°C the mean particle diameter increases for %CR = 67 and 87, and decreases for %CR = 46. The particle density increases for all samples, but most significantly for %CR = 67 and 87. As a result, the particle density of %CR = 46 remains more or less constant, while the particle area for %CR = 67 and 87 increases. The range of error is more considerable at 280°C compared to 180°C, indicating a more heterogenous particle distribution in %CR46-280, %CR67-280 and %CR87-280. When the samples are annealed to 330°C, the particles in %CR = 46 and 87 decrease in diameter and fewer particles are present in the samples compared to %CR46-280 and %CR87-280, respectively. The mean particle diameter decreases more significantly in %CR = 87 compared to %CR = 46. On the other hand, the particle size and density increase in %CR = 67. This is not consistent with the electrical conductivity measurements carried out for the samples annealed at 280°C and 330°C. In that case, the electrical conductivity increases from 27.00 to

27.04 MS/m and 26.64 to 26.79 MS/m for %CR = 46 and %CR = 87, respectively, and decreases from 26.75 to 26.66 MS/m for %CR = 67. After recrystallization, after annealing at 330°C, the particles are largest in the samples cold rolled to %CR = 67, and almost the same size in %CR = 46 and 87. The particle density is virtually the same for all samples after recrystallization.

5. DISCUSSION

The present study aims to investigate the influence of processing conditions and associated changes in microchemistry, i.e. amount elements in solid solution and the precipitation state (dispersoids) on the softening behaviour of the alloy, after different degrees of deformation and annealing temperatures, with a particular focus on concurrent precipitation. The evolution of electrical conductivity, the density and size of dispersoids, the recrystallized grain size and the final recrystallization texture will give an indication of the potential of concurrent precipitation, which in turn influence the softening reactions.

First, the evolution of the microstructure from the starting variants to the recrystallized samples will be discussed and attributed to the annealing curves. The effect of deformation on the electrical conductivity will be briefly discussed in the second part. Furthermore, the recrystallized microstructure and texture will be attributed to observed differences in the recrystallization behaviour. The focus in the fifth part will be on the results considering the particle analysis and the effects of concurrent precipitation during annealing. In the sixth part of this section, the effect of deformation on precipitation will be briefly discussed. Suggestions for further work will be investigated in the last section.

5.1 Microstructure Evolution

The subgrain size in HR, %CR46, %CR67 and %CR87 was found to be 3.17, 1.81, 1.41 and 1.04 μm, respectively, and thus found to decrease gradually with increasing degree of deformation. However, as mentioned in Section 4.4.2, the cold rolled subgrain size is most likely overestimated as a result of particles being identified as large subgrains. In addition, only one image was studied for each degree of deformation, and more images should have been analysed to provide proper statistics. The grain size will also be influenced by the chosen misorientation threshold used in MTEX, where a higher threshold will result in larger grain size. Several sources of error are present in the calculation of grain size, and the exact size can therefore not be trusted. The measured subgrain sizes for %CR46 and %CR67 are comparable to the samples annealed at 280°C which further indicates that the sizes have been overestimated. Nevertheless, the trend of decreasing subgrain size with increasing degree of deformation is in accordance with literature and is most likely valid. Sjølstad [17] compared the subgrain size versus degree of deformation for a cold rolled AA3103 alloy with earlier measurements, which is shown in Figure 5.1. It is seen that the alloy investigated in the present study follow a similar trend to what has been observed earlier, but the subgrain sizes are

significantly smaller in the earlier measurements than what has been measured from the present EBSD patterns.

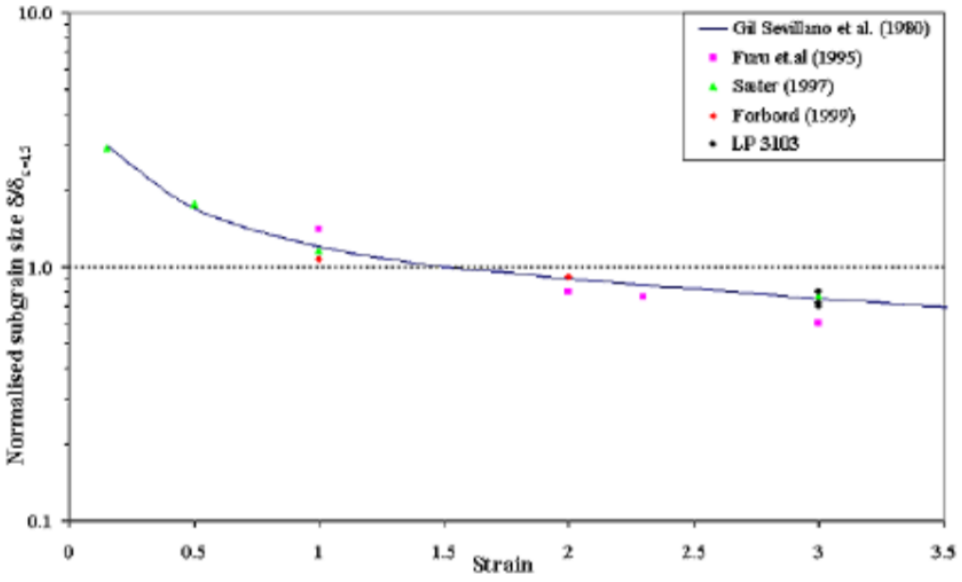

Figure 5.1: Normalised subgrain size versus strain for five earlier measurements [17].

The stored energy in the deformation structure (P_D) which is the driving force for recrystallization (cf. Eq. 2.5 Section 2.2.1), is characterized by subgrains of size δ and the cell interior dislocation density ρ_i. However, the latter can often be ignored as the dislocation density within the subgrains is relatively low. Thus, the stored energy can be estimated from the measured subgrain sizes, and the measured subgrain sizes suggest that the driving pressure for recrystallization is largest in the most deformed sample (%CR87) and lowest in the least deformed sample (%CR46). The fraction of HAGBs was also investigated, and it was measured to be 35.1%, 59.6% and 70.1% in %CR46, %CR67 and %CR87, respectively. Nucleation can occur at pre-existing HAGBs through SIBM and ordinary grain boundary nucleation. According to Elmasry et al. [111], the probability for an existing grain in the pre-deformed matrix to act as an effective nucleation site for recrystallization is proportional to the fraction of HAGBs, which indicates a higher potential for nucleation in the most deformed sample. From theory, it is well known that small particles below approximately 1 µm, or dispersoids, may greatly influence the recrystallization kinetics and affect the evolution of microstructure and texture during annealing of deformed aluminium. Materials with a large fraction of dispersoids, either pre-existing in the microstructure after deformation or concurrently precipitated upon annealing, will experience a back-driving force and slow the recrystallization kinetics. The Zener drag (P_Z) provides the back-driving force on the moving HAGBs upon

progressing recrystallization, where smaller and larger volume fractions of dispersoids (cf. Eq. 2.9 Section 2.3.2) will increase the retarding force from the Zener drag. Thus, the softening behaviour of the different cold reductions is determined by the effective driving pressure for recrystallization, $P_{eff} = P_D - P_Z$.

During annealing upon 180°C, the subgrain sizes were also found to decrease with increasing degree of deformation. Surprisingly, the size was found to decrease from the as cold rolled condition. According to theory, this cannot be the actual case, and sources of error introduced in the method can probably explain these unexpected results. From Figures 4.7 and 4.8 it is seen that the microstructures are relatively similar, which indicates that not much has happened during annealing at 180°C. As mentioned, MTEX detects constituent particles as relatively large grains. The reason for the smaller subgrain size measured can be partly attributed to variations in constituent particles present in the region of interest of the different images. More particles present will lead to an increased overestimation of grain size. Besides, only one image was analysed for the samples, apart from %CR46-180. The subgrain size in the samples annealed at 180°C should, according to theory, be slightly larger or more or less unchanged compared to the as cold rolled samples. Considering the fraction of HAGBs, the trend observed in the as cold rolled samples were also observed in %CR46-180, %CR67-180 and %CR87-180. However, the fraction was very similar for the two most deformed samples, 65.0% and 67.0%, respectively. The slight reduction in strength and hardness (see Figures 4.1, 4.2 and 4.4) can be attributed to the reduction of dislocation density during annealing.

When the annealing temperature is increased from 180°C to 280°C, the microstructure evolves from a non-recrystallized structure to a partly recrystallized structure, as shown in Figures 4.8 and 4.9. The annealing curves and hardness curve indicate that recovery has occurred between these annealing temperatures. According to literature, the subgrains coarsen during the final stage of recovery. During this period of heating, the subgrain size has increased from 1.51 to 1.87 µm, 1.19 to 1.58 µm and 0.90 to 1.48 µm in %CR = 46, %CR = 67 and %CR = 87, respectively. It is seen that growth is most significant in the most deformed sample with the smallest subgrain size, indicating a higher driving pressure for subgrain growth (cf. Eq. 2.8 Section 2.3.1). In Equation 2.8 the driving pressure is increased with decreasing subgrain radius, which is in accordance with the measurements obtained. It must be emphasised that the measurements from 180°C cannot be fully trusted.

As mentioned above, it is assumed that the driving force for recrystallization is most significant for the most deformed sample, and gradually decreasing with decreasing deformation. However, when comparing the softening behaviour of the different cold reductions it can be observed that the recrystallization kinetics are in fact not faster for the most deformed samples. The annealing curves in Figures 4.1, 4.2 and 4.3 suggest that recrystallization occurs at the lowest temperature for the samples cold rolled to %CR = 67 and at the highest temperature for the sample cold rolled to %CR = 46. The annealing and hardness curves indicate that recrystallization was completed at higher temperatures for %CR = 46 and 87 compared to %CR = 67. The results from EBSD displayed in Table 4.5 for the samples annealed at 280°C show that the fraction recrystallized is slightly larger for %CR67-280 than %CR87-280, and significantly lower for %CR46-280, thus being in accordance with the results from the annealing curves. In other words, the softening behaviour upon annealing after cold rolling is significantly influenced by the degree of deformation. The different behaviours observed are probably related to the retarding force from the Zener drag, which will be further discussed in Sections 5.3, 5.4 and 5.5.

The results from the hardness measurements are plotted against the results from the tensile tests in Figure 5.2. Hardness measurement is a fast and efficient way to monitor the softening behaviour after annealing compared to tensile testing, but tensile testing is known to give more reliable results. It is therefore interesting to investigate to what extent the measurements correlate. Hardness and yield strength show strong correlation at lower temperatures when the samples are deformed and partly recovered. At higher temperatures, especially close to the recrystallization temperature, the correlation is moderate. This suggests that hardness can give a good indication of the softening behaviour, but it must be used carefully in determining exact recrystallization kinetics.

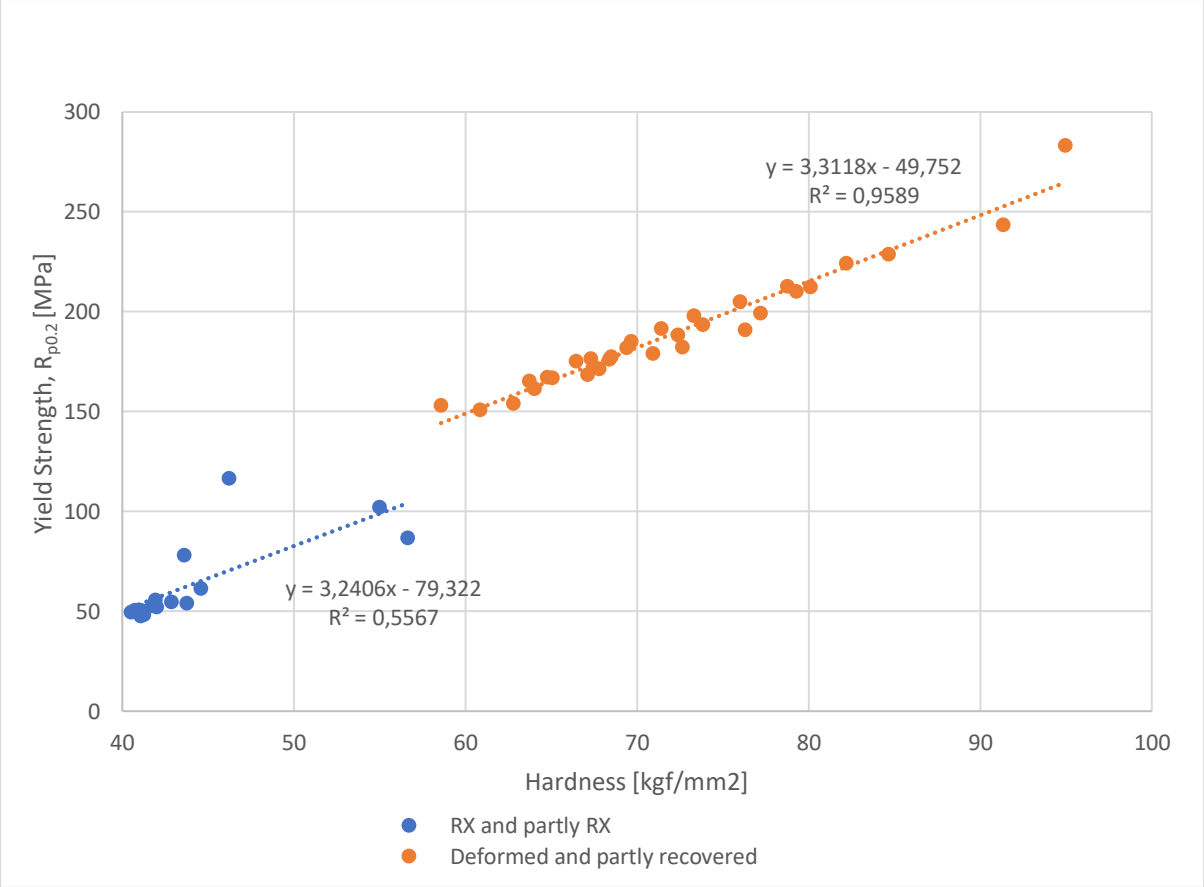

Figure 5.2: Hardness plotted against yield strength for the recrystallized (RX) and partly recrystallized samples, and the deformed and partly recovered samples, respectively. A trendline has been added to the chart to obtain the dotted linear lines.

Figure 5.3 shows the fraction of recrystallization calculated from the hardness values (cf. Eq. 3.1 in Section 3.2). This method provides far from correct values of the amount recrystallized, but it gives a rather good indication of the difference in recrystallization behaviour between the different cold reductions. As indicated by Figure 5.3, from 180°C the fraction recrystallized increases most significantly for %CR = 87, suggesting that recovery starts at the lowest temperature for this deformation. A rapid increase in fraction recrystallized can be observed at 275°C for %CR = 67 and at 283°C for %CR = 46. It is harder to tell exactly where a significant increase in fraction recrystallized occurs for %CR = 87. However, the curve indicates that the recrystallization temperature is lowest for %CR = 67, which is in accordance with the annealing curves and the EBSD measurements. As mentioned, the different behaviours observed are probably related to the retarding force from the Zener drag and will be further discussed in Sections 5.3, 5.4 and 5.5. The slope of the curves at the given temperatures is least steep for the most deformed samples, which suggests slower recrystallization kinetics for this cold

reduction. At 280°C the fraction recrystallized is virtually the same for %CR = 67 and %CR = 87.

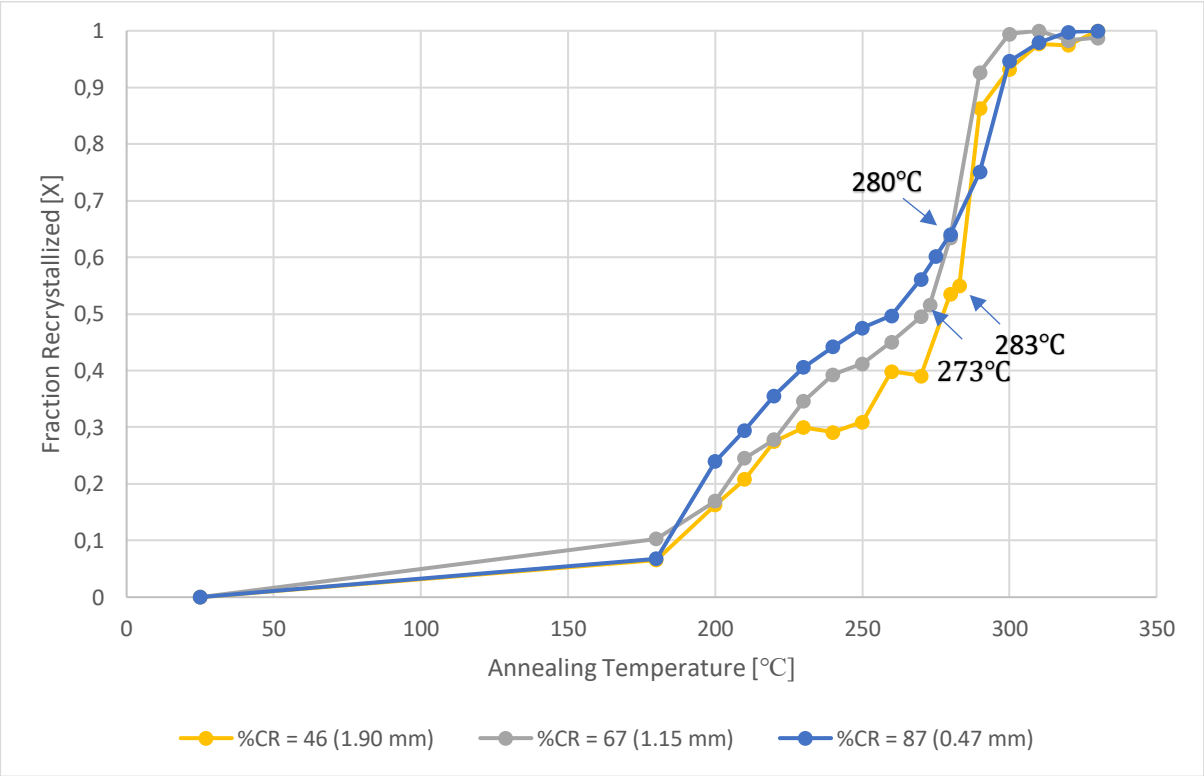

Figure 5.3: Fraction recrystallized as a function of annealing temperature.

5.2 Effect of Deformation on Electrical Conductivity

As mentioned in Section 3.3 it is expected that the electrical conductivity will decrease with increasing deformation. It is seen from Figure 4.5 in Section 4.3 that the electrical conductivity is highest for the as hot rolled sample, and second highest for the sample cold rolled to a thickness of 1.90 mm (%CR46), in accordance with theory. However, inconsistent values are observed for the two most deformed samples, where the electrical conductivity is higher for the most deformed sample (%CR87) compared to %CR67. This indicates that the measurements of electrical conductivity are uncertain. In addition, the measured differences between the different cold reductions during annealing are very small, at the same order of magnitude as the difference between %CR67 and %CR87 (≈ 0.4 MS/m), which makes it difficult to identify clear effects of precipitation.

The conductivity measuring instrument used in the present work is sensitive to temperature, as explained in Section 3.3. The temperature in the room possibly changed during testing, which can explain the unexpected variation for the two most deformed samples. All material was collected from the same coil and the preheating treatment was therefore similar for the as hot rolled sample and the as cold rolled samples. As the same alloy (AA3005) was investigated a difference in alloying elements can therefore not explain the difference in measured conductivity. A recalibration should have been performed between each measurement in order to fully avoid the temperature dependency. Again, it must be noted that the measured differences were very small, where the difference between the highest and smallest value was 0.93 MS/m.

5.3 Recrystallized Grain Size

Mainly two factors will influence the final recrystallized grain size. Higher deformations cause higher stored energy in the material and thus a larger driving force for recrystallization, which promotes nucleation of recrystallization and a smaller, more equiaxed grain size. Also, the presence of dispersoids, either as pre-existing particles or concurrently precipitated on the grain structure, favour the formation of coarse elongated recrystallized grains. The grain boundaries are pinned by precipitates, and the recrystallization thus is slowed down. From Table 4.6 in Section 4.4.5 it can be observed that the recrystallized grain sizes for the samples cold rolled to CR% = 46, 67 and 87, and subsequently annealed to a temperature of 330°C are 27.2, 18.8 and 19.7 µm, respectively. From theory, it is known that with increasing deformation the stored energy in the material will increase, and thus a higher effective driving force, P_{eff}, is achieved. Consequently, a smaller critical radius δ_C (cf. Eq. 2.10 Section 2.3.3) is needed for nucleation, which leads to more nucleation of recrystallization. N_{tot} will increase with a smaller critical radius and more nucleation of recrystallization, and the recrystallized grain size will thus be smaller (cf. Eq. 2.14 Section 2.3.3). It is therefore expected that the recrystallized grain size is smallest in the sample cold rolled to %CR = 87, and gradually increase with smaller deformations. However, the recrystallized grain size is slightly larger in the most deformed sample compared to the sample cold rolled to %CR = 67, indicating a higher driving pressure for recrystallization in the latter. This further indicates that the Zener drag from dispersoids must play a more significant role in %CR = 87 than in %CR = 67. The Zener drag, which retards both nucleation and growth, is increased as the particle radius, R, is decreased and the volume fraction of particles, f, is increased (cf. Eq. 2.9 Section 2.3.2). This suggests that smaller and/or more dispersoids are pre-existing in the sample and/or concurrently precipitated during

annealing. The grains in %CR = 67 will grow more freely with lesser influence from precipitates until they impinge with other growing grains. This theory can be supported by Nes and Slevolden [112] who studied two commercial pure Al alloys and a 3xxx Al alloy and found that the recrystallized grain size became coarse when concurrent precipitation slowed down the recrystallization. A similar tendency was also observed by Wang et al. [113] in an Al-Mn-Fe-Si alloy, by Vatne et al. [114] in an AA3103 alloy and by Engler et al. [115] in high purity Al1.3Mn.

Less important is the contribution from PSN, but this factor will also play a role in the determination of the recrystallized grain structure. Fewer large particles will reduce the PSN activity, i.e. less nucleation of recrystallization, resulting in both slower kinetics and larger grain size. Unfortunately, the size distributions of constituent particles have not been measured. The coarser grain size in %CR87-330 than %CR67-330 is consistent with the larger increase in electrical conductivity for the former between 200°C and 330°C (see Figure 4.5 in Section 4.3), suggesting more concurrent precipitation to take place. As explained in Section 3.3, alloying elements in the solid solution, such as Mn, will through a distortion of the atomic lattice reduce the conductivity. The development of electrical conductivity during annealing is a good indication of the precipitation behaviour of the alloy at different temperatures and deformation degrees because decomposition of a supersaturated solid solution occurs by nucleation and growth of a precipitate during heating of a sample (see Section 2.4). It must be noted that the main reason for the increase in electrical conductivity during recovery is the reduction of dislocation density. The difference in increase at higher temperatures, however, can be mainly attributed to concurrent precipitation. Therefore, the trendlines have been added at temperatures above 180°C.

The grain size measurements carried out with the linear intercept method presented in Table 4.7 in Section 4.4.6 provide an indication of the shape of the grains in the recrystallized samples. It was found that the recrystallized grains in %CR67-330 are finer and more equiaxed, while the grains in %CR87-330 and especially %CR46-330 are coarser and more elongated along RD. The qualitative analyses of the microstructures displayed in Figures 4.10 (a) – (d) indicated that the grains in %CR46-330 are more elongated than in %CR67-330. Tangen et. Al [44] observed that if precipitation took place prior to or by concurrent precipitation, this resulted in delayed recrystallization and a coarse and elongated grain structure. The more elongated grains achieved in %CR46-330 and %CR87-330 indicate that the effects of prior and/or concurrent precipitation are stronger in these materials, while the more equiaxed grains

in %CR67-330 indicate weaker effects of prior and/or concurrent precipitation. It must be emphasized that the differences in both grain size and shape are not big, but small differences are also observed for other properties such as electrical conductivity and the amount of recrystallization at given temperatures.

5.4 Recrystallization Texture

The recrystallization textures are presented in Section 4.4.5 with OIM-maps and in Section 4.5 with ODFs and fraction of different texture components. As the particle analysis carried out in the present work cannot be fully trusted (discussed in Section 5.5.1), the recrystallization texture can give a good indication of the precipitation behaviour in the recrystallized samples, as the pre-existing dispersoids and concurrent precipitation affect the recrystallization textures. The recrystallized sample cold rolled to %CR = 46 was dominated by the Cube- and ND-rotated Cube components, with a weak P-component. As the cold reduction increased to %CR = 67, the Cube-component, as well as the P-component, increased slightly, with a slight reduction of the ND-rotated Cube component. At the highest cold reduction, %CR = 87, the P-component increased significantly, followed by a significant decrease in the Cube- and ND-rotated Cube components. The texture was strongest in %CR67-330 and weakest in %CR87-330. In studies conducted by Wang et al. [113, 116] on Al-Mn-Fe-Si alloys, they found that the presence and strength of the P-texture were linked to a strong Zener effect by dispersoids, both pre-existing and particularly those coming from concurrent precipitation. These results were found to be consistent with earlier results by Tangen et al. [44] (see Section 2.5.2), although the effects of the P-component were much stronger in conditions of concurrent precipitation. Burger et al. [117] studied the addition of Mg in Al-Mn alloys and the role of Mn-dispersoids in the development of texture during recrystallization after hot and subsequent hot rolling. Different alloy compositions were investigated to achieve different dispersoid distributions, and it was found that P-texture (termed RX-texture in the paper) became stronger as the dispersoid density increased. From these papers, it is strongly indicated that the higher fraction of the P-component obtained in the recrystallized sample cold rolled to a reduction of %CR = 87 (%CR87-330) leads to more and smaller dispersoids, and that concurrent precipitation is more evident in this sample. A critical dispersoid volume fraction and size is required for the development of the P-component. In the same paper worked out by Burgers et al. a strong ND-rotated Cube texture was observed, which became less rotated, i.e. oriented closer to the exact cube orientation, as the dispersoid density decreased, and the ND-rotated Cube texture was stronger than the P-texture for all conditions. Figures 4.11 (a) and (b) in Section 4.5 show a

similar tendency, with very strong Cube- and ND-rotated Cube 22° components present in %CR46-330 and %CR67-330. The ND-rotated Cube 45° texture is significantly stronger in %CR46-330 compared to %CR67-330, indicating a lower dislocation density in the latter.

There could, however, be other explanations for the different recrystallization textures obtained in samples %CR46-330, %CR67-330 and %CR87-330. Liu and Morris [118] intensively studied the recrystallization textures of a continuous cast AA3015 alloy deformed to %CR = 70, 80 and 90, respectively, and subsequently annealed at different temperatures. In the recrystallized materials, the P-texture was found to increase in strength with increasing deformation. Similar conclusions were drawn in a study by Vatne et al. [114], who investigated the influence of both constituents and dispersoids on the recrystallization texture in AA3103. The Cube-texture was found to be the dominating texture component at low deformations, which is in accordance with the present study. Figure 4.12 shows that the Cube-component is the dominating component at low deformations, i.e. at %CR = 46 and 67. The P-texture only appeared after large reductions, and in the present work, the P-texture is highest at the largest cold reduction. The conclusions drawn in these two studies suggest that an increase in P-texture is partly due to increased deformation.

The final recrystallization texture was found to influence the grain structure in the study conducted by Engler et al. [115] of high purity Al1.3Mn. As previously mentioned, nucleation of recrystallization takes place in the deformation zones around large particles (>1 µm) through PSN. In the study, it was found that with increasing particle size and volume, the PSN-grains grow at the expense of Cube-grains, resulting in a weaker recrystallization texture with less exact Cube-orientation but more P- and ND-rotated Cube texture, as well as a finer grain structure. The Cube-texture is weakest, and the P-texture is most prominent in %CR = 87, but the cause for these textures are well discussed in the above. The recrystallized grain structure, however, is finest in %CR = 67, indicating more PSN-grains in this sample and thus suggesting accelerated recrystallization.

According to Sjølstad [17], Engler and Yang (1995) investigated the effect of precipitation of an Al1.3Mn alloy and found a higher dispersoid density in Copper-, S- and Goss oriented grains compared to Brass oriented grains. From Table 4.8 in Section 4.5, the fraction of Copper and Brass is more or less the same for all the cold rolled recrystallized conditions. However, the fraction of the S-component is clearly highest in the sample with cold reduction of %CR = 87, while the fraction of the Goss oriented grains was clearly highest in the sample with a cold

reduction of %CR = 46, further indicating that less concurrent precipitation is taking place in the sample with a cold reduction of %CR = 67.

Benum and Nes [46] have previously found concurrent precipitation to strengthen the Cube-texture. The studied Al-Fe-Si alloy had hot rolling texture prior to cold rolling, which is also expected in the current study, as the samples were hot rolled and partially recrystallized, as can be seen in Section 4.4.1. Some of the cube grains from hot rolling will survive deformation and will be responsible for the final Cube-texture after recrystallization. From the study, it was found that during concurrent precipitation, a higher fraction of grains will be Cube oriented compared to a sample without precipitation. From the discussion above, it has been indicated that most concurrent precipitation occurs in the samples cold rolled to a reduction of %CR = 87. However, it can be seen from Figure 4.12 that the amount of Cube grains decreases significantly from %CR = 67 to %CR = 87. This does not necessarily mean that less concurrent precipitation occurs in the latter, as a previous study by Liu et al. [119] has investigated the texture evolution during cold rolling. They found that with an initial texture of Cube oriented grains, the volume fraction of the Cube-texture decreased gradually with an increase in reduction. Therefore, concurrent precipitation and the amount of cold reduction will be competing factors on the influence of the Cube-texture, and it is difficult to say which factor will influence the Cube-texture the most.

5.5 Particle Analysis

The results from the particle analysis in Section 4.6 will be discussed in the following. First, the validity of the particle analysis will be considered, followed by a discussion around particle-breakup during cold rolling. Finally, the particle analysis will be attributed to pre-existing dispersoids and mainly concurrent precipitation.

5.5.1 Validity of the Particle Analysis

The particle analysis shows a significant decrease in particle area and density from the as cold rolled conditions to the first annealing temperature (180°C), as well as an overall decrease from the as cold rolled conditions to the final annealing temperature. There is no explanation for why the density of dispersoids is lower in an annealed sample compared to an as deformed sample. In fact, from theory, it is expected that the density will increase rather than decrease, especially at temperatures close to the recrystallization temperature. Three BSE images were taken per sample, and more than a few images should have been taken for each sample to achieve proper statistics. However, this alone cannot explain the irregular variations from the

particle analysis. If the limit for the smallest particle size is changed (55 nm in the present work) the same trends will still be observed. This is however not shown in the present study. The minimum and maximum threshold values for the markers have been chosen carefully, and the particle analysis in Python is quite reliable. The main problem with the analysis seems to be the differences in sample preparations, which makes it difficult to directly compare results. Holes from removed particles in the surface of samples prepared by electropolishing leads to an underestimation of density and possibly wrong estimation of size. Besides, it is impossible to say how many particles have been removed for each image taken in the different electropolished samples. Figure 5.4 shows the sample %CR46-280 prepared by electropolishing. The colours are inverted, so that white highlights holes where particles are removed. Chatterjee [120] discussed the aspects of the electropolishing technology and found one of the drawbacks of the sample preparation technique to be: "Multi-phase materials are difficult to electropolish because of the differential rate at which various phases are removed", which further indicates that dispersoids have been removed from the sample surface as a result of electropolishing. The white holes in the image are mostly observed along grain boundaries, which is typical for concurrently precipitated dispersoids.

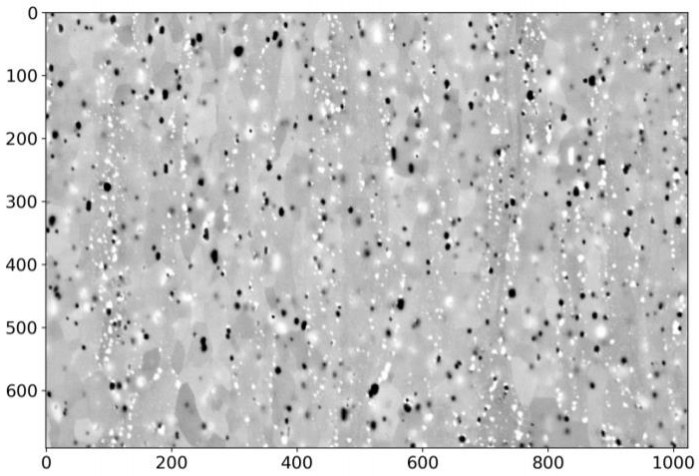

Figure 5.4: BSE image of %CR46-280 prepared by electropolishing. Colours are inverted.

5.5.2 Concurrent Precipitation

As the driving force for recrystallization is assumed to be higher in the most deformed sample, the influence of the retarding Zener force from dispersoids can be a possible explanation for why recrystallization kinetics are slower in %CR = 87 compared to %CR = 67. For %CR = 87 the largest increase in electrical conductivity was observed between 200℃ and 330℃, which

implies a higher potential for concurrent precipitation. It must be emphasised that the differences in the increase were low between the degrees of deformation (≈ 0.4 MS/m). However, the differences in recrystallization behaviour have also been found to be rather small, and it is therefore rational to treat the difference as a relatively significant difference. The higher increase in electrical conductivity, and thus higher potential for concurrent precipitation indicates that recrystallization kinetics are most inhibited in %CR = 87. During recrystallization at 280°C, the highest subgrain size was observed in %CR = 67. A higher critical subgrain size is required to nucleate recrystallized grains during concurrent precipitation. The lower subgrain size observed in %CR = 87 will most likely result in fewer grains to nucleate, and thus slower recrystallization kinetics.

When comparing the particle distribution of the as hot rolled sample with the as cold rolled samples some differences are observed. It is well known from theory [17, 121, 122] that coarse constituent particles break up with increasing deformation during cold rolling. The same trend was found for the dispersoids in this study. As mentioned in Section 4.6, less and coarser dispersoids are seen in the as hot rolled sample compared to the as cold rolled samples, and generally finer and more dispersoids are observed in the as cold rolled samples as the cold reduction increases. The measurements of the initial conditions are more reliable than the annealed samples, as the former do not contain holes from electropolishing. This change can be attributed to particle break-up of dispersoids taking place during deformation, which changes the size distribution of the particles by increasing the particle density and thus decreasing the particle size. The same trend was found in the study by Wang et al. [122] when the as-homogenized condition was compared with the as-deformed samples in different 3xxx Al alloys with different amounts of Mn in solid solution. However, the effect of break-up was best seen for the largest constituent particles, i.e. particles larger than 3-4 µm, and these particles have not been studied in the present work. The particles show no significant difference in the size and density for %CR67 and %CR87. However, a more profound change can be observed between %CR46 and %CR67. The particle distribution in %CR87 is different from %CR46 and %CR67, with a higher percentage at the peak, where the peak is positioned at lower particle sizes. A similar trend was found by Sjølstad [17], where a lack of break-up was observed for the most deformed samples, indicating the particles to be more sensitive to break-up during the first cold rolling passes. Still, it is difficult to explain why dispersoids break up, as this is common for large constituent particles and not small dispersoids. The tendency of more and smaller dispersoids with increasing deformation can be attributed to the method. The

electron beam can penetrate the material well beyond the surface region of a sample, and the information contained in the backscattered electrons comes from the whole interaction volume of diffraction. Consequently, the particles that are cut by the plane of polish above their equatorial plane appear to have a larger diameter than the real cross-section diameter, which must be taken into account [7].

Quantitative investigations of the dispersoids showed that the volume fraction of dispersoids decreases upon annealing to 180°C (see Figure 4.20). However, as discussed in the previous section, large uncertainties exist in the measured results. The annealed samples contain holes from removed particles as a result of electropolishing, and the correct density of dispersoids is most likely increasing at elevated temperatures before completed recrystallization, in accordance with literature. During annealing at low temperatures (180°C), the dispersoid structure is expected to be more or less unchanged. This assumption is based on the very low decrease of density observed in %CR = 46 when the as cold rolled sample is compared to the sample annealed to 180°C. If the density of dispersoids was decreasing, a more significant decrease would have been observed because of the relatively high number of removed particles (holes) present in the annealed sample (see Figure 4.15 (a)). Anyhow, the particle analysis can give an indication of the precipitation behaviour of dispersoids, but it must be kept in mind that the interpretations most likely are far from correct.

If it is assumed that the holes affect all the electropolished samples similarly, the fraction of dispersoids was found to increase most significantly in %CR = 46 from the initial cold rolled condition to annealing upon 280°C. Some of the dispersoids are most likely concurrently precipitated, while some act as “pre-existing” dispersoids because they have been precipitated before the onset of recrystallization. Considerable precipitation of dispersoids at low temperatures before the onset of recrystallization was also found by Huang et al. [123] during non-isothermal annealing of cold rolled Al-Mn-Fe-Si alloys. The smallest increase in the fraction of dispersoids was found in %CR = 67. At 280°C, the sample cold rolled to %CR = 46 and 87 contain a higher amount of dispersoids which gives rise to a considerable Zener drag retarding nucleation of recrystallization, thus slowing the softening reaction. This indicates that the Zener drag, P_Z, has such an influence on the effective driving pressure, P_{eff}, for %CR = 87 that the effective driving pressure is higher in %CR = 67. The results from the qualitative analysis of holes in Section 4.6 indicated that a much larger fraction of small dispersoids are present in %CR67-180 than what was found in the quantitative particle analysis, which explains the large decrease in dispersoid density observed in Figure 4.20. However,

significantly fewer and coarsened removed particles were observed in this sample upon annealing to 280°C, indicating that not much concurrent precipitation occurs in this sample, but that dispersoids are "pre-existing" at lower temperatures. For %CR = 87, however, an opposite trend was seen, with many small removed particles located at the grain boundaries upon annealing to 280°C. Dispersoids formed by concurrent precipitation, which are mostly found along grain or subgrain boundaries, retard nucleation of recrystallization more effectively than pre-existing dispersoids by pinning subgrain boundaries. Small removed particles were found at grain boundaries upon annealing to 180°C and 280°C in %CR = 46, possibly giving rise to even stronger pinning effects.

Figure 4.20 shows that the density of dispersoids decreases in the samples cold rolled to %CR = 46 and 87, while it increases in %CR = 67 in the temperature range between 280°C and 330°C. Two possible reactions can occur at elevated temperatures: Concurrent precipitation, which results in more and smaller dispersoids, and coarsening or dissolving of dispersed particles, which results in fewer and coarser dispersoids. It must be noted that dispersoids have not been studied in samples between annealing temperatures of 280°C and 330°C, which makes it difficult to describe the extent of concurrent precipitation in this temperature range. The decrease in dispersoid density observed for the samples cold rolled to %CR = 87 can be partially attributed to holes from electropolishing in the recrystallized sample. A significant amount of small, removed particles was observed in %CR87-330, which indicates that the density of dispersoids is, in fact, increasing when the annealing temperature is increased from 280°C to 330°C. This further suggests that precipitation takes place concurrently with the recrystallization reaction, resulting in slower recrystallization kinetics and a considerably retarded softening reaction. However, it must be noted that it is not possible to say if the density is decreasing or increasing in this temperature range. The observed decrease in the fraction of dispersoids in %CR = 46 and 87, as well as the assumed decrease in %CR = 67 (because of removed particles present at 280°C), can be applied to the change in electrical conductivity. At 290°C for %CR = 46 and 67 and at 300°C for %CR = 87, a drop in electrical conductivity is observed (see Figure 4.5). Li and Arnberg [60] studied the precipitation behaviour of dispersoids in DC-cast AA3003 alloy during heating and homogenization. They found that this drop may be because dispersoids can re-dissolve back into the matrix because of increased solubility of Mn in the matrix at higher temperatures. As a result, the area of dispersoid free zones increased with increasing temperature, which may explain the drop in the dispersoid density observed in the present study. A similar drop of conductivity was found in the study by

Huang et al. [123] for cold rolled Al-Mn-Fe-Si alloys ($\varepsilon = 3$) and by Li and Arnberg [124] in a non-deformed as cast AA3003 alloy. The particle size is most probably not affected by the removal of particles to the same extent as the particle density. It is seen that the particle diameter is decreased in %CR = 46 and 87 in the temperature range 280°C to 330°C (see Figure 4.19). %CR = 67 showed an increase in particle diameter in this temperature range. The variations in particle diameter suggest that concurrent is the main reaction occurring in %CR = 46 and 87, while particle coarsening is the predominant reaction in %CR = 67. To summarize, the most deformed samples seem to be the condition most affected by Zener pinning, while the intermediate condition (%CR = 67) is less affected by the effects from dispersoids and the Zener drag.

Pre-existing dispersoids formed during preheating can also have a profound effect on retarding recrystallization. They are, however, coarser than particles formed concurrently with recrystallization and presumably more randomly distributed, where many of them are located inside subgrains. Thus, they will provide a less effective Zener drag than concurrently precipitated dispersoids. As a result of the particle break up, a higher fraction of smaller pre-existing dispersoids are present in the most deformed sample, which may influence the softening behaviour to some extent.

5.6 Strain-Induced Precipitation

The recrystallized grain size, recrystallization texture and particle analysis show tendencies of higher amounts of concurrent precipitation in %CR = 87 compared to %CR = 67. Nucleation of a precipitate is mainly occurring at heterogeneities, such as clusters of vacancies, dislocations and grain boundaries (see Section 2.3.3). Thus, the heterogeneities will act as nucleation sites for precipitation and speed up diffusion significantly. A larger number of dislocations in the most deformed sample cause the precipitation reactions to go faster as a result of faster diffusion, known as pipe diffusion. The deformation effect over a large strain on precipitation behaviour in a cold rolled AA3003 alloy was studied by Zhao et al. [125]. They generally found electrical resistivity to decrease with increasing strain, and thus electrical conductivity to increase with increasing strain. The same tendency was found in the present work between %CR = 67 and %CR = 87, as previously discussed. Furthermore, they found a larger amount of fine precipitates in the most deformed sample as a result of prestrain induced dislocations. Even though it was expected to observe an accelerated precipitation growth with increased strain, as dislocations and subgrain boundaries are rapid diffusion paths, this was not the case. This implied that the effect of deformation on precipitate growth was minor, and the

main contribution of deformation to precipitation kinetics was attributed to promoted nucleation. Chen et. al [126] also studied a cold rolled AA3003 alloy and showed that cold rolling enhanced the rate of precipitation as an increased dislocation density increased the nucleation site density and reduced the nucleation barrier. Lok [58] studied the effect of recrystallization on precipitation in an undeformed and deformed AA3103 alloy and was able to show that the dispersoids nucleation rate and final number density was higher in the deformed material. The observed precipitation behaviour of the samples %CR = 67 and %CR = 87 are in accordance with what was observed in the above studies, where a higher degree of deformation favours the precipitation of small dispersoids.

5.7 Suggestions for Further Work

- In the present study, experiments were carried out on samples after cold rolling to reductions of 46%, 67% and 87%. It would be useful and interesting to also investigate the softening behaviour and associated precipitation behaviour of the sample cold rolled to a reduction of 80%, as this will give a more complete understanding of the softening behaviour.
- It is recommended to use the DI approach for indexing EBSD patterns for all the samples, as this method is highly precise and surpasses the performance of previously available methods. It would also be interesting to supplement the SEM-EBSD work with some transmission electron microscopy (TEM) investigations which have the potential to give even more details about the grain structure and recrystallization behaviour. In situ electron microscopy could also be of interest.
- In the present work, different sample preparations were carried out on the different samples. It is recommended to use the same sample preparation when obtaining statistics for the particle analysis and to avoid electropolishing due to the existing sources of error presented in Chapter 5.5.1.
- The presence of large constituent particles can greatly influence the recrystallization behaviour through PSN. Only small particles (dispersoids) were investigated in the present study, and it would be interesting and helpful to establish to what extent PSN can influence the softening behaviour of the different cold rolled samples.
- Moreover, it would be interesting to analyse the interaction between precipitation and softening reactions with TTT-diagrams. These diagrams can be used as a foundation for analysing the degree of recrystallization and concurrent precipitation, based on hardness and electrical conductivity measurements.

6. CONCLUSION

In the present work the influence of processing conditions and associated changes in microchemistry (i.e. amount elements in solid solution and precipitation state (dispersoids) on the softening behaviour of an AA3005 alloy have been investigated. The alloy was first hot rolled and subsequently cold rolled to different degrees of deformation. The different degrees of deformation were then annealed to different temperatures between 180°C and 330°C. Quantitative results for the microchemistry evolution in view of electrical conductivity as well as the size and volume fraction of dispersoids and its influence on the softening behaviour, in terms of mechanical properties, hardness, recrystallization texture and microstructure have been established. It is important to note that the differences observed between the different degrees of deformations were fairly small but still significant. The obtained results can be summarised as follows:

- It is shown that the softening behaviour upon annealing after cold rolling is significantly influenced by the degree of deformation. A higher degree of deformation was found to decrease the subgrain size in the as cold rolled conditions, and thus increase the amount of stored energy and the driving pressure for recrystallization. Nonetheless, recrystallization was found to initiate slightly earlier in %CR = 67 than in %CR = 87, not consistent with the increased driving pressure for recrystallization from the substructure alone. Differences in the dispersoid structures and possible concurrent precipitation also need to be taken into account, and the results from the softening behaviour indicate that the Zener drag has a larger influence on the effective driving pressure for recrystallization in the most deformed sample.
- When the cold reduction was increased from 67% to 87%, the difference in electrical conductivity during annealing as well as quantitative measurements and qualitative observations from the particle analysis indicated that some more concurrent precipitation occurred in the most deformed samples, consistent with more rapid and pronounced precipitation in the most deformed sample, promoted by faster diffusion (pipe diffusion) in the condition with the highest dislocation density (after cold rolling). This condition is thus also the one most affected by Zener pinning, and thus, in spite of the highest driving force for recrystallization (following the largest deformation degree), has a relatively slow softening kinetics. The %CR = 46 sample, on the other hand, has the lowest driving force for recrystallization and is also presumably least affected by concurrent precipitation giving comparable slow kinetics to the %CR = 87

sample. For the intermediate deformations (%CR = 67) both effects are less ‘extreme’ and the balance between driving force and Zener drag actually results in a somewhat faster softening kinetics.

- This analysis of the softening behaviour in the differently cold rolled samples are consistent with the differences in recrystallized grain structure and texture between the different cold rolled samples. Considering the recrystallization texture, the intensity of the P-texture was found to increase with the degree of deformation between 46% and 87%, with the most significant difference found between the two largest deformations (%CR = 67 to 87) The amount of P-texture is known to correlate strongly with the amount of concurrent precipitation, which clearly indicates that concurrent precipitation is most pronounced in the most heavily cold rolled sample. This is also consistent with a coarser and more elongated grain structure in the 87% sample than the 67% sample.
- It was hoped that the quantitative dispersoid analysis could confirm the assumptions and interpretations made above. Unfortunately, the dispersoid analysis turned out to be uncertain and inconclusive in this respect. Concerning the changes in dispersoid size and density for the cold rolled samples, it was apparently found that the dispersoids tended to become smaller and with a higher number density after cold rolling. This observation might indicate break-up of the dispersoids; however, this is a very unlikely process for small dispersoids, and it is believed that these effects are due to small differences between the different conditions, poor statistics and possible differences in specimen preparations. The same applies to the somewhat illogical changes in the dispersoid structure parameters during low-temperature annealing and the diverging behaviour at higher annealing temperatures. The quantitative dispersoid results may also be influenced by the fact that dispersoids less than 55 nm was not included in the analyses, which may give erroneous/misleading results about the actual behaviour.

7. REFERENCES

1. Hydro. *Physical Properties*. [cited 2019 02.04]; Available from: https://www.hydro.com/en/about-aluminium/Why-aluminium/Physical-properties/.
2. Aalco. *Introduction to Aluminium and its Alloys*. [cited 2019 02.04]; Available from: http://www.aalco.co.uk/datasheets/Aluminium-Alloy_Introduction-to-Aluminium-and-its-alloys_9.ashx.
3. Davies, J.R., *Aluminum and Aluminum Alloys*, in *Alloying: Understanding the Basics*. 2001, ASM International p. 351-416.
4. Hydro. *Recycling*. [cited 2019 02.04]; Available from: https://www.hydro.com/en/our-future/Environment/Recycling/.
5. Humphreys, J., G.S. Rohrer, and A. Rollett, *Chapter 15 - Control of Recrystallization*, in *Recrystallization and Related Annealing Phenomena (Third Edition)*, J. Humphreys, G.S. Rohrer, and A. Rollett, Editors. 2017, Elsevier: Oxford. p. 527-567.
6. Solberg, J.K., *Aluminium og Aluminiumlegeringer*, in *Teknologiske metaller og legeringer*. 2017. p. 191-242.
7. Wang, N., PhD Thesis: *Softening behaviour of Al-Mn-Fe-Si alloys during isothermal annealing*. 2013, NTNU.
8. Hirsch, J., K. F. Karhausen, and O. Engler, *Property Control in Production of Aluminum Sheet by Use of Simulation*. 2005. p. 705-725.
9. Alfed Aluminium Federation, *Aluminium Rolling.* [cited 2019 04.04]; Available from: http://www.alfed.org.uk/files/Fact%20sheets/18-aluminium-rolling.pdf
10. Boyer, H.E., *Heat Treating of Nonferrous Alloys.* Metallography, Microstructure, and Analysis, 2013. **2**(3): p. 190-195.
11. William D. Callister, J. and D.G. Rethwisch, *Dislocations and Strengthening Mechanisms*, in *Materials Science and Engineering*. 2014, Wiley. p. 216-250.
12. George E. Dieter, J., *Plastic Deformation of Single Crystals* in *Mechanical Metallurgy*. 1961, McGraw-Hill: New York p. 81-117.
13. Mecking, H., F. Kocks, and C. Hartig, *Taylor factors in materials with many deformation modes*. **35**. 1996.
14. Mordike, B.L. and P. Haasen, *Plastic deformation, work hardening and fracture*, in *Physical Metallurgy*. 1996, Cambridge University Press: Cambridge. p. 285-326.

15. Askeland, D.R., et al., *Imperfections in the Atomic Arrangement*, in *The Science and Engineering of Materials*. 1996, Springer Science+Business Media: Dordrecht. p. 80-110.
16. Humphreys, J., G.S. Rohrer, and A. Rollett, *Chapter 2 - The Deformed State*, in *Recrystallization and Related Annealing Phenomena (Third Edition)*, J. Humphreys, G.S. Rohrer, and A. Rollett, Editors. 2017, Elsevier: Oxford. p. 13-79.
17. Sjølstad, K., PhD Thesis: *Deformation and softening behaviour of commercial AlMn-alloys*. 2003, NTNU.
18. Marthinsen, K. *Lecture notes, MT8213 Modelling and simulation of materials microstructure and properties.* 2010.
19. Nord-Varhaug, K., et al., *Substructure Strengthening in Aluminium Alloys.* Materials Science Forum, 2000. **331-337**: p. 1387-1392.
20. Furu, T., R. Ørsund, and E. Nes, *Subgrain growth in heavily deformed aluminium—experimental investigation and modelling treatment.* Acta Metallurgica et Materialia, 1995. **43**(6): p. 2209-2232.
21. Gil Sevillano, J., P. van Houtte, and E. Aernoudt, *Large strain work hardening and textures.* Progress in Materials Science, 1980. **25**(2): p. 69-134.
22. Humphreys, J., G.S. Rohrer, and A. Rollett, *Chapter 14 - Continuous Recrystallization During and After Large Strain Deformation*, in *Recrystallization and Related Annealing Phenomena (Third Edition)*, J. Humphreys, G.S. Rohrer, and A. Rollett, Editors. 2017, Elsevier: Oxford. p. 509-526.
23. Vatne, H.E., et al., *Modelling recrystallization after hot deformation of aluminium.* Acta Materialia, 1996. **44**(11): p. 4463-4473.
24. A. Hughes, D. and N. Hansen, *A comparison of the evolution of cold and hot deformation microstructures and textures in fcc metals*. 2019.
25. Washburn, J. and G. Murty, *Effect of initial dislocation density on the stress-strain curve and on surface indication of slip in copper.* Canadian Journal of Physics, 1967. **45**(2): p. 523-539.
26. Bunkholt, S., PhD Thesis: *Subgrain Growth, Recovery Kinetics and Nucleation of Recrystallization of Cold Deformed Aluminium Alloys*. 2013, NTNU.
27. Huang, J.C. and G.T. Gray, *Microband formation in shock-loaded and quasi-statically deformed metals.* Acta Metallurgica, 1989. **37**(12): p. 3335-3347.
28. Hughes, D.A. and N. Hansen, *High angle boundaries formed by grain subdivision mechanisms.* Acta Materialia, 1997. **45**(9): p. 3871-3886.

29. Dorner, D. and S. Zaefferer, *Microstructure and Texture of Shear Bands in Cold Rolled Silicon Steel Single Crystals of Goss Orientation.* Solid State Phenomena, 2005. **105**: p. 239-244.
30. Inversen, J.T., *Implementation and Tesing of Numerical Models for Evolution of Microchemistry and Microstructure During Back-Annealing of Aluminium Alloys*. 2014: NTNU.
31. Askeland, D.R., et al., *Strain Hardening and Annealing*, in *The Science and Engineering of Materials*. 1996, Springer Science+Business Media: Dordrecht. p. 188-215.
32. Humphreys, J., G.S. Rohrer, and A. Rollett, *Chapter 1 - Introduction*, in *Recrystallization and Related Annealing Phenomena (Third Edition)*, J. Humphreys, G.S. Rohrer, and A. Rollett, Editors. 2017, Elsevier: Oxford. p. 1-11.
33. William D. Callister, J. and D.G. Rethwisch, *Applications and Processing of Metal Alloys*, in *Materials Science and Engineering*. 2014, Wiley. p. 408-466.
34. Humphreys, J., G.S. Rohrer, and A. Rollett, *Chapter 6 - Recovery After Deformation*, in *Recrystallization and Related Annealing Phenomena (Third Edition)*, J. Humphreys, G.S. Rohrer, and A. Rollett, Editors. 2017, Elsevier: Oxford. p. 199-244.
35. Raabe, D., *23 - Recovery and Recrystallization: Phenomena, Physics, Models, Simulation*, in *Physical Metallurgy (Fifth Edition)*, D.E. Laughlin and K. Hono, Editors. 2014, Elsevier: Oxford. p. 2291-2397.
36. Doherty, R.D., et al., *Current issues in recrystallization: a review.* Materials Science and Engineering: A, 1997. **238**(2): p. 219-274.
37. Humphreys, J., G.S. Rohrer, and A. Rollett, *Chapter 4 - The Structure and Energy of Grain Boundaries*, in *Recrystallization and Related Annealing Phenomena (Third Edition)*, J. Humphreys, G.S. Rohrer, and A. Rollett, Editors. 2017, Elsevier: Oxford. p. 109-143.
38. Huang, K. and R. Logé, *Zener Pinning*. 2016. p. 1-8.
39. Humphreys, F.J. and M.G. Ardakani, *Grain boundary migration and Zener pinning in particle-containing copper crystals.* Acta Materialia, 1996. **44**(7): p. 2717-2727.
40. Humphreys, J., G.S. Rohrer, and A. Rollett, *Chapter 9 - Recrystallization of Two-Phase Alloys*, in *Recrystallization and Related Annealing Phenomena (Third Edition)*, J. Humphreys, G.S. Rohrer, and A. Rollett, Editors. 2017, Elsevier: Oxford. p. 321-359.

41. Hansen, N. and B. Bay, *Initial stages of recrystallization in aluminium containing both large and small particles.* Acta Metallurgica, 1981. **29**(1): p. 65-77.
42. Humphreys, J., G.S. Rohrer, and A. Rollett, *Chapter 7 - Recrystallization of Single-Phase Alloys*, in *Recrystallization and Related Annealing Phenomena (Third Edition)*, J. Humphreys, G.S. Rohrer, and A. Rollett, Editors. 2017, Elsevier: Oxford. p. 245-304.
43. Paggi, A., G. Angella, and R. Donnini, *Strain induced grain boundary migration effects on grain growth of an austenitic stainless steel during static and metadynamic recrystallization.* Materials Characterization, 2015. **107**: p. 174-181.
44. Tangen, S., et al., *Effect of Concurrent Precipitation on Recrystallization and Evolution of the P-Texture Component in a Commercial Al-Mn Alloy.* Metallurgical and Materials Transactions A, 2010. **41**(11): p. 2970-2983.
45. Weinberg, M.C., D.P. Birnie, and V.A. Shneidman, *Crystallization kinetics and the JMAK equation.* Journal of Non-Crystalline Solids, 1997. **219**: p. 89-99.
46. Benum, S. and E. Nes, *Effect of precipitation on the evolution of cube recrystallisation texture.* Acta Materialia, 1997. **45**(11): p. 4593-4602.
47. A. Beck, P. and P. R. Sperry, *Strain Induced Grain Boundary Migration in High Purity Aluminum*. Vol. 21. 1950. 150-152.
48. Bellier, S.P. and R.D. Doherty, *The structure of deformed aluminium and its recrystallization—investigations with transmission Kossel diffraction.* Acta Metallurgica, 1977. **25**(5): p. 521-538.
49. Somerday, M. and F.J. Humphreys, *Recrystallisation behaviour of supersaturated Al–Mn alloys Part 1 – Al–1.3 wt-%Mn.* Materials Science and Technology, 2003. **19**(1): p. 20-29.
50. Hutchinson, W.B., *Recrystallisation textures in iron resulting from nucleation at grain boundaries.* Acta Metallurgica, 1989. **37**(4): p. 1047-1056.
51. L. Dillamore, I., et al., *Transition Bands and Recrystallization in Metals*. Vol. 329. 1972. 405-420.
52. Hjelen, J., R. Ørsund, and E. Nes, *On the origin of recrystallization textures in aluminium.* Acta Metallurgica et Materialia, 1991. **39**(7): p. 1377-1404.
53. Duggan, B.J., et al., *Deformation structures and textures in cold-rolled 70:30 brass.* Metal Science, 1978. **12**(8): p. 343-351.
54. Humphreys, F.J., *The nucleation of recrystallization at second phase particles in deformed aluminium.* Acta Metallurgica, 1977. **25**(11): p. 1323-1344.

55. Ye, L.Y., et al., *Particle-Stimulated Nucleation of Recrystallization for Grain-Size Control in 01420 Al-Li Alloy.* Materials Science Forum, 2007. **546-549**: p. 889-892.
56. Engler, O., X.W. Kong, and P. Yang, *Influence of particle stimulated nucleation on the recrystallization textures in cold deformed Al-alloys Part I—Experimental observations.* Scripta Materialia, 1997. **37**(11): p. 1665-1674.
57. Wikipedia. *Supersaturation*. [Cited 2019 15.04]; Available from: https://en.wikipedia.org/wiki/Supersaturation.
58. Lok, Z.J., PhD Thesis: *Microchemistry in aluminium sheet production*. 2005, Delft University of Technology.
59. Huang, K. and K. Marthinsen, *The Influence of Microchemistry and Processing Conditions on the Softening Behavior of Cold-Rolled Al-Mn-Fe-Si Alloys*, in *Light Metals 2015*, M. Hyland, Editor. 2016, Springer International Publishing: Cham. p. 157-162.
60. Li, Y.J. and L. Arnberg, *Quantitative study on the precipitation behavior of dispersoids in DC-cast AA3003 alloy during heating and homogenization.* Acta Materialia, 2003. **51**(12): p. 3415-3428.
61. Muggerud, A.M.F., *Transmission electron microscopy studies of dispersoids and constituent phases in Al-Mn-Fe-Si alloys*. 2014: NTNU.
62. C. M. De Haan, P., J. Van Rijkom, and J. A. H. Söntgerath, *The Precipitation Behaviour of High-Purity Al-Mn Alloys*. Vol. 217-222. 1996. 765-770.
63. Kolby, P., C. Sigli, and C.J. Simensen. *Solubility Limit of Mn and Si in Al-MnSi.* in *Proceedings of the 4th International Conference on Aluminium alloys: their Physical and Mechanical Properties*. 1994. Trondheim.
64. Bahadur, A., *Intermetallic phases in Al-Mn alloys*. Vol. 23. 1988. 48-54.
65. Flatøy, J.E.M., Master Thesis: *Process- and Alloy Development of Recyclable Aluminium Alloys*. 2011, NTNU.
66. Lodgaard, L. and N. Ryum, *Precipitation of dispersoids containing Mn and/or Cr in Al–Mg–Si alloys.* Materials Science and Engineering: A, 2000. **283**(1): p. 144-152.
67. Hornbogen, E., *Inhibition of recrystallization in supersaturated solid solutions by large amounts of cold work.* Journal of Materials Science, 1977. **12**(8): p. 1565-1572.
68. Hutchinson, B. and B. Duggan, *Influence of precipitation on recrystallization and texture development in an iron-1.2% copper alloy*. Vol. 12. 1978. 372-380.

69. Marshall, G.J., R.A. Ricks, and P.K.F. Limbach, *Controlling lower temperature recovery and recrystallisation in commercial purity aluminium.* Materials Science and Technology, 1991. **7**(3): p. 263-269.
70. Nes, E., N. Ryum, and O. Hunderi, *On the Zener drag.* Acta Metallurgica, 1985. **33**(1): p. 11-22.
71. Daaland, O. and E. Nes, *Recrystallization texture development in commercial Al□Mn□Mg alloys.* Acta Materialia, 1996. **44**(4): p. 1413-1435.
72. Zhang, J.-S., *21 - Creep Damage Physics*, in *High Temperature Deformation and Fracture of Materials*. 2010, Woodhead Publishing. p. 285-296.
73. Humphreys, J., G.S. Rohrer, and A. Rollett, *Appendix 1 - Texture*, in *Recrystallization and Related Annealing Phenomena (Third Edition)*. 2017, Elsevier: Oxford. p. 605-627.
74. Engler, O. and V. Randle, *Chapter 1 - Introduction*, in *Introduction to Texture Analysis*. 2009, CRC Press: Boca Raton. p. 3-14.
75. Verlinden, B., et al., *Chapter 8 Textural developments during thermo-mechanical processing*, in *Pergamon Materials Series*. 2007, Pergamon. p. 151-183.
76. Engler, O. and V. Randle, *Chapter 2 - Descriptors of Orientation* in *Introduction to Texture Analysis*. 2009, CRC Press: Boca Raton. p. 15-50.
77. Bunge, H.J., *Chapter 3 - Orientation Distributions*, in *Texture Analysis in Materials Science*, H.J. Bunge, Editor. 1982, Butterworth-Heinemann. p. 42-46.
78. Kallend, J.S., *Determination of the Orientation Distribution from Pole Figure Data*, in *Preferred Orientations in Polycrystals and Their Effect on Material Properties*, F. Kocks, C. Tomé, and H.R. Wenk, Editors. 2000, Cambridge University Press. p. 102-125.
79. Maurice, C. and J.H. Driver, *Hot rolling textures of f.c.c. metals—Part I. Experimental results on Al single and polycrystals.* Acta Materialia, 1997. **45**(11): p. 4627-4638.
80. Engler, O. and J. Hirsch, *Control of recrystallisation texture and texture-related properties in industrial production of aluminium sheet*. Vol. 100. 2009. 564-575.
81. Humphreys, J., G.S. Rohrer, and A. Rollett, *Chapter 3 - Deformation Textures*, in *Recrystallization and Related Annealing Phenomena (Third Edition)*, J. Humphreys, G.S. Rohrer, and A. Rollett, Editors. 2017, Elsevier: Oxford. p. 81-107.
82. Engler, O., *A Simulation of Recrystallization Textures of Al-Alloys With Consideration of the Probabilities of Nucleation and Growth*. Vol. 32. 1999.

83. Humphreys, J., G.S. Rohrer, and A. Rollett, *Chapter 12 - Recrystallization Textures*, in *Recrystallization and Related Annealing Phenomena (Third Edition)*, J. Humphreys, G.S. Rohrer, and A. Rollett, Editors. 2017, Elsevier: Oxford. p. 431-468.
84. L. Dillamore, I. and H. Katoh, *The Mechanisms of Recrystallization in Cubic Metals with Particular Reference to Their Orientation-Dependence*. Vol. 8. 1974. 73-83.
85. Daaland, O., et al., *On the Growth Rate of Cube-, Rotated Cube- and Rotated Goss-Grains in Commercial Aluminium Alloys.* Materials Science Forum, 1993. **113-115**: p. 115-120.
86. Engler, O., X. W Kong, and K. Lücke, *Recrystallisation textures of particle-containing Al–Cu and Al–Mn single crystals*. Vol. 49. 2001. 1701-1715.
87. Motra, H., J. Hildebrand, and A. Dimmig-Osburg, *Assessment of strain measurement techniques to characterise mechanical properties of structural steel*. Vol. 17. 2014.
88. Lim, H. and S. Hoag, *Plasticizer Effects on Physical–Mechanical Properties of Solvent Cast Soluplus® Films*. Vol. 14. 2013.
89. Alvi, M., et al., *Microstructural evolution during recrystallization in hot rolled Aluminum Alloy 1050*. 2003.
90. Askeland, D.R., et al., *Electrical Behaviour of Materials*, in *The Science and Engineering of Materials*. 1996, Springer Science+Business Media: Dordrecht. p. 618-671.
91. William D. Callister, J. and D.G. Rethwisch, *Electrical Properties*, in *Materials Science and Engineering*. 2014, Wiley. p. 725-784.
92. Altenpohl, D., *Aluminium und Aluminiumlegierungen*. 1965, Springer-Verlag: Berlin. p. 526.
93. 2.069, S. *Operating Instructions*. [Cited 2019 20.04]; Available from: http://www.mkckorea.com/catalog/foerster/sigmatest/Sigmatest%202.069%20Op%20Inst%20v3.12%20.pdf.
94. Stokes, D.J., *Principles of SEM*, in *Principles and Practice of Variable Pressure/Environmental Scanning Electron Microscopy (VP-ESEM)*. 2008, John Wiley & Sons, Ltd. p. 17-62.
95. GMBH, M.-P.-I.f.E. *Electron channeling contrast imaging - ECCI*. [Cited 2019 24.04] Available from: https://www.mpie.de/3079126/ECCI.
96. Ånes, H.W. *Particle Size Distribution from BSE image*. 2019; [Cited 2019 24.04]; Available from: https://github.com/hwagit/metallography-

notebooks/blob/master/particle_size_distribution_from_bse_image/particle_size_distribution_from_bse_image.ipynb.

97. Schwartz, A., M. Kumar, and B. Adams, *Electron Backscatter Diffraction in Material Science*. 2000.
98. Edwards, P. *Electron backscatter diffraction (EBSD)*. 2016; [Cited 2019 26.04]; Available from: http://gan-sem.phys.strath.ac.uk/techniques/electron-backscatter-diffraction-ebsd/.
99. Humphreys, F.J., *Review Grain and subgrain characterisation by electron backscatter diffraction.* Journal of Materials Science, 2001. **36**(16): p. 3833-3854.
100. Stojakovic, D., *Electron backscatter diffraction in materials characterization*. 2012. **6**.
101. Bachmann, F., R. Hielscher, and H. Schaeben, *Grain detection from 2d and 3d EBSD data—Specification of the MTEX algorithm.* Ultramicroscopy, 2011. **111**(12): p. 1720-1733.
102. Chen, Y.H., et al., *A Dictionary Approach to Electron Backscatter Diffraction Indexing.* Microscopy and Microanalysis, 2015. **21**(3): p. 739-752.
103. Callahan, P.G. and M. De Graef, *Dynamical Electron Backscatter Diffraction Patterns. Part I: Pattern Simulations.* Microscopy and Microanalysis, 2013. **19**(5): p. 1255-1265.
104. Marquardt, K., et al., *Quantitative electron backscatter diffraction (EBSD) data analyses using the dictionary indexing (DI) approach: Overcoming indexing difficulties on geological materials.* American Mineralogist, 2017. **102**(9): p. 1843-1855.
105. Wright, S.I., et al., *Introduction and comparison of new EBSD post-processing methodologies.* Ultramicroscopy, 2015. **159**: p. 81-94.
106. MTEX. *MTEX toolbox*. [Cited 2019 30.04]; Available from: https://mtex-toolbox.github.io/.
107. Hielscher, R., C. Silbermann, and E. Schmidl, *Denoising of Crystal Orientation Maps*. 2018.
108. Allain-Bonasso, N., et al., *A study of the heterogeneity of plastic deformation in IF steel by EBSD.* Materials Science and Engineering: A, 2012. **548**: p. 56-63.
109. Hielscher, R. and H. Schaeben, *A novel pole figure inversion method: specification of the MTEX algorithm.* Journal of Applied Crystallography, 2008. **41**(6): p. 1024-1037.

110. Ånes, H.W. *Sample Preparation for Texture Measurements in Siemens Diffractometer D5000*. 2018; [Cited 2019 30.04]; Available from: https://www.ntnu.no/wiki/display/imtlab/XRD?preview=/82478244/127993077/sample_preparation.pdf.
111. Elmasry, M., et al., *Negative Temperature Dependence of Recrystallized Grain Size: Formulation and Experimental Confirmation on Copper.* Materials (Basel, Switzerland), 2017. **10**(3): p. 308.
112. Nes, E. and S. Slevolden, *Mechanical Properties of New Strip Cast AlMnZr Alloys*. Vol. 55. 1979. 398-400.
113. Wang, N., Y. Li, and K. Marthinsen, *Article I: The softening behaviour of cold-rolled Al-Mn-Fe-Si-alloys influenced by concurrent precipitation*, in *Softening behaviour of Al-Mn-Fe-Si alloys during isothermal annealing (Doctoral thesis)*. 2013: NTNU. p. 105-150.
114. Vatne, H.E., O. Engler, and E. Nes, *Influence of particles on recrystallisation textures and microstructures of aluminium alloy 3103.* Materials Science and Technology, 1997. **13**(2): p. 93-102.
115. Engler, O., P. Yang, and X.W. Kong, *On the formation of recrystallization textures in binary Al-1.3% Mn investigated by means of local texture analysis.* Acta Materialia, 1996. **44**(8): p. 3349-3369.
116. Wang, N., Y. Li, and K. Marthinsen, *Article II: The influence of pre-existing dispersoids on the softening behaviour of cold-rolled Al-Mn-Fe-Si alloys*, in *Softening behaviour of Al-Mn-Fe-Si alloys during isothermal annealing (Doctoral thesis)*. 2013: NTNU. p. 151-192.
117. Burger, G., et al., *The Influence of Particle Dispersions and Processing Route in the Development of Recrystallization Textures in Aluminum Alloys.* Materials Science Forum, 1997. **242**: p. 101-110.
118. Liu, J. and J.G. Morris, *Recrystallization textures of continuous cast AA 3015 alloy: Development of the P orientation {011}〈566〉*. Metallurgical and Materials Transactions A, 2003. **34**(9): p. 2029-2032.
119. Liu, W.C., et al., *Effect of initial texture on texture evolution in cold-rolled AA 5182 aluminium alloy.* Philosophical Magazine, 2004. **84**(31): p. 3305-3321.
120. Chatterjee, B., *Science and Industry of Electropolishing*. Vol. **7**. 2015. p. 71-93.

121. Hill, T., PhD Thesis: *Evolution of second phase particles with deformation in aluminium alloys*. 2015: The University of Manchester.
122. Wang, N., et al. *The Influence of Processing Conditions on Microchemistry and the Softening Behavior of Cold Rolled Al-Mn-Fe-Si Alloys*. 2015. **6**, p. 61-61.
123. Huang, K., et al., *Evolution in microstructure and properties during non-isothermal annealing of a cold-rolled Al–Mn–Fe–Si alloy with different microchemistry states.* Materials Science and Engineering: A, 2015. **628**: p. 216-229.
124. Li, Y.J. and L. Arnberg, *Evolution of eutectic intermetallic particles in DC-cast AA3003 alloy during heating and homogenization.* Materials Science and Engineering: A, 2003. **347**(1): p. 130-135.
125. Zhao, Q., et al., *Strain-induced precipitation kinetics during non-isothermal annealing of Al-Mn alloys.* Journal of Alloys and Compounds, 2018. **735**: p. 2275-2280.
126. Chen, S.P., N.C.W. Kuijpers, and S. van der Zwaag, *Effect of microsegregation and dislocations on the nucleation kinetics of precipitation in aluminium alloy AA3003.* Materials Science and Engineering: A, 2003. **341**(1): p. 296-306.
127. Ånes, H.W., *MTEX Snippets.* 2019; [Cited 2019 12.06]; Available from: https://github.com/hwagit/mtex-snippets

APPENDIX A – CALCULATION EXAMPLE

A.1 Amount of Mn in Solid Solution

As mentioned in Section 3.3, Matthiessens rule (cf. Eq. 3.2) can be used to roughly estimate the amount of Mn in solid solution:

$$\frac{1}{\sigma} = 0.0267 + 0.032Fe_{ss}\% + 0.033Mn_{ss}\% + 0.0068Si_{ss}\% \qquad (A.1)$$

The solubility of Fe in aluminium is very low and nearly all the Fe content forms intermetallic primary particles, and the contribution from Si is much lower than for the two other elements. The contribution from Fe and Si to the change in electrical conductivity during annealing is often neglected, which results in the following equation:

$$\frac{1}{\sigma} = 0.0267 + 0.033Mn_{ss}\% \qquad (A.2)$$

By using the electrical conductivity measurements in Table 4.2 in Section 4.3, the amount of Mn in solid solution can be approximated for e.g. %CR46. The electrical conductivity for this sample is 25.93 MS/m, and the calculation of Mn in solid solution is shown below:

$$\frac{1}{25.93} = 0.0267 + 0.033Mn_{ss}\%$$

$$Mn_{ss}\% = \left(\frac{1}{25.93} - 0.0267\right) \Big/ 0.033 = \frac{0.0119}{0.033} = 0.360$$

APPENDIX B – POST-PROCESSING OF EBSD DATA

B.1 Matlab Script Denoising – MTEX

B.1.1 Denoising TSL

The EBSD patterns for HR, %CR46-280, %CR67-280, %CR87-280, %CR46-330, %CR67-330 and %CR87-330 collected by NORDIF UF-1100 and analysed by the TSL indexing approach were denoised using the script below. The script was made by Håkon Wiik Ånes.

```
% Plotting conventions
setMTEXpref('xAxisDirection', 'north');
setMTEXpref('zAxisDirection', 'intoPlane');
res = '-r200'; % Image resolution, dpi

% Crystal and specimen symmetry
cs = {'notindexed', crystalSymmetry('m-3m', [4.04 4.04 4.04],
'mineral', 'al')};
ss = specimenSymmetry('orthorhombic');

% Processing parameters
file = ['C:\Users\Example\'...
    'Example.osc'];
[path, fname] = fileparts(file);

% Read data
ebsd = loadEBSD(file, cs, 'convertEuler2SpatialReferenceFrame');

% Plot initial OM and quality map
oM = ipfHSVKey(ebsd('al'));
oM.inversePoleFigureDirection = xvector;
figure
plot(ebsd('al'), oM.orientation2color(ebsd('al').orientations))

figure
%plot(ebsd, ebsd.fit)
mtexColorMap white2black

% Keep original data
ebsd2 = ebsd;

% Remove low-quality measurements
filterVal = 2.0;
%ebsd2(ebsd2.confidenceindex < filterVal).phase = -1;
ebsd2(ebsd2.fit > filterVal).phase = -1;
%ebsd2(ebsd2.imagequality < filterVal).phase = -1;

% Reconstruct grains
mat1 = 10*degree; % Mean angle threshold
minPx1 = 10;
[grains, ebsd2.grainId, ebsd2.mis2mean] = calcGrains(ebsd2, 'angle',
mat1);
ebsd2(grains(grains.grainSize < minPx1)) = [];
```

```
[grains, ebsd2.grainId, ebsd2.mis2mean] = calcGrains(ebsd2, 'angle',
mat1)

% Denoise
F = halfQuadraticFilter;
F.alpha = 0.05;
F.threshold = 5*degree;
ebsd3 = smooth(ebsd2('indexed'), F, 'fill');

oM = ipfHSVKey(ebsd3('al'));
oM.inversePoleFigureDirection = xvector;
figure
plot(ebsd3('al'), oM.orientation2color(ebsd3('al').orientations))

% Reconstruct grains again
mat2 = 0.5*degree; % or 0.6*degree
minPx2 = 10
[grains, ebsd3.grainId, ebsd3.mis2mean] = calcGrains(ebsd3, 'angle',
mat2);
ebsd3(grains(grains.grainSize < minPx2)) = [];
[grains, ebsd3.grainId, ebsd3.mis2mean] = calcGrains(ebsd3, 'angle',
mat2);
grains = smooth(grains, 5);

% Separate LABs and HABs
gbal = grains('al').boundary('al', 'al');
mAngles = gbal.misorientation.angle./degree;
maxmori = max(mAngles);
hagb = 15;
[~, ~, gbid] = histcounts(mAngles, 'NumBins', 2, 'BinEdges',...
    [mat2 hagb maxmori]);

% Final denoising
ebsd4 = smooth(ebsd3('indexed'), F, 'fill');

export(ebsd4, 'C:\Users\Example\Example.txt')

% Plot boundaries on OM wrt. RD
oM2 = ipfHSVKey(ebsd4('al'));
oM2.inversePoleFigureDirection = xvector;
figure
plot(ebsd4('al'), oM2.orientation2color(ebsd4('al').orientations))
hold on
plot(gbal(gbid==1), 'linecolor', [0.7 0.7 0.7], 'linewidth', 1)
plot(gbal(gbid==2), 'linecolor', [0 0 0], 'linewidth', 1)
plot(grains('notindexed'), grains('notindexed').GOS, 'facecolor',
'k')
hold off
```

B.1.1 Denoising DI

The EBSD patterns for %CR46, %CR67, %CR87, %CR46-280, %CR67-280 and %CR87-280 collected by NORDIF UF-1100 and analysed by the DI approach were denoised using the script below. The script was made by Håkon Wiik Ånes.

```
% Plotting conventions
setMTEXpref('xAxisDirection', 'north');
setMTEXpref('zAxisDirection', 'intoPlane');
res = '-r200'; % Image resolution, dpi

% Crystal and specimen symmetry
cs = {'notindexed', crystalSymmetry('m-3m', [4.04 4.04 4.04],
'mineral', 'al')};
ss = specimenSymmetry('orthorhombic');

% Processing parameters
file = ['C:\Users\Example\'...
    'Example.ang'];
[path, fname] = fileparts(file);

% Read data
ebsd = loadEBSD(file, cs, 'convertEuler2SpatialReferenceFrame');

% Plot initial OM and quality map
oM = ipfHSVKey(ebsd('al'));
oM.inversePoleFigureDirection = xvector;
figure
plot(ebsd('al'), oM.orientation2color(ebsd('al').orientations))

figure
%plot(ebsd, ebsd.fit)
mtexColorMap white2black

% Keep original data
ebsd2 = ebsd;

% Remove low-quality measurements
filterVal = 0.2;
%ebsd2(ebsd2.iq < filterVal).phase = -1;
ebsd2(ebsd2.ci < filterVal).phase = -1;

% Reconstruct grains
mat1 = 10*degree; % Mean angle threshold
minPx1 = 10;
[grains, ebsd2.grainId, ebsd2.mis2mean] = calcGrains(ebsd2, 'angle',
mat1);
ebsd2(grains(grains.grainSize < minPx1)) = [];
[grains, ebsd2.grainId, ebsd2.mis2mean] = calcGrains(ebsd2, 'angle',
mat1)

% Denoise
F = halfQuadraticFilter;
```

```
F.alpha = 0.05;
F.threshold = 5*degree;
ebsd3 = smooth(ebsd2('indexed'), F, 'fill');

oM = ipfHSVKey(ebsd3('al'));
oM.inversePoleFigureDirection = xvector;
figure
plot(ebsd3('al'), oM.orientation2color(ebsd3('al').orientations))

% Reconstruct grains again
mat2 = 0.4*degree; % or 0.3*degree
minPx2 = 10;
[grains, ebsd3.grainId, ebsd3.mis2mean] = calcGrains(ebsd3, 'angle',
mat2);
ebsd3(grains(grains.grainSize < minPx2)) = [];
[grains, ebsd3.grainId, ebsd3.mis2mean] = calcGrains(ebsd3, 'angle',
mat2);
grains = smooth(grains, 5);

% Separate LABs and HABs
gbal = grains('al').boundary('al', 'al');
mAngles = gbal.misorientation.angle./degree;
maxmori = max(mAngles);
hagb = 15;
[~, ~, gbid] = histcounts(mAngles, 'NumBins', 2, 'BinEdges',...
    [mat2 hagb maxmori]);

% Final denoising
ebsd4 = smooth(ebsd3('indexed'), F, 'fill');

export(ebsd4, 'C:\Users\Example\Example.txt')

% Plot boundaries on OM wrt. RD
oM2 = ipfHSVKey(ebsd4('al'));
oM2.inversePoleFigureDirection = xvector;
figure
plot(ebsd4('al'), oM2.orientation2color(ebsd4('al').orientations))
hold on
plot(gbal(gbid==1), 'linecolor', [0.7 0.7 0.7], 'linewidth', 1)
plot(gbal(gbid==2), 'linecolor', [0 0 0], 'linewidth', 1)
plot(grains('notindexed'), grains('notindexed').GOS, 'facecolor',
'k')
hold off
```

B.2 Matlab Script Fraction Recrystallized – MTEX

The script below was used to measure grain- and subgrain size, GOS and amount of HAGBs, and thus fraction recrystallized, as described in Section 3.4.2. The script was made by Håkon Wiik Ånes, and the functions used in the script can be found on Github [127].

```
data = 'C:\Example\Example.txt'
cs = {'notindexed', crystalSymmetry('m-3m', [4.04 4.04 4.04],
'mineral', 'al')};
setMTEXpref('xAxisDirection', 'north');
setMTEXpref('zAxisDirection', 'intoPlane');
ebsd = loadEBSD(data, cs, 'convertEuler2SpatialReferenceFrame');

%% Reconstruct grains again
mat2 = 0.5*degree;
minPx2 = 10;
[grains, ebsd.grainId, ebsd.mis2mean] = calcGrains(ebsd, 'angle',
mat2);
ebsd(grains(grains.grainSize < minPx2)) = [];
[grains, ebsd.grainId, ebsd.mis2mean] = calcGrains(ebsd, 'angle',
mat2);
grains = smooth(grains, 5);

%% Calculate fraction recrystallized
[grains, grainsSub, grainsRex] =
ebsd_fraction_recrystallised(grains);

Xrex = sum(grains(grains.RX == 1).area) / (length(ebsd)*ebsd(2).y^2)
sum(grains.area .* grains.ECD) / sum(grains.area)

ebsd_write_grains_data(grains, 'C:\Example\GrainProperties')
```

B.3 OIM-Maps

The OIM-maps of %CR46-180, %CR46-280, %CR67-280, %CR87-280, %CR46-330, %CR67-330 and %CR87-330 not shown in Section 4.4 are presented below.

B.3.1 Annealed – 180°C

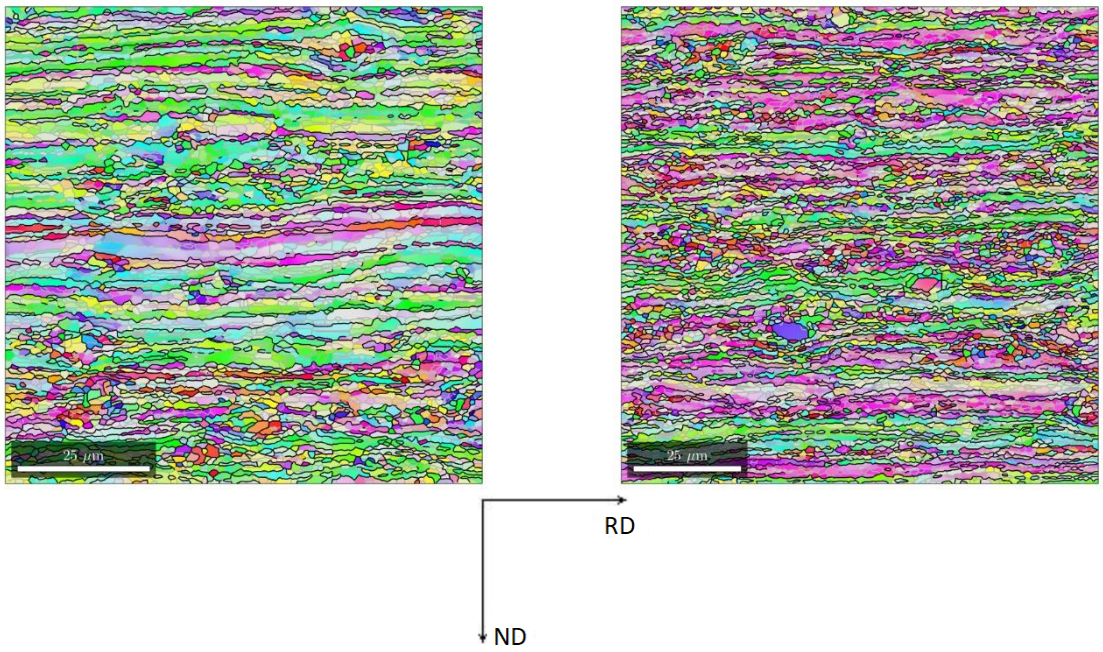

Figure B.1: OIM-maps (500x) of %CR46-180.

B.3.2 Annealed – 280°C

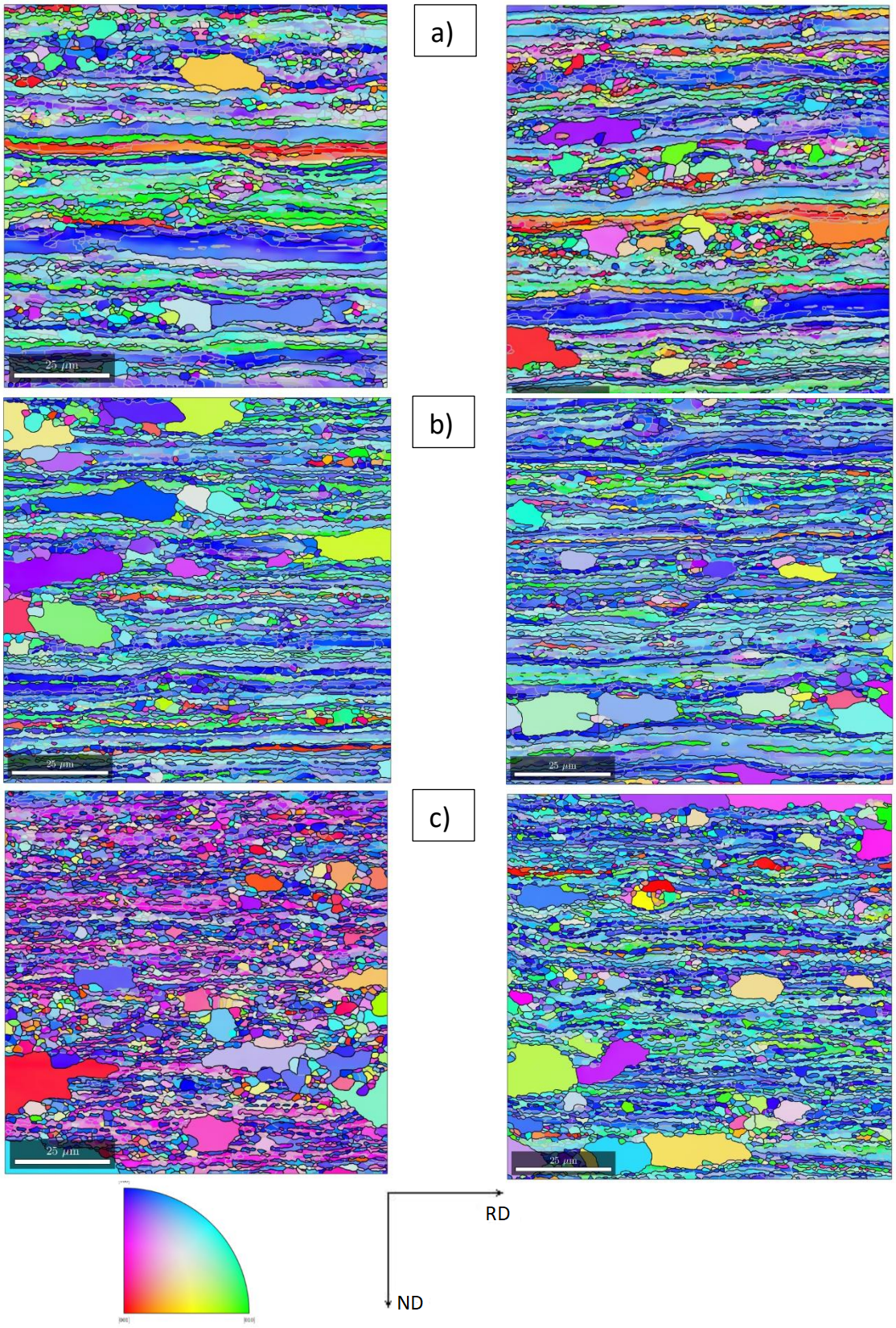

Figure B.2: OIM-maps (500x) of (a) %CR46-280, (b) %CR67-280 and (c) %CR87-280.

B.3.3 Annealed – 330°C

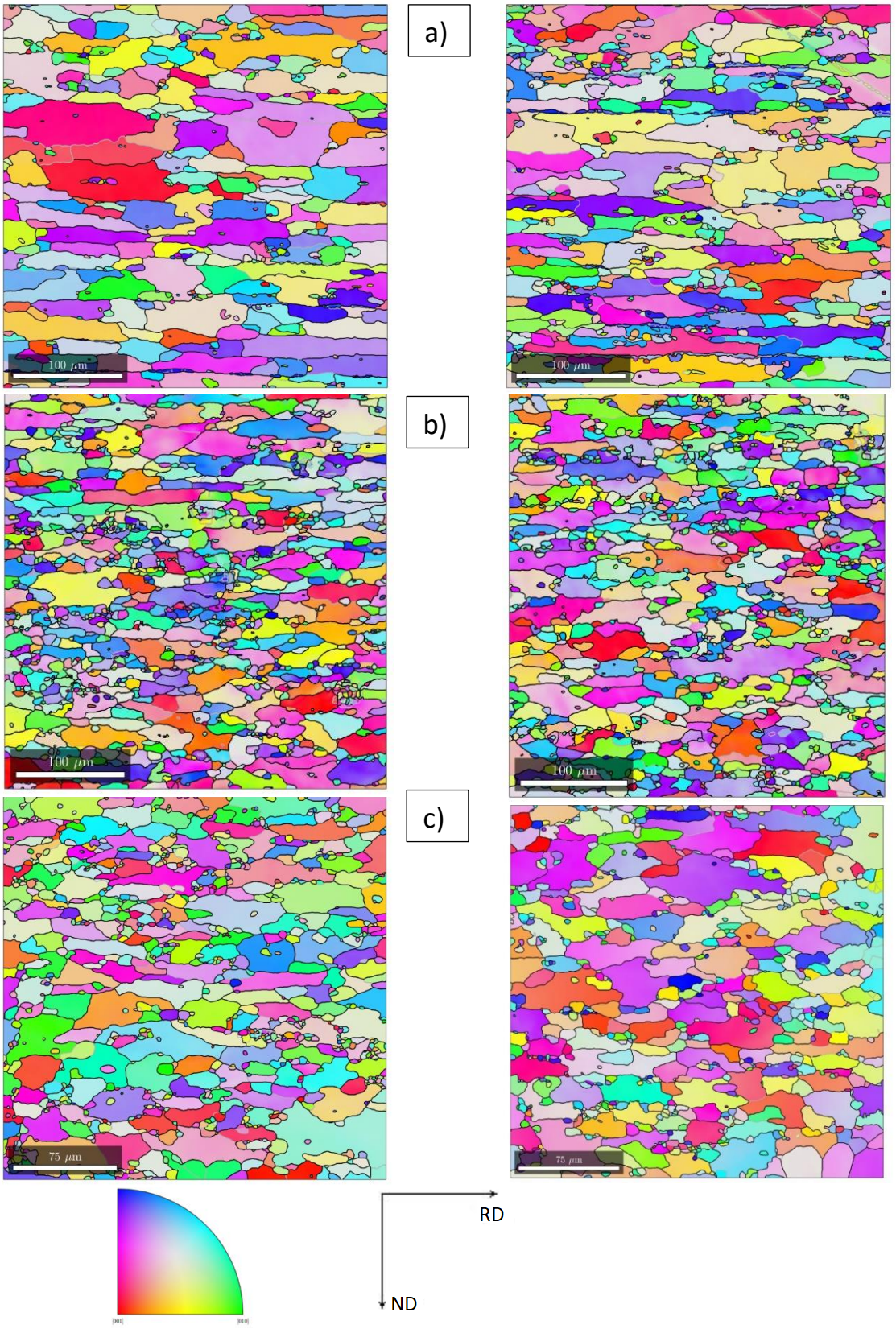

Figure B.3: OIM-maps of (a) %CR46-330 (200x), (b) %CR67-330 (200x) and (c) %CR87-330 (300x).

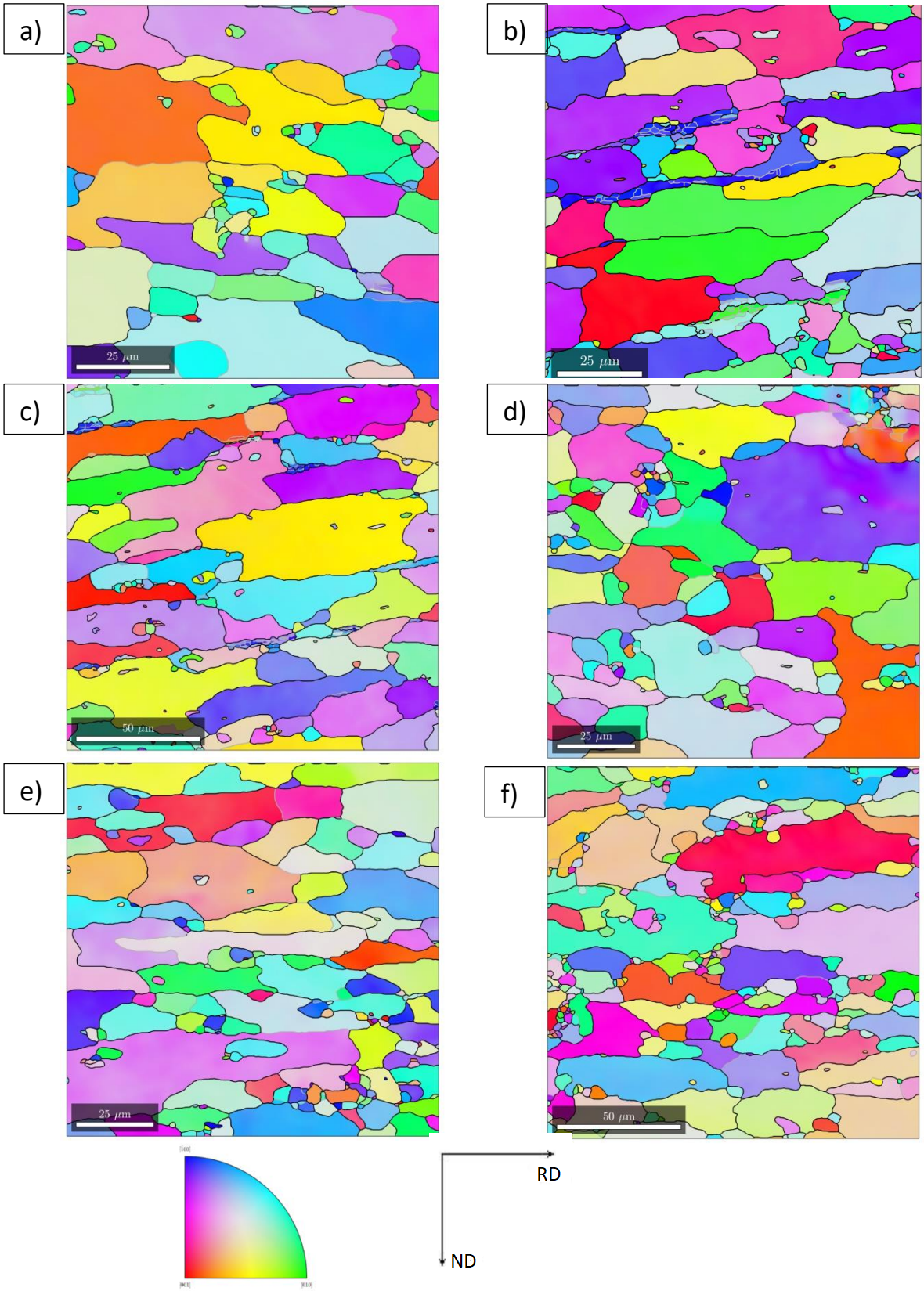

Figure B.4: OIM-maps (500x) of (a) – (c) %CR46-330, (d) – (e) %CR67-330 and (f) %CR87-330.

APPENDIX C – POST-PROCESSING OF TEXTURE-DATA

C.1 Matlab Script – MTEX

The script below was used to create an MTEX pole figure object from the four adjusted pole figures, and then calculate the ODF, plot intensities along fibres (beta and Cube-Goss) and calculate volume fractions of specific texture components, as described in Section 3.5. The script was made by Håkon Wiik Ånes.

```
%% Import pole figure data and create PoleFigure object
cs = crystalSymmetry('m-3m',[4.04 4.04 4.04],'mineral','Al');

path = ['C:\Example'];
fnamesPrefix = 'Example_R';

fnames = {
    [path fnamesPrefix '_pf111_uncorr.dat'],...
    [path fnamesPrefix '_pf200_uncorr.dat'],...
    [path fnamesPrefix '_pf220_uncorr.dat'],...
    [path fnamesPrefix '_pf311_uncorr.dat']};

% Specimen symmetry
ss = specimenSymmetry('1'); % Triclinic
ssO = specimenSymmetry('orthorhombic');

% Plotting convention
setMTEXpref('xAxisDirection','north');
setMTEXpref('zAxisDirection','outOfPlane');

% Set annotations to highlight spatial reference frame
pfAnnotations = @(varargin) text([vector3d.X,vector3d.Y],...

{'RD','TD'},'BackgroundColor','w','tag','axesLabels',varargin{:});
setMTEXpref('pfAnnotations',pfAnnotations);

h = {
    Miller(1,1,1,cs),...
    Miller(2,0,0,cs),...
    Miller(2,2,0,cs),...
    Miller(3,1,1,cs)};

% Load pole figures separately
columnNames = {'Polar Angle','Azimuth Angle','Intensity'};
pf1 = loadPoleFigure_generic(fnames{1},'ColumnNames',columnNames);
pf2 = loadPoleFigure_generic(fnames{2},'ColumnNames',columnNames);
pf3 = loadPoleFigure_generic(fnames{3},'ColumnNames',columnNames);
pf4 = loadPoleFigure_generic(fnames{4},'ColumnNames',columnNames);

% Construct pole figure object of the four pole figures
intensities = {
    pf1.intensities,...
    pf2.intensities,...
    pf3.intensities,...
```

```
    pf4.intensities};
pfs = PoleFigure(h,pf1.r,intensities,cs,ss);

%% Plot pole figures of raw, corrected data
figure
plot(pfs,'upper','projection','eangle','minmax')
mtexColorbar('location','southOutside')

%% Calculate the ODF using default settings
odf = calcODF(pfs)

% Set correct specimen symmetry for calculation of texture strength
odf.SS = ssO;

% Calculate texture strength
textureIndex = odf.textureindex
entropy = odf.entropy
odfMax = odf.max

%% ODF in {111} PF with specified contour levels
levelsPF = [0,1,2,3,4,5];

odf.SS = ss;
figure
plotPDF(odf,h,'upper','projection','eangle','contourf',levelsPF)
mtexColorbar

%% Plot ODF in Euler space phi2 sections
levelsODF = [0,1,2,3,4,8,12];

odf.SS = ssO;
figure
plot(odf,'phi2',[0 45 65]*degree,'contourf',levelsODF,'minmax')

figure
plot(odf,'sections',18,'contourf',levelsODF)

%% Plot inverse pole figure
figure
plotIPDF(odf,[xvector,yvector,zvector],'contourf','minmax') %
contoured
%plotIPDF(odf,[xvector,yvector,zvector]) % continuous
mtexColorMap WhiteJet % or e.g. white2black
mtexColorbar

%% Define ideal texture components and spread acceptance angle
br = orientation.byEuler(35*degree,45*degree,90*degree,cs,ssO);
cu = orientation.byEuler(90*degree,35*degree,45*degree,cs,ssO);
cube = orientation.byMiller([1 0 0],[0 0 1],cs,ssO);
cubeND22 = orientation.byEuler(22*degree,0,0,cs,ssO);
cubeND45 = orientation.byMiller([1 0 0],[0 1 1],cs,ssO);
goss = orientation.byMiller([1 1 0],[0 0 1],cs,ssO);
p = orientation.byMiller([0 1 1],[1 2 2],cs,ssO);
q = orientation.byMiller([0 1 3],[2 3 1],cs,ssO);
s = orientation.byEuler(59*degree,37*degree,63*degree,cs,ssO);
```

```
spread = 10*degree;

%% Calculate volume fractions Mi
Mbr = volume(odf,br,spread)
Mcu = volume(odf,cu,spread)
Mcube = volume(odf,cube,spread)
McubeND22 = volume(odf,cubeND22,spread)
McubeND45 = volume(odf,cubeND45,spread)
Mgoss = volume(odf,goss,spread)
Mp = volume(odf,p,spread)
Mq = volume(odf,q,spread)
Ms = volume(odf,s,spread)

%% Plot intensity along beta fibre from Cu to Brass and write
results to file
odf.SS = ssO;
f = fibre(cu,br,cs,ssO);

% generate list from fibres and evalute ODF at specific orientations
fibreOris = f.orientation;
evalOris = [];
evalIndex = [1 84 167 254 346 446 556 680 824 1000];
evalValues = zeros(1,10);
for i=1:10
    ori = fibreOris(evalIndex(i));
    evalOris = [evalOris ori];
    evalValues(i) = eval(odf,ori);
end

figure
plot(evalOris.phi2/degree,evalValues,'-o')
xlabel('\phi_2 \rightarrow','interpreter','tex')
ylabel('Orientation density f(g)','interpreter','tex')
xlim([45 90])

% Write fibre data to a csv file for further analysis
datafname = [path 'data_fibre_beta.csv'];

% Write header to file
fid = fopen(datafname,'w');
fprintf(fid,'%s\r\n',['phi1,Phi,phi2,fibreValue']);
fclose(fid);

% Write Euler angles and intensities to file
dlmwrite(datafname,[(evalOris.phi1/degree)'
(evalOris.Phi/degree)'...
    (evalOris.phi2/degree)' evalValues'],'-append')

%% Plot intensity along fibre from Cube to Goss and write results to
file
cube = orientation('Euler',0,0,0,cs,ssO);
goss = orientation('Euler',0,45*degree,0,cs,ssO);
f = fibre(cube,goss,cs,ssO);

% Generate list from fibres and evalute ODF at specific orientations
fibreOris = f.orientation;
```

```
evalOris = [];
evalIndex = [1 111 222 333 444 555 666 777 888 1000];
evalValues = zeros(1,10);
for i=1:10
    ori = fibreOris(evalIndex(i));
    evalOris = [evalOris ori];
    evalValues(i) = eval(odf,ori);
end

figure
plot(evalOris.Phi/degree,evalValues,'-o')
xlabel('\Phi \rightarrow','interpreter','tex')
ylabel('Orientation density f(g)','interpreter','tex')
xlim([0 45])

% Write fibre data to a csv file for further analysis
datafname = [path 'data_fibre_cube_goss.csv'];

% Write header to file
fid = fopen(datafname,'w');
fprintf(fid,'%s\r\n',['phi1,Phi,phi2,fibreValue']);
fclose(fid);

% Write Euler angles and intensities to file
dlmwrite(datafname,[(evalOris.phi1/degree)'
(evalOris.Phi/degree)'...
    (evalOris.phi2/degree)' evalValues'],'-append')
```

C.2 Pole Figures

The pole figures created in MTEX are presented below for %CR46-330, %CR67-330 and &CR87-330.

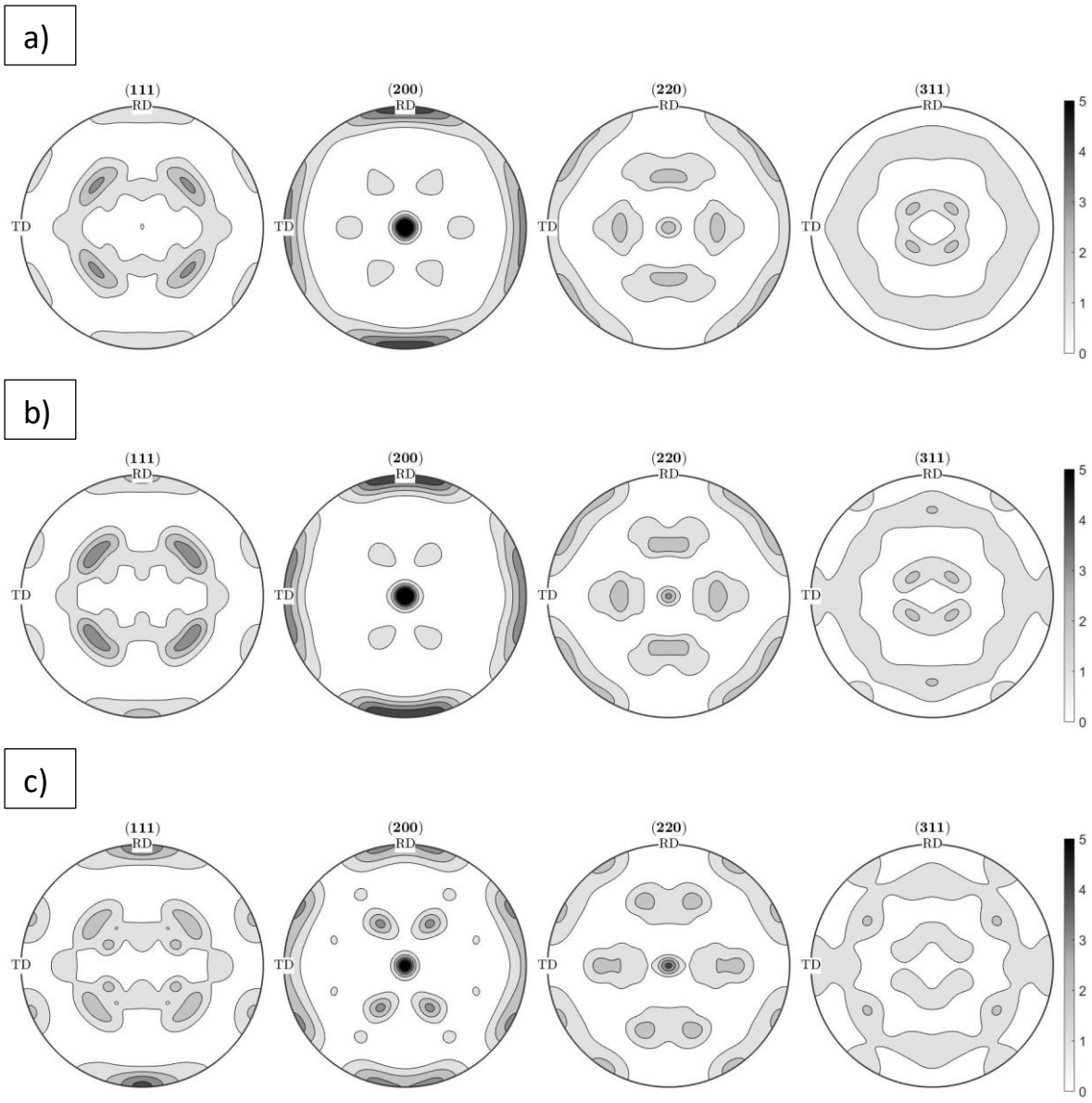

Figure C.1: Pole figures for (a) %CR46-330, (b) %CR67-330 and (c) %CR87-330.

APPENDIX D – PARTICLE ANALYSIS

D.1 SEM-BSE Images of Dispersoids

The SEM-BSE images taken at 5000x magnification not included in Section 4.6, as well as the images taken at 1000x magnification are presented below for all the samples studied in SEM.

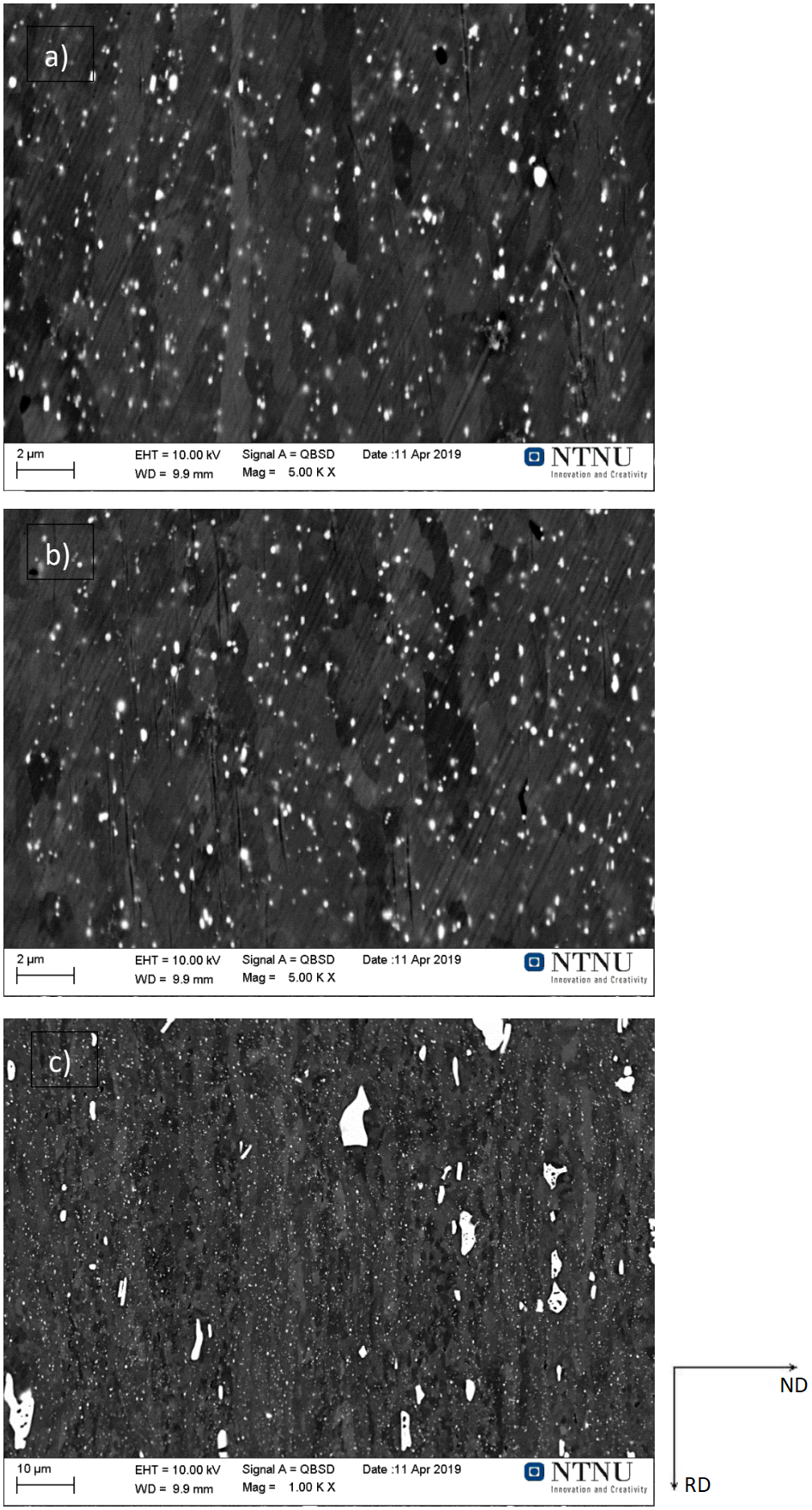

Figure D.1: SEM-BSE image of dispersoids present in HR taken at (a) – (b) 5000x and (c) 1000x.

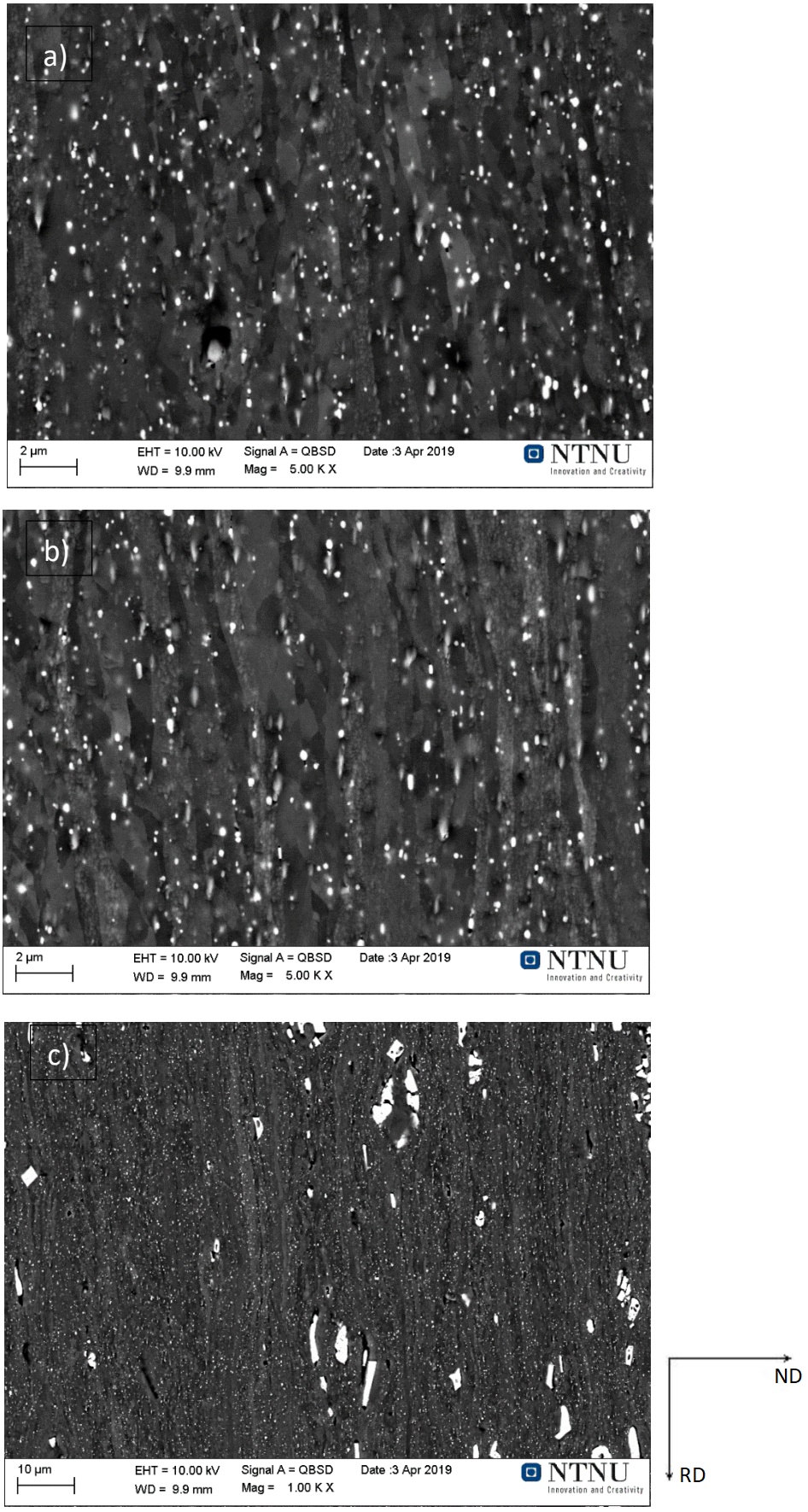

Figure D.2: SEM-BSE image of dispersoids present in %CR46 taken at (a) – (b) 5000x and (c) 1000x.

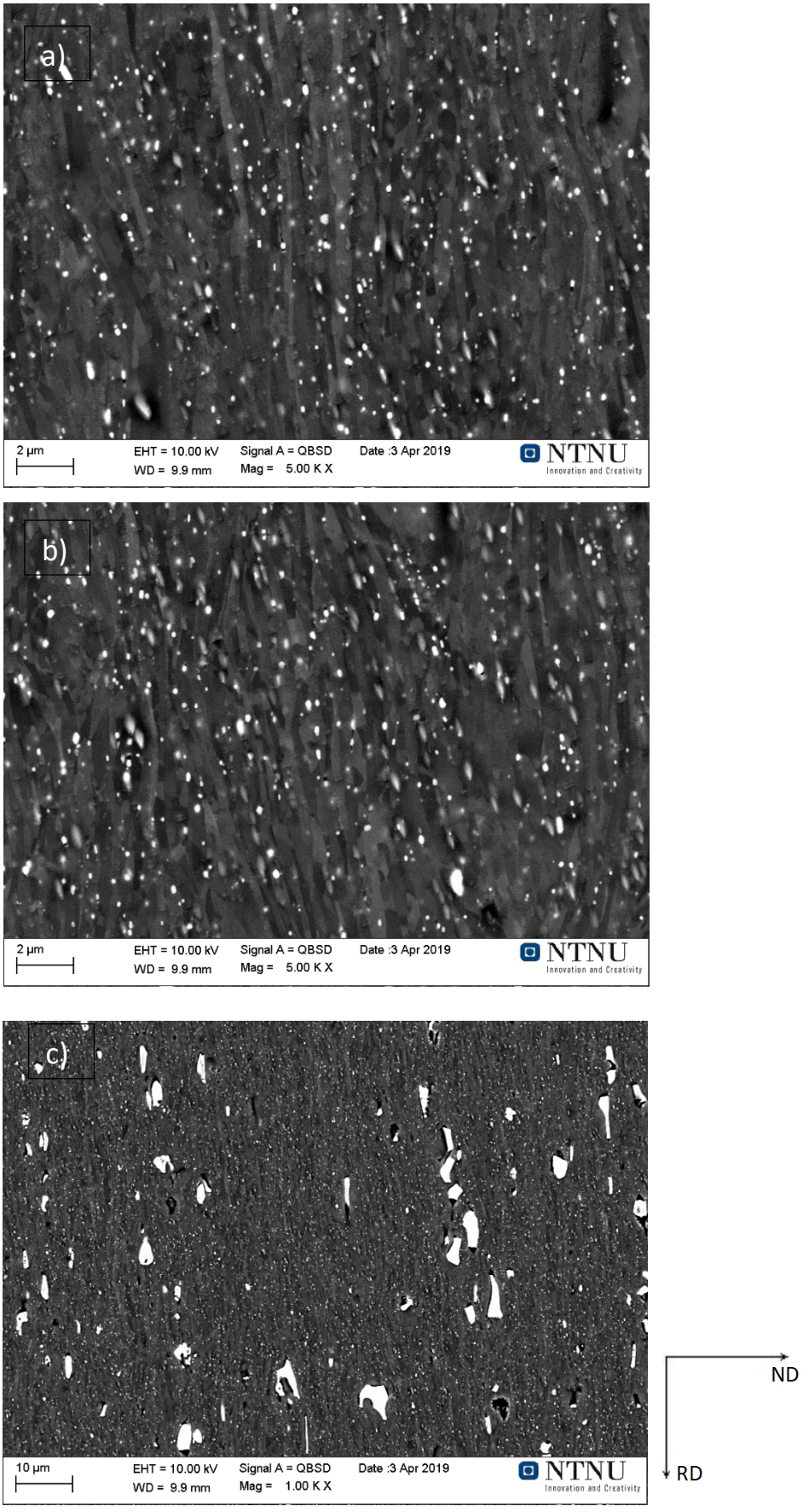

Figure D.3: SEM-BSE image of dispersoids present in %CR67 taken at (a) – (b) 5000x and (c) 1000x.

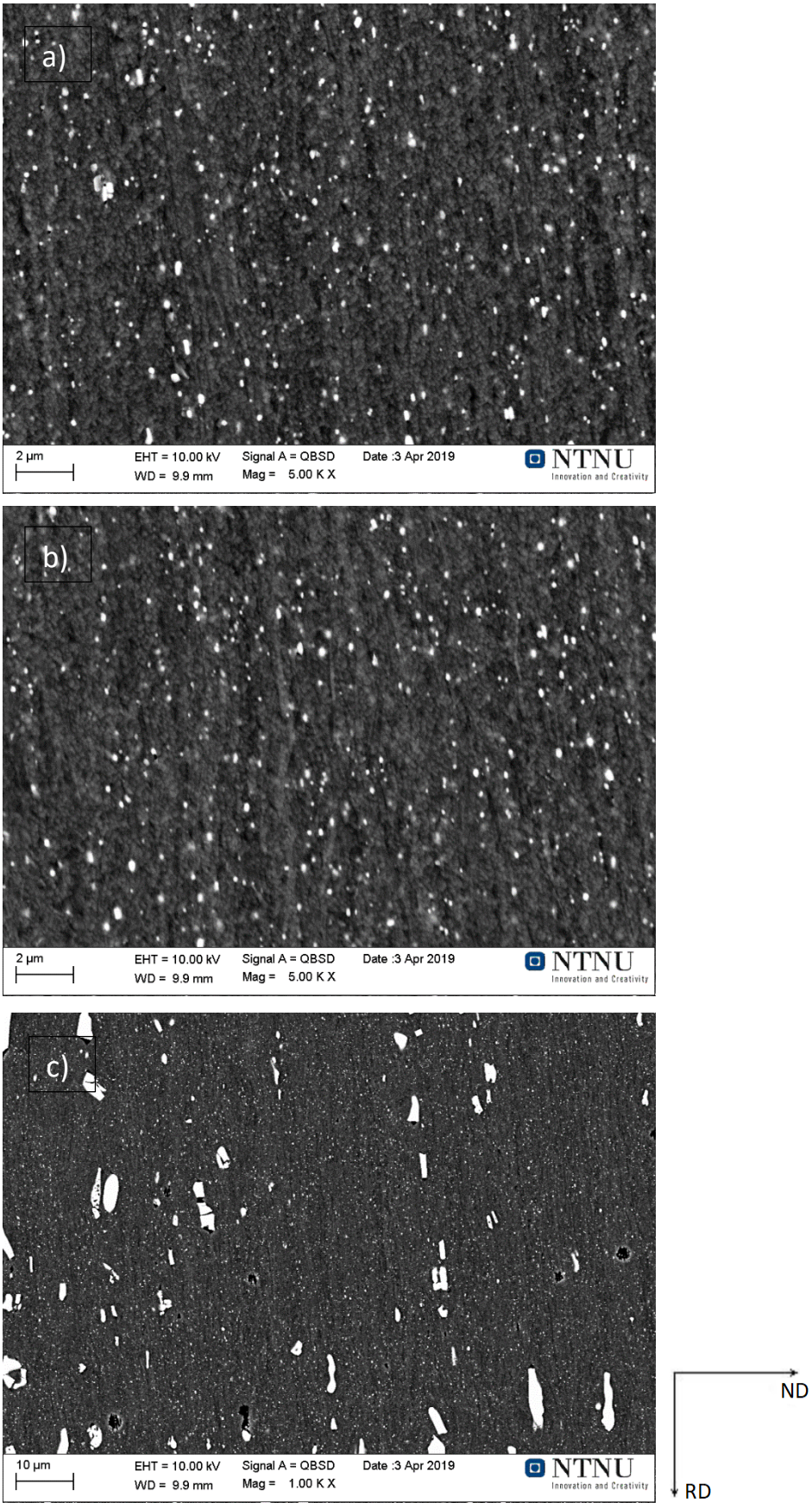

Figure D.4: SEM-BSE image of dispersoids present in %CR87 taken at (a) – (b) 5000x and (c) 1000x.

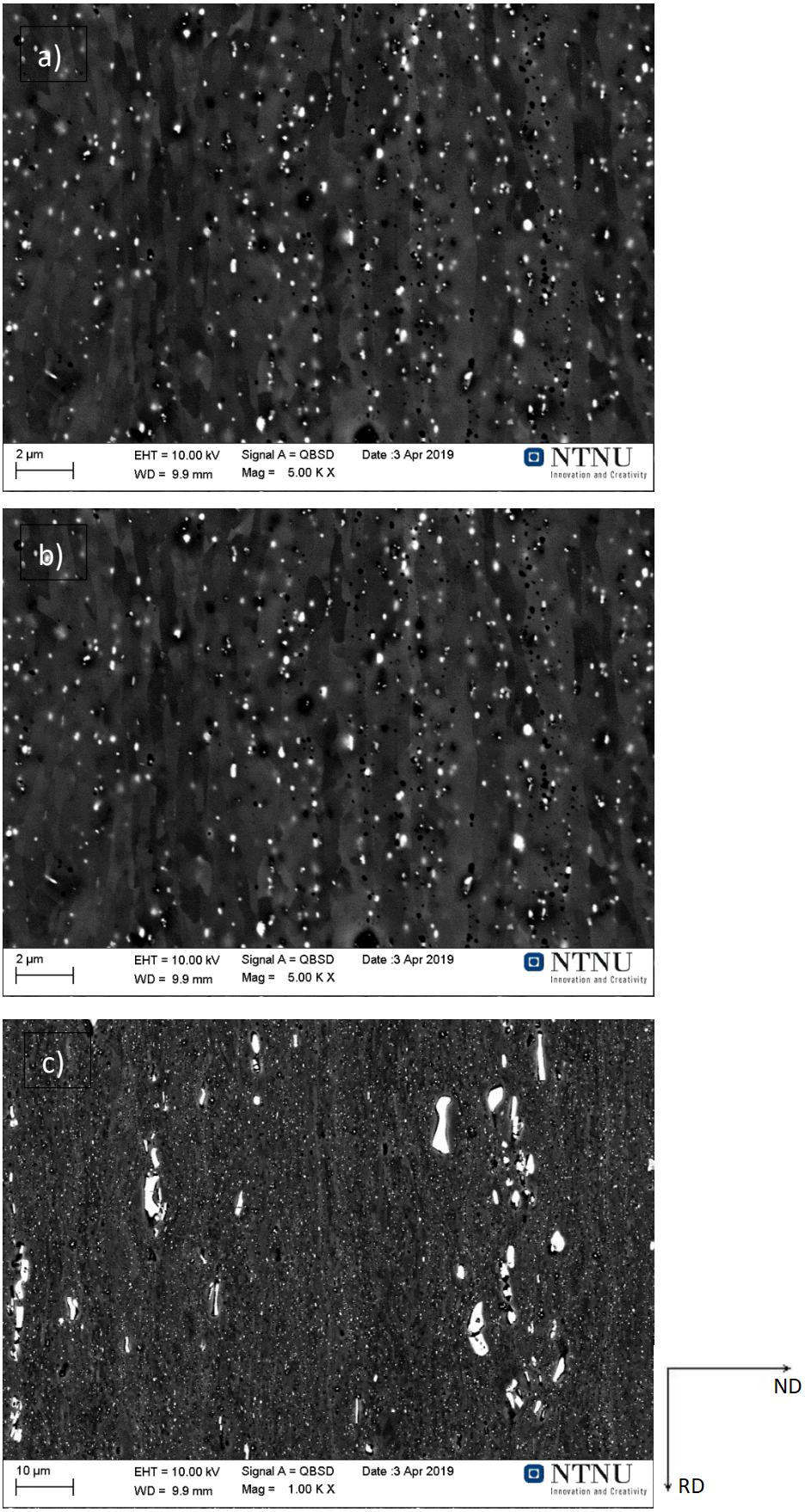

Figure D.5: SEM-BSE image of dispersoids present in %CR46-180 taken at (a) – (b) 5000x and (c) 1000x.

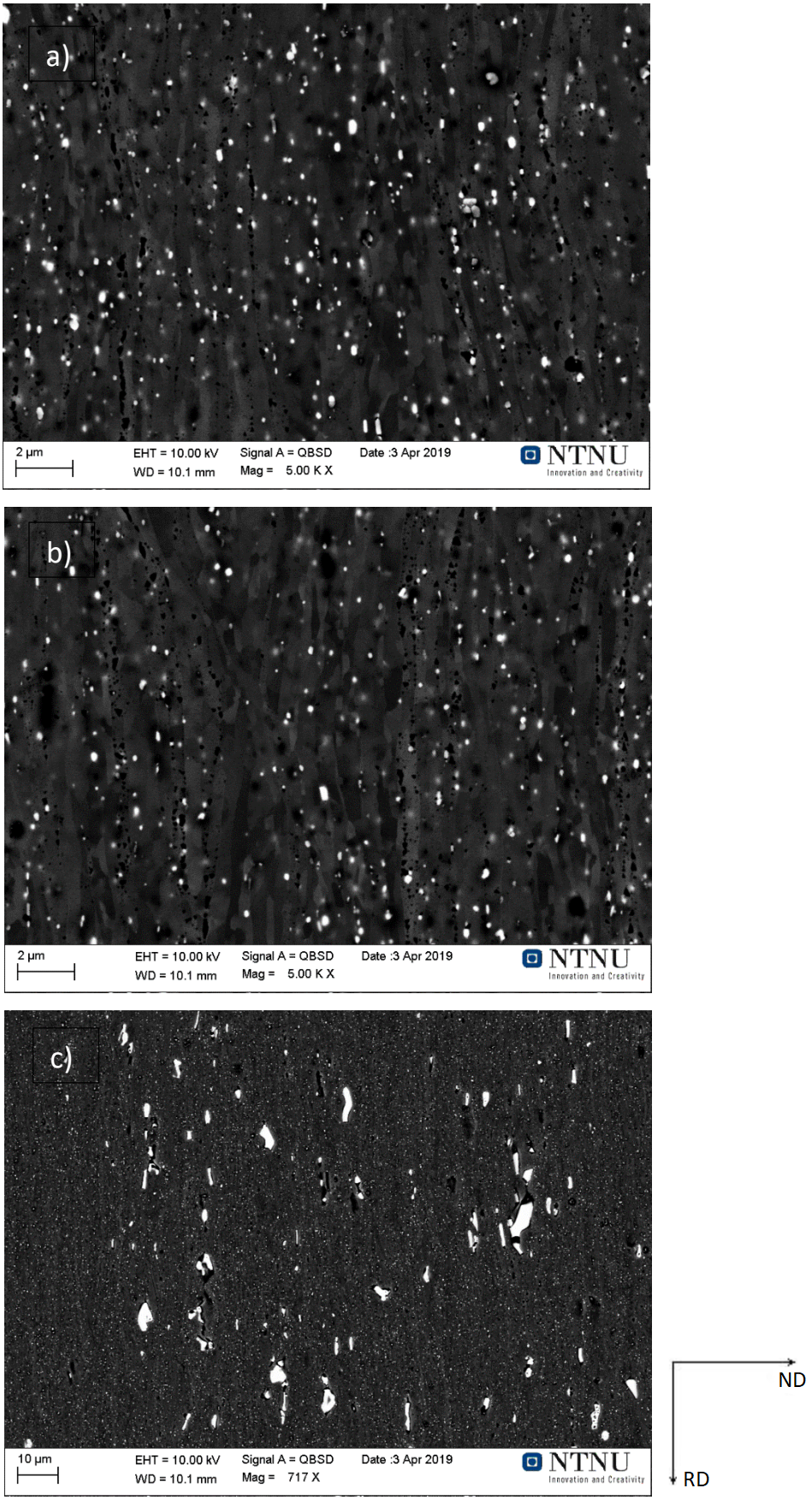

Figure D.6: SEM-BSE image of dispersoids present in %CR67-180 taken at (a) – (b) 5000x and (c) 717x.

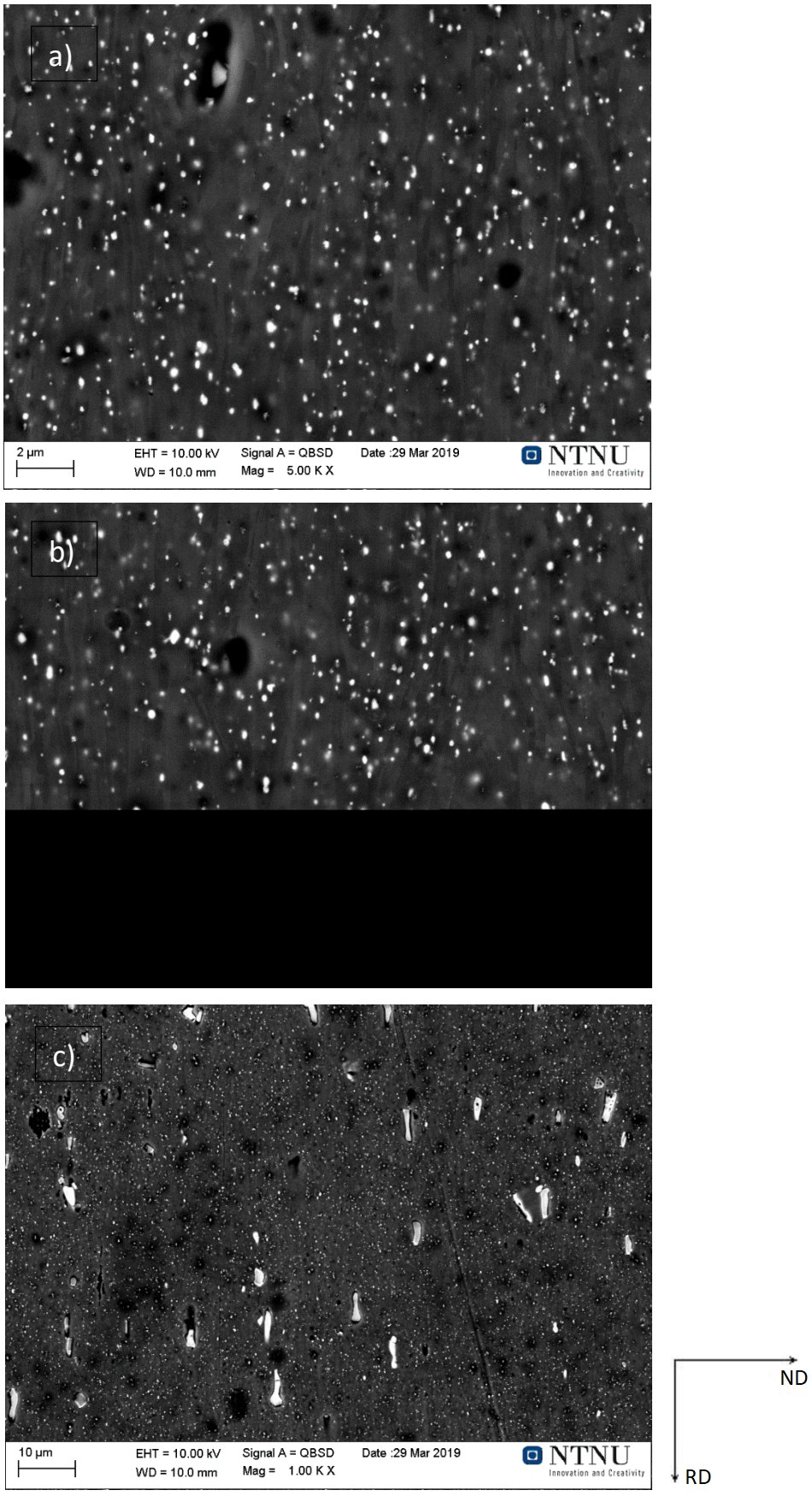

Figure D.7: SEM-BSE image of dispersoids present in %CR87-180 taken at (a) – (b) 5000x and (c) 1000x.

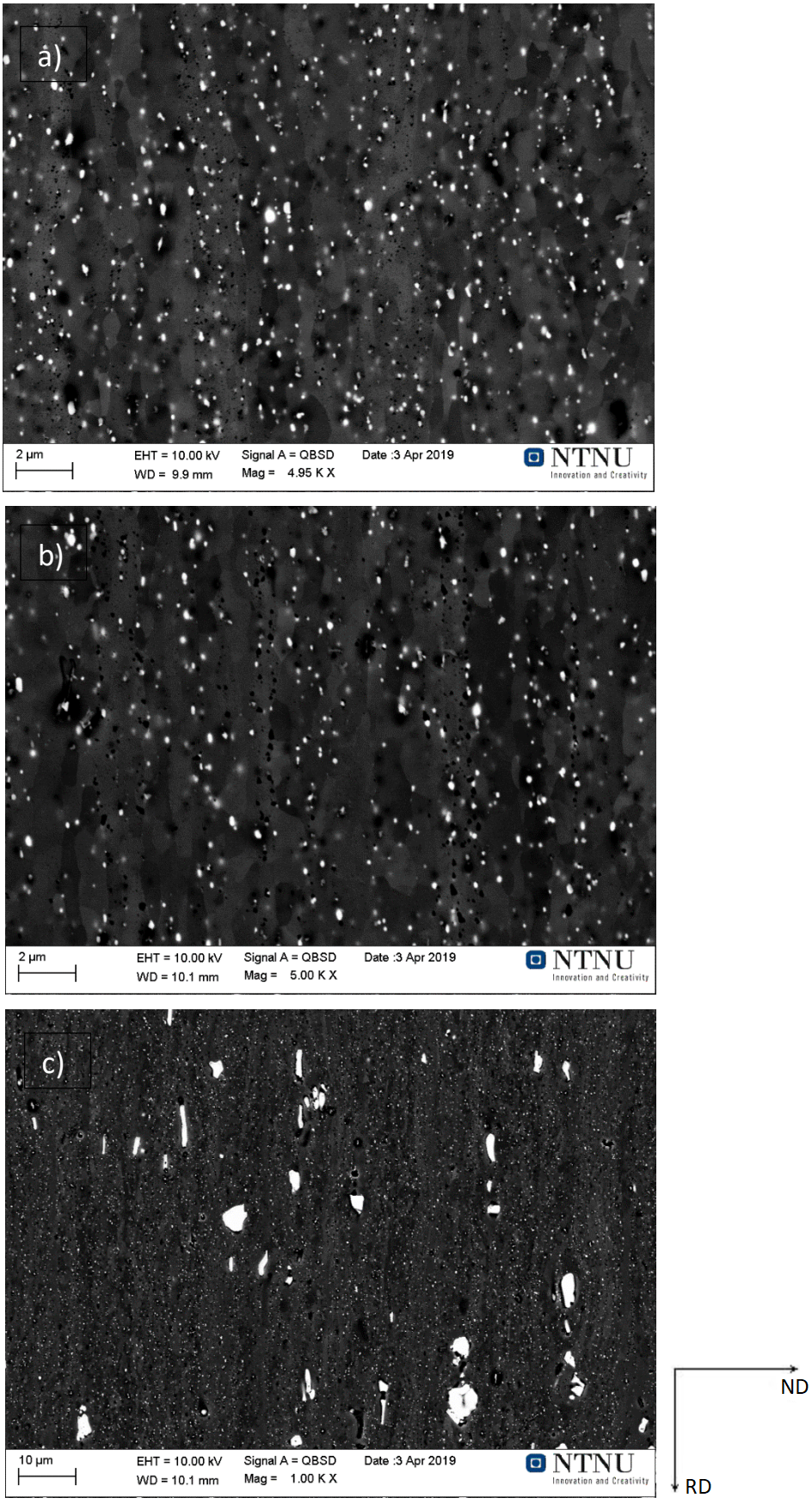

Figure D.8: SEM-BSE image of dispersoids present in %CR46-280 taken at (a) – (b) 5000x and (c) 1000x.

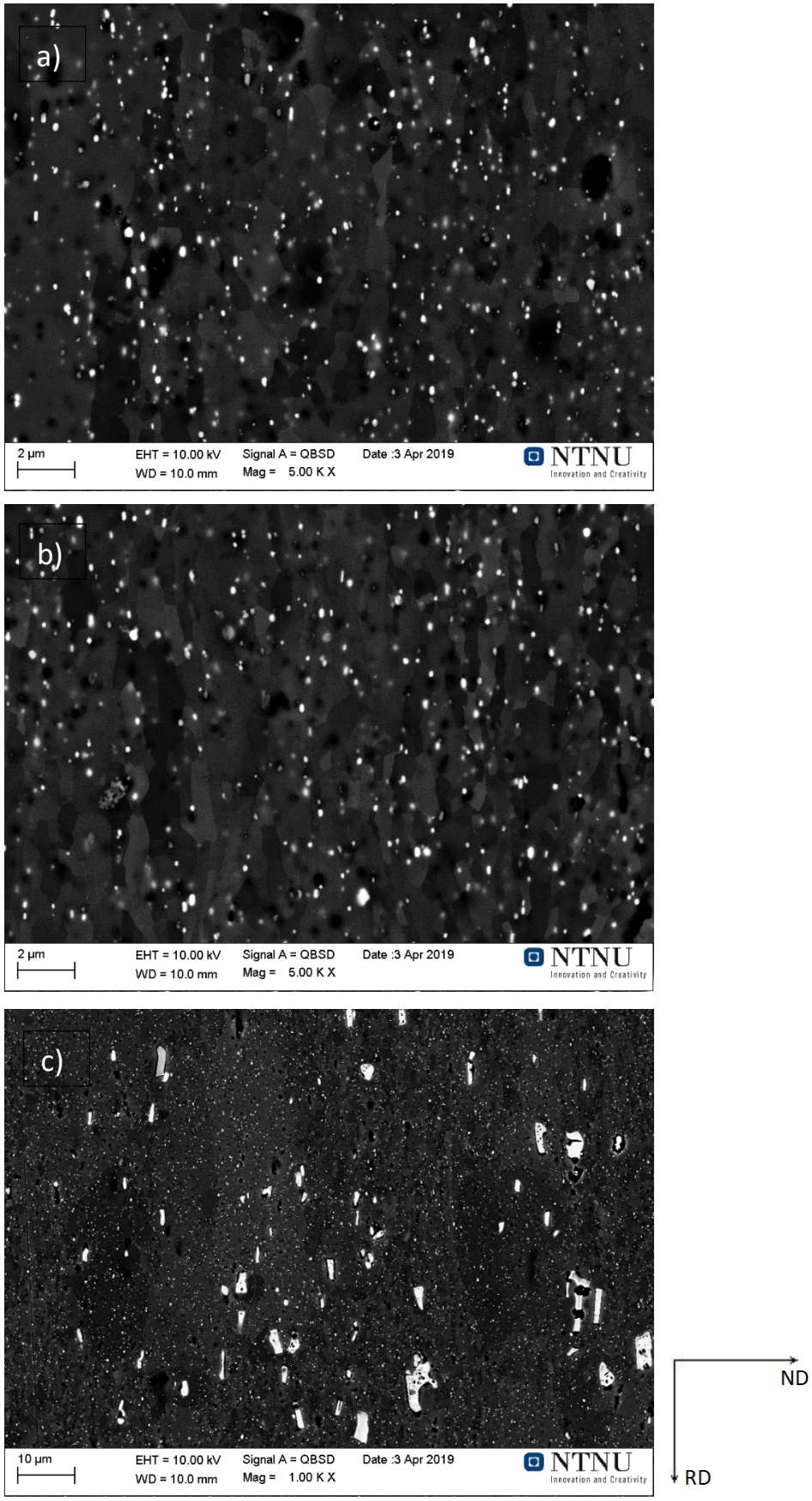

Figure D.9: SEM-BSE image of dispersoids present in %CR67-280 taken at (a) – (b) 5000x and (c) 1000x.

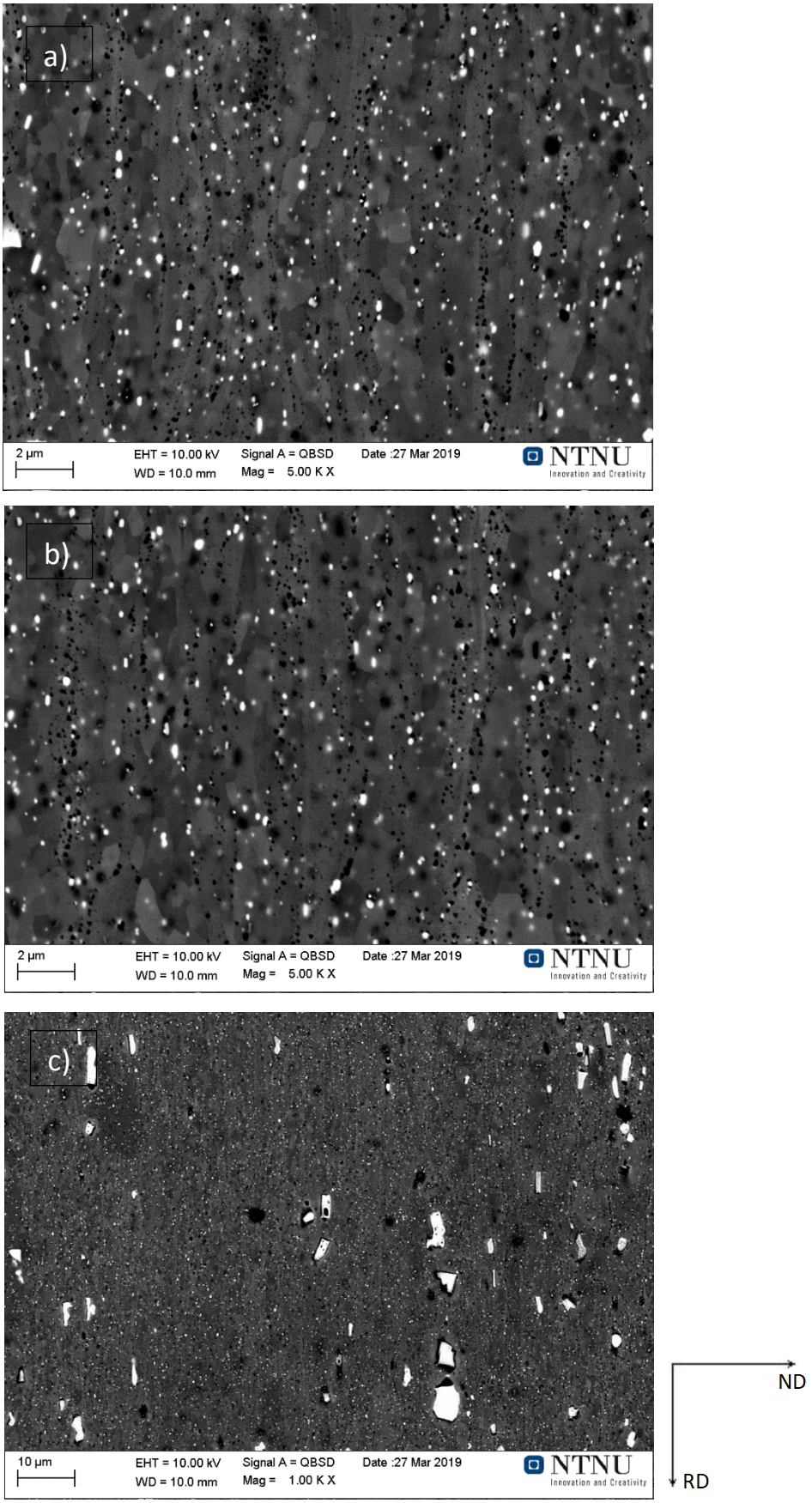

Figure D.10: SEM-BSE image of dispersoids present in %CR87-280 taken at (a) – (b) 5000x and (c) 1000x.

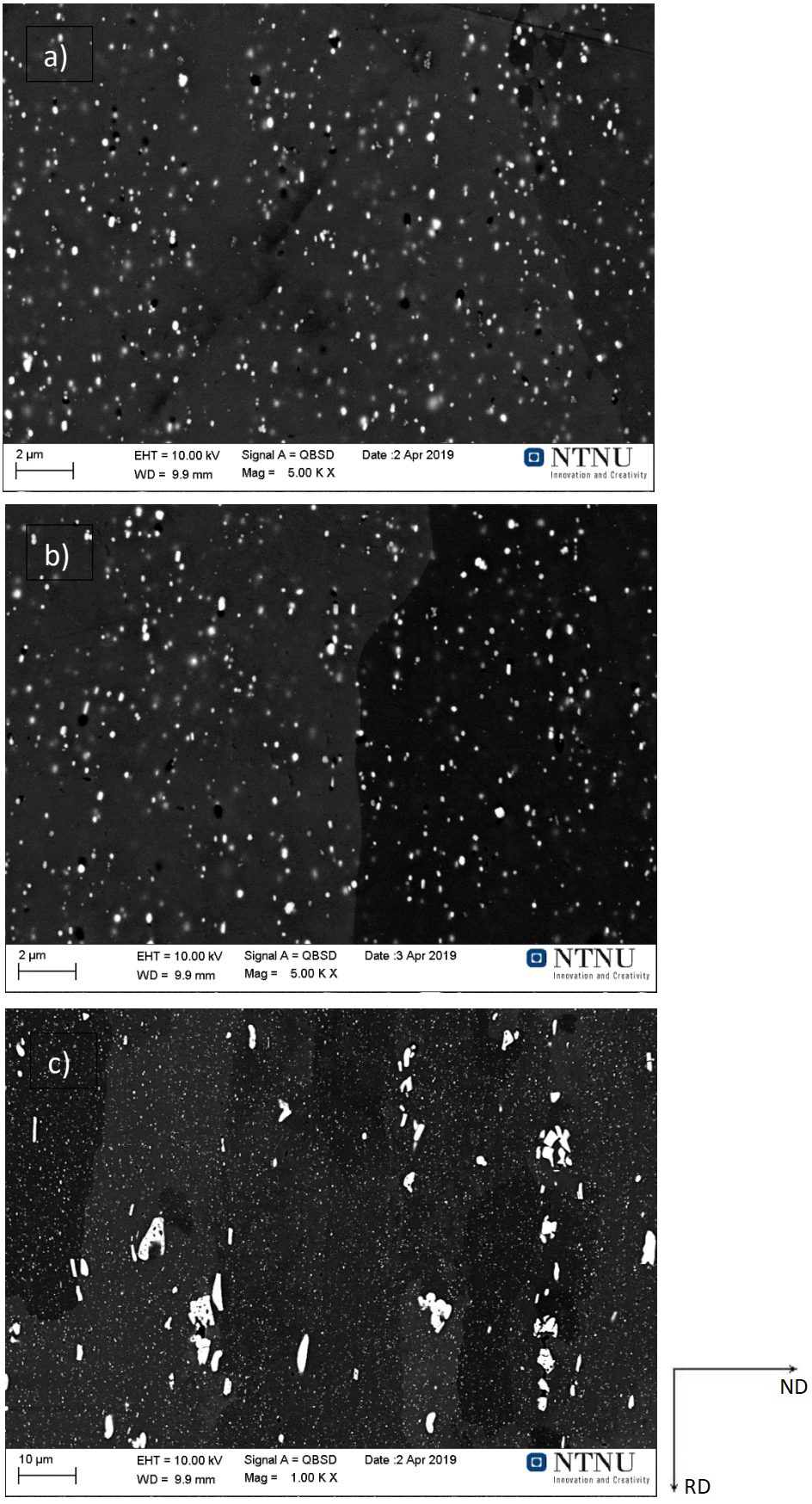

Figure D.11: SEM-BSE image of dispersoids present in %CR46-330 taken at (a) – (b) 5000x and (c) 1000x.

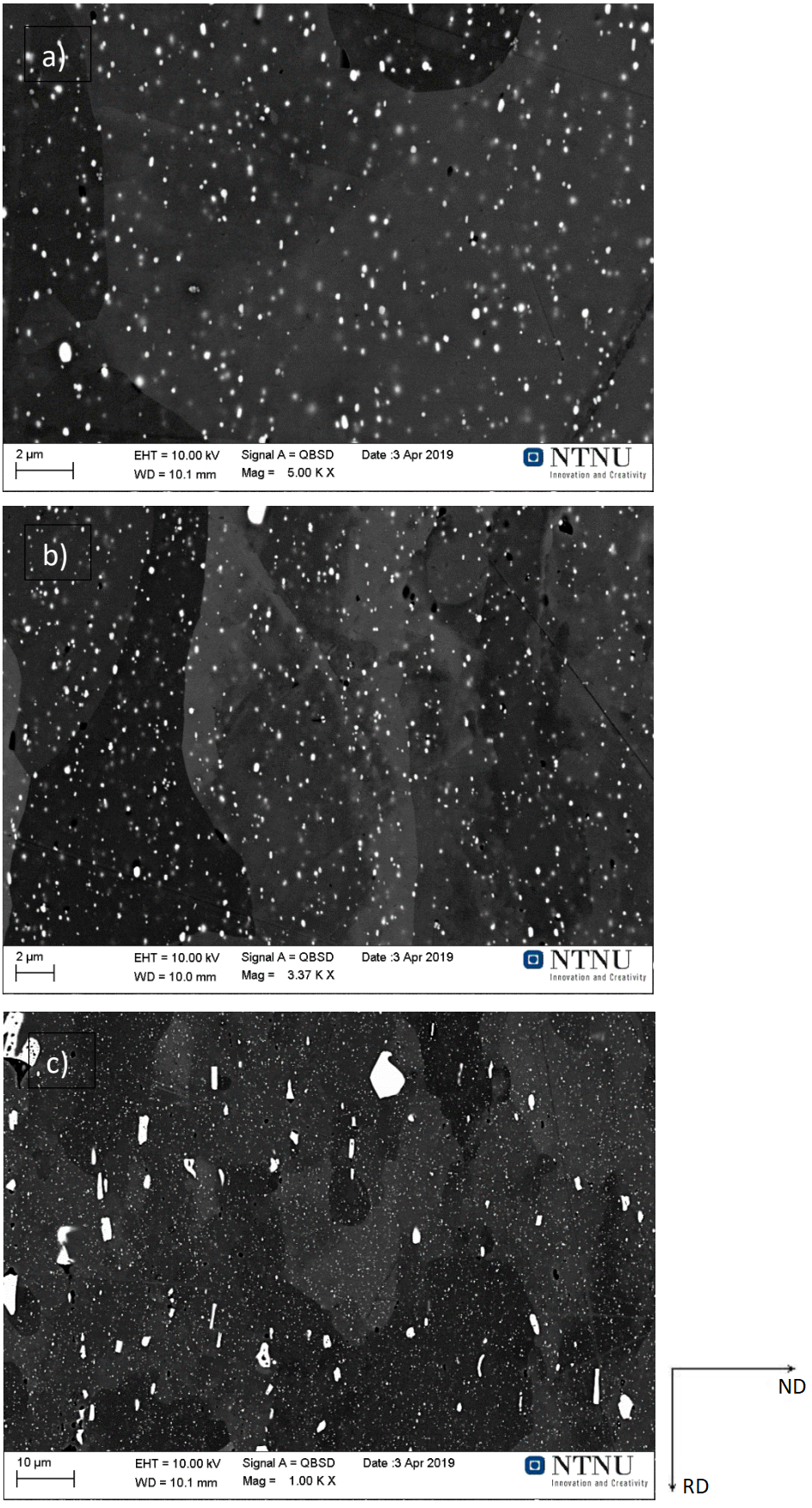

Figure D.12: SEM-BSE image of dispersoids present in %CR67-330 taken at (a) 5000x, (b) 3370x and (c) 1000x.

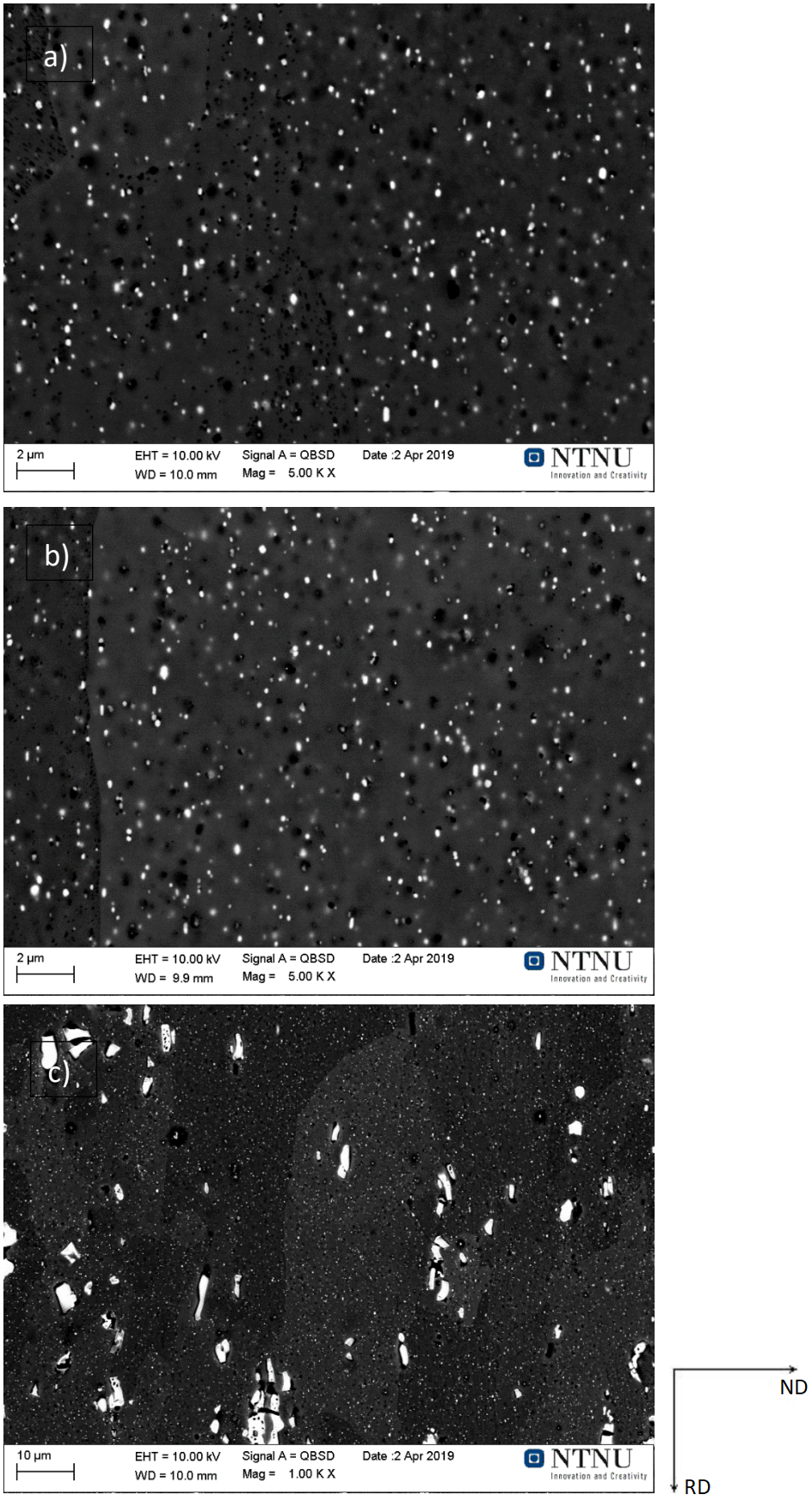

Figure D.13: SEM-BSE image of dispersoids present in %CR87-330 taken at (a) – (b) 5000x and (c) 1000x.

D.2 Python Script

The SEM-BSE images was analysed with Python, as described in Section 3.4.1. The script calculated the mean particle diameter, particle density, particle area and particle distribution.

```
import os
import numpy as np
import matplotlib.pyplot as plt
import pandas as pd
import scipy.optimize as sco
import scipy.special as scs
from skimage.filters import sobel
from skimage.color import rgb2gray, label2rgb
from skimage.exposure import rescale_intensity
from skimage import morphology
from skimage import measure
from scipy import ndimage as ndi

newparams = {'figure.figsize': (15, 7), 'axes.grid': False,
             'lines.markersize': 10, 'lines.linewidth': 2,
             'font.size': 15, 'figure.dpi': 200}
plt.rcParams.update(newparams)

# Read data from file
data = 'C:/Users/eirik/OneDrive/Documents/Python Scripts/5000x_3.tif'
datadir, fname = os.path.split(data)
fname, ext = os.path.splitext(fname)
bse = plt.imread(data)

# Crop away lower part with image data and NTNU logo
bse = bse[:691]

# Convert image to grayscale and 8 bit [0, 255] (don't need that high
depth)
bse = rgb2gray(bse)
bse = rescale_intensity(bse, out_range=np.uint8)
```

```
# Inspect image
plt.imshow(bse, cmap=plt.cm.inferno)
plt.colorbar();

# %% Elevation Map

elevation_map = sobel(bse)

plt.imshow(elevation_map, cmap=plt.cm.inferno)
plt.colorbar();

# %% Find markers

markers = np.zeros_like(bse)
markers[bse < 110] = 1
markers[bse > 120] = 2

plt.imshow(markers,                          cmap=plt.cm.nipy_spectral,
interpolation='nearest')
plt.colorbar();

# %% Water Shed
segmentation = morphology.watershed(elevation_map, markers)

plt.imshow(segmentation, cmap=plt.cm.gray, interpolation='nearest')
plt.colorbar();

# %% Segmentation

segmentation2 = ndi.binary_fill_holes(segmentation - 1)
labeled_particles, n = ndi.label(segmentation2)

print("{} particles were segmented.".format(n))
```

```
# Inspect segmentation
plt.imshow(bse, cmap=plt.cm.gray, interpolation='nearest')
plt.colorbar()
plt.contour(segmentation, linewidths=0.5, colors='r');

# %% Get properties of labeled regions
props = measure.regionprops(labeled_particles, intensity_image=bse)

# Initiate data frame with columns for properties of interest
props_columns = ['pixels', 'equivalent_diameter', 'eccentricity',
'perimeter',
                 'ellipse_major_axis',         'ellipse_minor_axis',
'centroid']
particles = pd.DataFrame(columns=props_columns)

# Image scale
scale = (1/45)*1e3  # [nm/px]

for region in props:
    particles.loc[len(particles)] = [region.area,
                                     region.equivalent_diameter    *
scale,
                                     region.eccentricity,
                                     region.perimeter * scale,
                                     region.major_axis_length      *
scale,
                                     region.minor_axis_length      *
scale,
                                     region.centroid]

# Remove too small particles
particles = particles[particles['pixels'] > 5]
particles = particles[particles['eccentricity'] >= 0]

n_new = len(particles)
```

```
print("{}/{} particles were removed after filtering on pixels and
eccentricity.".format(n - n_new, n))


# Set derived properties

particles['area'] = particles.pixels.values * scale**2

particles['circularity']                                                =
4*np.pi*particles.area.values/particles.perimeter.values**2


particles.sort_values(by='area', inplace=True)

particles.reset_index(inplace=True, drop=True)


# %%

particles = particles[particles['circularity'] > 0.1

                      ]


n_new2 = len(particles)

print("{}/{}   particles   were   removed   after   filtering   on
circularity.".format(n_new - n_new2, n_new))


# Plot inverse intensity map

plt.imshow(bse, cmap=plt.cm.gray_r, interpolation='nearest')

plt.colorbar()

plt.contour(segmentation, linewidths=0.5, colors='r');


for i, (x, y) in enumerate(particles.centroid.values):

    plt.text(y, x, s='%i' % i, fontdict={'size': 8})


    # %% Particle Size


def gamma(x, a, b):

    return b**a/scs.gamma(a)*x**(a - 1)*np.exp(-b*x)



def lognormal(x, s, m):

    return     1/(s*x*np.sqrt(2*np.pi))*np.exp(-0.5*((np.log(x)     -
m)/s)**2)
```

```
# Plot results
bin_width = 25
x_max = np.max(particles.equivalent_diameter)
num_bins = int(x_max/bin_width + 1)

# Frequency weighted particle
hist, bins = np.histogram(particles.equivalent_diameter, bins=num_bins)
centre = (bins[:-1] + bins[1:])/2

# Fit curve
#x_curves = np.linspace(particles.equivalent_diameter.min(),
#                       particles.equivalent_diameter.max(), 100)
#popt, pcov = sco.curve_fit(gamma, xdata=centre, ydata=hist, bounds=(0, 10))
#hist_fit = gamma(x_curves, *popt)

# Normalised area weighted particle size
hist_area, bins_area = np.histogram(particles.equivalent_diameter,
                                    bins=num_bins,
weights=particles.area,
                                    density=True)
hist_norm_area = hist_area/np.sum(hist_area)
centre_area = (bins_area[:-1] + bins_area[1:])/2

# Mean diameter and standard deviation
ecd_mean = particles.equivalent_diameter.mean()
ecd_std = particles.equivalent_diameter.std()

print("Mean diameter = {:.3E}nm\nSTD diameter = {:.2f}nm".format(ecd_mean, ecd_std))
# Plotting
bar_width = 0.8*bin_width
bar_align = 'center'
label_mean = r'$\bar{\delta}_{\mathrm{ECD}}$ = %i nm' % ecd_mean
```

```
# Frequency weighted

fig, ax = plt.subplots(figsize=(12, 5))

#label_fit = r'$\Gamma$ fit: $\alpha$ = %.2f, $\beta$ = %.2f' %
(popt[0], popt[1])

ax.bar(centre, hist, width=bar_width, align=bar_align)

ax.plot([ecd_mean, ecd_mean], [0, hist.max()], 'r', label=label_mean)

#ax.plot(x_curves, hist_fit, '-r', linewidth=3, label=label_fit)

ax.set_xlabel(r'Particle size $\delta_{\mathrm{ECD}}$ [nm]')

ax.set_ylabel('Frequency weighted')

ax.legend()

#plt.savefig(os.path.join(datadir,        'particle_size_freq.png'),
dpi=300,

#            bbox_inches='tight')

# Normalised area weighted

fig, ax = plt.subplots(figsize=(12, 5))

ax.bar(centre_area, hist_norm_area, width=bar_width, align=bar_align)

ax.plot([ecd_mean,   ecd_mean],   [0,   hist_norm_area.max()],   'r',
label=label_mean)

ax.set_xlabel(r'Particle size $\delta_{\mathrm{ECD}}$ [nm]')

ax.set_ylabel('Area weighted volume fraction')

ax.legend();

#plt.savefig(os.path.join(datadir,        'particle_size_area.png'),
dpi=300,

#           bbox_inches='tight')


# %% Image area

image_area = bse.size * scale**2 * 1e-12  # [mm^2]


# Density

density_frequency = len(particles) / image_area  # [#/mm^2]

density_area = 100*particles.pixels.sum() / bse.size  # [%]

print("Particle   density   =   {:.3E}   #/mm^2\nParticle   area   =
{:.2f}%".format(density_frequency,


density_area))
```

D.3 Particle Distributions

The particle distributions from the particle analysis for all samples (5000x) studies in SEM are presented below.

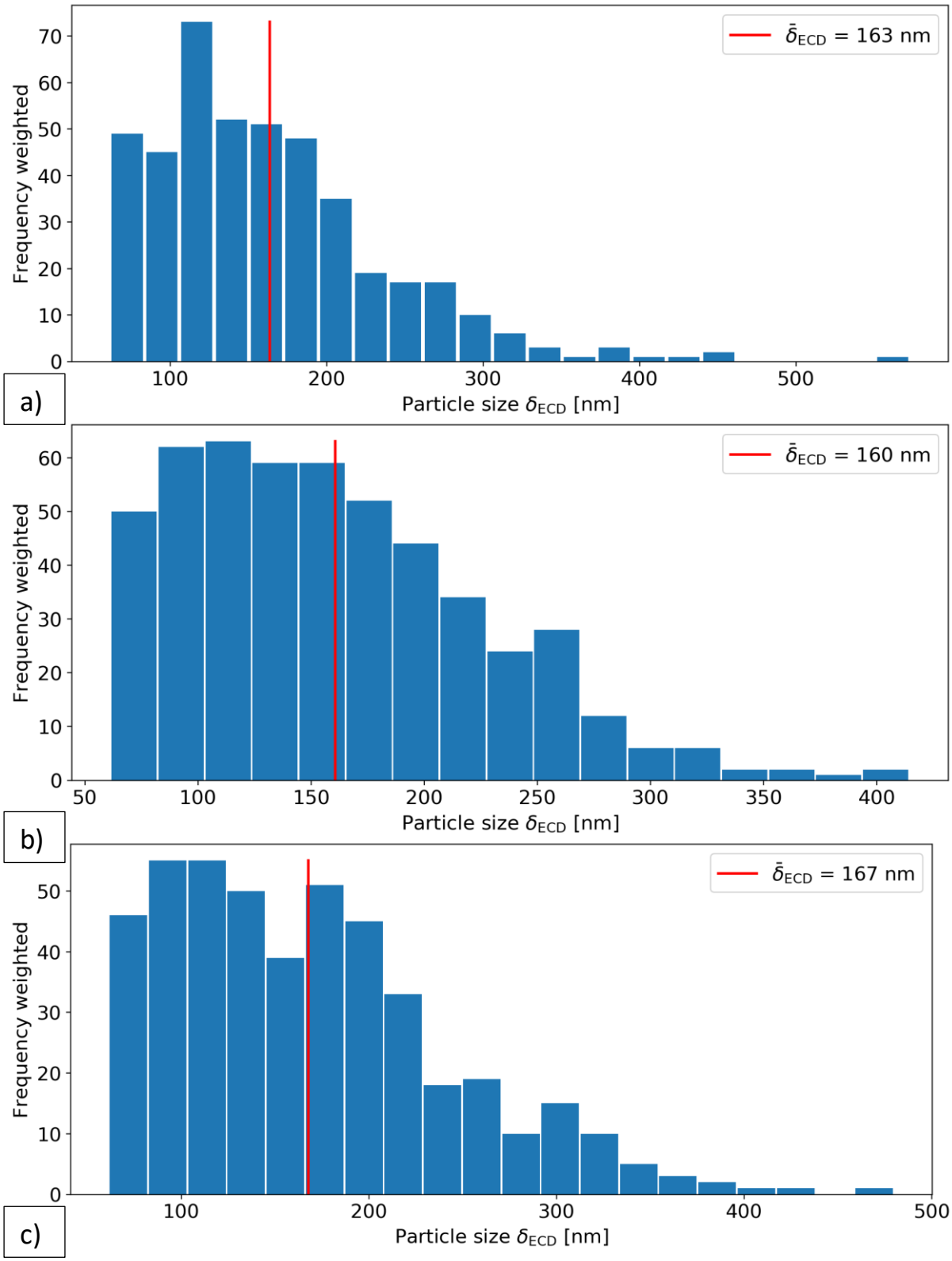

Figure D.14: Particle distribution of the images taken of HR.

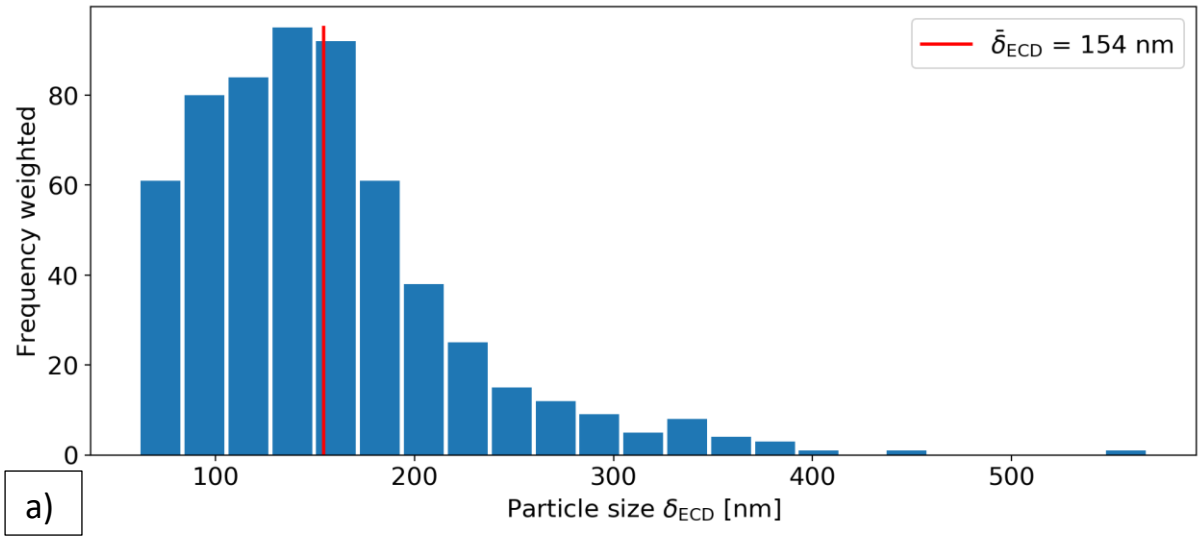

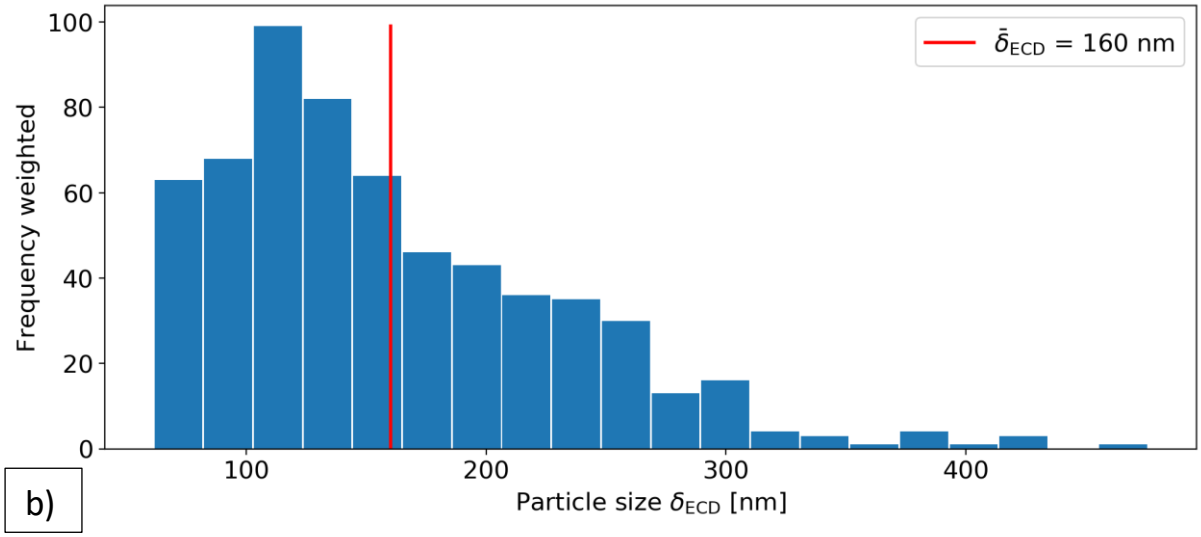

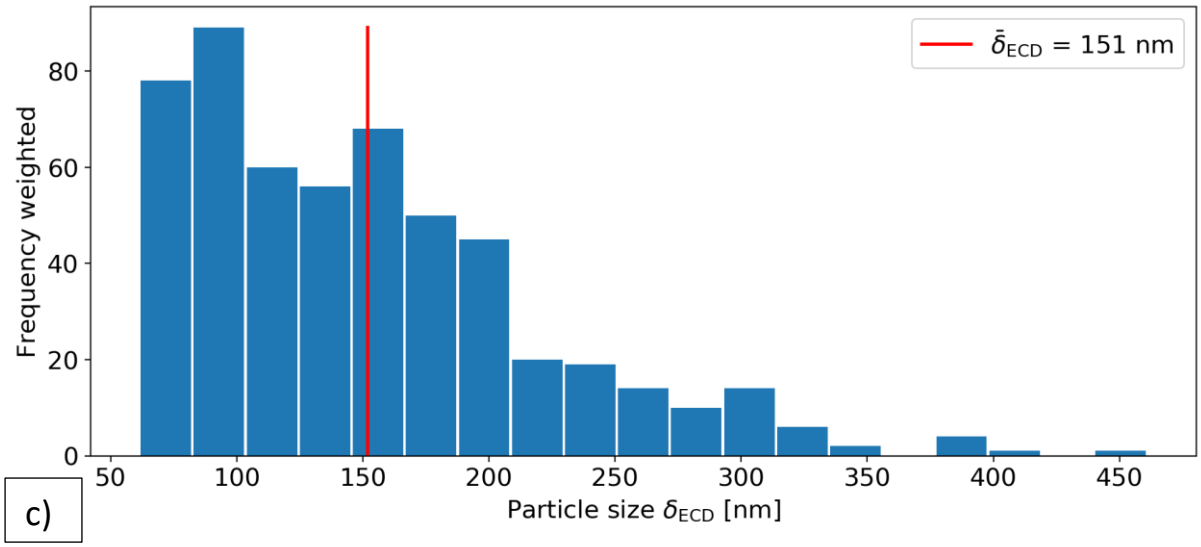

Figure D.15: Particle distribution of the images taken of %CR46.

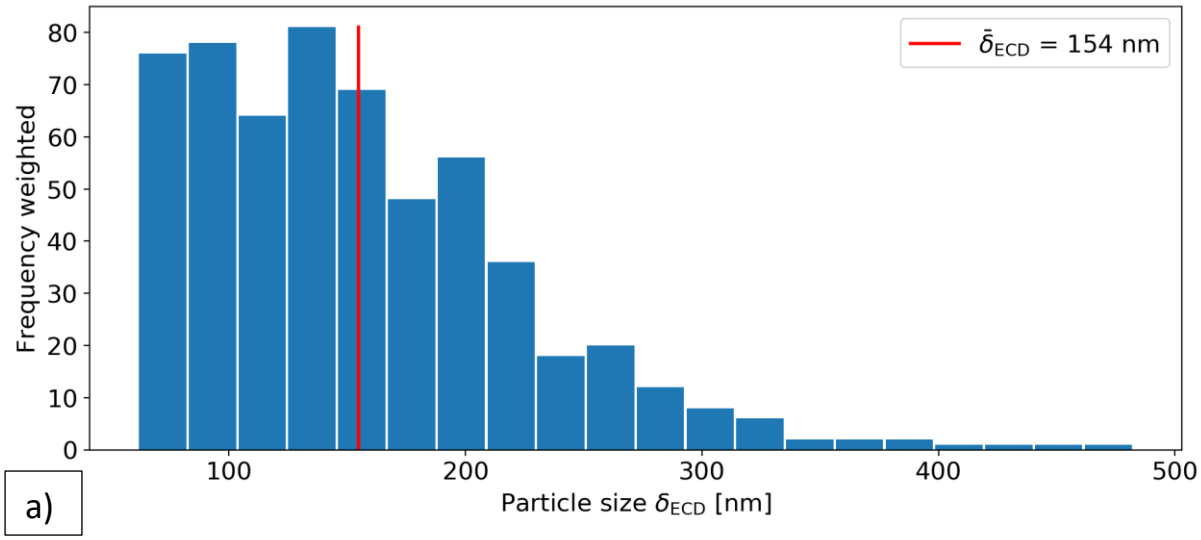

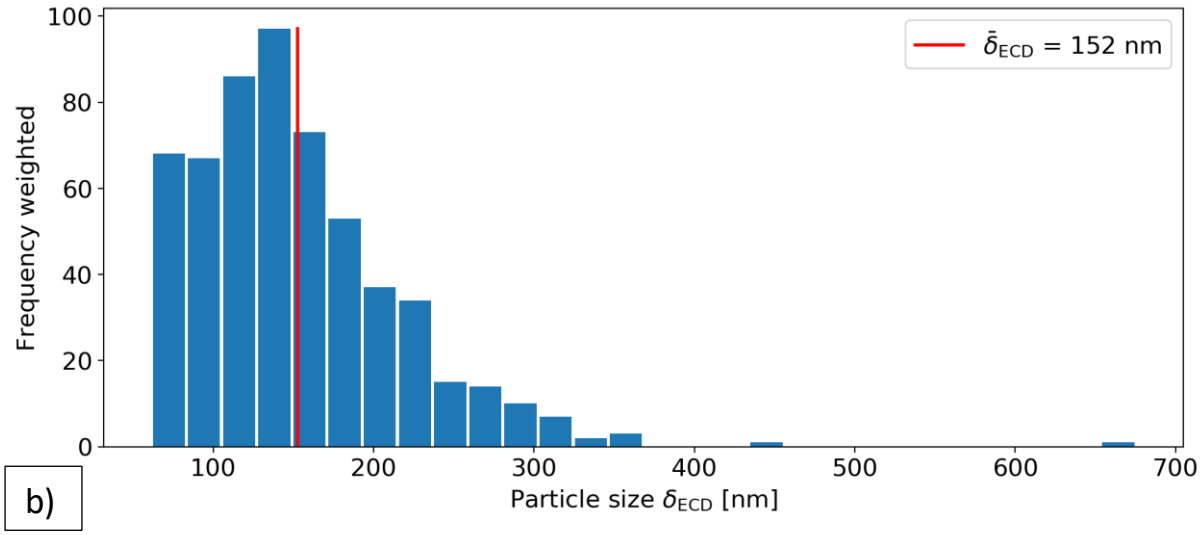

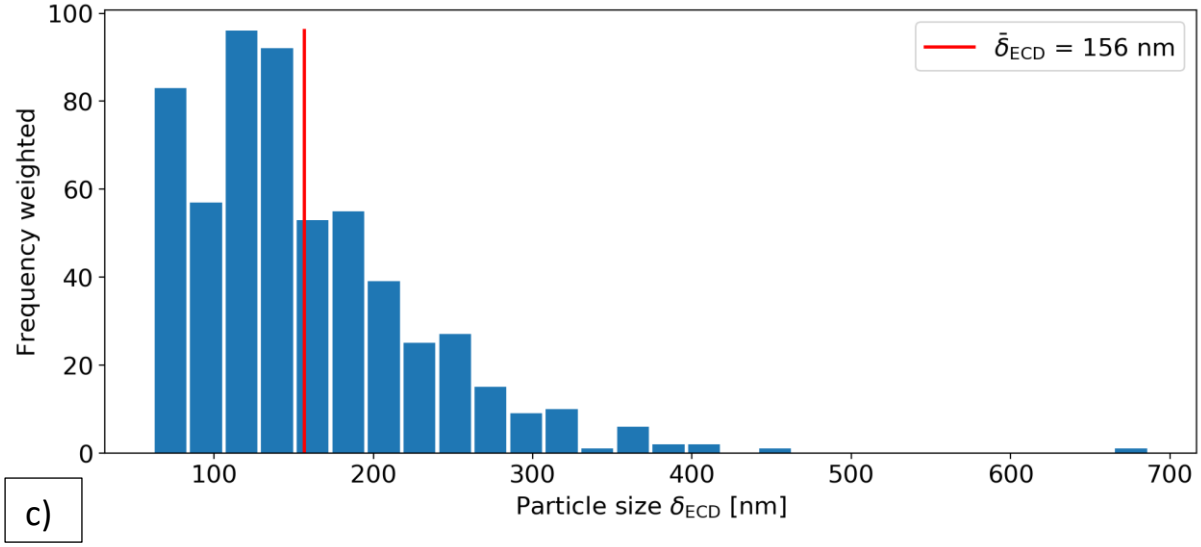

Figure D.16: Particle distribution of the images taken of %CR67.

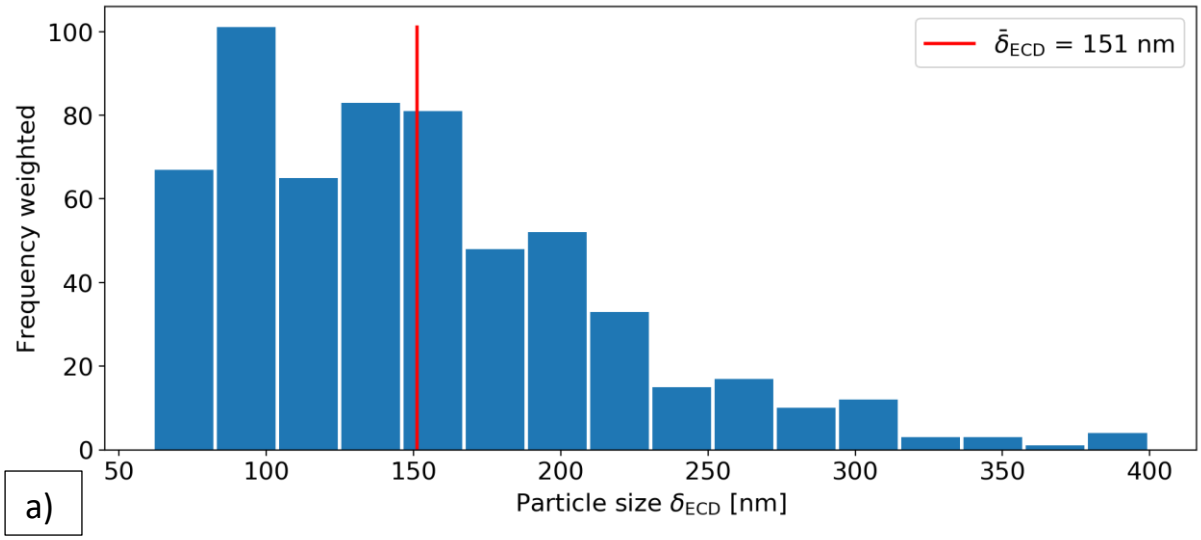

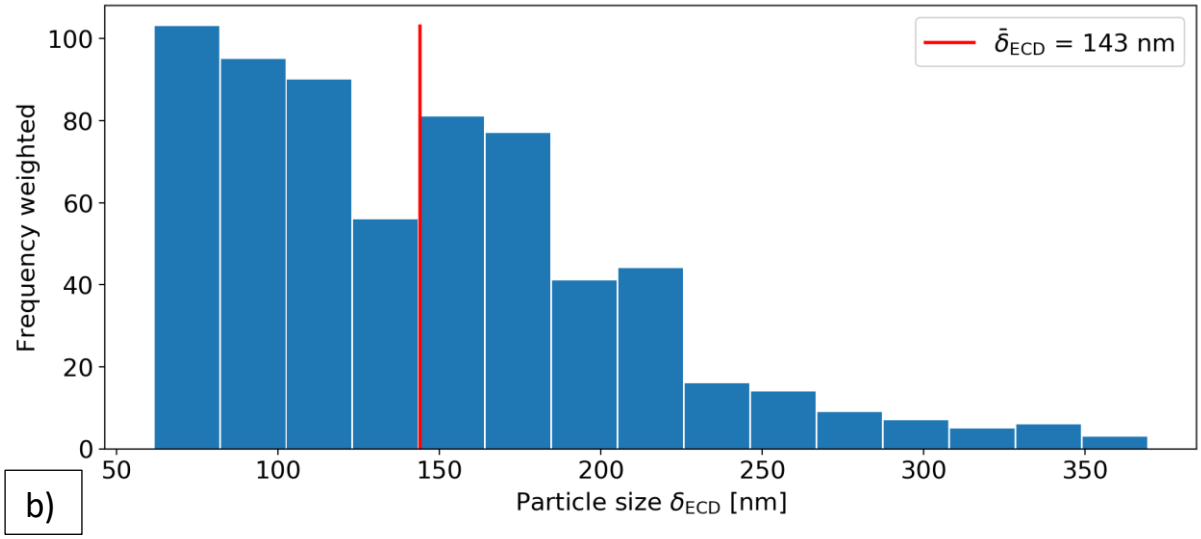

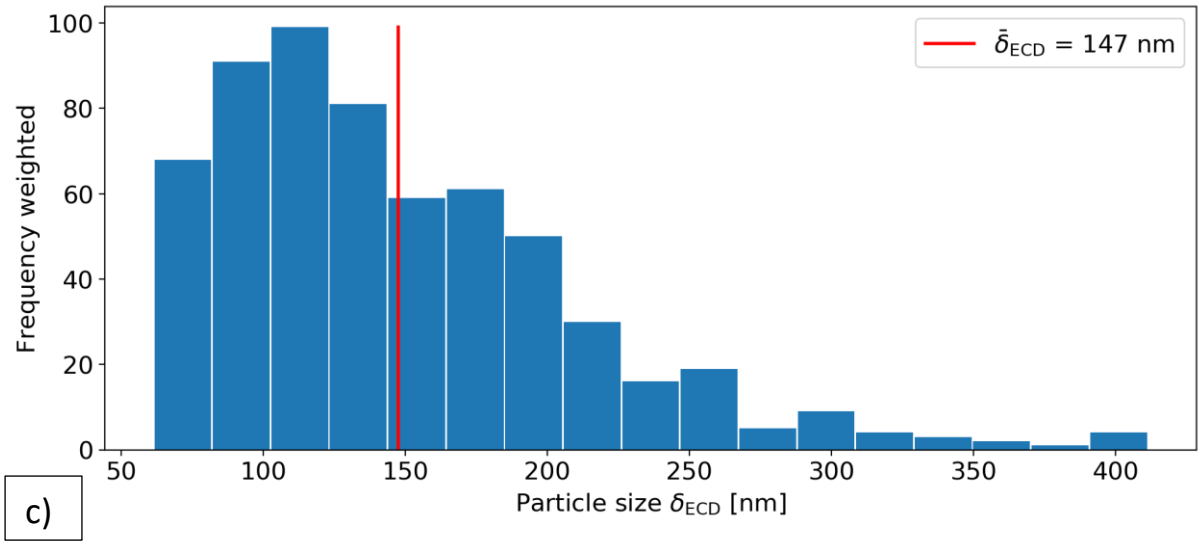

Figure D.17: Particle distribution of the images taken of %CR87.

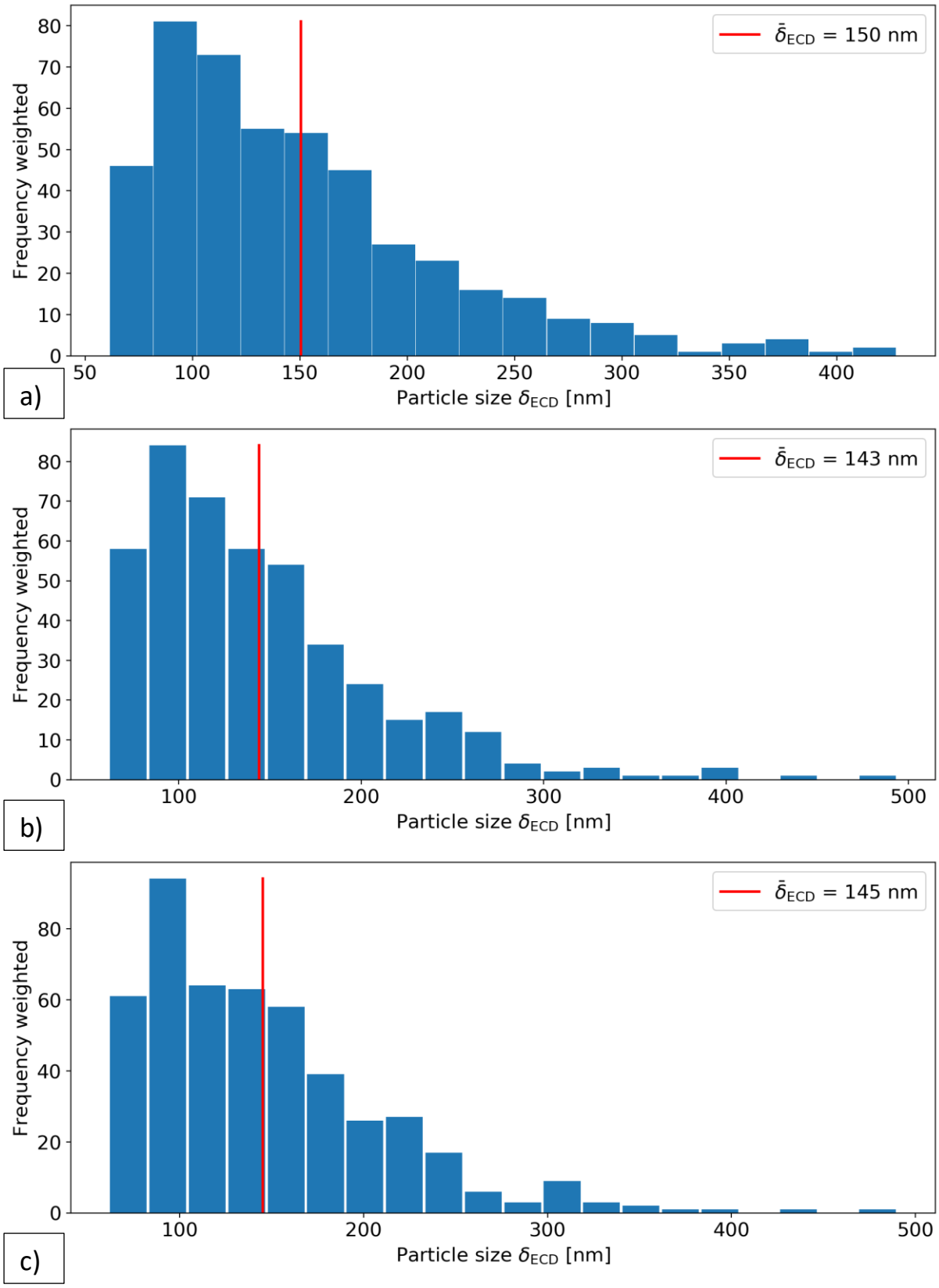

Figure D.18: Particle distribution of the images taken of %CR46-180.

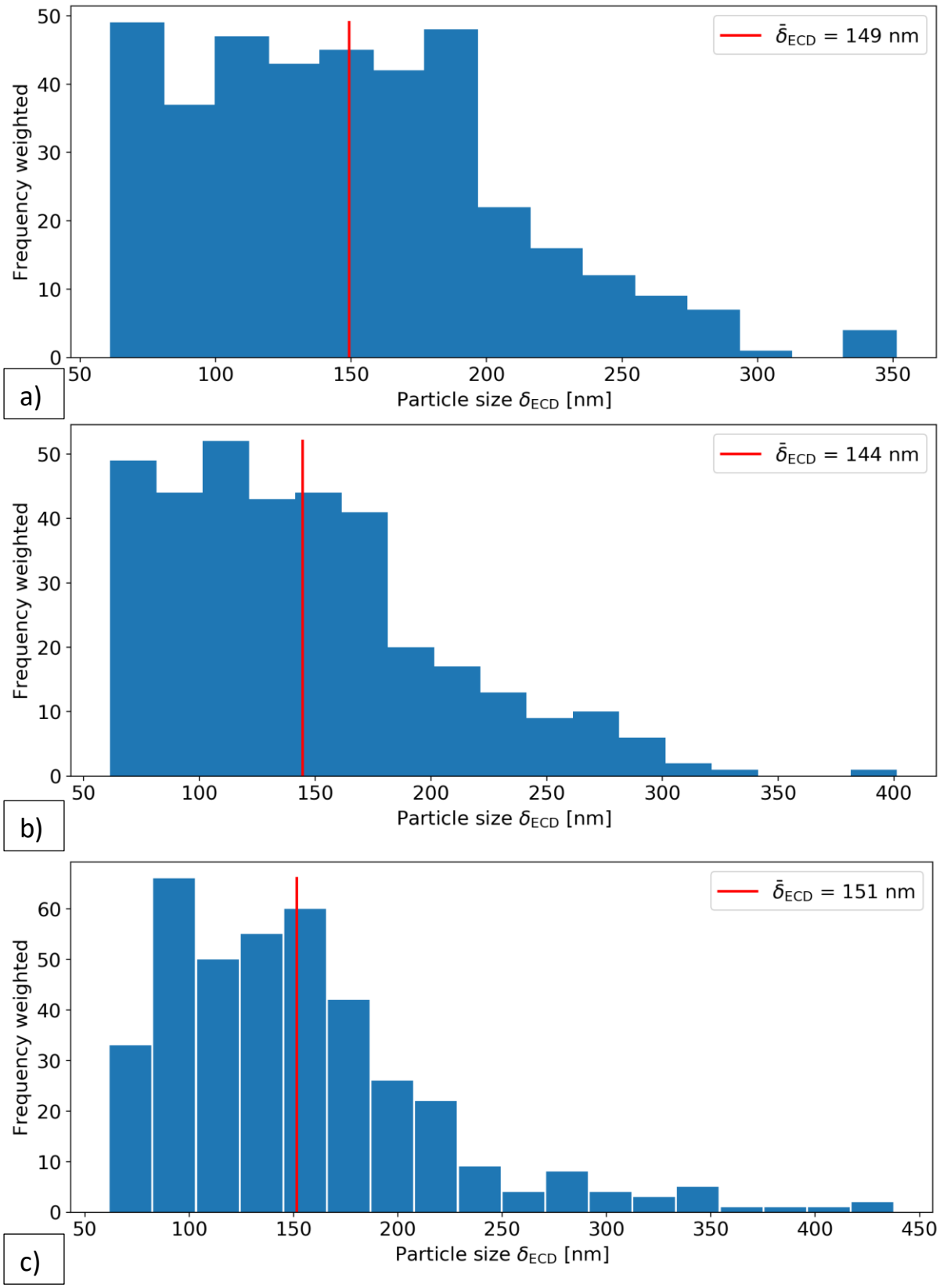

Figure D.19: Particle distribution of the images taken of %CR67-180.

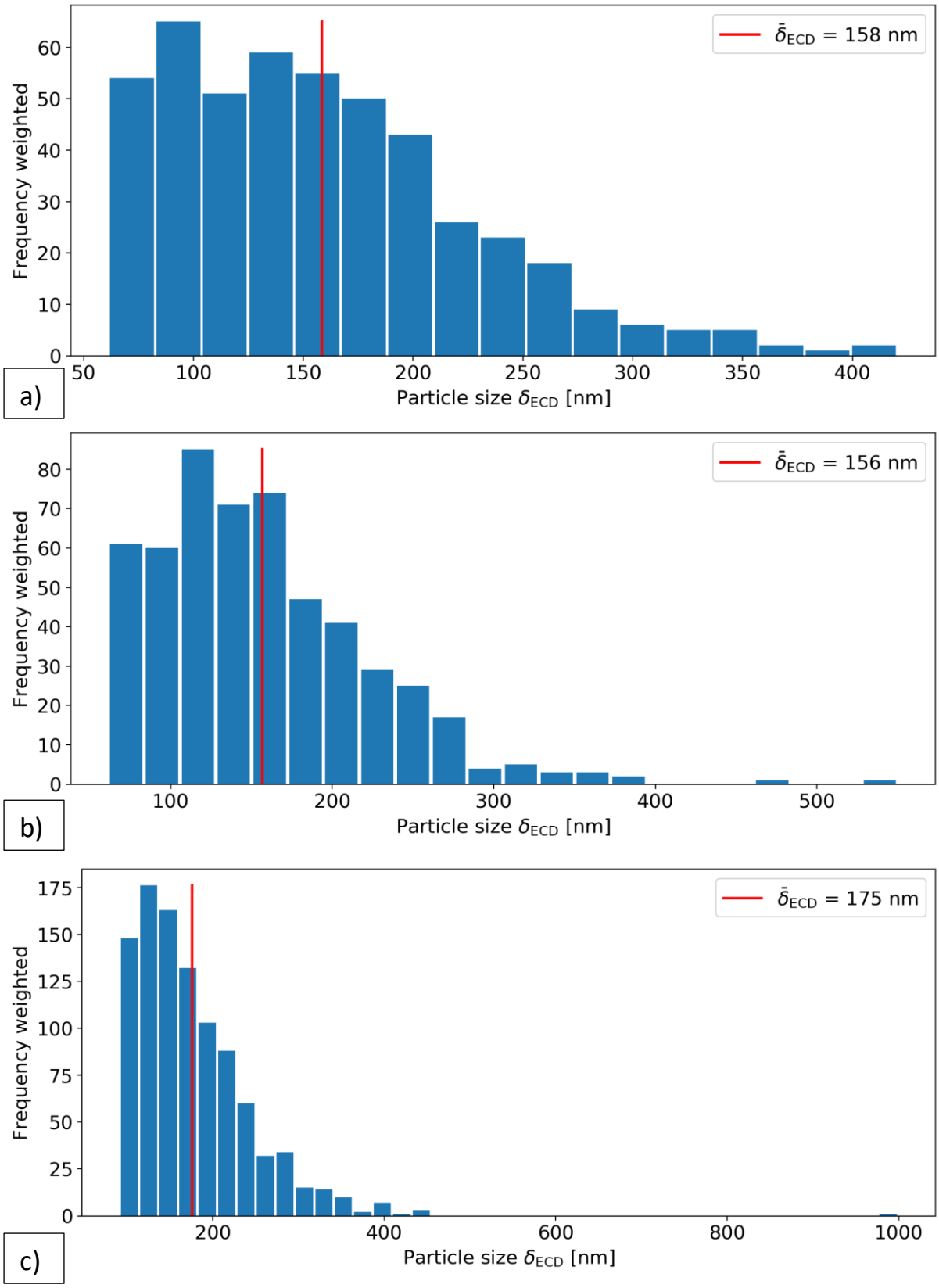

Figure D.20: Particle distribution of the images taken of %CR87-180.

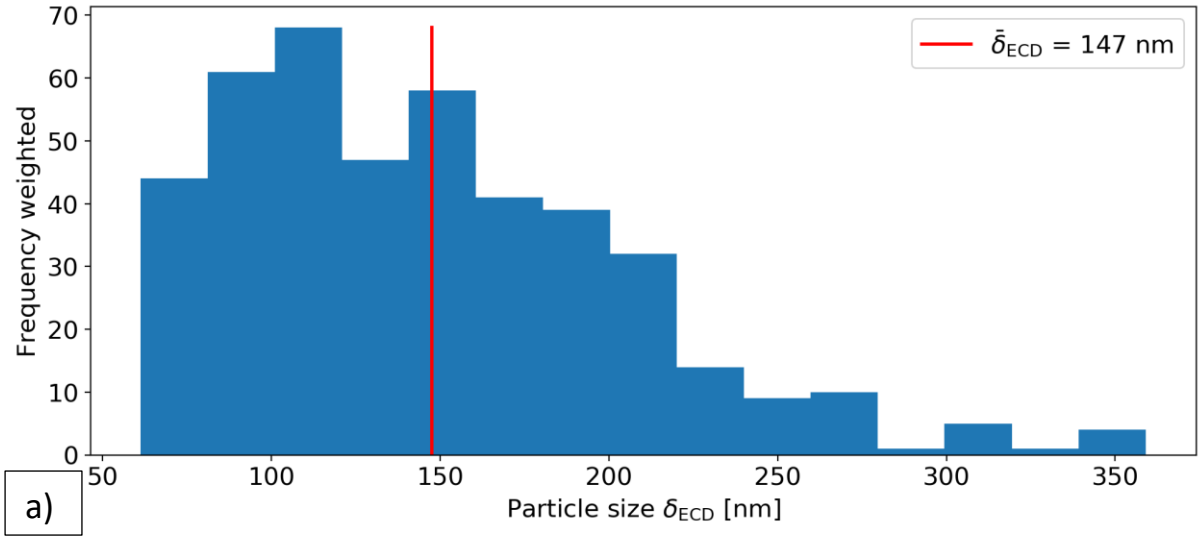

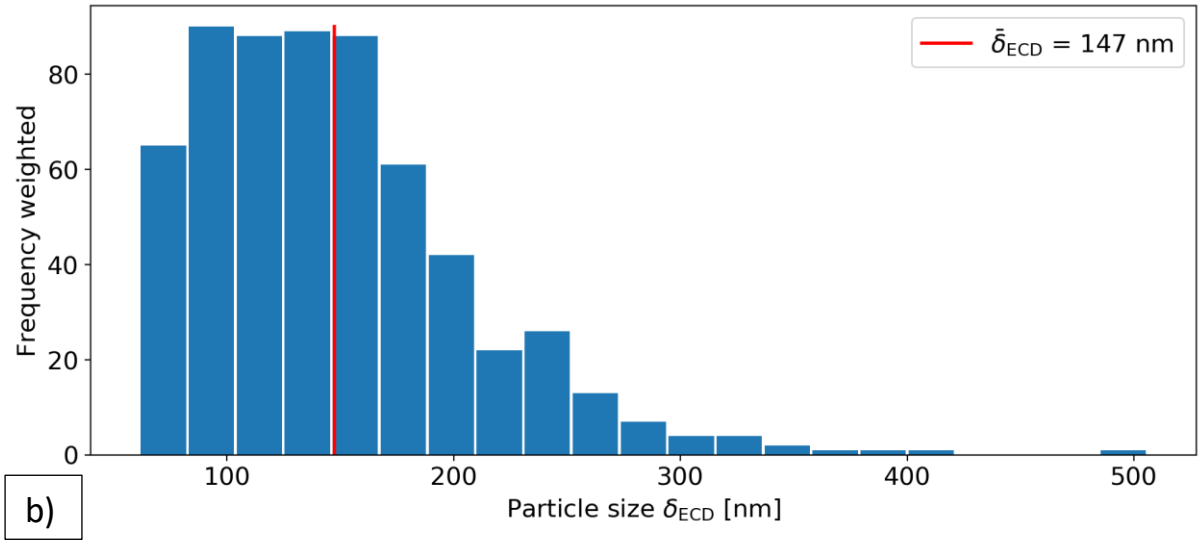

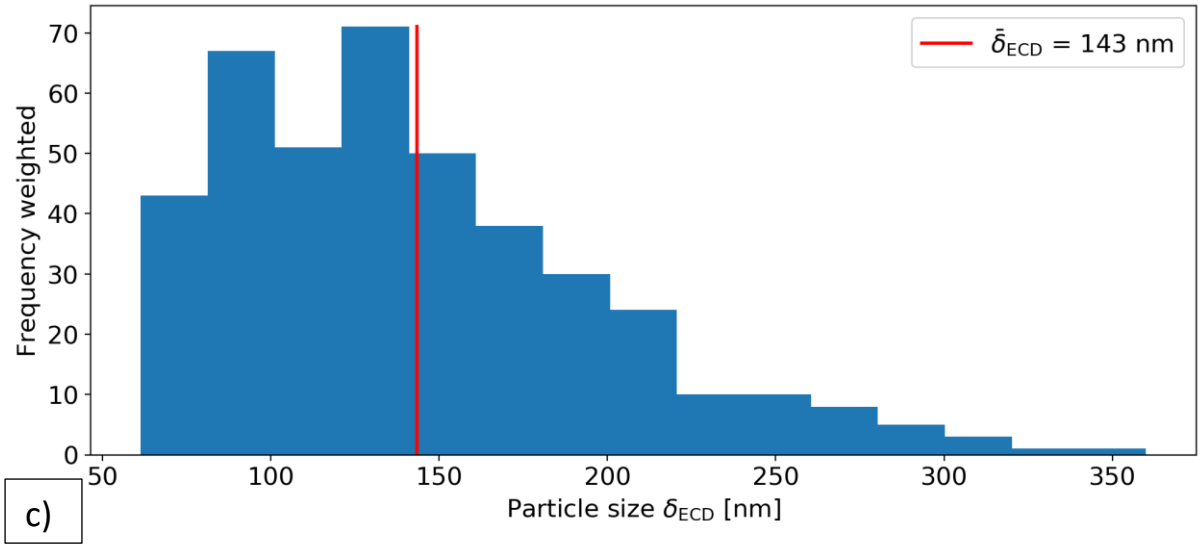

Figure D.21: Particle distribution of the images taken of %CR46-280.

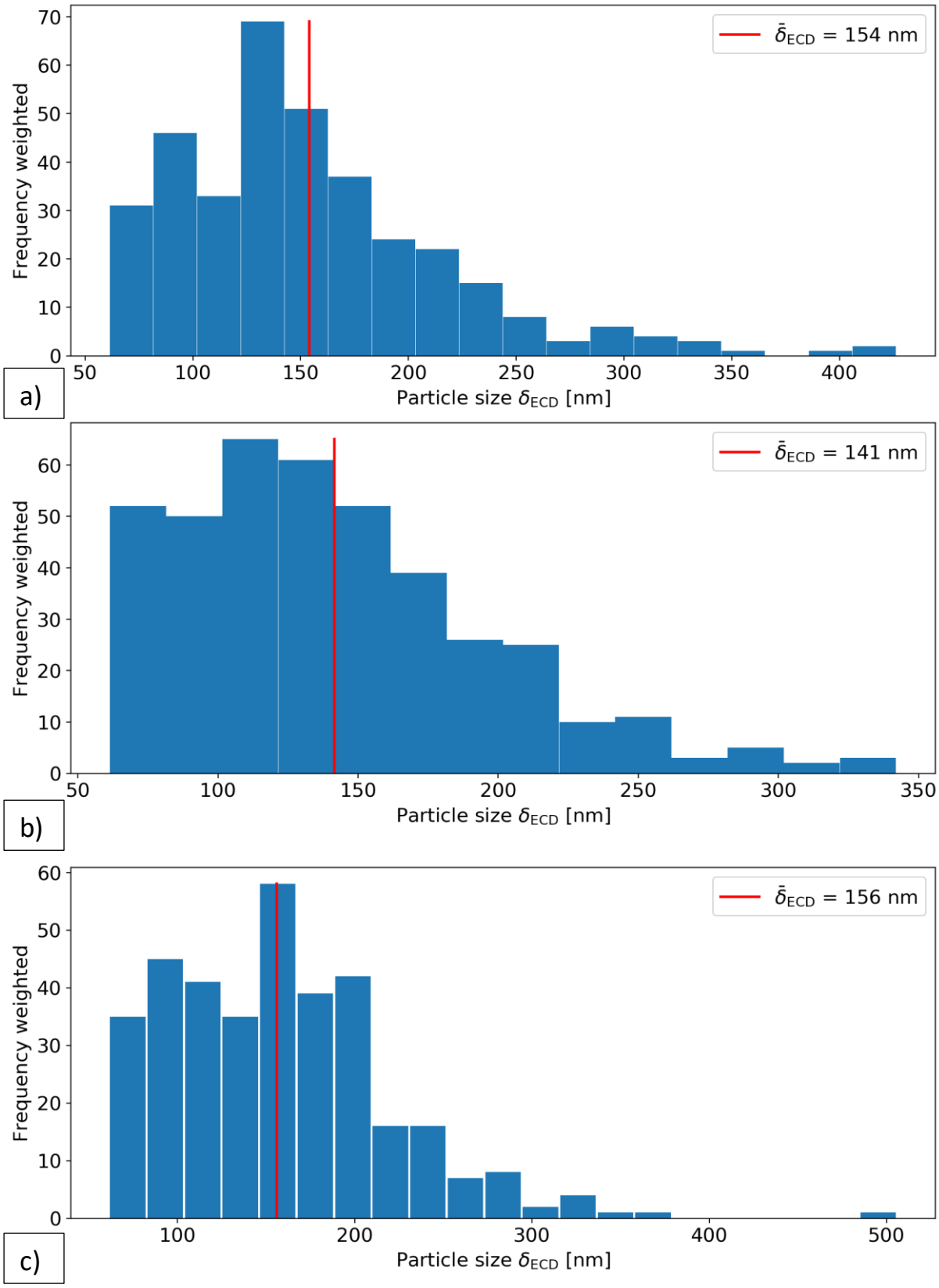

Figure D.22: Particle distribution of the images taken of %CR67-280.

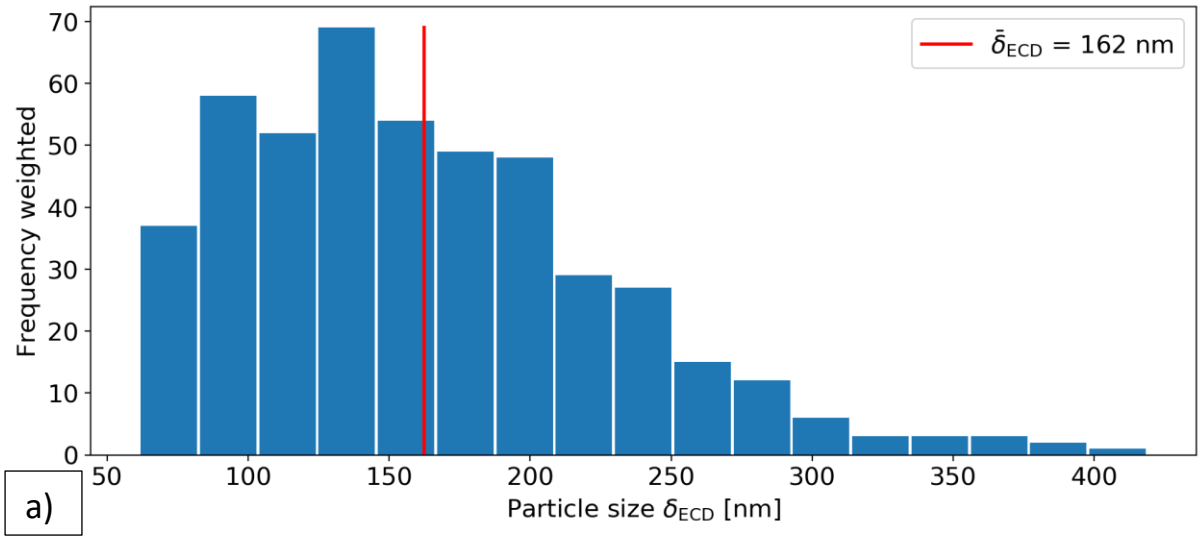

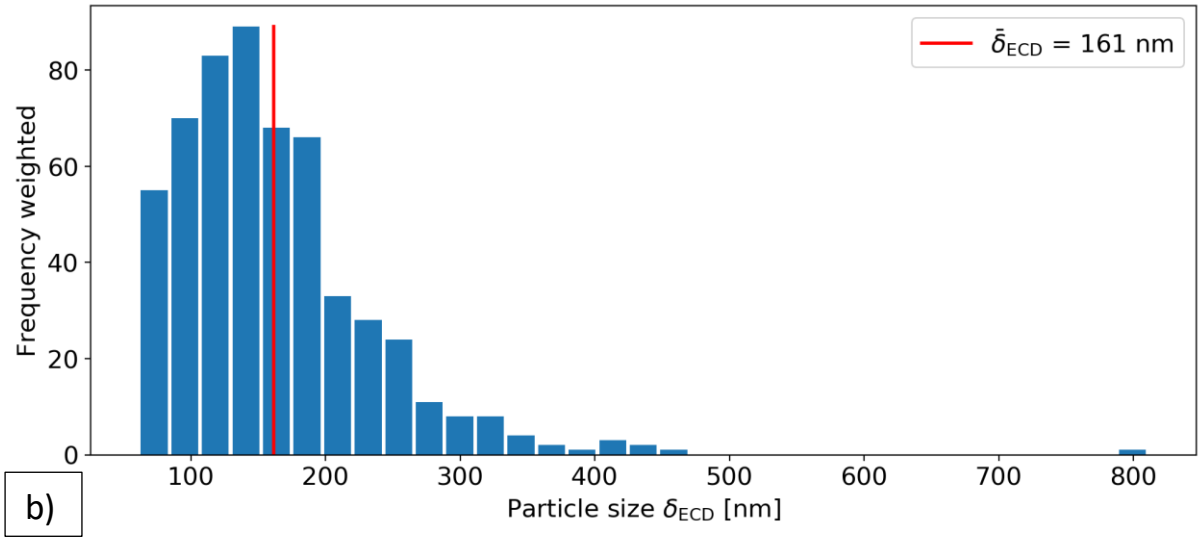

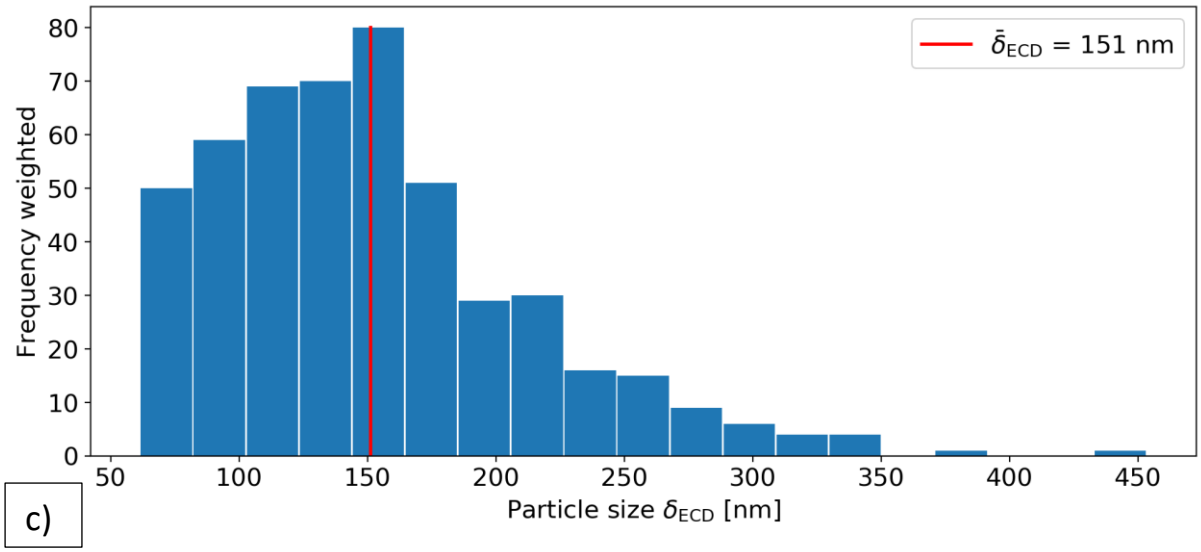

Figure D.23: Particle distribution of the images taken of %CR87-280.

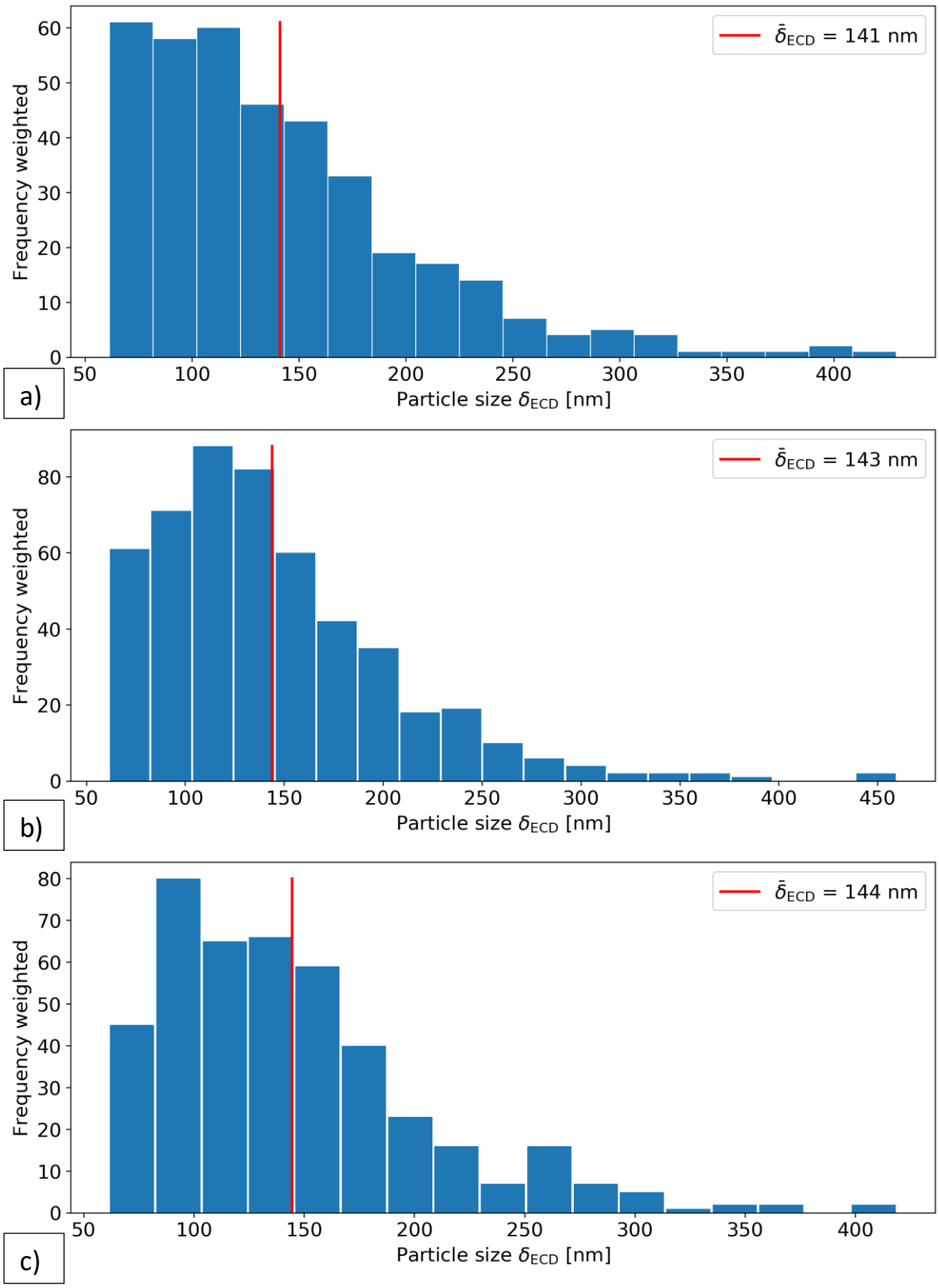

Figure D.24: Particle distribution of the images taken of %CR46-330.

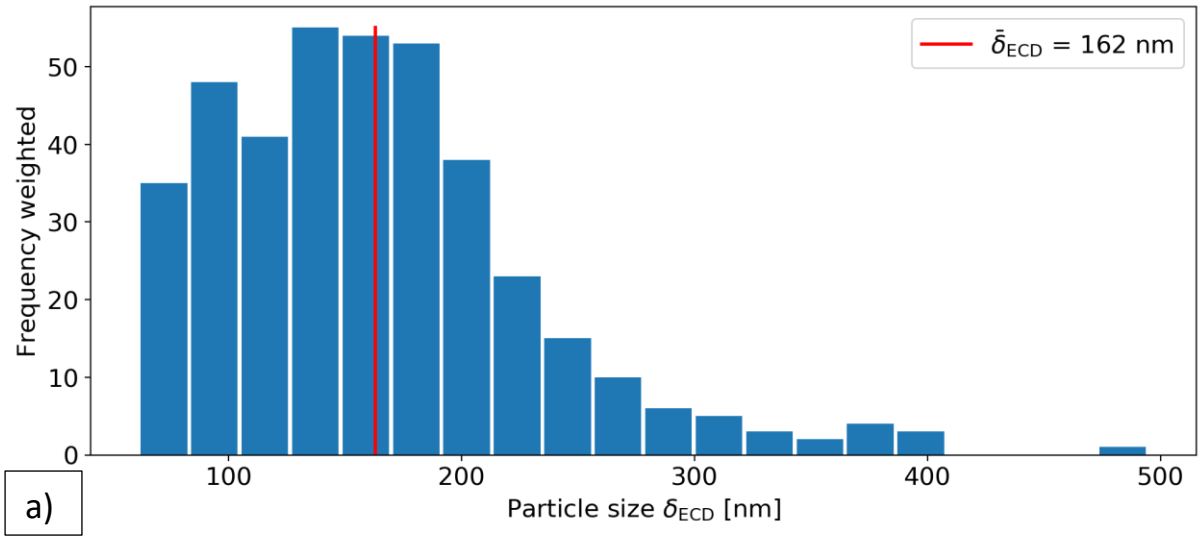

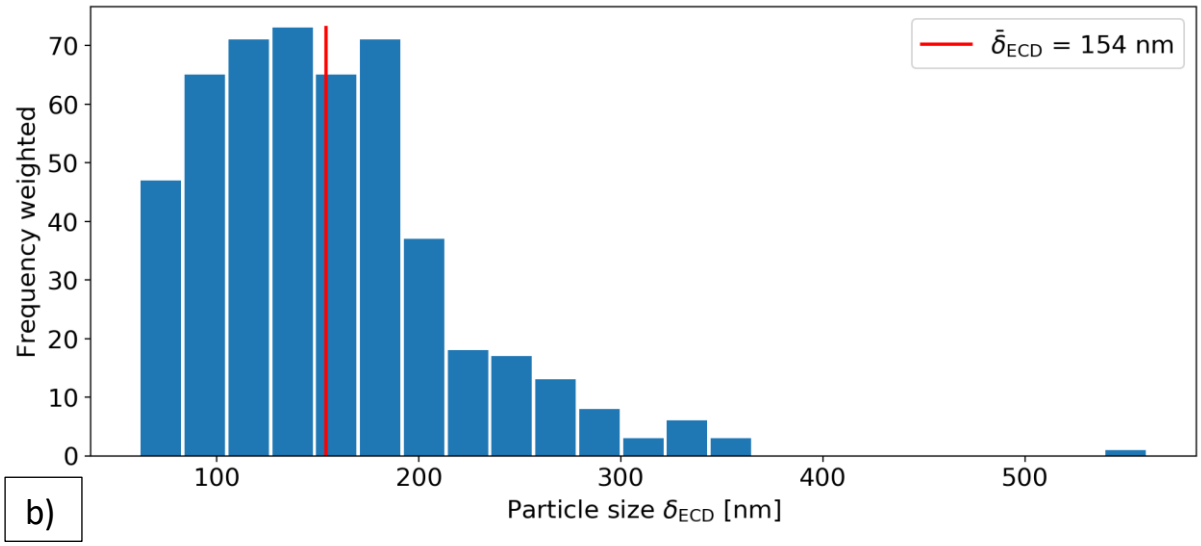

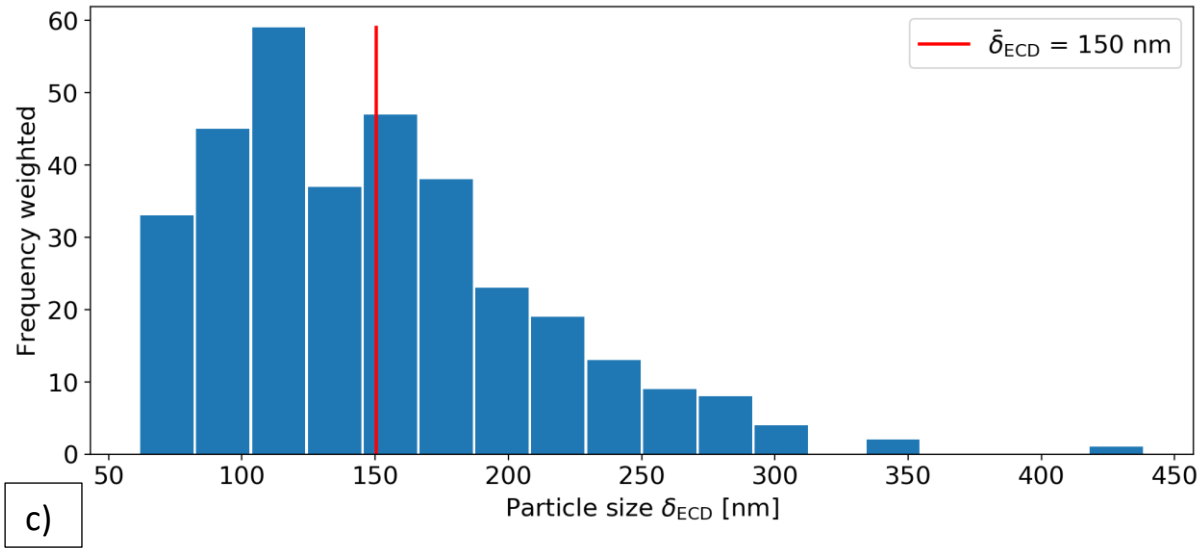

Figure D.25: Particle distribution of the images taken of %CR67-330.

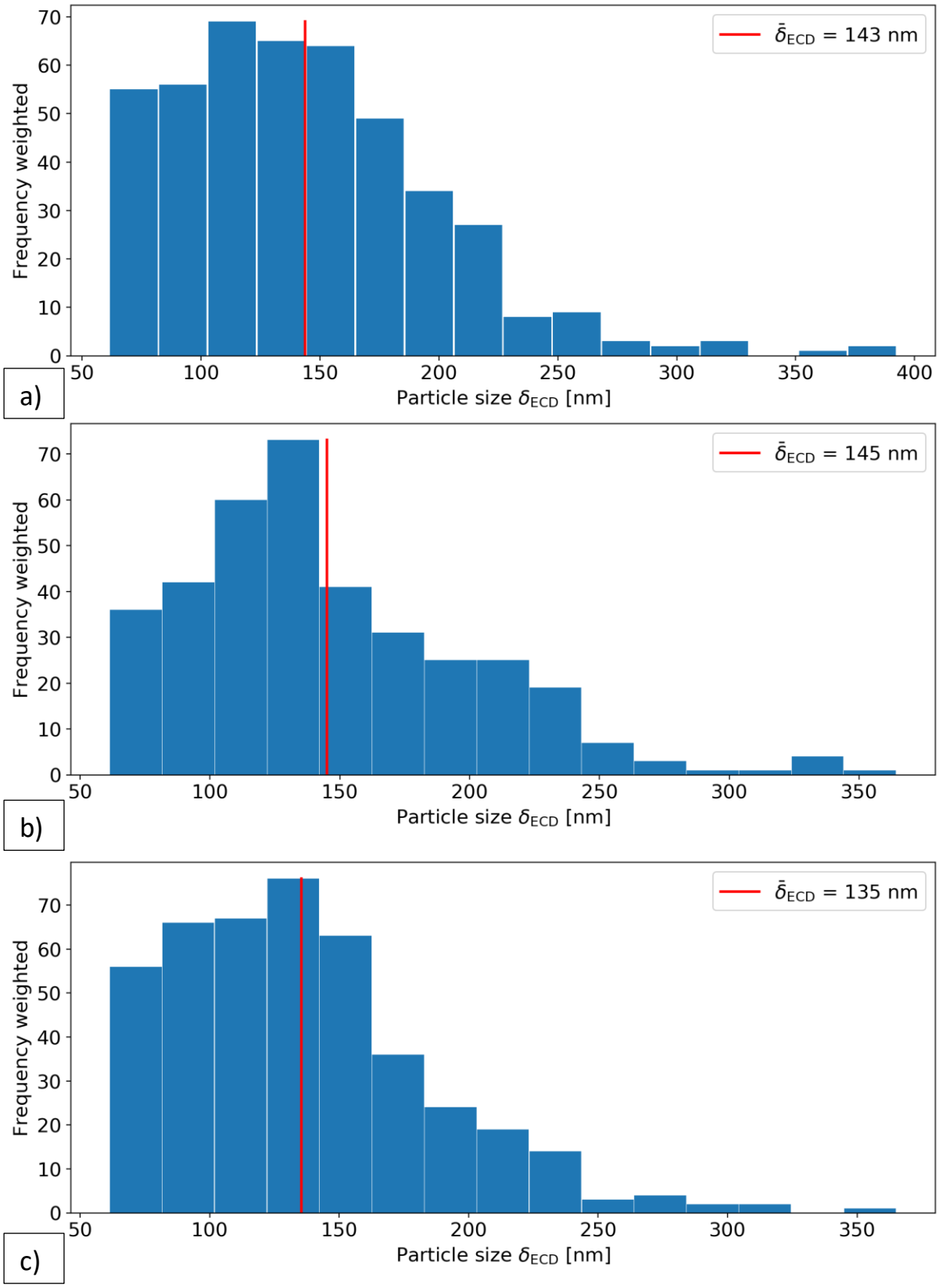

Figure D.26: Particle distribution of the images taken of %CR87-330.

Eirik Bugten Hamnes

Softening Behaviour of a Commercial Al-Mn-Mg Alloy

NTNU
Norwegian University of
Science and Technology